Digital reconstruction, quantitative morphometric analysis, and membrane properties of bipolar cells in the rat retina.

Rémi Fournel

Thesis for the degree of Philosophiae Doctor (PhD)
University of Bergen, Norway
2021

UNIVERSITY OF BERGEN

Digital reconstruction, quantitative morphometric analysis, and membrane properties of bipolar cells in the rat retina.

Rémi Fournel

Thesis for the degree of Philosophiae Doctor (PhD)
at the University of Bergen

Date of defense: 29.09.2021

Year: 2021

Title: Digital reconstruction, quantitative morphometric analysis, and membrane properties of bipolar cells in the rat retina.

Name: Rémi Fournel

Print: Skipnes Kommunikasjon / University of Bergen

Scientific environment

This project was performed in the Neural Networks Research Group at the Department of Biomedicine, University of Bergen, during the years 2016-2021 under the supervision of Professors Margaret Veruki and Espen Hartveit. As part of the European training network ***switchBoard***, this project received funding from the European Union's Horizon 2020 research and innovation program under the Marie Skłodowska-Curie grant agreement N°674901. Short research stays at the Molecular Sensory Physiology and Pharmacology Group, Department of Pharmacology and Toxicology, University of Innsbruck, Austria with Prof. Alexandra Koschak and at the Retinal Neurobiology in Health and Disease Group, Institute of Neuroscience, CNR, Pisa, Italy with Prof. Enrica Strettoi were financed by ***switchBoard.*** Additional financial support was provided by the Research Council of Norway (NFR 213776 and 261914 to M. L. Veruki and 182743, 189662, and 214216 to E. Hartveit) and the Norwegian Research School in Neuroscience.

Acknowledgments

First and foremost, I do not have enough words to express all my gratitude to my supervisor Professor Margaret Lin Veruki. I really thank you for your guidance, patience, and kindness during these five years. I appreciate that you were always available and open to the discussion whatever the question or the topic. I have learned much more working with you than simply great science, you have motivated, pushed me to work harder to become a better scientist and person, even keeping faith in me even when mine was faltering. I think I was really lucky to have you as my supervisor and without your help and patience, this work would have never been completed. I also want to express my gratitude to Professor Espen Hartveit for all his help and guidance. I am really thankful for those long discussions during the Monday meeting, which you have transformed into what I think is the best science training course I ever had on both developing my way of reasoning about research questions and my curiosity about the history of science. Your critical thinking, scrutiny, and insight have made you more than often the arbiter between Meg and me and have helped this project tremendously. I also want to thank you together as I am deeply impressed by the example you set for me by your hard work and the way you support and complete each other, working with you during those years made me often think you incarnate well this citation of Aristotle "the whole is greater than the sum of its parts". Thank you both for giving me that opportunity in your lab and for all the work done these past years.

I also want to express my thanks to Drs. Bas-Jan Zandt and Barbora Tencerova for welcoming me in the lab and showing me the rope of respectively the joy of coding and reconstructing and of patch-clamping. To my colleagues during all these years Drs. Àurea Castilho, Jeet B. Singh, Pablo Beltràn, Jian Hao Liu it was a great pleasure to work with you all, thank you for all of the nice time with the animated discussion during coffee and lunch breaks. Àurea, you are one of the kindest persons I know, and I wish you that the future will bring all that you deserved. Jeet, I wish you and your new family all the best in your new adventures in the US. Jian Hao, thank you for your always calm and rational thinking which has been often a precious help, and also for all your codes that save me so much time. I have known you as a scientist and I have no doubt you

will become a great medical doctor. Pablo, meeting you, I have been blessed with finding true friendship. I cannot recall all the time we spend discussing science and everything together, and all the nice moments we had in Bergen and around. I also have to thank you for welcoming me into your home when I needed it, without you this thesis would have probably never been finished. I have seen you from the start to the end of your Ph.D. and I am sure you will become a great scientist. Through you, I have to extend my thanks to Ida who has been so kind to welcome me and for all these cheerful evenings. I wish you both all by best. I also want to thank Torhild Fjordheim Sunde for your technical help and your unwavering cheerfulness (and let be honest your cakes).

I acknowledge the support of the people in the Department of Biomedicine. I would like especially to thank Elisabeth Hove and Margarethe Bittins for their help with the sometimes burdensome administrative works of the thesis and the training network.

I wish to show my appreciation to all the SwitchBoard fellowship for the great opportunity it gave me to travel across all Europe to learn so much, discover the quality and diversity in science across the small family that is the retina research. In this regard, I wish to address my special thanks to Professor Enrica Strettoi and Professor Alexandra Koschack for their warm welcome in their labs during my secondments, and to Professor Thomas Euler and Doctor Michaela Bitzer for their incredible work that makes this unique experience a success. I also want to thank all my fellow ESRs who have been with me during this training, and especially Maxime and Lucia for all the great times with had in Bergen, Innsbruck, and Tübingen and of course our memorable trip to Kerala.

Marine, my love, and best friend. Thank you for accepting the distance separating us despite how hard it was. Your unending support, encouragements, and precious advice during those years are the most precious gifts you ever give me.

To our family and our parents thank you for your love and support. Mom and Dad thank you for believing in me and your support even when sometimes the distance made things complicated. Maman, Papa et Vincent merci de toujours avoir été là.

Abstract

A basic principle of neuroscience is that structure reflects function. This has led to numerous attempts to characterize the complete morphology of types of neurons throughout the central nervous system. The ability to acquire and analyze complete neuronal morphologies has advanced with continuous technological developments for over 150 years, with progressive refinements and increased understanding of the precise anatomical details of different types of neurons.

Bipolar cells of the mammalian retina are short-range projections neurons that link the outer and inner retina. Their dendrites contact and receive input from the terminals of the light-sensing photoreceptors in the outer plexiform layer and their axons descend through the inner nuclear and inner plexiform layers to stratify at different levels of the inner plexiform layer. The stratification level of the axon terminals of different types of bipolar cells in the inner plexiform layer determines their synaptic connectivity and is an important basis for the morphological classification of these cells.

Between 10 and 15 different types of cone bipolar cells have been identified in different species and they can be divided into ON-cone bipolar cells (that depolarize to the onset of light) and OFF-cone bipolar cells (that depolarize to the offset of light). Different types of cone bipolar cells are thought to be responsible for coding and transmitting different features of our visual environment and generating parallel channels that uniquely filter and transform the inputs from the photoreceptors. There is a lack of detailed morphological data for bipolar cells, especially for the rat, where biophysical mechanisms have been most extensively studied. The work presented in this thesis provides the groundwork for the future goal of developing morphologically realistic compartmental models for cone and rod bipolar cells.

First, the contribution of gap junctions to the membrane properties, specifically input resistance, of bipolar cells was investigated. Gap junctions are ubiquitous within the retina, but it remains to be determined whether the strength of coupling between specific cell types is sufficiently strong for the cells to be functionally coupled via electrical synapses. There are gap junctions between the same class of bipolar cells,

and this appears to be a common circuit motif in the vertebrate retina. Surprisingly, our results suggested that the gap junctions between OFF-cone bipolar cells do not support consequential electrical coupling. This provides an important first step both to elucidate the potential roles for these gap junctions, and also for the development of compartmental models for cone bipolar cells.

Second, from image stacks acquired from multiphoton excitation microscopy, quantitative morphological reconstructions and detailed morphological analysis were performed with fluorescent dye-filled cone and rod bipolar cells. Compared to previous descriptions, the extent and complexity of branching of the axon terminals was surprisingly high. By precisely quantifying the level of stratification of the axon terminals in the inner plexiform layer, we have generated a reference system for the reliable classification of individual cells in future studies that are focused on correlating physiological and morphological properties. The workflow that we have implemented can be readily extended to the development of morphologically realistic compartmental models for these neurons.

Contents

List of publications

Paper I

Fournel, R., Hartveit, E., and Veruki, M.L. (2021).
Differential contribution of gap junctions to the membrane properties of ON- and OFF-bipolar cells of the rat retina.
Cell Mol Neurobiol 41(2):229-245.

Paper II

Fournel, R., Veruki, M.L., and Hartveit, E. (2021).
Digital reconstruction and quantitative morphometric analysis of bipolar cells in live rat retinal slices.
Manuscript.

Abbreviations

Symbol	Description	Units
3-D	three dimensional	
A17	A17 (or AI) type amacrine cell	
AII	AII type amacrine cell	
AMPA	α-amino-3-hydroxy-5-methyl-4-isoxazolepropionic acid	
cAMP	cyclic adenosine monophosphate	
Ca_V	voltage-gated calcium channel	
C_{fast}	patch pipette capacitance	pF
Chrm2	cholinergic receptor muscarinic 2 gene	
C_m	specific membrane capacitance	$\mu F \cdot cm^{-2}$
Cpne9	copine family member 9 gene	
C_{slow}	recorded cell membrane capacitance	pF
Cx	connexin	
d	diameter	nm
d_{max}	maximum sampling distance	μm
GABA	γ-aminobutyric acid	
GCL	ganglion cell layer	
GluMi	glutamatergic monopolar interneurone	
HCN	hyperpolarized-activated cyclic nucleotide-gated	
HEPES	4-(2-hydroxyethyl)-1-piperazineethanesulfonic acid	
I	current	pA
I_{Ca}	calcium current	
I_h	hyperpolarized-activated current	
I_{Na}	sodium current	
INL	inner nuclear layer	
IPL	inner plexiform layer	
I_{KIR}	inward rectifying potassium current	
K_V1.1-1.3	mammalian voltage-gated potassium channel of the *shaker* family	
Lrrtm1	leucine rich repeat transmembrane neuronal 1 gene	
M-cone	middle-wavelength sensible cone photoreceptor	
mGluR6	metabotropic glutamate receptor type 6	
MPE	multiphoton excitation	
MRF	Multi Run Fitter	
n	refractive index	
N_A	numerical aperture	
Na_V	voltage-gated sodium channel	
ON-ChAT	ON choline acetyltransferase labeled band	
ONL	outer nuclear layer	
OPL	outer plexiform layer	
PKARIIβ	protein kinase A regulatory subunit IIβ	

Symbol	Description	Units
PKCα	protein kinase Cα	
PRAXIS	point-to-point principal axis	
PSF	point-spread function	
r	resolution	μm
R_a	axial resistivity	Ω·cm
R_N	input resistance	GΩ
RBC	rod bipolar cell	
RC-circuit	electric circuit composed of parallel resistors and capacitors	
R_m	specific membrane resistance	kΩ·cm^{-2}
RNA	ribonucleic acid	
R_s	series resistance	MΩ
S-cone	short-wavelength sensible cone photoreceptor	
Serpini1	serpin family I member 1 gene	
Slitrk5	SLIT and NTRK like family member 5 gene	
SNR	signal to noise ratio	
Sox6	SRY-box transcription factor 6 gene	
TRPM1	transient receptor potential cation channel subfamily M member 1	
UV-cone	UV wavelength sensible cone photoreceptor	
vGluT1	type 1 vesicular glutamate transporter	
V_{rest}	resting potential	mV
ZD7288	4-ethylphenylamino-1,2-dimethyl-6-methylaminopyrimidinium chloride	
λ_{ex}	excitation light wavelength	nm

1. Introduction

More than 150 years ago, Ramòn y Cajal used the newly developed Golgi-Cox staining method to describe the incredible diversity and complexity of the morphology and connectivity of neurons in his detailed studies of various regions of the nervous system, notably the retina, cerebellum, and cortex in several mammalian, reptile, and avian species (Janssens et al., 1893). This work led him to develop the neuron doctrine and to define neurons as the morphological and functional units of the nervous system (Janssens et al., 1893). Understanding the nervous system requires knowing the properties of the different types of neurons and how these properties contribute to the role of individual neurons in neuronal circuits. Neurons can be studied at different levels, but the most fundamental level to understand their computing properties is the neuron passive properties. These passive properties are the combination of the passive properties of the neuronal membrane and the neuron morphology. In this thesis, we provide a detailed analysis of the morphology and study some membrane properties of the bipolar cells, a central element of the retina circuit connecting all the other retina neurons. These investigations provide some clues and the groundwork for the future goal of understanding the computation properties of bipolar cells.

1.1 The retina: a model of neuron circuitry

The retina is the part of the central nervous system involved in the early phase of the visual pathway, which ultimately gives rise to visual perception and, as such, can be considered as one of the most important means by which we gain information about our environment. The retina's role is first to detect the incident light then generate biochemical signals that are then analyzed in complex neuronal networks to extract numerous features of a given visual stimulus. This information is then sent via the optic nerve to higher visual pathway centers, where visual signals reach consciousness. The structure and accessibility of the retina make it an excellent system to investigate information-processing mechanisms in the central nervous system.

1.1.1 Laminar organization of the retina

The mammalian retina is a complex tissue with a very structured organization known and studied for more than a century (Polyak, 1953). This structure, divided into ten layers, reflects a strict positioning and relationship between the different retinal cells (Fig. **1.1**). Following the light path, the innermost layer is the *inner limiting membrane*, a basal lamina formed by astrocytes, and the Müller cells' end-feet. Together with the microglia, astrocytes and Müller cells are the three types of glial cells present in the retina. The Müller cells are the most abundant type of glial cell in the retina; they expand radially through the entire retina interacting with all the other cell types (Bringmann et al., 2006). Being the bridge between the blood vessels and the retinal neurons, they have a crucial role in the metabolism of the retina, providing energy to the neurons through glucose brought by the vascular circulation. Müller cells play an essential role in extracellular glutamate, extracellular potassium, and water homeostasis and are major actors in retina angiogenesis (Li et al., 2019).

Proximal to the inner limiting membrane, the next layer is the *nerve fiber layer,* composed of all the axons of the retinal ganglion cells. The cell bodies of ganglion cells and displaced amacrine cells, in similar proportions, form the next layer, the *ganglion cell layer* (GCL) (Perry and Walker, 1980). The dendrites of the ganglion cells and amacrine cells form complex connections with retinal bipolar cells in the next layer, the *inner plexiform layer* (IPL). Next is the *inner nuclear layer* (INL), where the soma of bipolar cells, amacrine cells, and horizontal cells are located. The synapses of the bipolar cells with the horizontal cells and the photoreceptors form the *outer plexiform layer* (OPL).

The photoreceptors span the subsequent four proximal layers of the retina: their pedicles interact with the dendrites of the bipolar cells in the *outer plexiform layer*, they have their nucleus laying in the outer nuclear layer with the nucleus of the Müller cells, the inner segment contains the mitochondria necessary to the cells to maintain the phototransduction. It is only in the *photoreceptor layer* that the light, having crossed through all the previously described layers, is finally detected in the outer segments of

the photoreceptors by interacting with the pigments contained in the membrane-bound lamellae or disks. This interaction induces the phototransduction cascade hyperpolarizing the photoreceptors (Stryer, 1991). Between the outer and the inner segments of the photoreceptor, the Müller cells form a zonula adherent or desmosome with the photoreceptors creating the *outer limiting membrane* (Bunt-Milam et al., 1985).

The last and outermost retinal membrane is the *retinal pigment epithelium,* composed of a monolayer of pigmented epithelium. At their apical side, the epithelium cells possess microvilli interacting closely with the outer segments of the photoreceptors. At their basal membrane, the epithelium cells rest on a layer of extracellular matrix called Bruch's membrane, making the separation with the choriocapillaries. These epithelium cells create structural support for the retina, and they have the functional role of absorbing the remaining light, sustaining the phototransduction, being the metabolic support of the photoreceptors, and secreting a variety of growth factors (for review see Lakkaraju et al., 2020; Strauss, 2005).

1.1.2 Neurons in the retina

The retina possesses five main classes of neurons that constitute an excitatory vertical circuit and two horizontal circuits. The three excitatory neuron classes are the photoreceptors that detect light, then the bipolar cells, and finally, the ganglion cells, which are the only output neurons of the retina. The two types of interneurons are the horizontal cells that regulate photoreceptors and bipolar cells and the amacrine cells that modulate bipolar cells and ganglion cells.

Photoreceptors

Mammalian retinas express two kinds of photoreceptors: cones and rods. The low noise in the rod photoreceptors and their ability, under dark adaptation, to detect single photons (Baylor et al., 1979; Hecht et al., 1942) are well suited for scotopic vision. In contrast, cones have higher noise but a faster light response, function over a vast range of intensity, avoid saturation in constant background illumination, and possess a short time constant for the recovery of responsiveness, making them well suited for light

detection in the photopic range (for review see Lamb, 2010). Both types of photoreceptors express light-sensitive molecules comprising an opsin protein with a light-sensitive chromophore attached. The rhodopsin pigment in rods has its absorption peak around ~500 nm (Hubbard, 1969). The cones can express one of four opsins, classified depending on their spectral absorption properties: two short-wavelength sensitive opsins, one middle-wavelength sensitive opsin, and one long-wavelength sensitive opsin. Like most nocturnal mammalian retinas, the murine retina is rod-dominated, with ~3% of the photoreceptors being cones (Szél et al., 1996).

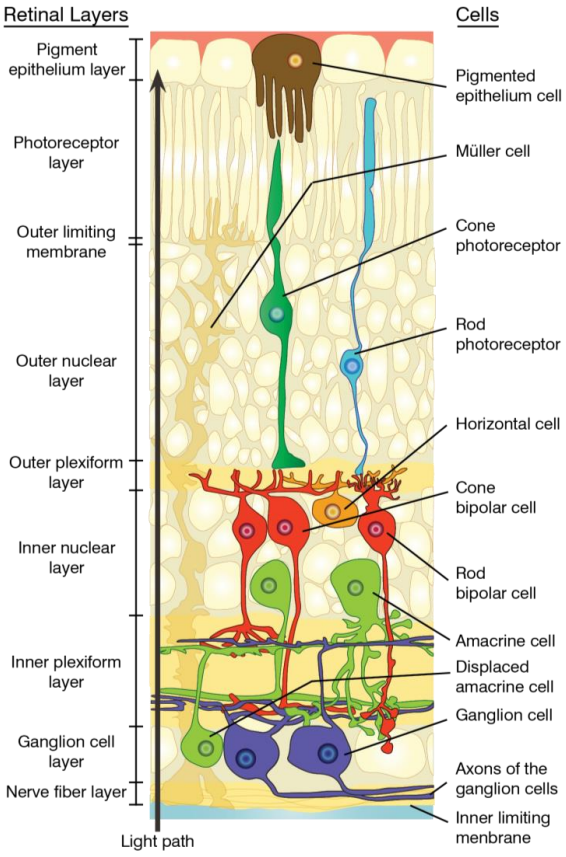

Figure 1.1: Schematic representation of the structure and laminar distribution of the cells in the mammalian retina. See text for explanation.

There is a steady release of glutamate from the photoreceptors in the dark at the synapses between photoreceptors, horizontal and bipolar cells due to the depolarizing inward current mediated by a cation permeable channel on their outer-segment membrane. The phototransduction cascade, resulting from photons and opsins interactions, closes the cation channels, which stops the depolarizing inward currents, thus hyperpolarizing the cell. This hyperpolarization reduces the synaptic release of glutamate from the photoreceptors (reviewed in Fu and Yau, 2007).

Bipolar cells

Bipolar cells will be described in greater detail below. For now, it is sufficient to say that they receive light-evoked signals from photoreceptors and that these inputs evoke different responses in the ~10-15 mammalian bipolar cell types (Euler et al., 2014). Bipolar cells form three classes and generate the main parallel pathways in the retina. The cone bipolar cells receive their input from the cone photoreceptors and based on their responses, they fall into two categories: ON-bipolar cells activated by light onset and the OFF-bipolar cells activated by light offset. The rod photoreceptors synapse into the rod bipolar cells, which are all ON-bipolar cells and represent more than 40% of all bipolar cells in rod-dominated retinas (Wässle et al., 2009).

Horizontal cells

Horizontal cells are the inhibitory interneurons of the outer plexiform layer retina circuit. Their cell bodies lie in the inner nuclear layer, and their processes all extend into the OPL. Horizontal cells express ionotropic glutamate receptors of the AMPA type at their dendrites, therefore, depolarize in response to glutamate release in the dark and hyperpolarize during light activation (Brandstätter et al., 1997; Hack et al., 2001; Schubert et al., 2006; Ströh et al., 2013). In the mammalian retina, horizontal cells are divided morphologically into two broad classes, referred to as type A for axonless and type B for axon-bearing horizontal cells. Murine species have only one type of axon bearing horizontal cell and lack the type A horizontal cells (Peichl and González-Soriano, 1994). The dendrites of axon-bearing horizontal cells are postsynaptic to cones, and their axon terminals are postsynaptic to rods. The primary function of the horizontal cells is to shape the receptive field of the bipolar cells through negative

feedback to cone and rod photoreceptors (for review, see Thoreson and Mangel, 2012; Diamond, 2017; Thoreson and Dacey, 2019).

Amacrine cells

The name "amacrine" cells (given by Ramòn y Cajal from the Greek: *α*, without; *μακφος*, long; *ινοσ*, fiber) comes from their lack of axonal processes. Instead, amacrine cells transmit synaptic output from the same neurites from which they receive inputs (Dowling and Boycott, 1966). The bipolar cells provide them with excitatory inputs, and in return, they provide a wide variety of feedback and feedforward inhibitory and excitatory inputs back to the inner plexiform circuit (Masland, 2012a). Feedback and feedforward mechanisms arise from contact through electrical synapses to bipolar cells (Dacheux and Raviola, 1986), ganglion cells (Marc et al., 2018; Pang et al., 2013; Xin and Bloomfield, 1997), and amacrine cells of the same (Hartveit and Veruki, 2012) or different type (Pan et al., 2010) and chemical synapses to bipolar cells, amacrine cells and ganglion cells (Diamond, 2017). The size of their dendritic arbors, small- or wide-field, and the primary neurotransmitter they release, are the main criteria to classify the amacrine cells. Thereby, amacrine cells are divided into four groups: wide-field GABAergic, small-field glycinergic, glutamatergic, and non-GABAergic non-glycinergic amacrine cells (Diamond, 2017). A recent connectomic study of a small volume from mouse retina identified morphologically 45 amacrine cell types (Helmstaedter et al., 2013). A single-cell transcriptomic study expanded this classification to reach 63 distinct amacrine cell profiles getting very close to a complete catalog (see discussion in Yan et al. 2020). Amacrine cell diversity in type, synaptic motif, and neurotransmitter release underlies complex mechanisms that transform ~12 bipolar cell information channels to the ~40 visual signal features encoded by ganglion cells. Although most of these mechanisms are still poorly understood, some pathways have started to give away their secrets (see below for the rod pathway and see Diamond, 2017, for review).

Ganglion cells

Like amacrine cells, ganglion cells integrate the inputs from bipolar cells, and they receive direct input from some amacrine cells (Masland, 2012b). Baden and colleagues

(2016) classified the mouse ganglion cells into 32 functional types depending on their Ca^{2+}-evoked response to a set of visual stimuli. This number of retinal ganglion cells is consistent with other studies using the same technique described previously for the amacrine cells, which clustered ~40 types of ganglion cells (Bae et al., 2018; Rheaume et al., 2018; Tran et al., 2019). Similar studies are not available in rat, but previous smaller-scale studies using the same technique in mouse showed similar morphological diversity in both species (see discussion in Sun et al., 2002b, 2002a). Ganglion cell axons form the nerve fiber layer and leave the retina creating the optic nerve. The ganglion cells project to ~40 different targets in the brain, mainly in the dorsal lateral geniculate nucleus and superior colliculus (*mouse*: Lawrence and Studholme, 2014; *rat* reviewed in Sefton et al., 2015).

1.1.3 Synapses and synaptic transmission in the retina

With the exception of the ganglion cells, most retinal neurons do not use action potentials but, instead, use a graded variation of their membrane potential to generate their output signals. For the photoreceptors and bipolar cells, this results in a variable but constant flux of glutamate release at their output synapse. A specialized synaptic structure called a ribbon synapse allows these cells to maintain a high synaptic vesicle release rate (for review, see LoGiudice and Matthews, 2009 and Tom Dieck and Brandstätter, 2006). Amacrine cells and horizontal cells use chemical synapses to send inhibitory inputs to their post-synaptic partners (Chapot et al., 2017; Kolb, 1979).

In addition to chemical synapses, retinal cells are also interconnected in complex networks through electrical synapses (Völgyi et al., 2013). Six connexin proteins assembled in a hemichannel within the cell membrane connect with another hemichannel in a neighboring cell to form a gap junction creating a functional electrical synapse (Kumar and Gilula, 1996). These electrical synapses can be either between neurons of the same class forming, homologous gap junctions, between neurons of different classes, forming heterologous gap junctions, or in some retinal neurons both exist (Trenholm and Awatramani, 2017). In photoreceptors, the primary electrical synapses are between cones and rods (Jin et al., 2020). Additionally, there is evidence

for homologous junctions between cones (DeVries et al., 2002). In invertebrates, rods make homologous junctions (Attwell et al., 1984; Zhang and Wu, 2005). Conversely, in mammals, the homologous coupling of rods is controversial. As mentioned before, gap junctions in horizontal cells modulate the receptive field size of bipolar cells (Thoreson and Mangel, 2012). Gap junctions in bipolar and amacrine cells allow for the spread of signals from rod to cone circuits and allow for synchrony between coupled networks; for more details see figure **1.2** and section **1.3.2**. Finally, in ganglion cells, electrical synapses promote synchronous spike activity. There is also evidence that coupling between ganglion cells can endow them with the capability to respond differentially to static and moving visual stimuli (for review, see Trenholm and Awatramani, 2019).

1.1.4 Bipolar cells in the visual pathways

ON/OFF dichotomy

The synaptic contact between photoreceptors and bipolar cells is where the main dichotomy of the ON- and OFF-pathways occurs. OFF-bipolar cells express ionotropic glutamate receptors, which depolarize the cell in response to the glutamate released in the dark and hyperpolarize the cell when light decreases the glutamate release from cones (Puller et al., 2013). ON-bipolar cells express the metabotropic glutamate receptor type 6 (mGluR6) (Masu et al., 1995). Under the glutamate influx from the photoreceptor, mGluR6 receptors inhibit the transient receptor potential cation channels subfamily M member 1 (TRPM1). At light onset, the decrease in glutamate released from cones reduces mGluR6 activation leading, to the release of the inhibition of TRPM1 channels. TRPM1 channels open and depolarizes the ON-cone bipolar cell (Koike et al., 2010). The ON and OFF inputs are then integrated into several circuits that compute different visual features (Euler et al., 2014).

The primary rod and cone pathways

The retina can detect the broadest range of input intensity of all the sensory organs, representing more than 18 log units of light intensity variation (Land and Nilson, 2012). The scotopic domain ranges from the lowest luminance detectable (10^{-6} cd.m^{-2}) to 10^{-2}

cd.m^{-2}. In this range of light intensities, the rod photoreceptors solely convey the visual stimulus. At luminosity above ~3 cd.m^{-2}, the photopic domain begins and the rods start to saturate, and the cone pathway dominates the visual processing (Land and Nilson, 2012). At scotopic light intensity, the luminosity is insufficient to activate the cone photoreceptors, and only the rod photoreceptors drive the light response through four different rod pathways. The primary rod pathway starts with the rod inputs transmitted to the rod bipolar cells (Fig. **1.2**). The rod bipolar cell axon terminal does not directly contact ganglion cells but forms, in the IPL, a tripartite synapse arranged as a dyad with two post-synaptic amacrine cells: the AII and A17 (Chun et al., 1993; Sandell et al., 1989; Strettoi et al., 1990). The A17 amacrine cell (also called AI) (Chun et al., 1993; Menger and Wässle, 2000; Nelson and Kolb, 1985) forms an inhibitory reciprocal synapse to the rod bipolar cell. A17s, in response to glutamatergic input, send GABAergic signals modulating the release of glutamate from rod bipolar cells (Chávez et al., 2006; Dacheux and Raviola, 1986; Dowling and Boycott, 1966; Hartveit, 1999; Kolb and Nelson, 1983; Raviola and Dacheux, 1987). Despite their large dendritic tree, A17 cells do not seem to be involved in transmitting information across the retina circuit. Instead, A17 cells create locally isolated feedback microcircuits with the rod bipolar cells at each of their varicosities (Elgueta et al., 2018; Grimes et al., 2010). The other post-synaptic partner, the narrow-field glycinergic AII amacrine cell, is the most numerous amacrine cell in the retina (~12 %) (Menger et al., 1998; Strettoi and Masland, 1996). In the primary rod pathway, AII amacrine cells drive the inputs from rod bipolar cells to the cone pathway (Fig. **1.2**). The bistratified structure of the AII amacrine cell drives its signaling output (Marc et al., 2014; Strettoi et al., 1992; Tsukamoto and Omi, 2017; Zandt et al., 2017). The outer stratified branches, called lobular dendrites, make inhibitory glycinergic synapses with the axon terminals of OFF cone bipolar cells, principally cone bipolar cell type *2* (Graydon et al., 2018), as well as with the dendrites of OFF α and δ ganglion cells and sustained-by-contrast ganglion cell (Demb and Singer, 2012; Jacoby et al., 2015). The branches stratifying in the inner part of the inner plexiform layer, called arboreal dendrites, make electrical synapses with the ON cone bipolar cells (Dacheux and Raviola, 1986; McGuire et al., 1984; Tsukamoto and Omi, 2017; Veruki and Hartveit, 2002b), transmitting a sign-conserved

signal from the rod bipolar cells to the ON ganglion cells through the bipolar cells. AII amacrines cells are also interconnected by gap junctions, forming a vast network of electrically coupled neurons (Veruki and Hartveit, 2002a).

In the mouse, however, the clear segregation between the rod and cone pathways at different light intensities is more nuanced than described above. Rod photoreceptors can be active at daylight (Altimus et al., 2010; Naarendorp et al., 2010; Pasquale et al., 2020; Tikidji-Hamburyan et al., 2017), and AII amacrine cells, the critical component of the rod bipolar cell pathway, are known to play a different role at photopic luminosity (Münch et al., 2009; Oesch and Diamond, 2009).

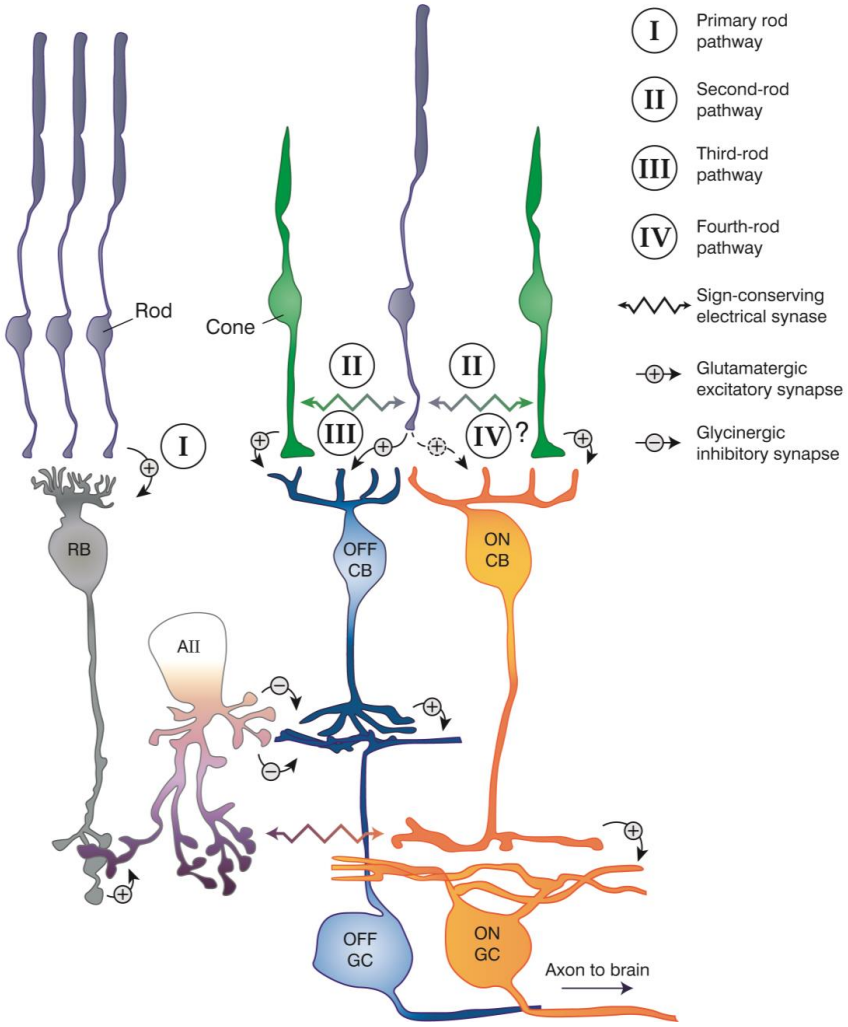

Figure 1.2: Diagram of four rod-driven signal pathways: I) Primary rod pathway: rods → rod bipolar cell (RB) → AII amacrine cell (AII). Then, AII cells send inputs to the OFF-cone bipolar and ganglion cells (OFF-CB, OFF-GC) via conventional synapses; and AII cells send inputs to ON-cone bipolar cell (ON-CB) via electrical synapses; II) Second-rod pathway: rods → cones → OFF-CB, ON-CB → OFF-GC, ON-GC; III) Third-rod pathway: rods → OFF-CB → OFF-GC; IV) Hypothesized fourth-rod pathway: rods → ON-CB → ON-GC.

1.2 Bipolar cells

1.2.1 Cell classification

The work outlined in this thesis investigates some properties of the retinal bipolar cells and how these properties might differ between the different bipolar cell types. The next section will address in detail how the different types of bipolar cells have been classified throughout history to reach a better understanding of the origin and limitation of the current bipolar cell type classifications in the different mammalian animal models.

Origins of the bipolar cell classification

The classification of bipolar cells starts at the dawn of cellular neuroscience, as the retina is one of the first regions studied by Ramòn y Cajal (1888a, 1888b), following the work of Dogiel (1888) and Tartuferi (1887) (Jones, 2011) using the argentic staining technique to reveal the morphology of neurons. In these early works, the main features of the morphological classification were already pointed out: (1) bipolar cell dendrites contact the photoreceptors in the outer plexiform layer with some different connection patterns; (2) bipolar cell axon terminals stratify in a laminar fashion at different depths of the inner plexiform layer with at least one type of bipolar cell stratifying at each of the five sublamina of the inner plexiform layer (Janssens et al., 1893). The first classification of bipolar cells was proposed based on the shape of the dendritic trees and dendritic tips by Polyak (1949), which he defines as mop-like, brush-like, and flat-topped bipolar cells. Based on their exclusive connectivity to the rod photoreceptor, mop-like bipolar cells were identified as rod bipolar cells, as for flat-topped and brush-like bipolar cells they contact cone photoreceptors thus were identified as cone bipolar cells. Cone bipolar cells were further divided into ON and OFF cone bipolar cells based on the functional response of the center of their receptive field (Kaneko, 1970; Werblin and Dowling, 1969). The functional cone bipolar cell types were identified morphologically based on the ultrastructure of their dendritic tips, which are either flat for the OFF-bipolar cells or invaginating in the photoreceptor

pedicle for the ON-bipolar cells (Boycott and Dowling, 1969; Dowling and Boycott, 1966; McGuire et al., 1984).

Early-works: Nomenclature and single-cell based morphological identification.

The first published identification of different types of mammalian cone bipolar cells used Golgi staining and identified 7-9 different cone bipolar cells in the squirrel retina (West, 1976, 1978). Shortly after, based on the functional response of vertebrate and mammalian ganglion cells to light stimuli, the inner plexiform layer was divided into two functional layers: an OFF layer called sublamina a (corresponding to Cajal's sublamina 1 and 2) and an ON layer called sublamina b (corresponding to Cajal's sublamina 3 to 5) (Nelson et al., 1978). Using this, Famiglietti (1981) developed a classification nomenclature segregating the OFF- and ON-bipolar cells based on their stratification level in sublamina a or sublamina b and the size of their dendritic field (narrow, medium, or wide), classifying nine types of cone bipolar cell based on Golgi staining with five OFF- and four ON-cone bipolar cells in cat and rabbit retina. In parallel, Kolb proposed a numerical classification of the cone bipolar cells based only on their level of axonal stratification resulting in eight types of cone bipolar cells (*cb1-8*), with type *1* being the cone bipolar stratifying the closest to the inner nuclear layer and type *8* stratifying furthest away (Famiglietti and Kolb, 1976; Famiglietti et al., 1977; Kolb et al., 1981). Afterward, McGuire (McGuire et al., 1984) combined the two previous nomenclature systems into a numerical classification of the bipolar cell type by axonal stratification level and dividing the bipolar cell types stratifying in sublamina a or b. This work used electron micrograph serial section reconstruction to identify four OFF bipolar cells and three ON bipolar cells. Using the same technique and classification system, Cohen and Sterling (Cohen and Sterling, 1990b, 1990a) extended the previous classifications to four types of OFF bipolar cells (*a1-4*) and five types of ON bipolar cells (*b1-5*) in the cat retina. However, the interest in the cat retina as a model organism shifted to smaller organisms like rats, mice, and rabbits, which have inherited the bipolar cell classification nomenclature developed for the cat. The first morphological classification of bipolar cells in rat and mouse retina used Kolb's nomenclature, focusing primarily on the axon terminal arborizations to classify these

cells. Those two classifications resulted both in the description of nine similar cone bipolar cells composed of four OFF bipolar cells (*type 1* to *4*) and five ON bipolar cells (*type 5* to *9*) (Euler and Wässle, 1995; Ghosh et al., 2004; Hartveit, 1997). In the rabbit, McGillem and Dacheux (2001) completed the classification started by Famiglietti using whole-cell recordings and sulforhodamine B injection. MacNeil and colleagues (2004) confirmed McGillem and Dacheux's classification and refined it using, in complement to the Golgi method, photofilling to image a large dataset (~300) of cells. The Golgi method is known for inconsistently staining some cell types, unlike the photofilling method, which reliably stains any targeted cells (MacNeil and Masland, 1998). By combining both methods, they expected to be able to target all existing bipolar cell types. They proposed a classification of cone bipolar cells in 12 types, six of each polarity.

Table 1.1: Markers of the bipolar cell types in mamallian species

	OFF-cone bipolar cells							ON-cone bipolar cells							RBC
Ground squirrel[a]	1a	1b	2	3a	3b	5a	5b	6a	6b	7a	7b	bb	-
	PKARIIβ (++) CaBP5 (++)	PKARIIβ (++) CaBP5 (+/-)	CaBP5 (+++) Calbindin (+++)	PKARIIβ (++)	Recoverin (+++) PKARIIβ (++)	PKCα (+)	PKCα (+++)	PKCα (++)	PKCα (+/-)	CD15 (+++) CaBP5 (+)	CaBP5 (+++)		PKCα[g] (+++)
	a1	a1w	a1-2i	a2	a2w	b3n	b3	b4w	b4	b5	b6	wf	-
Rabbit[b]				SCGN (++)	SCGN (++)	Calbindin (++)	Calbindin (++)		NK1 (+++)	SCGN (+)	SCGN (+++)		PKCα[g] (+++)
				Recoverin (+++)							Recoverin (+++)		
	1	2	3a	3b	4	5i	5t	5o	X	6	7	8	9	-
Mouse[c]		Syt2 (++)	HCN4 (++)	PKARIIβ (++)	Calsenilin (++)				lgfbp5* (++)		GUS8.4* (++)			PKCα[g] (+++)
	NK3R (++)	NK3R (++) PCP2* (+)								PCP2* (+) SCGN (++)	CLM1* (+/-)	CLM1* (+/-)	CLM1* (++)	PCP2* (++)
		SCGN (++)	SCGN (++) CaBP5 (++)		SCGN (++)		SCGN (++) CaBP5 (++)					SCGN (++)		
	Recoverin (++)													
	1	2	3a	3b	4	5a	5b	6	7	8	9	-
Rat				PKARIIβ[d] (++)	Calsenilin[d] (++)		HCN2[f] (++)	HCN2[f] (++)	HCN2[f] (++)	HCN2[f] (++)	HCN2[f] (++)	HCN2[f] (++)	PKCα[g] (++)
		HCN4[d] (++)					HCN4[e] (++)						
		HCN1[e] (++)					HCN1[e] (++)						

*Table 1.1: Markers either antibodies or transgenic mouse lines expressing fluorescent protein (indicated by *) used to identified and characterized retinal bipolar cell types in different mammalian models (+ indicated the strength of the markers).*
[a] Light et al., 2012; [b] MacNeil et al., 2004; [c] Euler et al., 2014; [d] Vielma et al., 2016; [e] Fyk-Kolodziek and Bourcho, 2007; [f] Ivanova and Müller, 2006; [g] Greferath et al., 1990 and Haverkamp and Wässle, 2000.

Molecular markers for the classification of bipolar cells

Molecular markers in the form of antibodies, specific fluorescent protein expression in transgenic lines, or both, extended those early studies based on single-cell morphology by refining the existing types. For example, in the mouse and rat retina, two markers K^+/Na^+ hyperpolarization-activated cyclic nucleotide-gated channel 4 (HCN4) and PKARIIβ (a regulatory subunit of PKA), further divided the OFF-bipolar type *3* into two types *3a* and *3b* respectively, as both populations stratify at the same depth but are labeled differentially (Mataruga et al., 2007; Vielma and Schmachtenberg, 2016) (Table **1.1**, Fig. **1.3**). Immunolabelling played an essential role in the classification of the bipolar cells in the squirrel retina. The combination of seven immunomarkers finalized an almost complete census of bipolar cell types as detailed in Table **1.1**, increasing the number of types from 7-9 in the early works of West and Fischer (Linberg et al., 1996a; West, 1976, 1978) to 13 in the latest classification (Fig. **1.3**, ground squirrel) (Cuenca et al., 2002; Light et al., 2012; Lindstrom et al., 2014; Puller et al., 2011). The molecular marker catalog to distinguish the different bipolar cell types is almost complete for the mouse retina except for types *5s* and *8* (reviewed in Euler et al., 2014). For the rat retina, immunomarkers for the OFF-bipolar cells are the same as in the mouse (Casini et al., 2000; Oyamada et al., 1999; Vielma and Schmachtenberg, 2016), but a clear molecular identification of the ON-cone bipolar cell types is still missing (Table **1.1**, mouse and rat) (Euler and Wässle, 1995; Fyk-Kolodziej and Pourcho, 2007; Ivanova and Müller, 2006). As for the rabbit, only six molecular markers are identified capable of targeting specifically five cone bipolar cells types (Table **1.1**, rabbit) (Brown and Masland, 1999; Casini et al., 2002; Jeon and Masland, 1995; MacNeil and Gaul, 2008; MacNeil et al., 2004; Massey and Mills, 1996). The dendritic and axonal processes of each retinal cell form a horizontal tile, which creates a regular horizontal mosaic across the retina surface with the other homotypical tiles (Wässle and Riemann, 1978). Moreover, the coverage factor between homotypical tiles is constant in each retinal cell type and is close to one for axonal coverage of bipolar cells of the same type (Wässle et al., 2009). This property has been used as a gold standard to confirm the correct classification of the bipolar cell types targeted with

molecular markers or reconstructed in large-scale connectomic studies as detailed below (Euler et al., 2014).

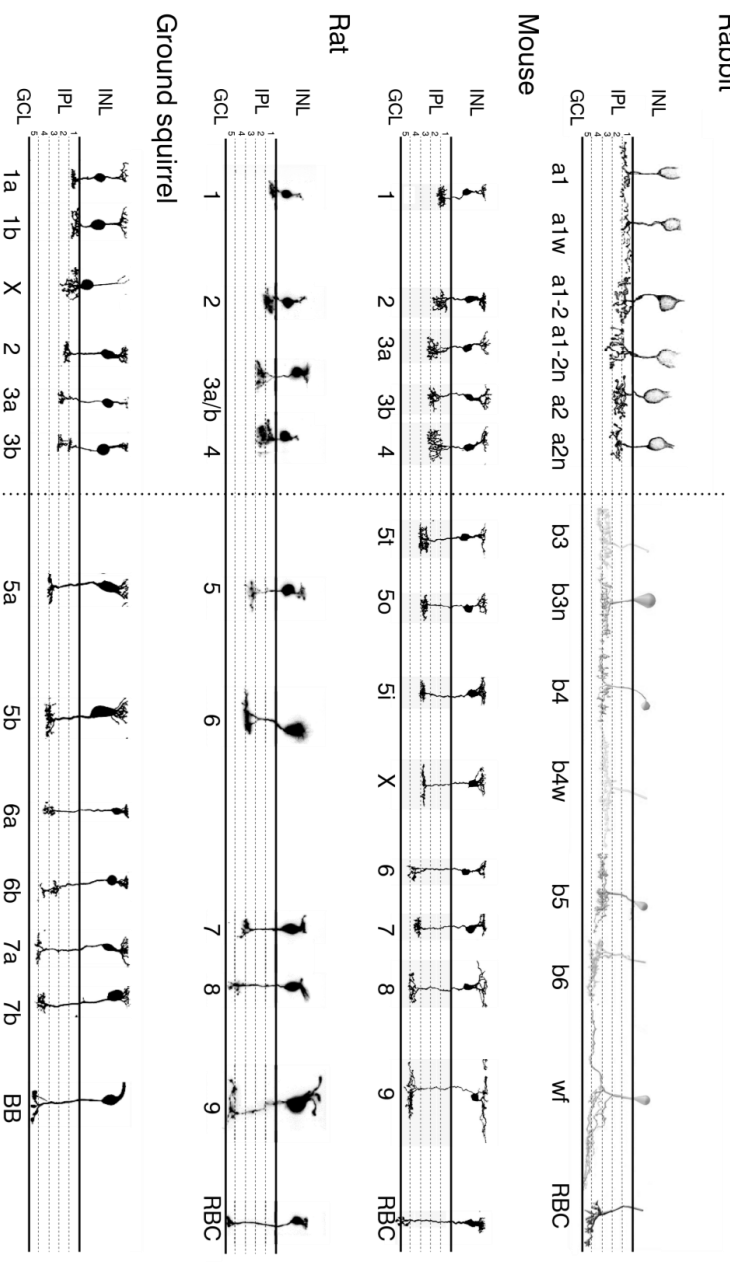

Figure 1.3: Cone bipolar cell types in the different mammalian retinas. ON- and OFF-cone bipolar cell types are divided by the vertical dotted line. The cell types displayed are regrouped by their stratification level in the IPL except the S-cone bipolar cellidentified in each species (wf, 9, and BB). Adapted from mouse: Baden and Osorio, 2019; rat: Hartveit, 1997; ground squirrel: Light et al., 2012; rabbit OFF-cone bipolar cell: MacNeil et al., 2004; rabbit ON-cone bipolar cell: Sigulinsky et al., 2020.

Large scale analysis of the retinal cells

In the last decade, several connectomic studies confirmed and have extended the classification of cone bipolar cells. Three large-scale studies were conducted recently, two in the mouse retina using serial block-face sectioning followed by scanning transmission electron microscopy (Briggman et al., 2011) and one in the rabbit using manual sectioning followed by automatic transmission electron microscopy (Anderson et al., 2009). As scanning block face electron microscopy does not permit labeling with molecular markers and cannot image synaptic ultrastructure, Helmstaedter et al. (2013) had to rely heavily on stratification level to confirm the previous mouse OFF-bipolar cells and type *7*, *8*, and *9* ON-cone bipolar cells classification (Wässle et al., 2009). They identified a new bipolar cell type called type *X* stratifying in a narrow band close to the type *5* bipolar cell previously described (Ghosh et al., 2004; Wässle et al., 2009), and were able to separate the type *5* into two clusters (*5A* and *5R*) based on their connection pattern with ganglion cells. In addition, they predicted the existence of an additional type 5. The type *5* classification was re-analyzed in a second connectomic study in which Greene et al. (2016) confirmed the prediction of Helmstaedter's study describing three type 5-like bipolar cells: *5i* (inner), *5o* (outer), and *5t* (thick) varying only by minute differences in their stratification profile and with *5i* corresponding to the *5A* described above. These studies resulted in dividing the mouse bipolar cells into 14 types (Fig **1.3**, Mouse).

Interestingly, a recent massive single-cell RNA profiling over 25,000 mouse bipolar cells followed by unsupervised clustering reached the same number of bipolar cell types, with the addition of a cluster they labeled *Cb1b* corresponding to the hybrid amacrine/bipolar cell called GluMi (glutamatergic monopolar amacrine) (Della Santina et al., 2016; Shekhar et al., 2016). Comparing their clusters to the previously established molecular catalog, they identified directly the five OFF-bipolar cell types, six including GluMi, and the ON-bipolar cell types *6* and *7*. To identify the unknown clusters, they targeted cluster-specific markers (either using transgenic mouse lines or antibodies) combined with sparse labeling of bipolar cells using viral infection to confirm the cells' morphology in each cluster. Two close clusters corresponded to types *8* and *9*, for which they could propose a clear molecular identification previously

missing, respectively *Serpini1*$^{+}$/C*pne9*$^{-}$ and *Serpini1*$^{+}$/*Cpne9*$^{+}$. The four other clusters corresponded to four type 5-like bipolar cells, which they labeled type *5A-D*, each possessing a unique molecular marker. *5A* (*Sox6*$^{+}$) has the same extended large dendritic branches similar to Helmstaedter's *5A* and corresponding to Greene's *5i*. *5D* (*Lrrtm1*$^{+}$) has a thin and wide axonal terminal reminiscent of type *X*. *5C* (*Slitrk5*$^{+}$) possesses a bistratified axon terminal, which could match Greene's pseudo-bistratified type *5t*, and the remaining type *5B* (*Chrm2*$^{+}$) could then correspond to *5o* (Greene et al., 2016; Helmstaedter et al., 2013; Shekhar et al., 2016).

As mentioned above, using manual sectioning rather than scanning block face sectioning allowed Marc and colleagues to use the detection of molecular markers and synaptic structures to annotate the different types of rabbit bipolar cells (Anderson et al., 2009; Marc et al., 2012). Taking advantage of this additional information, they used three parameters to classify the bipolar cells: (1) OFF-cone bipolar cells stratify primarily in sublayer a with some processes extending into the upper part of sublayer b, and ON-cone bipolar cells stratify into sublayer b, although some synaptic contacts occur in sublayer a; (2) ON- and OFF-cone bipolar cells have a robust primary glutamate signature, but only ON-cone bipolar cells have a mixed glycinergic signal; And (3) all OFF-cone bipolar cells are pre- and post-synaptic to AII amacrine cells and almost all ON-cone bipolar cells make heterologous electrical junctions with AII amacrine cells (Lauritzen et al., 2013, 2019; Marc et al., 2013, 2015; Sigulinsky et al., 2020). They confirmed the six types of OFF-cone bipolar cells as previously described and merged their nomenclature with the previous ones (MacNeil et al., 2004; McGillem and Dacheux, 2001) to label them: *a1*, *a1w*, *a1–2i*, *a2*, *a2w*, *ab2* where '*i*' denotes an interlaced axonal pattern, '*w*' denotes wide-field axonal arbors, and the number indicates a progressively more proximal stratification (Marc et al., 2013, 2015). The ON-cone bipolar cell type classification and its nomenclature evolved during their analysis to reach seven ON-cone bipolar cell types (Fig. **1.3**, Rabbit). Bipolar cell types *b5*, *b6*, and *wf* were easily clustered based on their stratification in sublamina 4 and 5. Bipolar cell types *b3*, *3n* and *4w* ('n' denotes narrow-field and 'w' wide-field axonal arbors) stratify closely to each other within sublamina 3, like the three types *5i*/*o*/*t* described in the mouse (Fig. **1.3**, Mouse). Similarly, they lack discriminating

morphological features. However, unlike in the mouse retina, frequency or distribution of synaptic ribbons (Tsukamoto and Omi, 2014, 2017) or connectivity with specific ganglion cells (Greene et al., 2016; Helmstaedter et al., 2013) did not provide discriminatory power. They managed to distinguish the four types *b3*/*3n*/*4*/*4w* based on the presence or absence of gap junctions with AII amacrine cells, combined with arbor size and tiling (Sigulinsky et al., 2020). Using the same connectivity and morphological parameters, Tsukamoto (2017) confirmed the existence of four type 5-like bipolar cell types in the mouse retina.

Rod bipolar cell classification

The mop-like bipolar cells were identified as rod bipolar cells based on their synaptic contact with the rod photoreceptors (Boycott and Dowling, 1969; Boycott and Kolb, 1973; Polyak, 1949). Since then, rod bipolar cells are thought to be a homogeneous cell type. Multiple factors support the homogeneity of the rod bipolar cell population. First, the protein kinase Cα (PKCα) antibody strongly stains a unique population of rod bipolar cells in all mammalian retinas studied (Greferath et al., 1990; Haverkamp and Wässle, 2000), which helped identify and investigate this cell type across various species. Second, the morphological properties of rod bipolar cells, their coverage factor and tiling of their dendritic fields, and their RNA expression profile concur in showing the rod bipolar cells as a homogeneous cell population in the mammalian retina (Euler et al., 2014; Helmstaedter et al., 2011; Shekhar et al., 2016). Pang and colleagues (2010) suggested that there may be two types of rod bipolar cells possessing two different response profiles, with one type seemingly relaying pure rod signals and the other relaying mixed rod and cone inputs. However, connectomic data show no evidence for two populations of rod bipolar cells based on their connectivity in the outer retina (Behrens et al., 2016). Nevertheless, a more detailed analysis of the primary rod pathway suggested that rod bipolar cells could have a spectrum of reciprocal inhibition via A17 amacrine cells, explaining the different profile responses (Tsukamoto and Omi, 2017).

1.2.2 Functional properties of cone bipolar cells

The division of bipolar cells into 11-15 different types leads to the question of the functional role of each type. The functional role of each bipolar cell type depends directly on their response properties. Aside from their different light responses as described previously, the first demonstration of a diversity of response properties in bipolar cell types even within the group of ON and OFF-cone bipolar cells, lies in their different temporal response properties, which are either transient or sustained (Awatramani and Slaughter, 2001; Roska and Werblin, 2001). Bipolar cells transmit their response properties to ganglion cells creating two temporal channels in the retinal circuit (Awatramani and Slaughter, 2000). It is generally understood that the transient cone bipolar cells have their axonal terminals stratifying in the central part of the IPL, whereas the sustained cone bipolar cells ramify at the inner and outer border of the IPL (Euler et al., 2014). Ca^{2+} and glutamate reporter imaging experiments confirmed that the output of the bipolar cell followed this rule (Baden et al., 2013; Borghuis et al., 2014). Light-evoked responses recorded in mouse bipolar cells showed that cone bipolar cell types *5*, *X*, and *7* display a high temporal tuning concordant with the imaging data. Moreover, bipolar cell type *7* responds to higher frequencies than the other transient ON-cone bipolar cell types. However, a subset of type *5-like* bipolar cells presents a sustained profile, and type *6* bipolar cells present an intermediate profile (Ichinose et al., 2014). OFF-cone bipolar cell sustained and transient profiles are mingled across sublamina a, as bipolar cell types *1*, *3b,* and *4* display sustained profiles, and bipolar cell types *2* and *3a* show transient profiles (Ichinose and Hellmer, 2016). Many factors shape bipolar cell response properties: (1) cell morphology, particularly the length and diameter of the dendritic and axonal processes, (2) photoreceptor inputs, (3) the type of glutamate receptors the cell expresses on its dendrites, (4) the intrinsic active conductances of the cell, and (5) the output synapses of the bipolar cells. All of these factors are considered below.

Photoreceptor inputs to the bipolar cells

Rod bipolar cells contact almost all the rod photoreceptors in their dendritic fields (Anastassov et al., 2019), and about 75% of the rod bipolar cells also make sparse

contact with cones (0 to 3) (Behrens et al., 2016). Despite quite a variation depending on the studies, the convergence between rods and RBCs is the strongest amongst bipolar cells with ~25 to 75 rods contacting a single RBC (Anastassov et al., 2019; Behrens et al., 2016; Tsukamoto and Omi, 2014). Most cone bipolar cells contact all the cones in their dendritic field without discriminating between S- and M-cones. Because the density of M-cones is higher than S-cones, bipolar cell signals tend to be biased toward green wavelengths. The main chromatic exceptions being the conserved S-cone selective ON-cone bipolar cell (Breuninger et al., 2011; Cohen and Sterling, 1990b; Famiglietti, 1981; Hartveit, 1997; Jeon et al., 1998; Li and DeVries, 2006; Pignatelli and Strettoi, 2004), the rabbit S-cone selective OFF-cone bipolar cell (Marshak and Mills, 2014; Mills et al., 2014), and the M-cone selective OFF-cone bipolar cell (Behrens et al., 2016; Li and DeVries, 2006). Mouse OFF-cone bipolar cell types *3a*, *3b*, and *4* make synapses with both cones and rods. Bipolar cell type *3b* contacts more rods than type *3a*, representing a functional difference between these two morphologically similar bipolar cell types (Behrens et al., 2016; Puller et al., 2013). Contrary to the OFF-cone bipolar cell types that contact all the cones present in their dendritic field, ON-cone bipolar cell types can be divided into two groups. The bipolar cell types *5i*, *7* follow the same rule as the OFF-bipolar cell type, but the other ON-cone bipolar cell types contact only a subset of the cones in their dendritic field. However, the functional consequence of this difference remains unclear (Behrens et al., 2016).

Receptors on bipolar cells dendrites

Each type of cone bipolar cell receives similar inputs from the cones. Thus, the first critical step to distinguish their functional properties is the kinetics of the glutamatergic receptors that cone bipolar cells express at their synapses with cones. All ON-bipolar cells express the same mGluR6 receptors at their dendritic synapses (Masu et al., 1995).

OFF-cone bipolar cells express two types of ionotropic glutamatergic receptors at their synapse with the photoreceptors: α-amino-3-hydroxy-5-methyl-4-isoxazolepropionic acid (AMPA) and kainate receptors. AMPA receptors activate in response to glutamate, then desensitize rapidly. Therefore, AMPA receptors mediate a more phasic and

transient response, whereas kainate receptors mediate a more tonic and sustained response (Traynelis et al., 2010). In the ground squirrel, Devries and colleagues showed that the cone bipolar cell type *b2,* which express only AMPA receptors, have a more transient temporal profile than the other OFF-cone bipolar cells, which express only kainate receptor (types *b1a/b*) or a mix of AMPA and kainate receptors (types *b3a/b*) (DeVries, 2000; Lindstrom et al., 2014). In addition, AMPA receptors are positioned close to the release site of the photoreceptors, while kainate receptors are located at the base of the synapse further from the release site. The glutamate diffusion from the release site to the kainate receptors reduces the variation of glutamate concentration activating the kainate receptors. This constant presence of glutamate reinforces the sustained response profile of the OFF-cone bipolar cells that express kainate receptors compared to the OFF-cone bipolar cells that express the more transient AMPA receptors (DeVries et al., 2006). In rodents, kainate receptors seem to be the dominant receptor type mediating the photoreceptor inputs to both transient and sustained OFF-cone bipolar cells (Baden et al., 2013; Borghuis et al., 2014; Buldyrev et al., 2012; Ichinose and Hellmer, 2016; Puller et al., 2013; Vielma and Schmachtenberg, 2016) and the exact contribution of AMPA receptors is unclear.

In addition to glutamatergic receptors, cone bipolar cells also express GABAergic receptors on their dendrites that mediate feedforward inputs from horizontal cells that create the center-surround receptive field of the bipolar cells and support contrast enhancement (Thoreson and Dacey, 2019). ON- and OFF-cone bipolar cells express different chloride transporter creating high chloride concentrations locally in their dendrites (Billups and Attwell, 2002; Borghuis et al., 2014; Duebel et al., 2006; Enz et al., 1995; Pang et al., 2010; Yin et al., 2020). The high chloride gradient triggers chloride efflux and excitation upon GABA input. Therefore, the same GABAergic input from horizontal cells provides ON- and OFF-cone bipolar cells with inhibitory input of the correct polarity (reviewed in Thoreson and Dacey, 2019). However, there is to date no evidence of bipolar cell-type-specific horizontal cell lateral inhibition.

Active ionic channels

Another critical factor in creating the diversity of response properties between the different bipolar cell types is the selective expression of voltage-gated channels. The intrinsic voltage-gated conductances influencing the response of the bipolar cell are HCN channel currents (I_h), Na^+ voltage-gated channel currents (I_{Na}), K^+ voltage-gated channel current (I_K), and T- and L-type Ca^{2+} currents. The voltage-gated channels can be expressed exclusively in the somatodendritic compartment like T-type Ca^{2+} channels (Hartveit, 1999; Satoh et al., 1998), some type of voltage-gated potassium channels (K_V1.1 and 1.3) (Klumpp et al., 1995a) and HCN1 in a subset of OFF-cone bipolar cells (Fyk-Kolodziej and Pourcho, 2007). Similarly, other voltage-gated channels are exclusively present at the axon terminal of bipolar cells, like HCN2 (Cangiano et al., 2007; Ivanova and Müller, 2006; Müller et al., 2003) and K_V1.2 (Klumpp et al., 1995b).

The bipolar cell ribbon synapse

The response of bipolar cells to sustained depolarization can, in some cases, be a transient synaptic transmission (Singer and Diamond, 2003). This non-linearity in the input-output relationship of bipolar cells is independent of presynaptic inhibition, the kinetics of postsynaptic receptors, and the activation of intrinsic conductances but instead is mediated by the ribbon synapses of bipolar cells (Singer and Diamond, 2003). As mentioned above, the voltage-gated calcium channels activating the synaptic transmission in the bipolar cell ribbon synapses are L-type calcium channels (Ca_V1.2-4) (Baumann et al., 2004; Berntson et al., 2003; Satoh et al., 1998). These Ca_V channels have a linear response function in the membrane potential operating range of the bipolar cells (Doering et al., 2005; Pangrsic et al., 2018) thus cannot be the origin of the non-linearity. Instead, the non-linearity in the transmission of the visual signal has been attributed to the dynamics of the small readily releasable pool of synaptic vesicles at the bipolar cell ribbon (Chávez et al., 2006; Jarsky et al., 2011; Oesch and Diamond, 2011; Oltedal and Hartveit, 2010; Zhou et al., 2006). Also, the different expression of the isoform of some synaptic ribbon proteins could modify the synaptic ribbon release properties and could allow mouse type *6* cone bipolar cells to provide both sustained and transient synaptic outputs at different synapses (Gierke et al., 2020). Another

interesting property of ribbon synapses is their capacity to use different multi-vesicular release modalities (Moser et al., 2020), which improves the temporal precision and efficiency of signal transmission (James et al., 2019). The non-linearity between bipolar cell input and output mediated at their ribbon synapses could explain the discrepancy between the response profiles of the bipolar cells to the photoreceptors inputs (Hellmer et al., 2016; Ichinose and Hellmer, 2016; Ichinose et al., 2014) and the output temporal properties of the different bipolar cell types measured with fluorescent glutamate reporters (Baden et al., 2013; Borghuis et al., 2014).

Electrical synapses of bipolar cells

In addition to chemical synapses, cone bipolar cells make electrical synapses with each other and amacrine cells (reviewed in Völgyi et al., 2013). Ultrastructural analysis of mammalian and non-mammalian vertebrate bipolar cells revealed the presence of gap junctions in the axon terminals of OFF- and ON-cone bipolar cells (Jacoby and Marshak, 1999; Kolb, 1979; Marc et al., 1988; Sigulinsky et al., 2020; Tsukamoto and Omi, 2014) and in dendrites of OFF and ON-cone bipolar cells (Raviola and Gilula, 1975; Umino et al., 1994). Of the 20 types of connexins that can form electrical junctions in the mouse (Söhl and Willecke, 2003), bipolar cells are immunoreactive to connexin 36 (Cx36) and connexin 45 (Cx45). Cx45 is found at the axon terminal of the mouse cone bipolar cells type *5* and *6* (Dedek et al., 2006) and in the dendrites and axon terminals of the OFF-cone bipolar cells (Hilgen et al., 2011). The dendrites of mammalian OFF-cone bipolar cells also contain Cx36 (Bolte et al., 2016; Feigenspan et al., 2004; Kántor et al., 2016, 2017; O'Brien et al., 2012). The axon terminal of ON-cone bipolar cell type *7* and potentially other ON-cone bipolar cell types also contain Cx36 (Dedek et al., 2006; Han and Massey, 2005a; Lin et al., 2005). The evidence for the presence of gap junctions in bipolar cells is complemented by tracer coupling experiments that show connections between rabbit and tiger salamander OFF-cone bipolar cells (Mills, 1999; Zhang and Wu, 2009) and between ON-cone bipolar cells in vertebrate retina (Zhang and Wu, 2009). Also, the electrical coupling has been confirmed by dual patch-clamp recording between bipolar cells in vertebrate retina (Arai et al., 2010; Kujiraoka and Saito, 1986) and between ON-cone bipolar cells and AII in the rat retina (Massey et al., 2003; Trexler et al., 2005; Veruki and Hartveit,

2002b, 2009). These data suggest that OFF- and ON-cone bipolar cells make electrical synapses with other cells of the same class. In the mouse retina, the gap junctions between OFF-cone bipolar cells are more frequently encountered than those between ON-cone bipolar cells (Tsukamoto and Omi, 2017). The primary coupling partners of ON-cone bipolar cells are AIIs (Chun et al., 1993; McGuire et al., 1984; Strettoi et al., 1992, 1994). The connexin composition of these electrical channels is different between cone bipolar cell types. Cone bipolar cell type *7* seems to form either heterotypic Cx45 or bihomotypic Cx45-Cx36 gap-junctions whereas bipolar cell type *5* and *6* form homotypic Cx36 gap junctions with the AIIs expressing Cx36 (Dedek et al., 2006; Han and Massey, 2005b; Li et al., 2008; Lin et al., 2005; Maxeiner et al., 2005). Three bipolar cell types (rabbit: *b3n*, *b6*, *b5*; mouse: *6*, *7*, *5a*) collect the majority of the AII output, one cell type completely lacks AII coupling (rabbit: *b3*; mouse: *5b*), and other types rarely contacts AII (rabbit: *b4*; mouse: *5c*) (Sigulinsky et al., 2020; Tsukamoto and Omi, 2017). Additionally, the measurement of the number of electrical synapses and their surface area suggests differential outputs for AIIs, with a clear preference for ON-cone bipolar cells that stratify closer to the INL in rabbits and mice (Sigulinsky et al., 2020; Tsukamoto and Omi, 2017). The AII is not the only amacrine cell coupled with bipolar cells, ON- and OFF-cone bipolar cells also make gap junctions with A8 amacrine cells (Kolb and Nelson, 1996; Lee et al., 2015; Yadav et al., 2019).

One well-established role of bipolar cell electrical synapses is in mediating the signal transfer between ON- and OFF-pathways and between rod and cone pathways (see section **1.1.4** and Kuo et al., 2016; Münch et al., 2009). The signal transfer through gap junctions spreads visual signals laterally, and this lateral spread is known to increase the sensitivity of retinal ganglion cells to spatiotemporally correlated inputs such as motion (Arai et al., 2010; Kuo et al., 2016). Bipolar cell coupling might also improve the signal-to-noise ratio in the retina circuit (Feigenspan et al., 2004). Finally, it is important to note that electrical synapses exhibit plasticity that modulates their conductance. Short-term plasticity mechanisms involve gating of the connexin channels themselves or modifications in the conductance of other ion channels that alter the ion flux across the gap junctions (O'Brien and Bloomfield, 2018). Electrical

synapses are also strongly modulated by both circadian rhythms and ambient light levels. During daytime or after exposure to bright light intensities, the coupling strength of the bipolar cells is reduced, which results in the lack of rod signals in the cone pathway (Ribelayga and Mangel, 2010; Ribelayga et al., 2008; Wang and Mangel, 1996). The underlying mechanisms of this modulation by light and circadian rhythms involve intracellular signaling cascades activated by dopamine and nitric oxide (see review O'Brien and Bloomfield, 2018; Trenholm and Awatramani, 2017).

2. Aims of the thesis

The dynamic and integrative properties of bipolar cells are determined by their morphology, passive membrane properties, cytoplasmic resistivity, and associated ion channel properties and distribution. It is a prerequisite to determine these properties in order to understand the mechanisms underlying signal transformation. The main objectives of this thesis were to characterize the morphological properties of the different types of bipolar cells in the rat retina with the future goal to develop realistic, morphology-based compartmental models of these different types. The resulting models can then serve as electrical skeletons, onto which active conductances and synaptic inputs can be added to build realistic models of these important neurons in the retina circuit.

Paper I

Paper I aimed to investigate the contribution of gap junctions to the membrane properties of bipolar cells. Gap junctions are ubiquitous within the retina, but it remains to be determined whether the gap junctions between specific cell types are sufficiently strong to mediate functionally relevant coupling via electrical synapses. A particularly interesting case of retinal gap junctions for which there is strong morphological evidence, but virtually no information regarding a putative functional role, are the gap junctions between both ON- and OFF-cone bipolar cells. Cells of the same class make gap junction contacts with each other, and this appears to be a common circuit motif in the vertebrate retina. In this study, we investigated the effect of the gap junction blocker meclofenamic acid (MFA) on the input resistance (R_N) of bipolar cells using whole-cell patch-clamp recording in acute slices from rat retina. We found that for ON-cone bipolar cells, R_N displayed a clear increase following the application of MFA, as expected for cells with gap junction-mediated electrical coupling. For rod bipolar cells, R_N did not increase in the presence of MFA, consistent with their lack of gap junctions. Surprisingly, however, given the substantial morphological evidence for the presence of gap junctions between OFF-cone bipolar cells, R_N for these cells did not increase following the application of MFA. Our results suggest that the gap junctions between

OFF-cone bipolar cells do not support consequential electrical coupling. This study provides an important first step both to elucidate the potential roles for these gap junctions and also for the development of compartmental models for cone bipolar cells.

Paper II

Paper II aimed to provide a quantitative morphological analysis of rod and cone bipolar cells of the rat retina. Although the morphology of bipolar cells has been studied qualitatively in several different mammalian retinas, there is a surprising lack of quantitative information about morphological parameters, including the pattern and extent of branching of the axon terminals in the IPL. In this study, we have used MPE microscopy to acquire image stacks of bipolar cells after filling them with fluorescent dye during whole-cell recording of visually targeted cells in rat retinal slices. After image deconvolution, we digitally and quantitatively reconstructed the complete morphologies of bipolar cells and performed detailed morphometric analysis to investigate which morphological properties can best be used for characterization and classification in experiments with combined structural and functional analysis. These morphological reconstructions will be used as the basis for future compartmental models.

3. Methodological considerations

3.1 Electrophysiology

3.1.1 The retinal slice preparation

The use of animals in this study was carried out under the approval of and in accordance with the regulations of the Animal Laboratory Facility at the Faculty of Medicine at the University of Bergen (accredited by the International Association for Assessment and Accreditation of Laboratory Animal Care). The procedure for tissue preparation was adapted from the protocol first described in Edwards *et al.*, 1989, later refined in Boos *et al.*, 1993 and Hartveit, 1996. Female rats (Wistar HanTac; 4-8 weeks postnatal) were placed 10 min in 100% oxygen to improve the retinal tissue's oxygenation and decrease the anesthesia's induction time, then deeply anesthetized using Isoflurane and killed by cervical dislocation. Eyeballs were removed by cutting the optic nerve and then dissected in HEPES buffered solution (in mM: 145 NaCl, 2.5 KCl, 2.5 $CaCl_2$, 1 $MgCl_2$, 5 Na-HEPES, 10 Glu, pH adjusted to 7.4 with HCl) at room temperature. Under a dissection microscope, the cornea and lens were removed by cutting the eyeball's circumference at the level or slightly below the *orata serrata*. Then, the vitreous was removed, the retina was isolated from the sclera and cut into four quadrants placed on filter paper in an interface chamber filled with an oxygenated medium (95% O_2 - 5% CO_2; pH 7.4). We use a medium developed to mimic the *in vivo* fluid nourishing the mammalian retina. Named after its designer Ames' medium can keep *in vitro* retina preparation in pristine condition for 10 h (standard time of an experiment) up to 52 h (Ames 3rd and Nesbett, 1981). Before each electrophysiological experiment, one quadrant was cut by hand into vertical slices with a thickness of approximately 200 μm, using a curved scalpel blade under a dissection microscope. This procedure has the advantage of being faster than using a tissue chopper or a vibratome, and given practice, results in slices of similar quality. Each batch of slices was used for up to 4 h before being replaced by a new batch. In experiments where we used irreversible drugs, slices were replaced immediately after recording and fresh slices were used for the subsequent experiments.

3.1.2 Visual targeting and cell identification

Slices were visualized using a BX51 WI, Olympus wide-field microscope with a 60x or 40x water-immersion objective, and Dodt gradient contrast videomicroscopy for the patch-clamp experiments performed to investigate the active properties of bipolar cells. Visualization was used to assess the health, the cutting angle of the slice, and target the cell type of interest.

Due to the retina's laminar organization, it is possible to target specific cell types depending on their location in the retinal slice preparation. All the bipolar cell somas are present in the INL (Fig. 1). The somas of rod bipolar cells are located mainly in the outer third part of the IPL, but as the most abundant type of bipolar cell in the rodent retina, it is also possible to find rod bipolar cells throughout the depth of the IPL. The somas of cone bipolar cells are located in the outer half of the INL and usually are smaller than the somas of rod bipolar cells (Boycott and Dowling, 1969). To visually determine the type of bipolar cell-targeted, the intracellular solution used to fill the recording pipette contained a fluorescent dye, either Lucifer Yellow or Alexa 594. At the end of the recording, the cells' morphology was visualized through the oculars and hand-drawn.

In some cases, image stacks were captured with a monochrome CoolSNAP$_{ES}$ camera (Teledyne Photometric, Tucson, Arizona, USA) to confirm the cells' identity. This stack was used to measure the level of stratification in the IPL of the recorded cell as a tool to determine the cell type (Euler et al., 2014; Hartveit, 1997). The physiological responses of the bipolar cells to hyperpolarization steps were recorded just following the establishment of the whole-cell recording and used as physiological «fingerprints» to help assess the bipolar cell type (Ivanova and Müller, 2006).

3.1.3 The patch-clamp technique

The roots of electrophysiology originate in the late eighteenth century with studies by Galvani and Volta. Their work demonstrated the effect of electricity capable of evoking the frog's leg muscle contraction, followed in the nineteenth century by the first

description of the muscular and neuronal action potential. However, modern electrophysiology began with the utilization of glass pipettes to record the intracellular electrical in the famous squid giant axon preparation by Huxley and Hodgkin (1952), leading to the characterization of the ionic basis of the neuronal action potential. In parallel, the development of the voltage-clamp principle (Cole, 1949; Marmont, 1949) created new ways to explore the neurons' electrophysiological properties. Another main methodological innovation came 26 years later when Neher and Sakmann (1976) developed the patch-clamp technique. The patch-clamp technique involves using glass pipettes, which, contrary to previously used sharp electrodes, have a large opening, and do not penetrate the cell membrane but form a high resistance seal with the cell membrane. The high resistance seal – also called gigaseal – resulted in a significant improvement to the signal-to-noise ratio of the electrical currents recorded, opening the new possibility of recording single-channel activity. Also, as the strength of the seal between the glass and the cellular membrane is stronger than the elasticity of the membrane itself, the patch-clamp pipette allowed to pull away part of the membrane attached to the glass electrode to record ionic current from small patches of neuron membrane (Hamill et al., 1981). By using these properties, various configurations are possible when performing patch-clamping. Whole-cell recording is the main configuration used in this thesis. In this configuration, after creating the seal between the cell and the glass pipette, negative pressure pulses are used to breach the cell membrane in the glass pipette's opening, creating a direct continuity between the intracellular compartment and the electrode. This configuration had the advantage of recording electrical signals with a high signal-to-noise ratio, a weak series resistance between the cell and the recording electrode, and direct control of the intracellular medium's composition.

However, the diffusional exchange between the cytoplasm and the pipette solution results in a wash-out of the endogenous nucleotides and ions, notably Ca^{2+} and cAMP. This change in the cytosol's physiological composition needs to be considered in the study of cyclic nucleotide-gated channels, like the HCN channels. Horn and Marty introduced a solution to this by using the perforated patch (Horn and Marty, 1988). The perforated patch consists of applying pore-forming antibiotics through the glass pipette

to achieve access to the intracellular electrical signal. Nystatin and amphotericin B are the two antibiotics classically used for performing patch experiments. They form pores permeable to the small monovalent ions Na^+, K^+, and Cl^- but are impermeable to divalent ions and molecules with a molecular weight above 200 (reviewed by Akaike and Harata, 1994). When the internal Cl^- concentration is critical, gramicidin can also be used, as this antibiotic creates pores that are not permeable to anions (Akaike, 1996). In the current work, we used the antibiotic *β*-escin. This molecule creates pores with the same ionic permeability, but with larger pores than nyastin and amphotericin B. These properties make that perforated patch perform with *β*-escin is more successful and can reach a low series resistance faster than the ones perform with nyastin or amphotericin B (Fan and Palade, 1998).

3.2 Single neuron reconstruction

The morphology of a neuron directly influences the signal propagation in its processes. To model the impact of the morphology on the response properties, it is necessary to develop a realistic compartment model of the neuron of interest. Creating realistic compartmental models of a single neuron requires access to the precise and detailed morphology of the neuron targeted. Several cell parameters, such as capacitance and axial resistivity are susceptible to the variation of morphological parameters. The best approach to capture a neuron's morphological data is to perform a digital reconstruction of its morphological structure. However, cell reconstruction methods possess several inherent pitfalls, the main ones being light microscopy image acquisition limitations, tissue handling, and observer bias.

3.2.1 Microscopy and image processing

The multiphoton excitation (MPE) microscopy is a type of light microscopy, which presents several advantages over the other type of fluorescence microscopy used in neuroscience. MPE microscopy is based on the principle first described in 1931 that two photons of low energy if they interact coincidentally with the same fluorophore, can excite the molecule as one photon of high energy (Göppert-Mayer, 1931).

However, it is only six decades later that this principle led to the invention of the first multiphoton microscope (Denk et al., 1990) when the development of lasers capable of rapid trains of short pulse made it possible.

By this principle, only the focal point is excited, and so MPE microscopy induces low photo-toxicity, allowing us to perform live imaging and electrophysiological recording simultaneously on the same cell. MPE microscopy is also more efficient than confocal laser scanning microscopy to perform volumetric imaging. It uses long excitation wavelengths limiting light absorption and light scattering, which are particularly relevant in our study as we image the tissue at a relatively high depth (usually up to 150 μm). We performed the image acquisition by MPE using a «Movable Objective Microscope» equipped with a mode-locked Ti:sapphire laser (Mai Tai DeepSee; SpectraPhysics, Irvine, CA, USA) tuned to 810 nm to image a cell filled with Alexa 594 via the patch pipette.

Another limitation of light microscopy, aside from light scattering, arises from the light diffraction happening at the microscope system level and particularly at the objective lens level. Light diffraction creates a blurring effect during imaging. This blurring effect is modeled by the point-spread function (PSF) of the microscopic system used. The PSF is the function by which the actual object imaged is convoluted into the fluorescent imaged obtained with microscopy. In other terms, each fluorescent point of the raw image is imaged as an identical blurry 3-D object, and the final fluorescent image is the result of the addition of all those blurry 3-D objects (Swedlow, 2013). Once measured or calculated, the PSF can restore the raw image using deconvolution, which reverses the blurring process by reassigning the out-of-focus light in the focus point. As mentioned above, MPE microscopy inherently possesses an optical sectioning property reducing the benefit of the out-of-focus light's reassignment. However, the deconvolution process's significant benefit comes from reducing the noise by averaging the out-of-focus light and improving image contrast (Wallace et al., 2001). Multiple approaches have been developed to perform deconvolution, and the more performant one is the use of constrained iterative algorithms. We deconvolved our image stacks using the Classical Maximal Likelihood Estimation algorithm

developed by SVI (Scientific Volume Imaging, Hilversum, The Netherlands) in Huygens Essential software (version *14* 64-bit) with a PSF theoretically calculated. The algorithm uses a user-specified parameter, the signal-to-noise ratio (SNR), to control the trade-off between the smoothness of the deconvolution and the amplification of the noise. If the SNR is set too high, it leads to the apparition of artifacts, and if too low, it decreases the resolution of the processed image. We estimated the optimal SNR value by deconvolving the same image stack with a range of different SNR values and comparing the intensity profile at different neuron imaged locations. The optimal SNR was selected as the highest SNR value before the intensity profiles' apparition of noise. For the deconvolution process to be accurate, the image's sampling density needs to be set at least at the Nyquist sampling frequency. The maximum sampling distance (d_{max}) respecting Nyquist rate for MPE microscopy is in the plane: $d_{xy,max} = \lambda_{ex}/4k \cdot N_A$ and in the optical axis: $d_{z,max} = \lambda_{ex} \cdot \sin\alpha/2k \cdot N_A \cdot (1 - \cos\alpha)$ where λ_{ex} is the wavelength of the irradiating light, k the number of excitation photons (set to 2 for MPE microscopy), $N_A (= n \cdot \sin\alpha)$ the numerical aperture of the microscope objective, n the refractive index of the medium (n = 1.33 for water), and α the half-aperture angle of the microscope objective (Heintzmann, 2006). If we used the configuration used in our microscope setup with an excitation wavelength of 810 nm for the Alexa 594 dye imaged with a 20x objective possessing a N_A of 0.95, $d_{xy,max}$ is close to 96 nm and $d_{z,max}$ close to 812 nm. The image stack deconvolved had pixel sizes between ~96 nm and ~72 nm with a Z-step set to 0.4 μm which satisfy the Nyquist rate sampling.

The resolution in light microscopy, apart from artifacts and aberration that can occur, is principally limited by light diffraction. This limit of the image resolution raises the issue of how the thinnest neuron processes are imaged. The resolution (r) of wide-field light microscopy can be approximated by the Rayleigh criterion: $r = 0.61 \cdot \lambda/N_A$. In the case of non-linear microscopy as MPE microscopy, only the wavelength of the excitation light need to be taking into account, and the resolution is improved by a factor of √2, giving the following equation for the Rayleigh criterion: $r = 0.61 \cdot \lambda_{ex}/1.31 \cdot N_A$ (Cox and Sheppard, 2004). In our setup, we obtain a theoretical

resolution limit approximating 0.36 μm. Sub-resolution process having a high enough intensity to be detected will be imaged as having their apparent diameter close to this resolution limit, creating for the thinnest neurites a discrepancy between the actual morphology and the reconstructed neuron. Taking this issue into account, we compared and corrected the average diameter of the thinnest neurites in our reconstructions to the smallest diameter found for bipolar cells neurites in electron micrographs and reconstruction from serial section transmission electron microscopy.

3.2.2 Morphological reconstruction

During quantitative morphological reconstruction, observer bias was controlled by 1) Using a state-of-the-art system: Neurolucida software (version 11 64-bit and NL 360 version 2018 64-bit; MBF Bioscience, Williston, VT, USA; (Glaser and Glaser, 1990) with an identical protocol to reconstructed all the bipolar cells, 2) Comparing the reconstructions with published bipolar cells reconstructions done by electron microscopy (Strettoi et al., 1994; Tsukamoto and Omi, 2017), 3) For some selected cells a second observer checked for reconstruction errors.

In Neurolucida, the soma can be reconstructed using either a series of contours along the Z-axis or using a unique contour drawn in the middle of the soma location. Using multiple contours allows having a more realistic reconstruction of the 3-D shape of the soma. However, we have observed that the soma's high dye concentration often leads to a saturation of the soma. This saturation can create an overestimation of the soma volume and surface area when reconstructed using multiple contours. Therefore, we reconstructed the soma using a single contour. Single contour soma reconstruction gives similar results to previously published data on the cell body volumes for rod bipolar cells (Oltedal et al., 2009).

One of the challenges in building models of the different bipolar cells is identifying the type of bipolar cells targeted during the patch-clamp experiments. For this purpose, we measured the stratification level of the different patch cells used for the modeling. From infrared images obtained in parallel with the MPE imaging, the strata of the IPL were delimited using Neurolucida's open delineation tool. With the different layers of the

retina labeled, it was possible to precisely assess the stratification level and the width of the stratification of the axon terminal of the different bipolar cells in the inner plexiform layer.

4. Overview of the results

4.1 Paper I

The objective of **Paper I** was to investigate if the morphologically identified gap junctions in the different types of retinal bipolar cells correspond physiologically to electrical synapses. We studied the changes in the input resistance of the different types of bipolar cells under the pharmacological blockade of gap junctions by MFA in single-cell and dual whole-cell patch-clamp recordings.

We took advantage of the established electrical coupling between ON-cone bipolar cells and AII amacrine cells (see section **1.1.4**) to examine how MFA influenced the membrane properties of electrically coupled cells. First, we performed dual patch recordings between AII and ON-cone bipolar cells to confirm their electrical coupling (**Paper I**, **Fig. 1D-E**). As previously reported, MFA application (100 μM) blocked the electrical synapses between these cells (Veruki and Hartveit, 2009, and **Paper I**, **Fig. 2A-B**). MFA application was also accompanied by an increase of the apparent membrane resistance (r_m) and input resistance (R_N) in both cells (**Paper I**, **Fig. 2C-D**). This result suggested that when an electrical coupling exists between two cells with similar coupling conductance, as the coupling between ON-cone bipolar cells and AII, blocking this coupling leads to an increase in R_N for both cells.

Next, we performed patch-clamp recording from individual ON-cone bipolar cells and monitored the effect of MFA on R_N. R_N was measured by applying small voltage pulses to the cells while in whole-cell voltage-clamp configuration (**Paper I**, **Fig. 3A-B**) in the presence of a bath solution pharmacologically blocking synaptic transmission, Na_V, and HCN channels. In all ON-cone bipolar cells, MFA application increased R_N (**Paper I**, **Fig. 3D**). Similar recordings were performed in eight OFF-cone bipolar cells (**Paper I**, **Fig. 4A-B**). In the OFF-cone bipolar cells, MFA application did not increase R_N, and instead, a slight decrease was observed in seven cells (**Paper I**, **Fig. 4C-D)**. MFA has been shown to affect certain K^+ channels such as $K_V7.2$-3, $K_{Ca}1.1$, channels, and $hK_V2.1$ (Lee and Wang, 1999; Peretz et al., 2005; Wu et al., 2001). As some of these

channels are expressed in cone bipolar cells (see section **1.3.2**), the decrease in R_N observed in OFF-bipolar cells may reflect the effect of MFA on these ionotropic channels. The effect of MFA on the membrane properties of rod bipolar cells was also observed. In these cells, R_N was stable with only minor fluctuation during MFA application (**Paper I**, **Fig. 5**). This is consistent with the absence of gap junctions and electrical coupling reported for rod bipolar cells (Strettoi et al., 1990; Veruki et al., 2006). MFA increased R_N only in ON-cone bipolar cells, and R_N increased up to a value similar to that for OFF-cone bipolar cells and rod bipolar cells in control solutions (**Paper I**, **Fig. 6A)**. This suggests that concerning R_N closing gap junction channels makes ON-cone bipolar cells electrically similar to OFF-cone and rod bipolar cells.

Next, we investigated if MFA differentially affects any of the different types of cone bipolar cells (**Paper I**, **Fig. 6B, C**). There was no difference in R_N between the different types of OFF-cone bipolar cells and no difference between the different types of ON-cone bipolar cells in control conditions. MFA application increase R_N on the different ON-cone bipolar cell types, even if this increase does not reach significativeness for type *8* and *6*. Similarly, in the three types of OFF-cone bipolar cells we recorded from, MFA application did not affect R_N. Unfortunately, we were not successful in obtaining recordings from the two rarer bipolar cell types, types *1* and *9*. Taken together, we concluded that there is no evidence for a type-specific effect of MFA in cone bipolar cells.

Finally, we investigated whether there was a cell type-specific difference in the relative amplitude of the gap junctional conductance and the non-gap junctional conductance. There was no difference between either conductance in the four different types of ON-cone bipolar cells (**Paper I**, **Fig. 6D**), suggesting that in these cell types, the contribution of gap junctional and non-gap junctional to the membrane conductance are similar.

4.2 Paper II

The project presented in **Paper II** aims to provide a detailed qualitative and quantitative analysis of the morphological properties of the different types of retinal bipolar cells. The morphological analysis of the bipolar cells was undertaken by performing morphological reconstructions based on multiphoton excitation microscopy image data from cells recorded in whole-cell patch clamp and filled with fluorescent dyes.

We performed whole-cell patch clamp recording on bipolar cells by targeting cell bodies in the most proximal two-third of the inner plexiform layer in rat retina slices. The identification of the type of bipolar cell was confirmed by switching the optical pathway from IR-DGC videomicroscopy to MPE fluorescence microscopy (**Paper II**, **Fig. 1**). The forward-scattered IR laser light enabled us to acquire simultaneous IR-LSGC images of the retina slice (**Paper II**, **Fig. 1A, B, C leftmost panels**) and perfectly on-line overlaying fluorescent images of the cell morphology (**Paper II**, **Fig. 1A, B, C rightmost panels**). After deconvolution and spatial alignment of the fluorescent image stacks, we performed an accurate digital reconstruction of 39 bipolar cells by manually tracing the neuron processes following the fluorescent signals across the MPE image stacks. The workflow for the reconstruction of an ON-cone bipolar cell is illustrated in **Paper II**, **Fig. 2**.

In the mammalian retina, 10 to 14 different types of bipolar cells have been identified depending on the species (see section **1.3.1** and Euler et al., 2014). The different types of bipolar cells all share similar characteristics that identified them as bipolar cells. Their soma is located in the IPL, they have one or more dendritic trees extending from the distal pole of their soma into the OPL, and they have one long axon stratifying and at different depth levels of the IPL (**Paper II**, **Fig. 3**). Cone bipolar cells with axon terminal stratifying and extending laterally in sublamina a and b correspond functionally to OFF and ON-cone bipolar cells (Famiglietti, 1981; Nelson et al., 1978). The stratification level of the axon terminal in the INL is also the main criteria used to define the types of cone bipolar cells in the rat retina (Euler and Wässle, 1995; Hartveit, 1997). Two examples are presented in **Fig. 3A,** and **3B (Paper II)** the axon terminal

of the cell in **Fig. 3A** stratify at the border between the INL and IPL and extend its processes down to the beginning of S2, which define the OFF-cone bipolar cell type *2*, in **Fig. 3B** the cell stratify at the border between S3 and extend only in half S4 which define the ON-cone bipolar cell type *6* (Euler and Wässle, 1995; Hartveit, 1997). Similarly, the 25 reconstructed cone bipolar cells were identified based on their stratification patterns with 10 OFF-cone bipolar cells and 14 ON-cone bipolar cells. Rod bipolar cells have a distinctive axon terminal morphology characterized by a smaller number of large varicosities located in the proximal part of the IPL (**Paper II, Fig. 3C**). The morphologies of the reconstructed bipolar cells are displayed in **Paper II, Fig. 4** and our material included rod bipolar cells (n = 14), OFF-cone bipolar cell type *2* (n = 2), *3* (n = 5), *4* (n = 3), and ON-cone bipolar cell type *5* (n = 5), *6* (n = 7), 7 (n = 3), and *8* (n = 1) lacking the rarer cone bipolar cell types *1* and *9*. The complexity of the branching patterns of the cone bipolar cell can be appreciated in the dendrograms shown in **Paper II, Fig. 5** (and **Paper II, Supp. Fig. 1**).

The qualitative description of the morphological properties of bipolar cells is sufficient to distinguish cone and rod bipolar cells and the different types of cone bipolar cells. However, it can be challenging to assign an individual cell correctly between two similar cone bipolar cell types. To improve our ability to assign the reconstructed cell to the correct bipolar cell types, we used our reconstructions to obtain a large panel of metric and topological parameters of neuronal morphology. The results of these analyses are summarized in **Paper II, Table 1, 2,** and **3**.

We analyzed the dendritic and axonal fields of the reconstructed bipolar cells by measuring the volume and surface area of the 3-D convex hulls of their axon terminals. Besides, we calculated the area, perimeter, Ferret maximum and minimum of the 2D convex hulls of the dendrites and axons skeletons projected on the XY plane. These projections are displayed in **Paper II, Fig.6**. For cone bipolar cells, the dendritic field area was either identical or smaller than that of the axonal terminal field. Conversely, for rod bipolar cells, the dendritic field area was consistently more extensive than the axon terminal field area (**Paper II, Fig. 6,7**). All bipolar cells have a similar dendritic field area (**Paper II, Table 1,2,3**); this difference corresponds to larger axon terminal

fields for cone bipolar cells than rod bipolar cells. This result indicates that all bipolar cells received inputs from similarly sized retinal regions, but cone bipolar cells distribute the information over a larger region in the inner plexiform layer (**Paper II, Fig. 7A**). Next, we investigated the correlation between dendritic and axonal field area to the dendritic and axon terminal branch length and number of segments to see whether this extended axonal field reflects a different axon terminal process organization, a simple scaling, or a more complex branching pattern. For both dendritic and axonal trees, the almost linear relationship indicates that the increased field area reflects an increasing branching complexity (**Paper II, Fig. 7C-F**).

Axon terminals of the cone bipolar cells presented a more complex branching than previously classically illustrated bipolar cells (Euler and Wässle, 1995; Famiglietti, 1981; Ghosh et al., 2004; MacNeil et al., 2004; Polyak, 1953). To quantify bipolar cell branching complexity, we analyzed the axon terminal parameters as a function of branch order. Bipolar axons are mostly unbranched except for a fraction of cone bipolar cells with ectopic branches along the axon shaft (Dumitrescu et al., 2009). Consequently, we used a central shaft ordering scheme to analyze the bipolar cell axon terminal parameters (**Paper II, Fig. 8**). The maximum branch order was typically between 21 and 23 for the cone bipolar cells with the two exceptions of cone bipolar cell type *6* which had the highest maximum branch order of 29 and type *8* the lowest (9) (**Paper II, Fig. 8A, relative occurrence**). For all cone bipolar cells, the distribution of all the parameters was slightly skewed toward lower branch order with a peak between branch order 10 and 12 (branch order 6 for cone bipolar cell type *8*) (**Paper II, Fig. 8B-G**). The distribution of all parameters for RBC differed clearly with the cone bipolar cells with a lower maximum branch order lower (5) and a distribution skewed toward the lowest branch orders (**Paper II, Fig. 8**).

Because the classification of cone bipolar cells into different types relies heavily on the stratification level of the axon terminal in the IPL, we decided to perform a detailed analysis of the distribution of the axon terminal process length, of the relative number of nodes, endings, and varicosities as a function of location across the height of the inner plexiform layer (**Paper II, Fig. 9**). The IPL thickness was divided into 100 equal

bins, and we created a separate stratification profile for each bipolar cell type (**Paper II, Fig. 9**). The different stratification properties marked a distinction between different types of cone bipolar cells, however, there was no clear difference between bipolar cell types regarding each specific parameter (**Paper II, Fig. 9A-E)**

The surface area of the axon terminal processes was used to display the probability density profile of each bipolar cell (Greene et al., 2016) (**Paper II, Fig. 9F)**, then we used the fifteenth and eighty-fifth percentile to define the stratification thickness of each bipolar cells and cluster the reconstructed bipolar cell in seven types (type *2* to *8*) (**Paper II, Fig. 9G)**, indicating that reconstruction based on MPE microscopy can provide classification data for individual cells.

Axonal varicosities are thought to be hotspots of synaptic inputs and outputs for bipolar cells (Boycott and Dowling, 1969; Dowling and Boycott, 1966; Kolb, 1979; McGuire et al., 1984; Sterling, 1983). As the distribution profiles of the axonal varicosities in the different bipolar cell types follow the same distribution as the other branching properties (**Paper II, Fig 9B**), we also analyze the size of the axonal varicosities defined as the diameter of the largest sphere that fitted within the projection of a given varicosity onto the XY plane. There was no difference in size or distribution within a bipolar cell type (**Paper II, Fig. 11A-G**) or difference in varicosities size between cell types (**Paper II, Fig. 11H**).

Besides analyzing the morphological properties of bipolar cell axon terminals as a function of the stratification level in the inner plexiform layer, and branch order, we used the Sholl analysis (Bird and Cuntz, 2019; Sholl, 1953) to analyzed the same properties as a function of eccentricity with the axon terminal (**Paper II, Fig. 12**). All parameters considered show minor differences between cone bipolar cell types with considerable overlap (**Paper II, Fig. 12B-J**). However, cone bipolar cell types *5* and *6* display a slight bimodal distribution of the parameters for sharing a peak with the other cone bipolar cell between 10-20 μm but with a second smaller peak at ~30 μm (**Paper II, Fig. 12B-J)**. Cone bipolar cell type *8* presents an overall larger average diameter than the other cone bipolar cells (**Paper II, Fig. 12I).**

Neural trees follow a general structural design with a systematic decrease in arbor density with an increase in arbor territory (Teeter and Stevens, 2011). We tested if the bipolar cell dendrites and axon terminals follow the same rule by analyzing the relationship between the tree volume and the density branch density. The fitted line slope was -0.44 and -0.33 for respectively the dendritic tree and axonal terminal, which corresponds to an exponent in linear space (cf. Teeter and Stevens, 2011) (**Paper II, Fig. 13**). These results make clear that bipolar cells adhere to the neuron general design principle. Similar to other retinal neurons (Zandt et al., 2017), bipolar cells display a relatively higher branching density than the large population of neuron cells studied by Teeter and Stevens (**Paper II, Fig. 13**).

In an earlier study from the lab, ten rod bipolar cells were reconstructed after being filled with biocytin (Oltedal et al., 2009). Comparing the morphometric properties of rod bipolar cells reconstructed in this thesis work to the previous ones, the two rod bipolar cell populations shared similar total surface area, however, biocytin filled rod bipolar cells present lower axon and dendritic endings points. These results indicated the biocytin filling is suboptimal and misses a number of the thin processes as previously reported for other retinal neurons (Zandt et al., 2017).

5. Discussion

The different types of bipolar cells are thought to form parallel channels of information within the retina circuit (Euler et al., 2014). The generation of these information channels arises initially from the different synaptic inputs the bipolar cells received from the photoreceptors (Behrens et al., 2016). Then, depending on the integrative properties of the different types of bipolar cells, each bipolar cell type extracts specific features of the photoreceptor inputs, such as contrast, temporal, and chromatic properties.

The integrative properties of a neuron depend on the neuron morphology and their membrane properties. The morphological data that have been studied in the bipolar cells were often limited to the level of stratification of these cells in the IPL and the size of their axon terminal (Euler et al., 2014). Most of these studies originate from Golgi impregnations (Boycott and Dowling, 1969; Linberg et al., 1996b; MacNeil et al., 2004). However, Golgi impregnations are known to incompletely stain the cells, often missing the thinnest processes, and thus cannot provide sufficient data to produce realistic bipolar cell reconstructions (Kang et al., 2017). Recent connectomic data give a more robust morphology of the different types of cone bipolar cells, but these data are only available in a limited number of species (mouse and rabbit) (Greene et al., 2016; Helmstaedter et al., 2013; Lauritzen et al., 2013). Importantly, other limitations of these connectomic studies are that they are only skeleton reconstructions, which lack the space-filling morphologic properties essential for modeling the integrative properties of the neurons (Helmstaedter et al., 2013), or that the morphological data of the bipolar cell reconstructions are not summarized quantitatively (Greene et al., 2016; Lauritzen et al., 2013; Tsukamoto and Omi, 2017). In this thesis, we performed a quantitative analysis of the morphological parameters of the rat bipolar cells. This quantitative morphological data generated a reference system for the reliable classification of individual bipolar cells in future studies. Additionally, the workflow that we have implemented can be readily extended to the development of morphologically realistic compartmental models for these neurons.

Aside from the neuron morphology, the integrative properties of neurons depend also on the proteins expressed at their membranes. Gap junctions are known to be expressed in the membrane of the axon terminals and dendrites of cone bipolar cells (Jacoby and Marshak, 1999; Kolb, 1979; Marc et al., 1988; Raviola and Gilula, 1975; Sigulinsky et al., 2020; Tsukamoto and Omi, 2014; Umino et al., 1994). However, their physiological role remains unclear (see **1.2.2**, Völgyi et al., 2013). As a first step to elucidate the contribution of the gap junction to the integrative properties of the bipolar cells, we investigated how gap junctions affect the input resistance of different bipolar cells. Surprisingly, our results suggested that the gap junctions expressed by OFF-cone bipolar cells do not support consequential electrical coupling.

5.1 Bipolar cell classification

Bipolar cell classification in the mammalian retina has been performed predominantly by differentiating the types of bipolar cells by their stratification level in the IPL (Euler et al., 2014). Similarly, in the rat retina, bipolar cells have been divided into ten types based on their stratification level from the innermost stratifying bipolar cell, the cone bipolar cell type *1*, to the rod bipolar cells stratifying close to the border between IPL and GCL (Euler and Wässle, 1995; Hartveit, 1997). We classified following this scheme the targeted bipolar cells in 8 groups: types *2-8* cone bipolar cells with the addition of the rod bipolar cells. In the mouse retina, additional types of cone bipolar cells have been described up to 14 to 15 different types of bipolar cells (Euler et al., 2014; Greene et al., 2016; Helmstaedter et al., 2013). The difference in the number of bipolar cell types between the rat and mouse, two closely related species with strong similarity in their behavior (Singleton et al., 2003), raises the question of the completeness of the classification scheme for the rat retina. For the OFF-cone bipolar cells, we are missing cone bipolar cell type *1*, which is the most rare OFF-cone bipolar cell type (Wässle et al., 2009). In 2016, Della Santina *et al.* identified a mouse retinal cell type named glutamatergic monopolar interneuron (GluMi) stratifying in the IPL at a similar level than cone bipolar cell type *1*. These neurons possessed synaptic ribbon structures to release glutamate like bipolar cells, but lacked dendrites completely and

thus morphologically looked like a small field amacrine cell (Della Santina et al., 2016). This non-canonical bipolar cell type has not been reported in the rat retina. However, we verified the morphology of the targeted cells using MPE microscopy before recording, and we excluded any cell lacking dendrites. As it is not possible to distinguish GluMi from a cone bipolar cell type *1* cell with truncated dendrites, we would not have targeted this cell type with our experimental protocol.

Mouse cone bipolar cell types *3a* and *3b* are two bipolar cell populations stratifying at the same depth of the IPL, which have been differentiated by their immunoreactivity to two different antibodies, respectively antibodies against HCN4 and PKARIIβ (Ghosh et al., 2004). Later studies confirmed that both cells respect the tiling rule and showed that type *3a* cone bipolar cells have a larger axon terminal field than type *3b* (Wässle et al., 2009). This difference in axonal field size was used as morphological criteria to differentiate the two cell types in connectomic studies (Helmstaedter et al., 2013). However, in our study, we could not separate cone bipolar cell type *3* as defined in the "classical" rat bipolar cell classification into two groups based on the size of the axon terminal field (Euler and Wässle, 1995; Hartveit, 1997). This result raises the question of whether or not these two types exist in the rat retina. Antibodies against HCN4 and PKARIIβ labeled two different populations of cone bipolar cell types *3* in the rat retina, which have different functional responses (Vielma and Schmachtenberg, 2016) confirming the separation of the cone bipolar cell types *3* into two different types *3a* and *3b* in the rat. However, the morphology of the bipolar cell types *3a* and *3b* in the rat retina have not been investigated. It would be of interest to perform similar morphological analysis as presented in this thesis but completed with the identification of the reconstructed cells using immunolabeling following the live recordings.

As cone bipolar cells tile the entire retina span with the same coverage and their density decreases as a function of their eccentricity (Martin and Grünert, 1992), retinal bipolar cell degree of eccentricity affects their axonal field size. Unfortunately, we could not keep track of the retinal eccentricity of our reconstructed cells. Thus, adding the variability in the axonal size brought by the degree of eccentricity with the relatively small number of type *3* cone bipolar cells that we reconstructed may explain our

inability to differentiate bipolar cell types *3a* and *3b* based only on morphological parameters.

Four ON-cone bipolar cell types *5i*, *5o*, *5t*, and *X*, all stratifying within sublamina 3, have been characterized in the mouse retina, whereas only the "classical" type *5* cone bipolar cell stratifies in the same sublamina of the rat retina (Euler and Wässle, 1995; Greene et al., 2016; Hartveit, 1997; Helmstaedter et al., 2011; Tsukamoto and Omi, 2017). The identification of these four types of ON-cone bipolar cells in the mouse was made possible by analyzing their subtle difference in stratification levels and connectivity patterns followed by confirmation of the tiling rule using connectomic data (Greene et al., 2016; Helmstaedter et al., 2013). One population of rat ON-cone bipolar cell type *5* expresses voltage-gated sodium channels (Ivanova and Müller, 2006; Ma et al., 2005). Furthermore, in the rat retina, antibodies against HCN2 label only a fraction of the cone bipolar cell stratifying in sublamina 3 (Fyk-Kolodziej and Pourcho, 2007). These results indicate the existence of different functional types of rat ON-cone bipolar cells co-stratifying within sublamina 3. However, the morphological parameters we used could not separate different clusters in the population of "classical" type *5* ON-cone bipolar cells, similarly to the lack of differential morphological features between the three mouse types *5i/o* and *t* (Greene et al., 2016).

It is important to note a difference between the types of the ON-cone bipolar cells described in the mouse and rat retina. Mouse ON-cone bipolar cell type *6* stratifies across almost all sublamina b (Greene et al., 2016; Helmstaedter et al., 2011), but in the rat retina, no bipolar cell possesses the same morphological property. This difference may represent a difference in the retina circuit, similar to other variations in retina circuit observed between closely related species, for example the mouse and rabbit direction selectivity circuits (Ding et al., 2016).

5.2 Electrical coupling of ON and OFF-cone bipolar cells

There is strong evidence for the presence of gap junctions at the dendrites (Feigenspan et al., 2004; Kántor et al., 2016; Mills, 1999; O'Brien et al., 2012) and axon terminals

(Kántor et al., 2017; Kolb, 1979; Tsukamoto and Omi, 2014, 2017) of the OFF-cone bipolar cells. Therefore, it is surprising that the application of MFA did not affect the input resistance of the OFF-cone bipolar cells. If MFA blocked the gap junction opening of the OFF-cone bipolar cells, we would expect to see an increase of the input resistance, like the increase we observed in ON-cone bipolar cells and also observed in other retinal cells expressing gap junction like AII amacrine cells (Veruki et al., 2010), A17 amacrine cells (Elgueta et al., 2018) and Golgi interneurons (Szoboszlay et al., 2016). There are two possible explanations for the lack of MFA effect: (1) either MFA is unable to block the gap junction opening in OFF-cone bipolar cells, or (2) in our recording conditions, the conductance of the gap junction in OFF-cone bipolar cell does not contribute to the input resistance of the OFF-cone bipolar cells.

The possibility of the former explanation seems unlikely for several reasons. First, MFA blocks the diffusion of biocytin between horizontal cells of both types A and B in the rabbit (Pan et al., 2007), which express Cx50 and Cx57 (Bolte et al., 2016; Pan et al., 2007). MFA can also block the electrical synapse current and dye diffusion between AII amacrine cells and ON-cone bipolar cells (Pan et al., 2007; Veruki et al., 2010). The connexin composition of the electrical synapses between AII amacrine cells and ON-cone bipolar cells differs depending on the ON-cone bipolar cell type and is either composed of a mixed of connexins (Cx36 and 45) or only Cx36 (Dedek et al., 2006; Han and Massey, 2005b; Li et al., 2008; Lin et al., 2005; Maxeiner et al., 2005). These results taken together suggest that MFA presents a weak to no specificity to any types of connexins. As MFA activity was not tested on the 20 different types of connexins that can form electrical junctions in the rodents (Söhl and Willecke, 2003), it is impossible to rule out that OFF-cone bipolar cells express a type of connexin not affected by MFA. However, retinal cells expressed only a subset of connexin types, and in the IPL out of 13 types tested (Cx26, 30, 30.3, 31, 31.1, 32, 36, 37, 40, 43, 45, 46, and 50), only Cx36 and 45 are expressed (Güldenagel et al., 2000). In a transgenic mouse model expressing a connexin 45-EGFP fusion protein, Cx45 is expressed in the dendrites and axon terminals of the OFF-cone bipolar cells (Hilgen et al., 2011). Cx36 labeling is found expressed in the dendrites of mouse and macaque OFF-cone bipolar

cells and human midget OFF-cone bipolar cells (Feigenspan et al., 2004; Kántor et al., 2016; O'Brien et al., 2012) and in the axon terminal of the human OFF-cone bipolar cell DB3 and midget OFF-cone bipolar cells (Kántor et al., 2017). Thus, the two types of connexins expressed in the OFF-cone bipolar cells should be blocked by MFA (Pan et al., 2007; Veruki et al., 2010). Additionally, the nearly identical values of input resistance for OFF-cone bipolar cells in control conditions and for ON-cone bipolar cells after MFA took effect enforces the hypothesis that the lack of MFA effect on OFF-cone bipolar is due to the absence of electrical coupling in those cells rather than the presence of connexin insensible to MFA. This observation suggests that OFF-cone bipolar cells in the rat retina are effectively uncoupled electrically.

Then, the only reasonable explanation for lack of MFA effect is that under our recording conditions, we cannot measure the contribution of the low conductance of the gap junctions to the input resistance in OFF-cone bipolar cells. The conductance of the electrical synapses depends on the number of connexons, their conductance, and the average open probability. There is no report on the number of connexons in OFF-cone bipolar cells. Because connexons form hexagonal arrays in gap junction (Benedetti and Emmelot, 1965), the surface area of the gap junctions indicate the number of connexons, and there are reports that OFF-cone bipolar cell gap junctions are relatively small (Kolb, 1979). The other possibility is that the open probability of the gap junctions could be low under our recording conditions. The exact connectivity map of the gap junctions of the OFF-cone bipolar cells is not clear.

Nevertheless, the OFF-cone bipolar cell gap junction partners seem to be mainly other OFF-cone bipolar cells of either the same or of a different type, and there is also the report of gap junction between different branches of the same bipolar cell (Tsukamoto and Omi, 2014, 2017). The complete connectivity maps of the rabbit ON-cone bipolar cell electrical synapses have been defined in a recent study (Sigulinsky et al., 2020). Like OFF-cone bipolar cells, the main gap junction partners of the ON-cone bipolar cells are other ON-cone bipolar cells of either the same or different types (Sigulinsky et al., 2020; Tsukamoto and Omi, 2017).

Additionally, ON-cone bipolar cells also make canonical electrical synapses with AII amacrines (Dacheux and Raviola, 1986; Hartveit and Veruki, 2012; McGuire et al., 1984; Tsukamoto and Omi, 2017). It is not currently possible to distinguish the relative conductance of each partner of ON-cone bipolar cells experimentally. However, we measured a similar junctional conductance in all the different types of ON-cone bipolar cells, and it has been reported that the number of electrical synapses between specific types of ON-cone bipolar cells and AII amacrine cells varies (Sigulinsky et al., 2020; Tsukamoto and Omi, 2017). Therefore, it is probable that contrary to OFF-cone bipolar cells, the homologous gap junctions between ON-cone bipolar cells participates in the input resistance of the cells under our recording conditions.

As previously discussed in the introduction, several plasticity mechanisms regulate the conductance of the gap junction on different time scales (O'Brien and Bloomfield, 2018). Notably, circadian rhythms and ambient light levels strongly modulate electrical synapses in the retina via signaling cascades activated notably by dopamine and nitric oxide (see review O'Brien and Bloomfield, 2018; Trenholm and Awatramani, 2017). There is no evidence if the same mechanisms take place in the OFF-cone bipolar cells, but figuring if and how the coupling strength in OFF-cone bipolar cells is affected by different light intensity could give more insight into the functional role of the connexons in the OFF-cone bipolar cells. If the weak coupling strength between OFF-cone bipolar cells we observed is unchanged regardless of the condition, the function of the gap junction channels could be to enable chemical and/or metabolic coupling within local subcellular domains, or to play a structural role, e.g., as adhesion molecules (Mills, 1999; Pereda, 2016).

Despite the evidence for the presence of gap junction at both dendrites and axon terminal of both ON- and OFF-cone bipolar cells (Feigenspan et al., 2004; Kántor et al., 2016, 2017; Kolb, 1979; O'Brien et al., 2012; Tsukamoto and Omi, 2014, 2017), there are only a few reports of solid evidence of functional coupling between cone bipolar cells. In the rabbit, homotypical dye coupling was demonstrated between *a1w* bipolar cells (MacNeil et al., 2004; Mills, 1999). The only functional electrical coupling report is found in Mb1 (ON) cone bipolar cells in the goldfish retina (Arai et

al., 2010). Electrical coupling between coupled Mb1 cell pairs acted as a low-pass filter that could transmit Ca^{2+} spikes, which prolonged the current response in postsynaptic ganglion cells (Arai et al., 2010). Reproducing similar experiments with dual patching of coupled pairs would be crucial to understand the functional role of the electrical synapses between cone bipolar cells in the mammalian retina. However, concerning the number of bipolar cells types (Euler and Wässle, 1995; Euler et al., 2014; Ghosh et al., 2004; Hartveit, 1997; Light et al., 2012; Sigulinsky et al., 2020) and the complexity of the coupling network extrapolated from connectomic data (Sigulinsky et al., 2020; Tsukamoto and Omi, 2017), this task will need to access animals with fluorescently labeled cell types. The most completed catalog of labeled cell types available is in the mouse (Euler et al., 2014), but comparison to other relevant mammalian models like rat, rabbit and ground squirrel will be of interest.

5.3 Morphometric analysis of the bipolar cells

The correct estimation of the diameter of the processes of the reconstructed cells is critical for the correct estimation of the integrative properties of any given neuron. Any discrepancy between the diameter of the processes of the live cell and of the reconstructed cell would affect any modeling of the passive membrane properties of this neuron, notably its specific capacitance and axial resistance. One limitation of the MPE microscopy to perform realistic reconstruction of neuronal cells is that the thinnest dendritic and inter-varicosities processes have sub-resolution diameters. Therefore, the diameters of these thin processes cannot be adequately imaged and reconstructed. There are no connectomic data available for the rat cone bipolar cells providing volumetric data. However, we estimated the minimum diameter of the thinnest dendritic and axonal processes by measuring these diameters in previously published electron microscopy micrographs of rat cone bipolar cells (Brandstätter et al., 1994; Cao et al., 2015; Chun et al., 1993, 1999; Koulen et al., 1997; Sassoè-Pognetto et al., 1994), constraining the minimum diameter of the reconstructed dendritic and axonal processes to respectively 0.12 and 0.15 μm.

Performing cell reconstructions based on MPE microscopy data brings several limitations, raising the question of its relevance compared to other imaging technics. Electron microscopy resolution in the nanometer range allows for a correct estimation of the diameter of the thinnest neuronal processes (Brandstätter et al., 1994; Cao et al., 2015; Chun et al., 1993, 1999; Koulen et al., 1997; Sassoè-Pognetto et al., 1994). As previously mentioned, the connectomic data provided from the acquisition of small volumes of mouse and rabbit retina were able to identify new types of cone bipolar cells by reconstructing a large number of bipolar cells, confirming cell types by tiling and segregating cell types based on their connectivity to specific ganglion cell types (Greene et al., 2016; Helmstaedter et al., 2013). However, the connectomic data's substantial size brings challenges in data analysis and neuron segmentation (Lichtman et al., 2014). Neuron segmentation needs to be performed by numerous trained human annotators, particularly in dense neural tissue like the retina, where automatic reconstruction algorithms cannot resolve complex locations where multiple neurites are densely intertwined (Helmstaedter, 2013). Even then, reconstruction can be incomplete and suffer from branch loss (Helmstaedter, 2013). We also performed manual reconstruction, but the advantage of MPE microscopy is that each cell is clearly labeled, allowing for a faster reconstruction performed with a limited number of human annotators. The limited size of the tissue volume that can be acquired in block-face electron microscopy cannot account for the diversity in axonal field size we observed between cells of the same types at different eccentricities (see cone bipolar cells type *2* in **Paper II, Fig. 6A**). The constraint on the acquisition volume is also a limiting factor for reconstructing complete bipolar cells in species with cone bipolar cells possessing large axonal fields (Anderson et al., 2011).. In the rabbit connectomic reconstruction the OPL had to be excluded from the acquisition to reconstruct a more extensive section of the retina surface to allow complete reconstruction of cone bipolar cells with large axonal fields like the wide-field ON-cone bipolar cells (Marc et al., 2012). By excluding the OPL from the acquisition any information on the dendritic tree of the rabbit cone bipolar cells were then lose.

Another advantage of MPE microscopy is its very low phototoxicity, which enables live recording. Performing live recording gives some advantages for the

reconstructions by avoiding fixation artifacts that limit the distortions in the cell morphology that negatively affects the cell reconstructions and modeling.

5.4 Future perspectives

Despite the evidence for the presence of gap junction at both dendrites and axon terminal of both ON- and OFF-cone bipolar cells (Feigenspan et al., 2004; Kántor et al., 2016, 2017; Kolb, 1979; O'Brien et al., 2012; Tsukamoto and Omi, 2014, 2017), there are only a few reports of solid evidence of functional coupling between cone bipolar cells. In the rabbit, homotypical dye coupling was demonstrated between a1w bipolar cells (MacNeil et al., 2004; Mills, 1999). The only functional electrical coupling report is found in Mb1 (ON) cone bipolar cells in the goldfish retina (Arai et al., 2010). Electrical coupling between coupled Mb1 cell pairs acted as a low-pass filter that could transmit Ca^{2+} spikes, which prolonged the current response in postsynaptic ganglions cells (Arai et al., 2010). Reproducing similar experiments with dual patching of coupled pairs would be crucial to understand the functional role of the electrical synapses between cone bipolar cells in the mammalian retina. However, concerning the number of bipolar cells types (Euler and Wässle, 1995; Euler et al., 2014; Ghosh et al., 2004; Hartveit, 1997; Light et al., 2012; Sigulinsky et al., 2020) and the complexity of the coupling network extrapolated from connectomic data (Sigulinsky et al., 2020; Tsukamoto and Omi, 2017) this task will need the access animals with fluorescently labeled cell types. The most completed catalog of labeled cell types available is in the mouse (Euler et al., 2014), but comparison to other relevant mammalian models like rats, rabbits, and ground squirrels will be of interest. Similarly, animals with fluorescently labeled cell types will be particularly interesting to refine the classification of the bipolar cell types in the rat retina. Besides, reproducing the connectomic study of the retina circuit in other species than rabbit and mouse will be of interest to reveal differences in the retina circuit and refine bipolar cell classification.

It was an explicit goal of the present study to establish a workflow for MPE microscopy of bipolar cells filled with fluorescent dye during whole-cell recording that can be extended to encompass compartmental modeling to develop models that can serve as

electrical skeletons. For high-quality models, the morphological reconstructions must be generated from the same neurons from which electrophysiological data are obtained (Carnevale and Hines, 2006; Major, 2001). To our knowledge, no such reconstructions have been published for cone bipolar cells and none seem available in any of the publicly accessible databases of morphologically reconstructed neurons (e.g. NeuroMorpho.Org; Ascoli et al., 2007). The published reconstructions generated from deep connectomic data (Greene et al., 2016; Helmstaedter et al., 2013) do not have accompanying physiological data and cannot be used for high-quality compartmental modeling.

The RC-circuit model is a single compartment model that can accurately reflect some neuron properties (Carandini et al., 1996). However, bipolar cells have complex dendritic and axon terminal processes as we illustrated with our reconstructions, making it difficult to assume they are isopotential. Thus, their response properties would not be accurately accounted for in such a simple model. The linear cable theory equations first developed in the early 20th century (Hermann, 1905) and completed in the latter half of the century (Hodgkin and Huxley, 1952; Rall, 2003) can be derived to calculate the spread of signals into neurons with complex neuronal processes with some simplifications rules (Rall, 2003). However, solving differential equations for large and complex neurons is difficult, moreover few neurons follow these rules, and applying these simplifications to neurons with morphologies that do not respect these rules leads to erroneous results (Holmes et al., 1992). The solution is to divide the model into tiny isopotential compartments, modeled by RC-circuits, connected by resistors, which model the axial resistance of intracellular medium to the diffusion of membrane potential variation across the cell, then use discrete time steps to compute the cable equation in each compartment (Rall, 1964). In computer simulations, the number of compartments must be limited, and that number is an essential aspect of the trade-off between simulation accuracy and computing time. Traditionally, the approach to simulating such a model was to divide each cylinder of the reconstructed model as an isopotential compartment and increase the number of electrical segments manually by an odd number in each cylinder to reduce the simulation error. Such models create an adequate spatial grid in some regions but a much thinner one than necessary which

increases the simulation burden. Hines and Carnevale have developed an improved approach in NEURON environment by using a fraction of the length constant of an alternative current injected at a frequency high enough for the membrane resistance contribution to the decay of the signals becoming negligible compared to the capacitive components (Carnevale and Hines, 2006). Using NEURON environment to simulate the response of the realistic compartmental model response developed in Paper II to the same protocol used in the patch-clamp recording used in Paper I with the electrophysiological recording of the reconstructed cell to we could estimate the passive electrical properties of the bipolar cells using direct fitting. To do so NEURON's Multiple Run Fitter tool (Carnevale and Hines, 2006; Clements and Redman, 1989) minimize the sum of squared error (χ^2) between the model and the live cell current response to the voltage step by using the point-to-point principal axis (PRAXIS) algorithm (Brent, 1973) by adjusting fitted parameters. Using the three passive electrical properties of the neuron as fitting parameters: specific capacitance (C_m), specific membrane resistance (R_m), axial resistivity (R_a), the simulation results would estimate the different bipolar cell passive properties and results in completed passive realistic multicompartmental bipolar cell models.

It will be of interest to use such morphologically realistic passive models to investigate the degree of compartmentalization of bipolar cell axon terminals and the putative role of gap junctions in this compartmentalization as it has been shown in other retinal cells like the A17 (Elgueta et al., 2018).

The transient and sustained response properties of ON- and OFF-cone bipolar cells (Awatramani and Slaughter, 2000; Roska and Werblin, 2001) partially originate from their actives conductances (Hellmer et al., 2016; Ichinose et al., 2014). In rod bipolar cells, I_h has been shown to endow the cell with frequency–tuning (Cangiano et al., 2007). HCN channels are differentially expressed in the different types of cone bipolar cells, and their exact expression pattern is still unclear (Fyk-Kolodziej and Pourcho, 2007; Ivanova and Müller, 2006; Vielma and Schmachtenberg, 2016). To understand how I_h affects and defines type-specific bipolar cell response properties, it will be important to develop type-specific I_h models. Realistic models will serve as skeletons

to add these current models to investigate their implication on the bipolar cell response properties. Similarly, passive models will also be of interest to use as a tool to investigate the functional properties endowed to some bipolar cell types by other active conductances known to be express differentially between bipolar cell types such as I_{Na} (Cui and Pan, 2008; Hellmer et al., 2016; Ichinose and Lukasiewicz, 2007; Ivanova and Müller, 2006; Ma et al., 2005; Saszik and Devries, 2012; Vielma and Schmachtenberg, 2016), I_K (Van Hook et al., 2019; Ma et al., 2005) or I_{KIR} (Ma et al., 2004) but also investigated the role of other potentially expressed channels like for example the BK channels (Shekhar et al., 2016).

6. Concluding remarks

Aside from the main dichotomies of the retina circuit between rod and cone inputs and ON versus OFF responses, there is a lack of understanding of the specific functions of each bipolar cell type in the retina circuit. The function of the bipolar cells depends on their dynamic and integrative properties, which are determined by their morphology, passive membrane properties, cytoplasmic resistivity, and associated ion channel properties and distribution. In this thesis work, we investigated the morphological properties, passive membrane properties in rat ON-cone, OFF-cone, and rod bipolar cells, and the contribution of the gap junctions to their membrane properties. This work has been carried out by using a combination of electrophysiological recording and live imaging by MPE microscopy followed by manual reconstruction and multicompartmental model building.

We have shown that gap junctions contributed to the input resistance in the ON-cone bipolar cell types, whereas gap junctions do not contribute to the membrane properties of the OFF-cone bipolar cells and rod bipolar cells. This differential role of the gap junction between the ON- and OFF-cone bipolar cells give new insight into the functional role of gap junctions in the retina circuit.

We provided for the first time a detailed analysis of the morphological properties of the different bipolar cell types, focusing on soma size, dendritic tree size and structure, and axonal branching and terminal structure. Bipolar cells have more complex axon terminals and dendritic trees than previously described and the size increment link to the eccentricity directly reflects an increase in complexity of the neuron trees. This complexity may reflect unexpected additional computation in the axon terminal of the bipolar cells than previously expected.

Through this work, we provided solid foundations to build multicompartmental models that will become powerful tools to explore in new ways the function of the bipolar cells in the retina circuit.

References

Akaike, N. (1996). Gramicidin perforated patch recording and intracellular chloride activity in excitable cells. Prog. Biophys. Mol. Biol. *65*, 251–264.

Akaike, N., and Harata, N. (1994). Nystatin perforated patch recording and its applications to analyses of intracellular mechanisms. Jpn. J. Physiol. *44*, 433–473.

Altimus, C.M., Güler, A.D., Alam, N.M., Arman, A.C., Prusky, G.T., Sampath, A.P., and Hattar, S. (2010). Rod photoreceptors drive circadian photoentrainment across a wide range of light intensities. Nat. Neurosci. *13*, 1107–1112.

Ames III, A., and Nesbett, F.B. (1981). In Vitro Retina as an Experimental Model of the Central Nervous System. J. Neurochem. *37*, 867–877.

Anastassov, I.A., Wang, W., and Dunn, F.A. (2019). Synaptogenesis and synaptic protein localization in the postnatal development of rod bipolar cell dendrites in mouse retina. J. Comp. Neurol. *527*, 52–66.

Anderson, J.R., Jones, B.W., Yang, J.H., Shaw, M. V., Watt, C.B., Koshevoy, P., Spaltenstein, J., Jurrus, E., Kannan, U., Whitaker, R.T., et al. (2009). A computational framework for ultrastructural mapping of neural circuitry. PLoS Biol. *7*, 0493–0512.

Anderson, J.R., Jones, B.W., Watt, C.B., Shaw, M. V, Yang, J.H., Demill, D., Lauritzen, J.S., Lin, Y., Rapp, K.D., Mastronarde, D., et al. (2011). Exploring the retinal connectome. Mol Vis *17*, 355–379.

Arai, I., Tanaka, M., and Tachibana, M. (2010). Active roles of electrically coupled bipolar cell network in the adult retina. J. Neurosci. *30*, 9260–9270.

Ascoli, G.A., Donohue, D.E., and Halavi, M. (2007). NeuroMorpho.Org: A central resource for neuronal morphologies. J. Neurosci. *27*, 9247–9251.

Attwell, D., Wilson, M., and Wu, S.M. (1984). A quantitative analysis of interactions between photoreceptors in the salamander (Ambystoma) retina. J. Physiol. *352*, 703–

737.

Awatramani, G.B., and Slaughter, M.M. (2000). Origin of transient and sustained responses in ganglion cells of the retina. J. Neurosci. *20*, 7087–7095.

Awatramani, G.B., and Slaughter, M.M. (2001). Intensity-dependent, rapid activation of presynaptic metabotropic glutamate receptors at a central synapse. J. Neurosci. *21*, 741–749.

Baden, T., and Osorio, D. (2019). The retinal basis of vertebrate color vision. Annu. Rev. Vis. Sci. *5*, 177–200.

Baden, T., Euler, T., Weckström, M., and Lagnado, L. (2013). Spikes and ribbon synapses in early vision. Trends Neurosci. *36*, 480–488.

Baden, T., Berens, P., Franke, K., Román Rosón, M., Bethge, M., and Euler, T. (2016). The functional diversity of retinal ganglion cells in the mouse. Nature *529*, 345–350.

Bae, J.A., Mu, S., Kim, J.S., Turner, N.L., Tartavull, I., Kemnitz, N., Jordan, C.S., Norton, A.D., Silversmith, W.M., Prentki, R., et al. (2018). Digital museum of retinal ganglion cells with dense anatomy and physiology. Cell *173*, 1293-1306.e19.

Baumann, L., Gerstner, A., Zong, X., Biel, M., and Wahl-Schott, C. (2004). Functional characterization of the L-type Ca2+ channel Ca v1.4α1 from mouse retina. Investig. Ophthalmol. Vis. Sci. *45*, 708–713.

Baylor, D.A., Lamb, T.D., and Yau, K.W. (1979). Responses of retinal rods to single photons. J. Physiol. *288*, 613–634.

Behrens, C., Schubert, T., Haverkamp, S., Euler, T., and Berens, P. (2016). Connectivity map of bipolar cells and photoreceptors in the mouse retina. Elife *5*, 1–20.

Benedetti, E.L., and Emmelot, P. (1965). Electron microscopic observations on negatively stained plasma membranes isolated from rat liver. J. Cell Biol. *26*, 299–

305.

Berntson, A., Taylor, W.R., and Morgans, C.W. (2003). Molecular identity, synaptic localization, and physiology of calcium channels in retinal bipolar cells. J. Neurosci. Res. *71*, 146–151.

Billups, D., and Attwell, D. (2002). Control of intracellular chloride concentration and GABA response polarity in rat retinal ON bipolar cells. J. Physiol. *545*, 183–198.

Bird, A.D., and Cuntz, H. (2019). Dissecting sholl analysis into its functional components. Cell Rep. *27*, 3081-3096.e5.

Bolte, P., Herrling, R., Dorgau, B., Schultz, K., Feigenspan, A., Weiler, R., Dedek, K., and Janssen-Bienhold, U. (2016). Expression and Localization of Connexins in the Outer Retina of the Mouse. J. Mol. Neurosci. *58*, 178–192.

Boos, R., Schneider, H., and Wässle, H. (1993). Voltage- and transmitter-gated currents of all-amacrine cells in a slice preparation of the rat retina. J. Neurosci. *13*, 2874–2888.

Borghuis, B.G., Looger, L.L., Tomita, S., and Demb, J.B. (2014). Kainate receptors mediate signaling in both transient and sustained OFF bipolar cell pathways in mouse retina. J Neurosci *34*, 6128–6139.

Boycott, B.B., and Dowling, J.E. (1969). Organization of the primate retina: Light microscopy. Philos. Trans. R. Soc. Lond. B. Biol. Sci. *255*, 109–184.

Boycott, B.B., and Kolb, H. (1973). The connections between bipolar cells and photoreceptors in the retina of the domestic cat. J. Comp. Neurol. *148*, 91–114.

Brandstätter, J.H., Hartveit, E., Sassoè-Pognetto, M., and Wässle, H. (1994). Expression of NMDA and high-affinity kainate receptor subunit mRNAs in the adult rat retina. Eur. J. Neurosci. *6*, 1100–1112.

Brandstätter, J.H., Koulen, P., and Wässle, H. (1997). Selective synaptic distribution of kainate receptor subunits in the two plexiform layers of the rat retina. J. Neurosci.

17, 9298–9307.

Brent, R.P. (1973). A new algorithm for minimizing a function of several variables without calculating derivatives. In Algorithms for Minimization Without Derivatives, Englewood Cliffs, ed. (New Jersey), pp. 116–156.

Breuninger, T., Puller, C., Haverkamp, S., and Euler, T. (2011). Chromatic bipolar cell pathways in the mouse retina. J. Neurosci. *31*, 6504–6517.

Briggman, K.L., Helmstaedter, M., and Denk, W. (2011). Wiring specificity in the direction-selectivity circuit of the retina. Nature *471*, 183–190.

Bringmann, A., Pannicke, T., Grosche, J., Francke, M., Wiedemann, P., Skatchkov, S.N., Osborne, N.N., and Reichenbach, A. (2006). Müller cells in the healthy and diseased retina. Prog. Retin. Eye Res. *25*, 397–424.

Brown, S.P., and Masland, R.H. (1999). Costratification of a population of bipolar cells with the direction-selective circuitry of the rabbit retina. J. Comp. Neurol. *408*, 97–106.

Buldyrev, I., Puthussery, T., and Taylor, W.R. (2012). Synaptic pathways that shape the excitatory drive in an OFF retinal ganglion cell. J Neurophysiol *107*, 1795–1807.

Bunt-Milam, A.H., Saari, J.C., Klock, I.B., and Garwin, G.G. (1985). Zonulae adherentes pore size in the external limiting membrane of the rabbit retina. Investig. Ophthalmol. Vis. Sci. *26*, 1377–1380.

Cangiano, L., Gargini, C., Della Santina, L., Demontis, G.C., and Cervetto, L. (2007). High-Pass Filtering of Input Signals by the Ih Current in a Non-Spiking Neuron, the Retinal Rod Bipolar Cell. PLoS One *2*.

Cao, Y., Sarria, I., Fehlhaber, K.E., Kamasawa, N., Orlandi, C., James, K.N., Hazen, J.L., Gardner, M.R., Farzan, M., Lee, A., et al. (2015). Mechanism for selective synaptic wiring of rod photoreceptors into the retinal circuitry and its role in vision. Neuron *87*, 1248–1260.

Carandini, M., Mechler, F., Leonard, C.S., and Movshon, J.A. (1996). Spike train encoding by regular-spiking cells of the visual cortex. J. Neurophysiol. *76*, 3425–3441.

Carnevale, N.T., and Hines, M.L. (2006). The NEURON Book (Cambridge: Cambridge University Press).

Casini, G., Brecha, N.C., Bosco, L., and Rickman, D.W. (2000). Developmental expression of neurokinin-1 and neurokinin-3 receptors in the rat retina. J. Comp. Neurol. *421*, 275–287.

Casini, G., Sabatini, A., Catalani, E., Willems, D., Bosco, L., and Brecha, N.. (2002). Expression of the neurokinin 1 receptor in the rabbit retina. Neuroscience *115*, 1309–1321.

Chapot, C.A., Euler, T., and Schubert, T. (2017). How do horizontal cells 'talk' to cone photoreceptors? Different levels of complexity at the cone–horizontal cell synapse. In Journal of Physiology, (Blackwell Publishing Ltd), pp. 5495–5506.

Chávez, A.E., Singer, J.H., and Diamond, J.S. (2006). Fast neurotransmitter release triggered by Ca influx through AMPA-type glutamate receptors. Nature *443*, 705–708.

Chun, M.-H., Han, S.-H., Chung, J.-W., and Wässle, H. (1993). Electron microscopic analysis of the rod pathway of the rat retina. J. Comp. Neurol. *332*, 421–432.

Chun, M.-H., Oh, S.-J., Kim, I.-B., and Kim, K.-Y. (1999). Light and electron microscopical analysis of nitric oxide synthase-like immunoreactive neurons in the rat retina. Vis. Neurosci. *16*, 379–389.

Clements, J.D., and Redman, S.J. (1989). Cable properties of cat spinal motoneurones measured by combining voltage clamp, current clamp and intracellular staining. J. Physiol. *409*, 63–87.

Cohen, E., and Sterling, P. (1990a). Demonstration of cell types among cone bipolar

neurons of cat retina. Philos. Trans. R. Soc. Lond. B. Biol. Sci. *330*, 305–321.

Cohen, E., and Sterling, P. (1990b). Convergence and divergence of cones onto bipolar cells in the central area of cat retina. Philos. Trans. R. Soc. Lond. B. Biol. Sci. *330*, 323–328.

Cole, K.S. (1949). Dynamic electrical characteristics of the squid axon membrane. Arch. Sci. Physiol. (Paris). *3*, 253–258.

Cox, G., and Sheppard, C.J.R. (2004). Practical limits of resolution in confocal and non-linear microscopy. Microsc. Res. Tech. *63*, 18–22.

Cuenca, N., Deng, P., Linberg, K.A., Lewis, G.P., Fisher, S.K., and Kolb, H. (2002). The neurons of the ground squirrel retina as revealed by immunostains for calcium binding proteins and neurotransmitters. J. Neurocytol. *31*, 649–666.

Cui, J., and Pan, Z.-H. (2008). Two types of cone bipolar cells express voltage-gated Na+ channels in the rat retina. Vis. Neurosci. *25*, 635.

Dacheux, R.F., and Raviola, E. (1986). The rod pathway in the rabbit retina: A depolarizing bipolar and amacrine cell. J. Neurosci. *6*, 331–345.

Dedek, K., Schultz, K., Pieper, M., Dirks, P., Maxeiner, S., Willecke, K., Weiler, R., and Janssen-Bienhold, U. (2006). Localization of heterotypic gap junctions composed of connexin45 and connexin36 in the rod pathway of the mouse retina. Eur. J. Neurosci. *24*, 1675–1686.

Demb, J.B., and Singer, J.H. (2012). Intrinsic properties and functional circuitry of the AII amacrine cell. Vis. Neurosci. *29*, 51–60.

Denk, W., Strickler, J.H., and Webb, W.W. (1990). Two-photon laser scanning fluorescence microscopy. Science *248*, 73–76.

DeVries, S.H. (2000). Bipolar cells use kainate and AMPA receptors to filter visual information into separate channels. Neuron *28*, 847–856.

DeVries, S.H., Qi, X., Smith, R., Makous, W., and Sterling, P. (2002). Electrical coupling between mammalian cones. Curr. Biol. *12*, 1900–1907.

DeVries, S.H., Li, W., and Saszik, S. (2006). Parallel Processing in Two Transmitter Microenvironments at the Cone Photoreceptor Synapse. Neuron *50*, 735–748.

Diamond, J.S. (2017). Inhibitory interneurons in the retina: Types, circuitry, and function. Annu. Rev. Vis. Sci. *3*, 1–24.

Ding, H., Smith, R.G., Poleg-Polsky, A., Diamond, J.S., and Briggman, K.L. (2016). Species-specific wiring for direction selectivity in the mammalian retina. Nature *535*, 105–110.

Doering, C.J., Hamid, J., Simms, B., McRory, J.E., and Zamponi, G.W. (2005). Cav1.4 encodes a calcium channel with low open probability and unitary conductance. Biophys. J. *89*, 3042–3048.

Dogiel, A.S. (1888). Über das verhalten der nervösen elemente in der retina der ganoiden, reptilien, vögel und säugetiere. Anat Anz *3*, 133–143.

Dowling, J.E., and Boycott, B.B. (1966). Organization of the primate retina: Electron microscopy. Proc. R. Soc. London. Ser. B. Biol. Sci. *166*, 80–111.

Duebel, J., Haverkamp, S., Schleich, W., Feng, G., Augustine, G.J., Kuner, T., and Euler, T. (2006). Two-photon imaging reveals somatodendritic chloride gradient in retinal ON-type bipolar cells expressing the biosensor clomeleon. Neuron *49*, 81–94.

Dumitrescu, O.N., Pucci, F.G., Wong, K.Y., and Berson, D.M. (2009). Ectopic retinal ON bipolar cell synapses in the OFF inner plexiform layer: Contacts with dopaminergic amacrine cells and melanopsin ganglion cells. J. Comp. Neurol. *517*, 226–244.

Edwards, F.A., Konnerth, A., Sakmann, B., and Takahashi, T. (1989). A thin slice preparation for patch clamp recordings from neurones of the mammalian central nervous system. Pflugers Arch. *414*, 600–612.

Elgueta, C., Leroy, F., Vielma, A.H., Schmachtenberg, O., and Palacios, A.G. (2018). Electrical coupling between A17 cells enhances reciprocal inhibitory feedback to rod bipolar cells. Sci. Rep. *8*, 3123.

Enz, R., Brandstätter, J.H., Hartveit, E., Wässle, H., and Bormann, J. (1995). Expression of GABA receptor rho 1 and rho 2 subunits in the retina and brain of the rat. Eur. J. Neurosci. *7*, 1495–1501.

Euler, T., and Wässle, H. (1995). Immunocytochemical identification of cone bipolar cells in the rat retina. J. Comp. Neurol. *361*, 461–478.

Euler, T., Haverkamp, S., Schubert, T., and Baden, T. (2014). Retinal bipolar cells: elementary building blocks of vision. Nat. Rev. Neurosci. *15*, 507–519.

Famiglietti, E. V. (1981). Functional architecture of cone bipolar cells in mammalian retina. Vision Res. *21*, 1559–1563.

Famiglietti, E. V., and Kolb, H. (1976). Structural basis for ON-and OFF-center responses in retinal ganglion cells. Science (80-.). *194*, 193–195.

Famiglietti, E. V., Kaneko, A., and Tachibana, M. (1977). Neuronal architecture of on and off pathways to ganglion cells in carp retina. Science (80-.). *198*, 1267–1269.

Fan, J.S., and Palade, P. (1998). Perforated patch recording with β-escin. Pflugers Arch. Eur. J. Physiol. *436*, 1021–1023.

Feigenspan, A., Janssen-Bienhold, U., Hormuzdi, S., Monyer, H., Degen, J., Söhl, G., Willecke, K., Ammermüller, J., and Weiler, R. (2004). Expression of connexin36 in cone pedicles and OFF-cone bipolar cells of the mouse retina. J. Neurosci. *24*, 3325–3334.

Fu, Y., and Yau, K.W. (2007). Phototransduction in mouse rods and cones. Pflugers Arch. Eur. J. Physiol.

Fyk-Kolodziej, B., and Pourcho, R.G. (2007). Differential distribution of hyperpolarization-activated and cyclic nucleotide-gated channels in cone bipolar cells

of the rat retina. J. Comp. Neurol. *501*, 891–903.

Ghosh, K.K., Bujan, S., Haverkamp, S., Feigenspan, A., and Wässle, H. (2004). Types of Bipolar Cells in the Mouse Retina. J. Comp. Neurol. *469*, 70–82.

Gierke, K., von Wittgenstein, J., Hemmerlein, M., Atorf, J., Joachimsthaler, A., Kremers, J., Cooper, B.H., Varoqueaux, F., Regus-Leidig, H., and Brandstätter, J.H. (2020). Heterogeneous presynaptic distribution of munc13 isoforms at retinal synapses and identification of an unconventional bipolar cell type with dual expression of munc13 isoforms: A study using munc13-exfp knock-in mice. Int. J. Mol. Sci. *21*, 1–20.

Glaser, J.R., and Glaser, E.M. (1990). Neuron imaging with Neurolucida--a PC-based system for image combining microscopy. Comput. Med. Imaging Graph. *14*, 307–317.

Göppert-Mayer, M. (1931). Über elementarakte mit zwei quantensprüngen. Ann. Phys. *401*, 273–294.

Graydon, C.W., Lieberman, E.E., Rho, N., Briggman, K.L., Singer, J.H., and Diamond, J.S. (2018). Synaptic transfer between rod and cone pathways mediated by AII amacrine cells in the mouse retina. Curr. Biol. *28*, 2739-2751.e3.

Greene, M.J., Kim, J.S., and Seung, H.S. (2016). Analogous convergence of sustained and transient inputs in parallel ON and OFF pathways for retinal motion computation. Cell Rep. *14*, 1892–1900.

Greferath, U., Grünert, U., and Wässle, H. (1990). Rod bipolar cells in the mammalian retina show protein kinase C-like immunoreactivity. J. Comp. Neurol. *301*, 433–442.

Grimes, W.N., Zhang, J., Graydon, C.W., Kachar, B., and Diamond, J.S. (2010). Retinal parallel processors: More than 100 Independent microcircuits operate within a single Interneuron. Neuron *65*, 873–885.

Güldenagel, M., Söhl, G., Plum, A., Traub, O., Teubner, B., Weiler, R., and Willecke, K. (2000). Expression patterns of connexin genes in mouse retina. J. Comp. Neurol. *425*, 193–201.

Hack, I., Frech, M., Dick, O., Peichl, L., and Brandstätter, J.H. (2001). Heterogeneous distribution of AMPA glutamate receptor subunits at the photoreceptor synapses of rodent retina. Eur. J. Neurosci. *13*, 15–24.

Hamill, O.P., Marty, A., Neher, E., Sakmann, B., and Sigworth, F.J. (1981). Improved patch-clamp techniques for high-resolution current recording from cells and cell-free membrane patches. Pflügers Arch. Eur. J. Physiol. *391*, 85–100.

Han, Y., and Massey, S.C. (2005a). Electrical synapses in retinal ON cone bipolar cells: subtype-specific expression of connexins. Proc Natl Acad Sci U S A *102*, 13313–13318.

Han, Y., and Massey, S.C. (2005b). Electrical synapses in retinal ON cone bipolar cells: Subtype-specific expression of connexins. Proc. Natl. Acad. Sci. U. S. A. *102*, 13313–13318.

Hartveit, E. (1996). Membrane currents evoked by ionotropic glutamate receptor agonists in bipolar cells in the rat retinal slice preparation. Investig. Ophthalmol. Vis. Sci. *37*.

Hartveit, E. (1997). Functional organization of cone bipolar cells in the rat retina. J. Neurophysiol. *77 VN-r*, 1716–1730.

Hartveit, E. (1999). Reciprocal synaptic interactions between rod bipolar cells and amacrine cells in the rat retina. J. Neurophysiol. *81*, 2923–2936.

Hartveit, E., and Veruki, M.L. (2012). Electrical synapses between AII amacrine cells in the retina: Function and modulation. Brain Res. *1487*, 160–172.

Haverkamp, S., and Wässle, H. (2000). Immunocytochemical analysis of the mouse retina. J. Comp. Neurol. *424*, 1–23.

Hecht, S., Shlaer, S., and Pirenne, M.H. (1942). Energy, quanta, and vision. J. Gen. Physiol. *25*, 819–840.

Heintzmann, R. (2006). Band limit and appropriate sampling in microscopy. Cell Biol. Four-Volume Set *3*, 29–36.

Hellmer, C.B., Zhou, Y., Fyk-Kolodziej, B., Hu, Z., and Ichinose, T. (2016). Morphological and physiological analysis of type-5 and other bipolar cells in the Mouse Retina. Neuroscience *315*, 246–258.

Helmstaedter, M. (2013). Cellular-resolution connectomics: Challenges of dense neural circuit reconstruction. Nat. Methods *10*, 501–507.

Helmstaedter, M., Briggman, K.L., and Denk, W. (2011). High-accuracy neurite reconstruction for high-throughput neuroanatomy. Nat. Neurosci. *14*, 1081–1088.

Helmstaedter, M., Briggman, K.L., Turaga, S.C., Jain, V., Seung, H.S., and Denk, W. (2013). Connectomic reconstruction of the inner plexiform layer in the mouse retina. Nature *500*, 168–174.

Hermann, L. (1905). Beiträge zur physiologie und physik des nerven. Pflüger, Arch. Für Die Gesammte Physiol. Des Menschen Und Der Thiere *109*, 95–144.

Hilgen, G., von Maltzahn, J., Willecke, K., Weiler, R., and Dedek, K. (2011). Subcellular distribution of connexin45 in OFF bipolar cells of the mouse retina. J. Comp. Neurol. *519*, 433–450.

Hodgkin, A.L., and Huxley, A.F. (1952). A quantitative description of membrane current and its application to conduction and excitation in nerve. J. Physiol. *117*, 500–544.

Holmes, W.R., Segev, I., and Rall, W. (1992). Interpretation of time constant and electrotonic length estimates in multicylinder or branched neuronal structures. J. Neurophysiol. *68*, 1401–1420.

Van Hook, M.J., Nawy, S., and Thoreson, W.B. (2019). Voltage- and calcium-gated

ion channels of neurons in the vertebrate retina. Prog. Retin. Eye Res. *72*, 100760.

Horn, R., and Marty, A. (1988). Muscarinic activation of ionic currents measured by a new whole-cell recording method. J. Gen. Physiol. *92*, 145–159.

Hubbard, R. (1969). Absorption spectrum of rhodopsin: 500 nm absorption band. Nature *221*, 432–435.

Ichinose, T., and Hellmer, C.B. (2016). Differential signalling and glutamate receptor compositions in the OFF bipolar cell types in the mouse retina. J Physiol *5944*, 883–894.

Ichinose, T., and Lukasiewicz, P.D. (2007). Ambient light regulates sodium channel activity to dynamically control retinal signaling. J. Neurosci. *27*, 4756–4764.

Ichinose, T., Fyk-Kolodziej, B., and Cohn, J. (2014). Roles of ON cone bipolar cell subtypes in temporal coding in the mouse retina. J. Neurosci. *34*, 8761–8771.

Ivanova, E., and Müller, F. (2006). Retinal bipolar cell types differ in their inventory of ion channels. Vis Neurosci *23*, 143–154.

Jacoby, R.A., and Marshak, D.W. (1999). Synaptic connections of DB3 diffuse bipolar cell axons in macaque retina. J. Comp. Neurol. *416*, 19–29.

Jacoby, J., Zhu, Y., Devries, S.H., and Schwartz, G.W. (2015). An amacrine cell circuit for signaling steady illumination in the retina. Cell Rep. *13*, 2663–2670.

James, B., Darnet, L., Moya-Díaz, J., Seibel, S.H., and Lagnado, L. (2019). An amplitude code transmits information at a visual synapse. Nat. Neurosci. *22*, 1140–1147.

Janssens, F., Van Gehuchten, A., Ramon y Cajal, S., Denys, J., and Martin, I. (1893). La cellule - receuil de cytologie et d'histologie générale (Carnoy, JB).

Jarsky, T., Cembrowski, M., Logan, S.M., Kath, W.L., Riecke, H., Demb, J.B., and Singer, J.H. (2011). A synaptic mechanism for retinal adaptation to luminance and

contrast. J. Neurosci. *31*, 11003–11015.

Jeon, C.-J., and Masland, R.H. (1995). A population of wide-field bipolar cells in the rabbit's retina. J. Comp. Neurol. *360*, 403–412.

Jeon, C.J., Strettoi, E., and Masland, R.H. (1998). The major cell populations of the mouse retina. J Neurosci *18*, 8936–8946.

Jin, N., Zhang, Z., Keung, J., Youn, S.B., Ishibashi, M., Tian, L.M., Marshak, D.W., Solessio, E., Umino, Y., Fahrenfort, I., et al. (2020). Molecular and functional architecture of the mouse photoreceptor network. Sci. Adv. *6*, 1–16.

Jones, E.G. (2011). Cajal's debt to Golgi. Brain Res. Rev. *66*, 83–91.

Kaneko, A. (1970). Physiological and morphological identification of horizontal, bipolar and amacrine cells in goldfish retina. J. Physiol. *207*, 623–633.

Kang, H.W., Kim, H.K., Moon, B.H., Lee, S.J., Lee, S.J., and Rhyu, I.J. (2017). Comprehensive Review of Golgi Staining Methods for Nervous Tissue. Appl. Microsc. *47*, 63–69.

Kántor, O., Benkő, Z., Énzsöly, A., Dávid, C., Naumann, A., Nitschke, R., Szabó, A., Pálfi, E., Orbán, J., Nyitrai, M., et al. (2016). Characterization of connexin36 gap junctions in the human outer retina. Brain Struct. Funct. *221*, 2963–2984.

Kántor, O., Varga, A., Nitschke, R., Naumann, A., Énzsöly, A., Lukáts, Á., Szabó, A., Németh, J., and Völgyi, B. (2017). Bipolar cell gap junctions serve major signaling pathways in the human retina. Brain Struct. Funct. *222*, 2603–2624.

Klumpp, D.J., Song, E. joo, and Pinto, L.H. (1995a). Identification and localization of K+ channels in the mouse retina. Vis. Neurosci. *12*, 1177–1190.

Klumpp, D.J., Song, E.J., Ito, S., Sheng, M.H., Jan, L.Y., and Pinto, L.H. (1995b). The Shaker-like potassium channels of the mouse rod bipolar cell and their contributions to the membrane current. J. Neurosci. *15*, 5004–5013.

Koike, C., Numata, T., Ueda, H., Mori, Y., and Furukawa, T. (2010). TRPM1: A vertebrate TRP channel responsible for retinal ON bipolar function. Cell Calcium *48*, 95–101.

Kolb, H. (1979). The inner plexiform layer in the retina of the cat: electron microscopic observations. J. Neurocytol. *8*, 295–329.

Kolb, H., and Nelson, R. (1983). Rod pathways in the retina of the cat. Vision Res. *23*, 301–312.

Kolb, H., and Nelson, R. (1996). Hyperpolarizing, small-field, amacrine cells in cone pathways of cat retina. J. Comp. Neurol. *371*, 415–436.

Kolb, H., Nelson, R., and Mariani, A. (1981). Amacrine cells, bipolar cells and ganglion cells of the cat retina: A Golgi study. Vision Res. *21*, 1081–1114.

Koulen, P., Kuhn, R., Wässle, H., and Brandstätter, J.H. (1997). Group I metabotropic glutamate receptors mGluR1α and mGluR5a: Localization in both synaptic layers of the rat retina. J. Neurosci. *17*, 2200 LP – 2211.

Kujiraoka, T., and Saito, T. (1986). Electrical coupling between bipolar cells in carp retina. Proc. Natl. Acad. Sci. U. S. A. *83*, 4063–4066.

Kumar, N.M., and Gilula, N.B. (1996). The gap junction communication channel. Cell *84*, 381–388.

Kuo, S.P., Schwartz, G.W., and Rieke, F. (2016). Nonlinear Spatiotemporal Integration by Electrical and Chemical Synapses in the Retina. Neuron *90*, 320–332.

Lakkaraju, A., Umapathy, A., Tan, L.X., Daniele, L., Philp, N.J., Boesze-Battaglia, K., and Williams, D.S. (2020). The cell biology of the retinal pigment epithelium. Prog. Retin. Eye Res.

Lamb, T.D. (2010). Phototransduction: Adaptation in Cones. In Encyclopedia of the Eye, (Elsevier), pp. 354–360.

Land, M.F., and Nilson, D.-E. (2012). Animal Eyes (New York, NY: Oxford Univeristy Press Inc.).

Lauritzen, J.S., Anderson, J.R., Jones, B.W., Watt, C.B., Mohammed, S., Hoang, J. V., and Marc, R.E. (2013). ON cone bipolar cell axonal synapses in the OFF inner plexiform layer of the rabbit retina. J. Comp. Neurol. *521*, 977–1000.

Lauritzen, J.S., Sigulinsky, C.L., Anderson, J.R., Kalloniatis, M., Nelson, N.T., Emrich, D.P., Rapp, C., McCarthy, N., Kerzner, E., Meyer, M., et al. (2019). Rod-cone crossover connectome of mammalian bipolar cells. J. Comp. Neurol. *527*, 87–116.

Lawrence, P.M., and Studholme, K.M. (2014). Retinofugal projections in the mouse. J. Comp. Neurol. *522*, 3733–3753.

Lee, Y.T., and Wang, Q. (1999). Inhibition of hKv2.1, a major human neuronal voltage-gated K+ channel, by meclofenamic acid. Eur. J. Pharmacol. *378*, 349–356.

Lee, S.C.S., Meyer, A., Schubert, T., Hüser, L., Dedek, K., and Haverkamp, S. (2015). Morphology and connectivity of the small bistratified A8 amacrine cell in the mouse retina. J. Comp. Neurol. *523*, 1529–1547.

Li, W., and DeVries, S.H. (2006). Bipolar cell pathways for color and luminance vision in a dichromatic mammalian retina. Nat. Neurosci. *9*, 669–675.

Li, X., Kamasawa, N., Ciolofan, C., Olson, C.O., Lu, S., Davidson, K.G.V., Yasumura, T., Shigemoto, R., Rash, J.E., and Nagy, J.I. (2008). Connexin45-containing neuronal gap junctions in rodent retina also contain connexin36 in both apposing hemiplaques, forming bihomotypic gap junctions, with scaffolding contributed by zonula occludens-1. J. Neurosci. *28*, 9769–9789.

Li, X., Liu, J., Hoh, J., and Liu, J. (2019). Müller cells in pathological retinal angiogenesis. Transl. Res. *207*, 96–106.

Lichtman, J.W., Pfister, H., and Shavit, N. (2014). The big data challenges of

connectomics. Nat. Neurosci. *17*, 1448–1454.

Light, A.C., Zhu, Y., Shi, J., Saszik, S., Lindstrom, S., Davidson, L., Li, X., Chiodo, V.A., Hauswirth, W.W., Li, W., et al. (2012). Organizational motifs for ground squirrel cone bipolar cells. J. Comp. Neurol. *520*, 2864–2887.

Lin, B., Jakobs, T.C., and Masland, R.H. (2005). Different functional types of bipolar cells use different gap-junctional proteins. J. Neurosci. *25*, 6696–6701.

Linberg, K.A., Suemune, S., and Fisher, S.K. (1996a). Retinal neurons of the California ground squirrel, Spermophilus beecheyi: A Golgi study. J. Comp. Neurol. *365*, 173–216.

Linberg, K.A., Suemune, S., and Fisher, S.K. (1996b). Retinal neurons of the California ground squirrel, Spermopilus beecheyi: A Golgi study. J. Comp. Neurol. *365*, 173—216.

Lindstrom, S.H., Ryan, D.G., Shi, J., and DeVries, S.H. (2014). Kainate receptor subunit diversity underlying response diversity in retinal off bipolar cells. J. Physiol. *592*, 1457–1477.

LoGiudice, L., and Matthews, G. (2009). The role of ribbons at sensory synapses. Neuroscientist *15*, 380–391.

Ma, Y.-P., Cui, J., and Pan, Z.-H. (2005). Heterogeneous expression of voltage-dependent Na+ and K+ channels in mammalian retinal bipolar cells. Vis. Neurosci. *22*, 119–133.

Ma, Y.P., Cui, J., Hu, H.J., and Pan, Z.H. (2004). Mammalian retinal bipolar cells express inwardly rectifying K+ currents (IKir) with a different distribution than that of Ih. J. Neurophysiol. *90*, 3479–3489.

MacNeil, M.A., and Gaul, P.A. (2008). Biocytin wide-field bipolar cells in rabbit retina selectively contact blue cones. J. Comp. Neurol. *506*, 6–15.

MacNeil, M.A., and Masland, R.H. (1998). Extreme diversity among amacrine cells:

Implications for function. Neuron *20*, 971–982.

MacNeil, M.A., Heussy, J.K., Dacheux, R.F., Raviola, E., and Masland, R.H. (2004). The population of bipolar cells in the rabbit retina. J. Comp. Neurol. *472*, 73–86.

Major, G. (2001). Passive cable modeling - A practical introduction. In Computational Neuroscience, (Boca Raton), pp. 209–232.

Marc, R.E., Liu, W.L.S., and Muller, J.F. (1988). Gap junctions in the inner plexiform layer of the goldfish retina. Vision Res. *28*, 9–24.

Marc, R.E., Jones, B.W., Lauritzen, J.S., Watt, C.B., and Anderson, J.R. (2012). Building retinal connectomes. Curr. Opin. Neurobiol. *22*, 568–574.

Marc, R.E., Jones, B.W., Watt, C.B., Anderson, J.R., Sigulinsky, C., and Lauritzen, S. (2013). Retinal connectomics: Towards complete, accurate networks. Prog. Retin. Eye Res. *37*, 141–162.

Marc, R.E., Anderson, J.R., Jones, B.W., Sigulinsky, C.L., and Lauritzen, J.S. (2014). The AII amacrine cell connectome: a dense network hub. Front. Neural Circuits *8*, 1–13.

Marc, R.E., Jones, B.W., Sigulinsky, C., Anderson, J.R., and Lauritzen, J.S. (2015). High-resolution synaptic connectomics. In New Techniques in Systems Neuroscience, A.D. Douglass, ed. (Cham: Springer International Publishing), pp. 1–28.

Marc, R.E., Sigulinsky, C.L., Pfeiffer, R.L., Emrich, D., Anderson, J.R., and Jones, B.W. (2018). Heterocellular coupling between amacrine cells and ganglion cells. Front. Neural Circuits *12*, 1–23.

Marmont, G. (1949). Studies on the axon membrane. I. A new method. J. Cell. Comp. Physiol. *34*, 351–382.

Marshak, D.W., and Mills, S.L. (2014). Short-wavelength cone-opponent retinal ganglion cells in mammals. Vis. Neurosci. *31*, 165–175.

Martin, P.R., and Grünert, U. (1992). Spatial density and immunoreactivity of bipolar cells in the macaque monkey retina. J. Comp. Neurol. *323*, 269–287.

Masland, R.H. (2012a). The tasks of amacrine cells. Vis. Neurosci. *29*, 3–9.

Masland, R.H. (2012b). The neuronal organization of the retina. Neuron *76*, 266–280.

Massey, S.C., and Mills, S.L. (1996). A calbindin-immunoreactive cone bipolar cell type in the rabbit retina. J. Comp. Neurol. *366*, 15–33.

Massey, S.C., O'Brien, J.J., Trexler, E.B., Li, W., Keung, J.W., Mills, S.L., and O'Brien, J. (2003). Multiple neuronal connexins in the mammalian retina. Cell Commun. Adhes. *10*, 425–430.

Masu, M., Iwakabe, H., Tagawa, Y., Miyoshi, T., Yamashita, M., Fukuda, Y., Sasaki, H., Hiroi, K., Nakamura, Y., Shigemoto, R., et al. (1995). Specific deficit of the ON response in visual transmission by targeted disruption of the mGIuR6 gene. Cell *80*, 757–765.

Mataruga, A., Kremmer, E., and Müller, F. (2007). Type 3a and type 3b OFF cone bipolar cells provide for the alternative rod pathway in the mouse retina. J. Comp. Neurol. *502*, 1123–1137.

Maxeiner, S., Dedek, K., Janssen-Bienhold, U., Ammermüller, J., Brune, H., Kirsch, T., Pieper, M., Degen, J., Krüger, O., Willecke, K., et al. (2005). Deletion of connexin45 in mouse retinal neurons disrupts the rod/cone signaling pathway between AII amacrine and ON cone bipolar cells and leads to impaired visual transmission. J. Neurosci. *25*, 566–576.

McGillem, G.S., and Dacheux, R.F. (2001). Rabbit cone bipolar cells: Correlation of their morphologies with whole-cell recordings. Vis. Neurosci. *18*, 675–685.

McGuire, B.A., Stevens, J.K., and Sterling, P. (1984). Microcircuitry of bipolar cells in cat retina. J. Neurosci. *4*, 2920–2938.

Menger, N., and Wässle, H. (2000). Morphological and physiological properties of

the A17 amacrine cell of the rat retina. Vis. Neurosci. *17*, 769–780.

Menger, N., Pow, D. V., and Wässle, H. (1998). Glycinergic amacrine cells of the rat retina. J. Comp. Neurol. *401*, 34–46.

Mills, S.L. (1999). Unusual coupling patterns of a cone bipolar cell in the rabbit retina. Vis. Neurosci. *16*, 1029–1035.

Mills, S.L., Tian, L.M., Hoshi, H., Whitaker, C.M., and Massey, S.C. (2014). Three distinct blue-green color pathways in a mammalian retina. J. Neurosci. *34*, 1760–1768.

Müller, F., Scholten, A., Ivanova, E., Haverkamp, S., Kremmer, E., and Kaupp, U.B. (2003). HCN channels are expressed differentially in retinal bipolar cells and concentrated at synaptic terminals. Eur. J. Neurosci. *17*, 2084–2096.

Münch, T.A., Da Silveira, R.A., Siegert, S., Viney, T.J., Awatramani, G.B., and Roska, B. (2009). Approach sensitivity in the retina processed by a multifunctional neural circuit. Nat. Neurosci. *12*, 1308–1316.

Naarendorp, F., Esdaille, T.M., Banden, S.M., Andrews-Labenski, J., Gross, O.P., and Pugh, E.N. (2010). Dark light, rod saturation, and the absolute and incremental sensitivity of mouse cone vision. J. Neurosci. *30*, 12495–12507.

Neher, E., and Sakmann, B. (1976). Single-channel currents recorded from membrane of denervated frog muscle fibres. Nature *260*, 799–802.

Nelson, R., and Kolb, H. (1985). A17: A broad-field amacrine cell in the rod system of the cat retina. J. Neurophysiol. *54*, 592–614.

Nelson, R., Famiglietti, E. V, and Kolb, H. (1978). Intracellular staining reveals different levels of stratification for on- and off-center ganglion cells in cat retina. J. Neurophysiol. *41*, 472–483.

O'Brien, J., and Bloomfield, S.A. (2018). Plasticity of retinal gap junctions: Roles in synaptic physiology and disease. Annu. Rev. Vis. Sci. *4*, 79–100.

O'Brien, J.J., Chen, X., Macleish, P.R., O'Brien, J., and Massey, S.C. (2012). Photoreceptor coupling mediated by connexin36 in the primate retina. J. Neurosci. *32*, 4675–4687.

Oesch, N., and Diamond, J. (2009). A night vision neuron gets a day job. Nat. Neurosci. *12*, 1209–1211.

Oesch, N.W., and Diamond, J.S. (2011). Ribbon synapses compute temporal contrast and encode luminance in retinal rod bipolar cells. Nat. Neurosci. *14*, 1555–1561.

Oltedal, L., and Hartveit, E. (2010). Transient release kinetics of rod bipolar cells revealed by capacitance measurement of exocytosis from axon terminals in rat retinal slices. J. Physiol. *588*, 1469–1487.

Oltedal, L., Veruki, M.L., and Hartveit, E. (2009). Passive membrane properties and electrotonic signal processing in retinal rod bipolar cells. J Physiol *587*, 829–849.

Oyamada, H., Takatsuji, K., Senba, E., Mantyh, P.W., and Tohyama, M. (1999). Postnatal development of NK1, NK2, and NK3 neurokinin receptors expression in the rat retina. Dev. Brain Res. *117*, 59–70.

Pan, F., Mills, S.L., and Massey, S.C. (2007). Screening of gap junction antagonists on dye coupling in the rabbit retina. Vis. Neurosci. *24*, 609–618.

Pan, F., Paul, D.L., Bloomfield, S.A., and Völgyi, B. (2010). Connexin36 is required for gap junctional coupling of most ganglion cell subtypes in the mouse retina. J. Comp. Neurol. *518*, 911–927.

Pang, J.J., Gao, F., Lem, J., Bramblett, D.E., Paul, D.L., and Wu, S.M. (2010). Direct rod input to cone BCs and direct cone input to rod BCs challenge the traditional view of mammalian BC circuitry. Proc. Natl. Acad. Sci. U. S. A. *107*, 395–400.

Pang, J.J., Paul, D.L., and Wu, S.M. (2013). Survey on amacrine cells coupling to retrograde-identified ganglion cells in the mouse retina. Investig. Ophthalmol. Vis. Sci. *54*, 5151–5162.

Pangrsic, T., Singer, J.H., and Koschak, A. (2018). Voltage-gated calcium channels: Key players in sensory coding in the retina and the inner ear. Physiol. Rev. *98*, 2063–2096.

Pasquale, R., Umino, Y., and Solessio, E. (2020). Rod photoreceptors signal fast changes in daylight levels using a CX36-independent retinal pathway in mouse. J. Neurosci. *40*, 796–810.

Peichl, L., and González-Soriano, J. (1994). Morphological types of horizontal cell in rodent retinae: A comparison of rat, mouse, gerbil, and guinea pig. Vis. Neurosci. *11*, 501–517.

Pereda, A.E. (2016). The variable strength of electrical synapses. Neuron *90*, 912–914.

Peretz, A., Degani, N., Nachman, R., Uziyel, Y., Gibor, G., Shabat, D., and Attali, B. (2005). Meclofenamic acid and diclofenac, novel templates of KCNQ2/Q3 potassium channel openers, depress cortical neuron activity and exhibit anticonvulsant properties. Mol. Pharmacol. *67*, 1053–1066.

Perry, V.H., and Walker, M. (1980). Amacrine cells, displaced amacrine cells and interplexiform cells in the retina of the rat. Proc. R. Soc. London. Ser. B, Biol. Sci. *208*, 415–431.

Pignatelli, V., and Strettoi, E. (2004). Bipolar cells of the mouse retina: A gene gun, morphological study. J. Comp. Neurol. *476*, 254–266.

Polyak, S. (1949). Retinal structure and colour vision. Structure 24–56.

Polyak, S. (1953). Santiago Ramón y Cajal and his investigation of the nervous system. J. Comp. Neurol. *98*, 3–8.

Puller, C., Ondreka, K., and Haverkamp, S. (2011). Bipolar cells of the ground squirrel retina. J. Comp. Neurol. *519*, 759–774.

Puller, C., Ivanova, E., Euler, T., Haverkamp, S., and Schubert, T. (2013). OFF

bipolar cells express distinct types of dendritic glutamate receptors in the mouse retina. Neuroscience *243*, 136–148.

Rall, W. (1964). Theory of physiological properties of dendrites. In Neural Theory and Modelling, Reiss, ed. (Standford), pp. 73–97.

Rall, W. (2003). Theoretical Significance of Dendritic Trees for Neuronal Input-Output Relations. In The Theoretical Foundation of Dendritic Function, (The MIT Press), p.

Ramón y Cajal, S. (1888a). Estructura de la retina de las aves. Rev. Trim. Histol. Norm. Patol. *1*, 1–10.

Ramón y Cajal, S. (1888b). Morfologia y conexiones de los elementos de la retina de las aves. Rev. Trim. Histol. Norm. Patol. *1*, 11–16.

Raviola, E., and Dacheux, R.F. (1987). Excitatory dyad synapse in rabbit retina. Proc. Natl. Acad. Sci. U. S. A. *84*, 7324–7328.

Raviola, E., and Gilula, N.B. (1975). Intramembrane organization of specialized contacts in the outer plexiform layer of the retina. A freeze-fracture study in monkeys and rabbits. J. Cell Biol. *65*, 192–222.

Rheaume, B.A., Jereen, A., Bolisetty, M., Sajid, M.S., Yang, Y., Renna, K., Sun, L., Robson, P., and Trakhtenberg, E.F. (2018). Single cell transcriptome profiling of retinal ganglion cells identifies cellular subtypes. Nat. Commun. *9*, 1–17.

Ribelayga, C., and Mangel, S.C. (2010). Identification of a circadian clock-controlled neural pathway in the rabbit retina. PLoS One *5*.

Ribelayga, C., Cao, Y., and Mangel, S.C. (2008). The circadian clock in the retina controls rod-cone coupling. Neuron *59*, 790–801.

Roska, B., and Werblin, F. (2001). Vertical interactions across ten parallel, stacked representations in the mammalian retina. Nature *410*, 583–587.

Sandell, J.H., Masland, R.H., Raviola, E., and Dacheux, R.F. (1989). Connections of indoleamine-accumulating cells in the rabbit retina. J. Comp. Neurol. *283*, 303–313.

Della Santina, L., Kuo, S.P., Yoshimatsu, T., Okawa, H., Suzuki, S.C., Hoon, M., Tsuboyama, K., Rieke, F., and Wong, R.O.L. (2016). Glutamatergic Monopolar Interneurons Provide a Novel Pathway of Excitation in the Mouse Retina. Curr. Biol. *26*, 2070–2077.

Sassoè-Pognetto, M., Wässle, H., and Grünert, U. (1994). Glycinergic synapses in the rod pathway of the rat retina: cone bipolar cells express the alpha 1 subunit of the glycine receptor. J. Neurosci. *14*, 5131–5146.

Saszik, S., and Devries, S.H. (2012). A mammalian retinal bipolar cell uses both graded changes in membrane voltage and all-or-nothing Na + spikes to encode light. J. Neurosci. *32*, 297–307.

Satoh, H., Aoki, K., Watanabe, S.I., and Kaneko, A. (1998). L-type calcium channels in the axon terminal of mouse bipolar cells. Neuroreport *9*, 2161–2165.

Schubert, T., Weiler, R., and Feigenspan, A. (2006). Intracellular calcium is regulated by different pathways in horizontal cells of the mouse retina. J. Neurophysiol. *96*, 1278–1292.

Sefton, A.J., Dreher, B., Harvey, A.R., and Martin, P.R. (2015). Visual system. In The Rat Nervous System, (Elsevier), pp. 947–983.

Shekhar, K., Lapan, S.W., Whitney, I.E., Tran, N.M., Macosko, E.Z., Kowalczyk, M., Adiconis, X., Levin, J.Z., Nemesh, J., Goldman, M., et al. (2016). Comprehensive classification of retinal bipolar neurons by single-cell transcriptomics. Cell *166*, 1308-1323.e30.

Sholl, D.A. (1953). Dendritic organization in the neurons of the visual and motor cortices of the cat. J. Anat. *87*, 387–406.

Sigulinsky, C.L., Anderson, J.R., Kerzner, E., Rapp, C.N., Pfeiffer, R.L., Rodman,

T.M., Emrich, D.P., Rapp, K.D., Nelson, N.T., Lauritzen, J.S., et al. (2020). Network architecture of gap junctional coupling among parallel processing channels in the mammalian retina. J. Neurosci. *40*, 4483–4511.

Singer, J.H., and Diamond, J.S. (2003). Sustained Ca2+ entry elicits transient postsynaptic currents at a retinal ribbon synapse. J. Neurosci. *23*, 10923–10933.

Singleton, G.R., Hinds, L.A., Krebs, C.J., and Spratt, D.M. (2003). Rats, mice and people: rodent biology and managemen.

Söhl, G., and Willecke, K. (2003). An update on connexin genes and their nomenclature in mouse and man. Cell Commun. Adhes. *10*, 173–180.

Sterling, P. (1983). Microcircuitry of the cat retina. Annu. Rev. Neurosci. *6*, 149–185.

Strauss, O. (2005). The retinal pigment epithelium in visual function. Physiol. Rev. *85*, 845–881.

Strettoi, E., and Masland, R.H. (1996). The number of unidentified amacrine cells in the mammalian retina. Proc. Natl. Acad. Sci. U. S. A. *93*, 14906–14911.

Strettoi, E., Dacheux, R.F., and Raviola, E. (1990). Synaptic connections of rod bipolar cells in the inner plexiform layer of the rabbit retina. J. Comp. Neurol. *295*, 449–466.

Strettoi, E., Raviola, E., and Dacheux, R.F. (1992). Synaptic connections of the narrow-field, bistratified rod amacrine cell (AII) in the rabbit retina. J. Comp. Neurol. *325*, 152–168.

Strettoi, E., Dacheux, R.F., and Raviola, E. (1994). Cone bipolar cells as interneurons in the rod, pathway of the rabbit retina. J. Comp. Neurol. *347*, 139–149.

Ströh, S., Sonntag, S., Janssen-Bienhold, U., Schultz, K., Cimiotti, K., Weiler, R., Willecke, K., and Dedek, K. (2013). Cell-specific cre recombinase expression allows selective ablation of glutamate receptors from mouse horizontal cells. PLoS One *8*, e83076.

Stryer, L. (1991). Visual excitation and recovery. J. Biol. Chem. *266*, 10711–10714.

Sun, W., Li, N., and He, S. (2002a). Large-scale morphological survey of mouse retinal ganglion cells. J. Comp. Neurol. *451*, 115–126.

Sun, W., Li, N., and He, S. (2002b). Large-scale morophological survey of rat retinal ganglion cells. Vis. Neurosci. *19*, 483–493.

Swedlow, J.R. (2013). Quantitative fluorescence microscopy and image deconvolution. In Methods in Cell Biology, (Academic Press), pp. 407–426.

Szél, Á., Röhlich, P., Caffé, A.R., and Van Veen, T. (1996). Distribution of cone photoreceptors in the mammalian retina. Microsc. Res. Tech. *35*, 445–462.

Szoboszlay, M., Lőrincz, A., Lanore, F., Vervaeke, K., Silver, R.A., and Nusser, Z. (2016). Functional Properties of Dendritic Gap Junctions in Cerebellar Golgi Cells. Neuron *90*, 1043–1056.

Tartuferi, F. (1887). Sull'anatomia della retina. Int. Monatsschrift Anat Physiol *4*, 421–441.

Teeter, C.M., and Stevens, C.F. (2011). A general principle of neural arbor branch density. Curr. Biol. *21*, 2105–2108.

Thoreson, W.B., and Dacey, D.M. (2019). Diverse cell types, circuits, and mechanisms for color vision in the vertebrate retina. Physiol. Rev. *99*, 1527–1573.

Thoreson, W.B., and Mangel, S.C. (2012). Lateral interactions in the outer retina. Prog. Retin. Eye Res. *31*, 407–441.

Tikidji-Hamburyan, A., Reinhard, K., Storchi, R., Dietter, J., Seitter, H., Davis, K.E., Idrees, S., Mutter, M., Walmsley, L., Bedford, R.A., et al. (2017). Rods progressively escape saturation to drive visual responses in daylight conditions. Nat. Commun. *8*, 1–17.

Tom Dieck, S., and Brandstätter, J.H. (2006). Ribbon synapses of the retina. Cell

Tissue Res. *326*, 339–346.

Tran, N.M., Shekhar, K., Whitney, I.E., Jacobi, A., Benhar, I., Hong, G., Yan, W., Adiconis, X., Arnold, M.E., Lee, J.M., et al. (2019). Single-cell profiles of retinal ganglion cells differing in resilience to injury reveal neuroprotective genes. Neuron *104*, 1039-1055.e12.

Traynelis, S.F., Wollmuth, L.P., McBain, C.J., Menniti, F.S., Vance, K.M., Ogden, K.K., Hansen, K.B., Yuan, H., Myers, S.J., and Dingledine, R. (2010). Glutamate receptor ion channels: Structure, regulation, and function. Pharmacol. Rev. *62*, 405–496.

Trenholm, S., and Awatramani, G.B. (1995). Myriad roles for gap junctions in retinal circuits (University of Utah Health Sciences Center).

Trenholm, S., and Awatramani, G.B. (2017). Dynamic properties of electrically coupled retinal networks. In Network Functions and Plasticity, (Elsevier), pp. 183–208.

Trexler, E.B., Li, W., and Massey, S.C. (2005). Simultaneous contribution of two rod pathways to AII amacrine and cone bipolar cell light responses. J. Neurophysiol. *93*, 1476–1485.

Tsukamoto, Y., and Omi, N. (2014). Some OFF bipolar cell types make contact with both rods and cones in macaque and mouse retinas. Front. Neuroanat. *8*, 105.

Tsukamoto, Y., and Omi, N. (2017). Classification of Mouse Retinal Bipolar Cells: Type-Specific Connectivity with Special Reference to Rod-Driven AII Amacrine Pathways. Front. Neuroanat. *11*, 1–25.

Umino, O., Maehara, M., Hidaka, S., Kita, S., and Hashimoto, Y. (1994). The network properties of bipolar–bipolar cell coupling in the retina of teleost fishes. Vis. Neurosci. *11*, 533–548.

Veruki, M.L., and Hartveit, E. (2002a). Electrical synapses mediate signal

transmission in the rod pathway of the mammalian retina. J. Neurosci. *22*, 10558–10566.

Veruki, M.L., and Hartveit, E. (2002b). AII (rod) amacrine cells form a network of electrically coupled interneurons in the mammalian retina. Neuron *33*, 935–946.

Veruki, M.L., and Hartveit, E. (2009). Meclofenamic acid blocks electrical synapses of retinal AII amacrine and ON-cone bipolar cells. J. Neurophysiol. *101*, 2339–2347.

Veruki, M.L., Mørkve, S.H., and Hartveit, E. (2006). Activation of a presynaptic glutamate transporter regulates synaptic transmission through electrical signaling. Nat. Neurosci. *9*, 1388–1396.

Veruki, M.L., Oltedal, L., and Hartveit, E. (2010). Electrical coupling and passive membrane properties of AII amacrine cells. J. Neurophysiol. *103*, 1456–1466.

Vielma, A.H., and Schmachtenberg, O. (2016). Electrophysiological fingerprints of OFF bipolar cells in rat retina. Sci. Rep. *6*, 30259.

Völgyi, B., Kovács-öller, T., Atlasz, T., Wilhelm, M., and Gábriel, R. (2013). Gap junctional coupling in the vertebrate retina: Variations on one theme? Prog. Retin. Eye Res. *34*, 1–18.

Wallace, W., Schaefer, L.H., and Swedlow, J.R. (2001). A working person's guide to deconvolution in light microscopy. Biotechniques *31*, 1076–1097.

Wang, Y., and Mangel, S.C. (1996). A circadian clock regulates rod and cone input to fish retinal cone horizontal cells. Proc. Natl. Acad. Sci. U. S. A. *93*, 4655–4660.

Wässle, H., and Riemann, H.J. (1978). The mosaic of nerve cells in the mammalian retina. Proc. R. Soc. London - Biol. Sci. *200*, 441–461.

Wässle, H., Puller, C., Muller, F., and Haverkamp, S. (2009). Cone contacts, mosaics, and territories of bipolar cells in the mouse retina. J Neurosci *29*, 106–117.

Werblin, F.S., and Dowling, J.E. (1969). Organization of the retina of the mudpuppy,

Necturus maculosus. II. Intracellular recording. J. Neurophysiol. *32*, 339–355.

West, R.W. (1976). Light and electron microscopy of the ground squirrel retina: Functional considerations. J. Comp. Neurol. *168*, 355–377.

West, R.W. (1978). Bipolar and horizontal cells of the gray squirrel retina: Golgi morphology and receptor connections. Vision Res. *18*, 129–136.

Wu, S.-N., Jan, C.-R., and Chiang, H.-T. (2001). Fenamates stimulate BKCa channel activity in the human osteoblast-like MG-63 cells. J. Investig. Med. *49*, 522–533.

Xin, D., and Bloomfield, S.A. (1997). Tracer coupling pattern of amacrine and ganglion cells in the rabbit retina. J. Comp. Neurol. *383*, 512–528.

Yadav, S.C., Tetenborg, S., and Dedek, K. (2019). Gap junctions in A8 amacrine cells are made of connexin36 but are differently regulated than gap junctions in AII amacrine cells. Front. Mol. Neurosci. *12*, 1–15.

Yan, W., Laboulaye, M.A., Tran, N.M., Whitney, I.E., Benhar, I., and Sanes, J.R. (2020). Mouse retinal cell atlas: Molecular identification of over sixty amacrine cell types. J. Neurosci. *40*, 5177–5195.

Yin, C., Ishii, T., and Kaneda, M. (2020). Two types of Cl transporters contribute to the regulation of intracellular Cl concentrations in ON- and OFF-type bipolar cells in the mouse retina. Neuroscience *440*, 267–276.

Zandt, B.-J.J., Liu, J.H., Veruki, M.L., and Hartveit, E. (2017). AII amacrine cells: quantitative reconstruction and morphometric analysis of electrophysiologically identified cells in live rat retinal slices imaged with multi-photon excitation microscopy. Brain Struct. Funct. *222*, 151–182.

Zhang, A.J., and Wu, S.M. (2009). Receptive fields of retinal bipolar cells are mediated by heterogeneous synaptic circuitry. J. Neurosci. *29*, 789–797.

Zhang, J., and Wu, S.M. (2005). Physiological properties of rod photoreceptor electrical coupling in the tiger salamander retina. J. Physiol. *564*, 849–862.

Zhou, Z.-Y., Wan, Q.-F., Thakur, P., and Heidelberger, R. (2006). Capacitance measurements in the mouse rod bipolar cell identify a pool of releasable synaptic vesicles. J. Neurophysiol. *96*, 2539–2548.

Paper I

Cellular and Molecular Neurobiology (2021) 41:229–245
https://doi.org/10.1007/s10571-020-00845-y

ORIGINAL RESEARCH

Differential Contribution of Gap Junctions to the Membrane Properties of ON- and OFF-Bipolar Cells of the Rat Retina

Rémi Fournel[1] · Espen Hartveit[1] · Margaret Lin Veruki[1]

Received: 15 January 2020 / Accepted: 8 April 2020 / Published online: 22 April 2020

Abstract
Gap junctions are ubiquitous within the retina, but in general, it remains to be determined whether gap junction coupling between specific cell types is sufficiently strong to mediate functionally relevant coupling via electrical synapses. From ultrastructural, tracer coupling and immunolabeling studies, there is clear evidence for gap junctions between cone bipolar cells, but it is not known if these gap junctions function as electrical synapses. Here, using whole-cell voltage-clamp recording in rat (male and female) retinal slices, we investigated whether the gap junctions of bipolar cells make a measurable contribution to the membrane properties of these cells. We measured the input resistance (R_N) of bipolar cells before and after applying meclofenamic acid (MFA) to block gap junctions. In the presence of MFA, R_N of ON-cone bipolar cells displayed a clear increase, paralleled by block of the electrical coupling between these cells and AII amacrine cells in recordings of coupled cell pairs. For OFF-cone and rod bipolar cells, R_N did not increase in the presence of MFA. The results for rod bipolar cells are consistent with the lack of gap junctions in these cells. However, for OFF-cone bipolar cells, our results suggest that the morphologically identified gap junctions between these cells do not support a junctional conductance that is sufficient to mediate effective electrical coupling. Instead, these junctions might play a role in chemical and/or metabolic coupling between subcellular compartments.

Keywords Cone bipolar cells · Connexin 36 · Connexin 45 · Electrical coupling · Gap junctions · Retina

Introduction

Gap junctions are seemingly ubiquitous components of neural circuits throughout the vertebrate retina (reviewed by Völgyi et al. 2013). As such, the retina has long been a model system for studying how gap junctions mediate electrical coupling and how they play an important role in signaling, plasticity, and neurodegeneration (reviewed by Trenholm and Awatramani 2017; O'Brien and Bloomfield 2018). For a few of these gap junctions, a clear physiological role in the processing of visual signals has been identified. For example, homologous coupling between cone photoreceptors (DeVries et al. 2002) and rod photoreceptors (Li et al. 2012) enhance the signal-to-noise ratio, and heterologous gap junctions between AII amacrine and ON-cone bipolar cells are thought to mediate signal transfer between ON- and OFF-pathways under both scotopic (reviewed by Bloomfield and Dacheux 2001) and photopic conditions (Manookin et al. 2008; Münch et al. 2009; Kuo et al. 2016). However, a clear functional role for most gap junctions in the retina remains to be determined.

A particularly interesting case of retinal gap junctions for which there is strong morphological evidence, but virtually no information regarding a putative functional role, are the gap junctions between different types of cone bipolar cells. There are roughly 10–12 types of cone bipolar cells in mammalian retina and as many as 20 different types in non-mammalian retina. These types are generally divided into ON-types that depolarize at light onset and OFF-types that depolarize at light offset (reviewed by Euler et al. 2014). Ultrastructural studies in teleost and mammalian retina have found evidence for gap junctions between dendrites of both OFF- and ON-cone bipolar cells (Raviola and Gilula 1975; Umino et al. 1994), between axon terminals of OFF-cone bipolar cells (Kolb 1979; Marc et al. 1988; Jacoby and

✉ Espen Hartveit
espen.hartveit@uib.no

✉ Margaret Lin Veruki
margaret.veruki@uib.no

[1] Department of Biomedicine, University of Bergen, Jonas Lies vei 91, 5009 Bergen, Norway

Marshak 2000; Tsukamoto and Omi 2015), and between axon terminals of ON-cone bipolar cells (Cohen and Sterling 1990; Tsukamoto and Omi 2017). These electron-microscopic studies are supported by light-microscopic studies of immunolabelling for connexin 36 (Cx36) and connexin 45 (Cx45). Cx36 has been found at the dendrites of OFF-cone bipolar cells (mouse: Feigenspan et al. 2004; macaque: O'Brien et al. 2012; human: Kántor et al. 2016; Kántor et al. 2017) and at the axon terminals of ON-cone bipolar cells (mouse: Han and Massey 2005; Lin et al. 2005; Dedek et al. 2006). In mouse, Cx45 has been found at both the dendrites and axon terminals of OFF-cone bipolar cells (Lin et al. 2005; Hilgen et al. 2011) and the axon terminals of ON-cone bipolar cells (Dedek et al. 2006). These ultrastructural and immunolabeling studies are complemented by evidence for tracer coupling between OFF-cone bipolar cells in rabbit retina (Mills 1999) and between both ON- and OFF-cone bipolar cells in tiger salamander retina (Zhang and Wu 2009). In addition, both tracer coupling and electrical coupling (using dual patch-clamp recording) has been observed between Mb1 bipolar cells in goldfish retina (Arai et al. 2010). Finally, electrical coupling between adjacent bipolar cells was observed with paired intracellular recordings in carp retina (Kujiraoka and Saito 1986). Taken together, there is substantial evidence that both ON- and OFF-cone bipolar cells make gap junction contacts with other cells of the same class, and that this is a common circuit motif in the vertebrate retina. In contrast, there are no reports of gap junctions between rod bipolar cells (e.g., Strettoi et al. 1990).

The different types of bipolar cells are thought to form parallel channels encoding distinct stimulus properties such as contrast, chromatic features, and temporal properties (reviewed by Euler et al. 2014), and it is not at all clear how gap junctions between bipolar cells are consistent with this view. Thus, the question arises as to whether all morphologically identified gap junctions correspond physiologically to electrical synapses. Arguably, the most direct approach to answer this question would be to perform dual recordings from pairs of visually identified cone bipolar cells, ideally in genetically modified animals with fluorescently labeled cells that could be targeted for recording. Even when such animals become available, the electrical coupling between ON-cone bipolar cells and AII amacrine cells (Veruki and Hartveit 2002b) could confound measurements for ON-cone bipolar cells, limiting the approach to OFF-cone bipolar cells. An alternative approach, that we present here, is to perform electrophysiological recording from single neurons and examine if pharmacological block of gap junction-mediated electrical coupling increases the input resistance (R_N) of the cells (cf. Alcamí and Pereda 2019). For both AII amacrine cells (Veruki et al. 2010) and A17 amacrine cells (Elgueta et al. 2018), the gap junction blocker meclofenamic acid (MFA) evokes an increase of R_N, fully consistent with the simultaneously observed block of junctional conductance (in paired recordings from electrically coupled cells) and the evidence for homologous coupling between AII (Kolb and Famiglietti 1974; Vaney 1991; Strettoi et al. 1992; Veruki and Hartveit 2002a) and A17 amacrines (Li et al. 2002; Grimes et al. 2014; Elgueta et al. 2018). Similar observations have also been made for Golgi cell interneurons in the cerebellar cortex (Szoboszlay et al. 2016). Thus, if MFA evokes a similar increase of R_N for other neurons with morphological evidence for gap junctions, it is reasonable to assume that the increase of R_N corresponds to a reduction of the junctional conductance between electrically coupled cells. Here we investigated the effect of MFA on the R_N of bipolar cells in the rat retina. For ON-cone bipolar cells, R_N displayed a clear increase, as expected for cells with gap junction-mediated electrical coupling. For rod bipolar cells, R_N did not increase in the presence of MFA, consistent with their lack of gap junctions. Surprisingly, given the substantial morphological evidence for the presence of gap junctions between OFF-cone bipolar cells, R_N for these cells did not increase following application of MFA. Our results suggest that the gap junctions between OFF-cone bipolar cells do not support consequential electrical coupling.

Materials and Methods

Retinal Slice Preparation

General aspects of the methods have previously been described in detail (Hartveit 1996). The use of animals in this study was carried out under the approval of and in accordance with the regulations of the Animal Laboratory Facility at the Faculty of Medicine at the University of Bergen (accredited by AAALAC International). Male and female albino rats (Wistar HanTac, bred in-house or purchased from Taconic Bioscience, Denmark; 4–7 weeks postnatal) had ad libitum access to food and water and were kept on a 12/12 light/dark cycle. Animals were deeply anaesthetized with isoflurane (IsoFlo vet 100%; Abbott Laboratories) in 100% O_2 and killed by cervical dislocation. After removing the eyes and dissecting out the retinas, retinal slices were cut by hand with a curved scalpel blade at a thickness of ~ 100 to ~ 150 µm. In some experiments, the slices were visualized with a conventional, upright microscope (BX51WI; Olympus) with a ×60 (0.9 NA) or ×40 (0.8 NA) water immersion objective (Olympus). Infrared (IR) video microscopy was performed with an IR-sensitive analog CCD camera (VX55; TILL Photonics) and either differential interference contrast (IR-DIC) or Dodt gradient contrast (IR-DGC; Luigs & Neumann) for contrast enhancement. In other experiments, the slices were visualized using a custom-modified "Movable Objective Microscope" (MOM; Sutter Instrument) with a

×20 water immersion objective (XLUMPLFL; 0.95 NA; Olympus) and IR-DGC videomicroscopy. The cell bodies of the recorded cells were generally located 15–30 µm below the surface of the slice. Electrophysiological recording and imaging were carried out at room temperature (22–25 °C). Anesthesia, dissection, and preparation of slices were done under normal room illumination. During recording at conventional upright microscopes, the room lights were dimmed moderately for the purpose of observing monitor displays better. During recording at the MOM for multiphoton excitation (MPE) microscopy, the room lights were dimmed and the preparation was located in a cage covered by black cloth. Taken together, we consider the slices to be light adapted (cf. Veruki and Hartveit 2002b).

Solutions and Drugs

The extracellular perfusing solution was continuously bubbled with 95% O_2–5% CO_2 and had the following composition (in mM): 125 NaCl, 25 $NaHCO_3$, 2.5 KCl, 2.5 $CaCl_2$, 1 $MgCl_2$, 10 glucose, pH 7.4 (osmolarity ~300 mOsm). For single recordings of bipolar cells, the recording pipettes were filled with (in mM): 125 K-gluconate, 5 KCl, 8 NaCl, 10 Hepes, 0.2 EGTA, 4 MgATP, 0.4 Na_3GTP (pH adjusted to 7.3 with KOH). For visualization of the cells by fluorescence microscopy after the recording, the pipette solution contained Alexa Fluor 594 (40 or 60 µM). All Alexa Fluor dyes were used as hydrazide sodium salts (Invitrogen/Thermo Fisher Scientific). In experiments with simultaneous dual recording from electrically coupled cells using low-resistance recording pipettes and conventional patch-clamp amplifiers (see below), the pipettes for AII amacrine cells were filled with (in mM): 125 K-gluconate, 8 NaCl, 10 Hepes, 1 $CaCl_2$, 5 EGTA, 4 MgATP, 2*N*-(2,6-dimethylphenylcarbamoylmethyl)triethylammonium bromide (QX-314), 0.1 Alexa Fluor 488 (pH adjusted to 7.3 with KOH), and the pipettes for bipolar cells were filled with (in mM): 130 KCl, 8 NaCl, 10 Hepes, 1 $CaCl_2$, 5 EGTA, 4 MgATP, 0.04 Alexa Fluor 594 (pH adjusted to 7.3 with KOH). In similar experiments using higher-resistance pipettes and switch-clamp amplifiers, the pipettes for both AII amacrine and bipolar cells were filled with (in mM): 125 K-gluconate, 5 KCl, 8 NaCl, 10 Hepes, 0.2 EGTA, 4 MgATP (pH adjusted to 7.3 with KOH). For visualization by fluorescence microscopy, this pipette solution contained Lucifer yellow (1 mg/ml).

The theoretical liquid junction potential (the potential of the extracellular solution relative to that of the intracellular solution) was calculated with the software program JPCalcW (Molecular Devices, Sunnyvale, CA, USA) and in recordings with conventional patch-clamp amplifiers (see below), all membrane holding potentials (V_{hold}) were automatically corrected for the liquid junction potential on-line by the data acquisition software (Patchmaster; HEKA Elektronik, Lambrecht/Pfalz, Germany). For other recordings, we corrected the membrane holding potentials for the liquid junction potential during off-line analysis.

Drugs were added directly to the extracellular solution used to perfuse the slices. The concentrations of drugs were as follows (µM; supplier Tocris Bioscience, Bristol, UK; unless otherwise noted): 10 bicuculline methochloride, 1 strychnine (Research Biochemicals Inc., Natick, MA, USA), 10 6-cyano-7-nitroquinoxaline-2,3-dione (CNQX), 50 (1,2,5,6-tetrahydropyridin-4-yl)methylphosphinic acid (TPMPA), 0.3 or 1 tetrodotoxin (TTX), 50 4-ethylphenylamino-1,2-dimethyl-6-methylaminopyrimidinium chloride (ZD7288), and 20 (RS)-3-(2-carboxypiperazin-4-yl)-propyl-1-phosphonic acid (CPP). To block electrical coupling via gap junctions, we added 100 µM 2-[(2,6-dichloro-3-methylphenyl)amino]benzoic acid sodium salt (MFA; Sigma-Aldrich) to the extracellular solution (Veruki and Hartveit 2009). Solutions were either made up freshly for each experiment or were prepared from concentrated aliquots stored at − 20 °C.

Electrophysiological Recording and Data Acquisition

Patch pipettes were pulled from thick-walled borosilicate glass (outer diameter, 1.5 mm; inner diameter, 0.86 mm; Sutter Instrument, Novato, CA, USA). In all single-cell recordings, the pipettes were coated with Parafilm (American National Can; Greenwich, CT, USA) to reduce their effective capacitance.

For electrophysiological recording, we used the whole-cell configuration of the patch-clamp technique, either with conventional patch-clamp amplifiers (continuous single-electrode voltage-clamp; CSEVC; EPC10-triple or EPC10-USB-dual; HEKA Elektronik) or with discontinuous (switched) single-electrode voltage-clamp (DSEVC) amplifiers (SEC-05LX-BF; npi Electronic, Tamm, Germany). All single-cell recordings were performed with CSEVC amplifiers. Dual, simultaneous recordings between electrically coupled cells were either performed with a CSEVC amplifier or with two DSEVC amplifiers. All amplifiers were controlled by Patchmaster software (HEKA Elektronik).

For recordings with CSEVC amplifiers, we used lower-resistance pipettes where the open-tip resistance ranged from ~7 to ~10 MΩ when filled with intracellular solution. After establishing a GΩ-seal, currents caused by the recording electrode capacitance were automatically measured and neutralized by the amplifier (C_{fast} function of Patchmaster software). After breaking into the cell, currents caused by the cell membrane capacitance were partially neutralized by the amplifier (C_{slow} function of Patchmaster software). Signals were low-pass filtered (analog 3- and 4-pole Bessel filters in series) with a corner frequency (− 3 dB) at 1/5 of the inverse of the sampling interval (typically 50 µs).

Simultaneous, dual recordings of electrically coupled cell pairs with CSEVC amplifiers were performed as described for single cells, but when we recorded currents to estimate a cell's membrane capacitance, the voltage-clamp stimuli were sent simultaneously to both amplifiers to eliminate junctional currents between the two cells. Dual recordings with DSEVC amplifiers were performed as described in earlier studies from our laboratory (Veruki and Hartveit 2009; Veruki et al. 2010).

Whole-cell voltage-clamp recording with CSEVC amplifiers was used to sample current responses used during offline analysis to estimate R_s and R_N. For sampling capacitative current transients, the C_{slow} capacitance neutralization circuitry was disabled and the time constant of the internal stimulus filter was set to 2 µs. The sampling interval was set to 10 µs and before sampling, signals were low-pass filtered (analog 3-pole Bessel filter) with a corner frequency (− 3 dB) of 30 kHz. Current responses were evoked by 20 ms long voltage pulses of alternating amplitudes of ± 5 or − 10 mV from the holding potential of − 60 mV. Groups of 100 responses were acquired at intervals of 100 ms and averaged online. When we sampled other current responses, the C_{slow} capacitance neutralization circuitry was re-enabled and the time constant of the internal stimulus filter was set to 20 µs.

Image Acquisition for MPE Microscopy and Wide-Field Fluorescence Microscopy

For MPE microscopy, fluorescence from neurons filled with Alexa 594 was imaged with the MOM equipped with a mode-locked Ti:sapphire laser (Mai Tai DeepSee; Spectra-Physics) tuned to 810 nm (for additional details, see Zandt et al. 2017). An image stack was acquired as a series of optical sections (1024 × 1024 pixels) with *XY* pixel size ~ 70 to ~ 80 nm (depending on the magnitude of the digital zoom factor) and collected at a focal plane interval of 0.4 µm. For each image stack, we acquired two channels and at each focal plane two images were averaged on-line. The first channel sampled the fluorescence light as described above. The second channel was used for IR laser scanning gradient contrast imaging (IR-LSGC; Yasuda et al. 2004) and sampled the forward-scattered IR laser light after it passed the substage condensor and a Dodt gradient contrast tube (Luigs & Neumann). MPE microscopy and image acquisition were controlled by ScanImage software (version 3.8.1; Pologruto et al. 2003) running under Matlab (The Mathworks).

In the experiments with dual recording of electrically coupled cells using CSEVC amplifiers, we used wide-field fluorescence microscopy to acquire image stacks of the cells filled with Alexa 594 via the patch pipette (TILLvisION system with a Polychrome V light source and an Imago QE cooled CCD camera; TILL Photonics; for a detailed description, see Castilho et al. 2015). Deconvolution of Z stacks acquired by MPE or wide-field fluorescence microscopy for morphology and generation of maximum intensity projections was performed as described in Zandt et al. (2017).

Data Analysis and Presentation

To estimate the steady-state G_j between two electrically coupled cells, we used current responses obtained with dual voltage-clamp recording. For the calculations, we assumed an equivalent-circuit model (see, e.g., Veruki et al. 2010). For the dual recordings with DSEVC amplifiers, we assumed that R_s was effectively zero. For this case, the junction current (I_j) corresponds to the current evoked in the postsynaptic cell when the presynaptic cell is stepped from V_{hold} and G_j can be calculated directly from Ohm's law (Veruki et al. 2010; for a detailed analysis, see Hartveit and Veruki 2010) according to Eq. (1) for voltage pulses applied to cell *a* of a pair and according to Eq. (2) for voltage pulses applied to cell *b* of a pair

$$G_j = \frac{-I_b}{V_a - V_b} \tag{1}$$

$$G_j = \frac{-I_a}{V_b - V_a} \tag{2}$$

where I_a is I_j measured in cell *a*, I_b is I_j measured in cell *b*, and V_a and V_b are the voltages of cell *a* and cell *b*, respectively. Each measurement of G_j was obtained by plotting I_j versus the junction voltage (V_j) for a series of different voltage pulses and by calculating G_j as the slope of a straight line fitted to the I_j–V_j relationship. For a given cell pair, G_j was calculated as the average of the G_j values obtained for both directions of coupling.

For the dual voltage-clamp recordings, the (apparent) membrane resistance was estimated according to Eq. (3) when stepping cell *a* (r_{m1})

$$r_{m1} = \frac{V_a - V_b}{I_a + I_b} \tag{3}$$

and according to Eq. (4) when stepping cell *b* (r_{m2})

$$r_{m2} = \frac{V_b - V_a}{I_a + I_b} \tag{4}$$

We use the term apparent for the membrane resistance estimated from Eqs. (3) and (4) because it only eliminates the contribution from the G_j between the two cells of a pair, but not that from G_j between each cell and the other cells to which they are coupled. Each measurement of r_m was obtained by plotting the voltage versus the current and by

calculating r_m as the slope of a straight line fitted to the *V–I* relationship.

In dual recordings of electrically coupled cells, the input resistance (R_N) of either cell cannot be estimated directly when both cells are recorded in voltage clamp. Instead, R_N was obtained indirectly by calculating it from the apparent membrane resistances (r_{m1}, r_{m2}) and G_j according to Eq. (5) for cell *a* (R_{N1}) and Eq. (6) for cell *b* (R_{N2})

$$\frac{1}{R_{N1}} = \frac{1}{r_{m1}} + \frac{1}{R_j + r_{m2}} \quad or \quad R_{N1} = \frac{r_{m1}\left(r_{m2} + R_j\right)}{r_{m1} + r_{m2} + R_j} \tag{5}$$

$$\frac{1}{R_{N2}} = \frac{1}{r_{m2}} + \frac{1}{R_j + r_{m1}} \quad or \quad R_{N2} = \frac{r_{m2}\left(r_{m1} + R_j\right)}{r_{m1} + r_{m2} + R_j} \tag{6}$$

where r_{m1} is the apparent membrane resistance of cell *a* (estimated from Eq. (3)), r_{m2} is the apparent membrane resistance of cell *b* (estimated from Eq. (4)), and R_j is the inverse of the junctional conductance G_j (estimated from Eqs. (1) and (2)).

For whole-cell, voltage-clamp recordings of single bipolar cells, R_N was estimated from the resistive (steady-state) current responses evoked by 20 ms voltage pulses (− 5 or − 10 mV amplitude) by dividing the nominal voltage pulse amplitude by the baseline-subtracted current response amplitude (averaged over a 4 ms interval from 15 to 19 ms after onset of the voltage pulse). Each current response used for this measurement was obtained by averaging 100 individual responses evoked by consecutive voltage pulses (− 5 or − 10 mV). The same current responses were also used for off-line calculation of I_{hold} and R_s. I_{hold} was calculated by averaging the baseline current over a 4.5 ms interval preceding onset of the voltage pulse. R_s was estimated by fitting the decay phase during the voltage pulse with a double exponential function and dividing the amplitude of the voltage pulse by the peak current amplitude extrapolated to the onset of the voltage pulse. When examining the effect of MFA on R_N and I_{hold}, we averaged the results for seven data points (obtained over a 3 min period), both during the control period and after application of MFA. The average I_{hold} prior to application of MFA was − 5.8 ± 10.0 pA (range − 34 to 21 pA). Following exposure to MFA, the average I_{hold} was − 7.3 ± 7.2 pA (range − 34 to 4.2 pA) and the average absolute change in I_{hold} was 5.4 pA (range 0.03 to 31 pA; $n = 32$ cells).

Data were analyzed off-line with Fitmaster (HEKA Elektronik), IGOR Pro (WaveMetrics), Excel, and GraphPad Prism (GraphPad Software). Experimental data are presented as means ± S.D. (n = number of cells). The number of individual traces included in the averaged current traces in the figures are stated for each case. Statistical analyses with comparisons between or within groups were performed using Student's two-tailed *t* test (paired or unpaired as appropriate) or one-way ANOVA, as indicated in the text. Differences were considered statistically significant at the $P < 0.05$ level. For illustration purposes, most raw data records were either low-pass filtered (digital non-lagging Gaussian filter; − 3 dB at 0.5–1 kHz) or smoothed by a binomial smoothing function (IGOR Pro) to emphasize the kinetics of the response.

Results

Properties of Electrical Coupling Between ON-Cone Bipolar and AII Amacrine Cells

In the mammalian retina, there is strong evidence for electrical coupling between ON-cone bipolar cells and AII amacrine cells (Veruki and Hartveit 2002b; Massey et al. 2003; Trexler et al. 2005). We took advantage of this to examine how MFA influences the membrane properties of cells with verified electrical coupling. The most direct way to demonstrate and quantify functional electrical coupling is by simultaneous, dual recording from visually targeted cells in the in vitro retina. AII amacrine cells can be visually targeted for recording according to the size and location of the cell body in the proximal part of the inner nuclear layer and the thick apical dendrite that tapers as it descends into the inner plexiform layer (Fig. 1a, b). In contrast, ON-cone bipolar cells cannot be directly targeted, but their cell bodies tend to be located distally in the inner nuclear layer, proximal to the majority of rod bipolar cell bodies in the most distal part, close to the outer plexiform layer (Fig. 1a, c). To increase the likelihood of recording from electrically coupled pairs of AII amacrine cells and ON-cone bipolar cells, we first targeted an AII amacrine cell and then searched for a presumed ON-cone bipolar cell body as close as possible to a vertical line across the inner nuclear layer that passed through the AII cell body. All cells were filled with fluorescent dyes and the complete morphologies were visualized during (MPE microscopy) or after (wide-field fluorescence microscopy) the electrophysiological recording.

An example of an AII amacrine cell and an ON-cone bipolar cell that were electrically coupled can be seen in Fig. 1. In this example, a total of three cells (one AII amacrine and two cone bipolar cells) were targeted and recorded (Fig. 1a). Fluorescence imaging of the AII amacrine displayed the typical bistratified morphology with arboreal and lobular dendrites in the proximal and distal parts of the inner plexiform layer, respectively (Fig. 1b). The two cone bipolar cells, filled with a different dye than the AII, were visualized separately (Fig. 1c). The bipolar cells could be identified as specific cell types based on the stratification and shape of their axon terminals within the inner

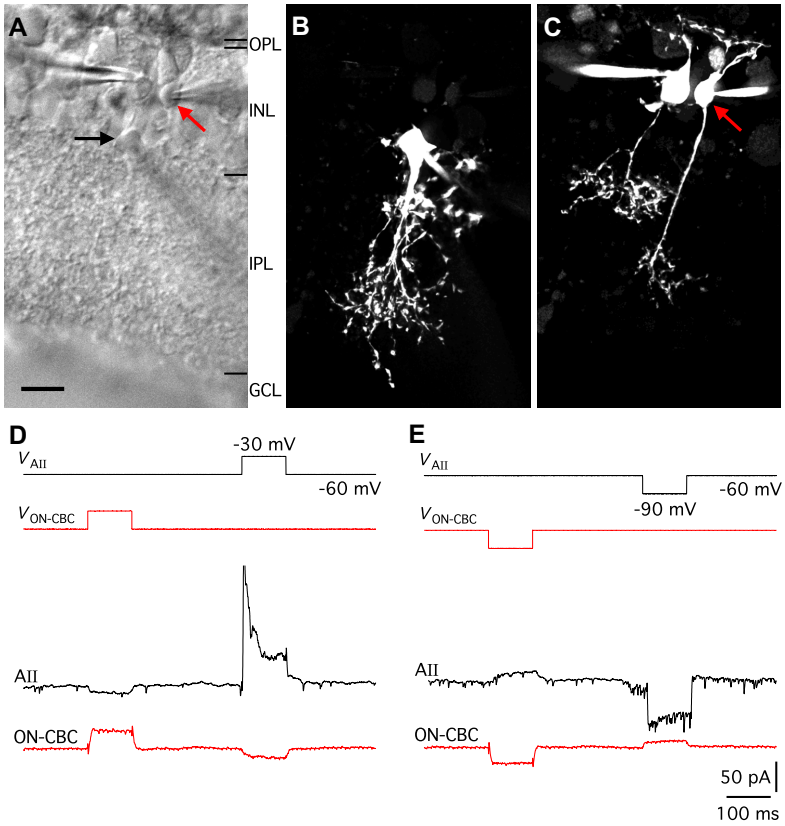

Fig. 1 Physiological evidence for gap junction coupling between AII amacrine cells and ON-cone bipolar cells in rat retinal slices. **a** Infrared differential interference contrast (IR-DIC) videomicrograph of a retinal slice with whole-cell recording pipettes attached to an AII amacrine cell (black arrow; cell body visible at border between the inner nuclear layer and the inner plexiform layer) and two cone bipolar cells (cell bodies located in the inner nuclear layer; red arrow points to ON-cone bipolar cell). Same cells in (**a**–**e**). Here and later, retinal layers indicated by black (or white) horizontal lines: *OPL* outer plexiform layer, *INL* inner nuclear layer, *IPL* inner plexiform layer, *GCL* ganglion cell layer. **b** AII amacrine cell filled with Alexa 488 via patch pipette. Here, and in (**c**), maximum intensity projection (MIP; along *Z* axis) generated from wide-field fluorescence stack after deconvolution. **c** OFF-cone bipolar cell (left; type 3) and ON-cone bipolar cell (right, red arrow; type 6) filled with Alexa 594 via patch pipettes. **d**, **e** Simultaneous, dual recording of AII amacrine cell and ON-cone bipolar cell electrically coupled to each other. **d** With both cells in voltage clamp (V_{hold} = − 60 mV), 100-ms depolarizing voltage pulses (from V_{hold} to − 30 mV) were applied sequentially to AII amacrine cell (V_{AII}) and ON-cone bipolar cell (V_{ON-CBC}). Depolarization of AII amacrine cell resulted in outward current in AII (lower black trace) and inward current in ON-cone bipolar cell (lower red trace). Depolarization of ON-cone bipolar cell resulted in outward current in ON-cone bipolar cell (lower red trace) and inward current in AII (lower black trace). **e** With both cells in voltage clamp (V_{hold} = − 60 mV), 100-ms hyperpolarizing voltage pulses (from V_{hold} to − 90 mV) were applied sequentially to AII amacrine cell (V_{AII}) and ON-cone bipolar cell (V_{ON-CBC}). Hyperpolarization of AII amacrine cell resulted in inward current in AII (lower black trace) and outward current in ON-cone bipolar cell (lower red trace). Hyperpolarization of ON-cone bipolar cell resulted in inward current in ON-cone bipolar cell (lower red trace) and outward current in AII (lower black trace). Each trace represents a single trial. For this experiment, no pharmacological blockers were added to the extracellular solution, but for the AII amacrine cell, voltage-gated Na^+ channels were blocked by QX-314 in the pipette solution. Scale bar: 10 µm (**a**–**c**)

plexiform layer (Euler and Wässle 1995; Hartveit 1997). Of the two bipolar cells, one was a type 6 ON-cone bipolar (Fig. 1c, right), and the other was a type 3 OFF-cone bipolar cell (Fig. 1c, left). The OFF-cone bipolar cell was leaky and only weakly connected through a chemical synapse to the AII, and as it is not relevant to the results presented here, it will not be further commented on.

In such a paired recording of an AII amacrine and an ON-cone bipolar cell, with both cells recorded in whole-cell voltage clamp, electrical coupling is immediately apparent

when a voltage pulse is applied to either cell. A depolarizing voltage pulse (+ 30 mV relative to V_{hold} = − 60 mV) applied to the ON-cone bipolar cell or the AII amacrine cell (i.e., the presynaptic cell) evoked an inward current in the postsynaptic cell (i.e., the non-stepped cell; Fig. 1d). Correspondingly, a hyperpolarizing voltage pulse (− 30 mV relative to V_{hold} = − 60 mV) applied to the ON-cone bipolar cell or the AII amacrine cell evoked an outward current in the postsynaptic cell (Fig. 1e). For each direction of coupling, we estimated G_j as the slope of a straight line fitted to the I_j versus V_j relationship. As previously observed in our laboratory (Veruki and Hartveit 2002b), the junctional conductance was very similar for both directions of coupling and we calculated G_j as the average of the conductance values measured for each direction. For this cell pair the junctional conductance was calculated to be ~ 400 pS.

MFA Blocks Electrical Coupling Between ON-Cone Bipolar and AII Amacrine Cells

Using paired recordings from electrically coupled ON-cone bipolar cells and AII amacrine cells, we have previously demonstrated that MFA blocks the electrical synapses between these cells (Veruki and Hartveit 2009). Here, we have re-analyzed data obtained in the previous study to quantify the effect of MFA on input resistance (R_N) and apparent membrane resistance (r_m) and, importantly, to examine how the MFA-evoked changes of these parameters develop in parallel with the gradual reduction of the junctional conductance (G_j). This analysis is similar to that previously reported from our laboratory for pharmacological uncoupling of AII amacrine cells (Veruki et al. 2010). The dual recording paradigm provides direct evidence for the block of electrical coupling by MFA and predicts that the concomitant changes of membrane properties can be expected to occur during similar recording from single cells.

In a dual recording of an ON-cone bipolar cell and an AII amacrine cell electrically coupled to each other, adding MFA (100 µM) to the bath solution completely blocked the junctional conductance (Fig. 2a). The onset of block was rapid and could essentially be observed as soon as MFA reached the recording chamber. However, the blocking action of MFA was fairly slow and it typically took ~ 20 to 30 min before the electrical coupling had been completely blocked (Fig. 2a). For the cell pair illustrated in Fig. 2, we were able to maintain the recording for almost 3 h and during washout of MFA, the electrical coupling partially recovered. Figure 2b illustrates example responses of the two cells evoked by the voltage-clamp stimuli at three different time points during the recording: in the control condition (a), during complete block of coupling by MFA (b), and after partial recovery following washout of MFA (c). From a comparison of the responses of each cell in the control condition and during complete block of electrical coupling, it is apparent that the block of coupling by MFA was accompanied by an increase of R_N for each cell.

To analyze the effect of MFA in more detail, we calculated both r_m and R_N for each cell for all measurements during the recording time illustrated in Fig. 2a. In recordings from single cells, all cells electrically coupled to the recorded cell would be free to change their membrane potential. In the paired recording, however, both cells were held in voltage clamp, thus, the postsynaptic cell is not free to change its voltage when the membrane potential of the presynaptic cell is changed. This complicates the calculation of the R_N of the stepped cell (see "Materials and Methods" section). Figure 2c and d illustrate r_m and R_N for the ON-cone bipolar and the AII amacrine cell and how the values changed during application of MFA. In the control condition, r_m was higher than R_N (Fig. 2c, d). At the point in time when electrical coupling was completely blocked by MFA, the two values were essentially identical, both for the ON-cone bipolar and the AII amacrine cell. For the ON-cone bipolar cell, R_N changed from ~ 0.6 GΩ in control to ~ 2 GΩ after complete block of electrical coupling (Fig. 2c). For the AII, the corresponding change was from ~ 0.7 GΩ to ~ 5 GΩ (Fig. 2d). These results suggest that if a retinal neuron is electrically coupled to other neurons, with functional properties of coupling similar to those for ON-cone bipolar cell to AII amacrine cell coupling, it should be possible to detect a change in R_N when the coupling is blocked. The magnitude of the change will depend both on the total number of cells coupled to the recorded cell and on the junctional conductances between the cells. In paired recordings between ON-cone bipolar cells and AII amacrine cells in rat retina, we have previously measured an average junctional conductance of 1.2 nS (range between 0.1 and 3.3 nS; including types 5, 6, 7, and 8; Veruki and Hartveit 2002b). To our knowledge, however, there is no information concerning the number of ON-cone bipolar cells directly coupled to an AII amacrine cell in rat retina.

MFA Evokes a Marked Increase of the Input Resistance of ON-Cone Bipolar Cells

We next recorded from single ON-cone bipolar cells in voltage clamp (V_{hold} = − 60 mV) and measured R_N by applying small voltage pulses (− 5 and − 10 mV) relative to V_{hold}. Throughout the recording period, the bath solution contained pharmacological blockers of neurotransmitter receptors (glutamate, GABA, glycine), voltage-gated Na^+ channels and I_h (see "Materials and Methods" section). For the cell illustrated in Fig. 3a–c (a type 6 cone bipolar cell), R_N in the control condition was ~ 0.74 GΩ. After ~ 12 min recording, we added MFA to the bath and continued the recording for another ~ 30 min (Fig. 3c). During this period,

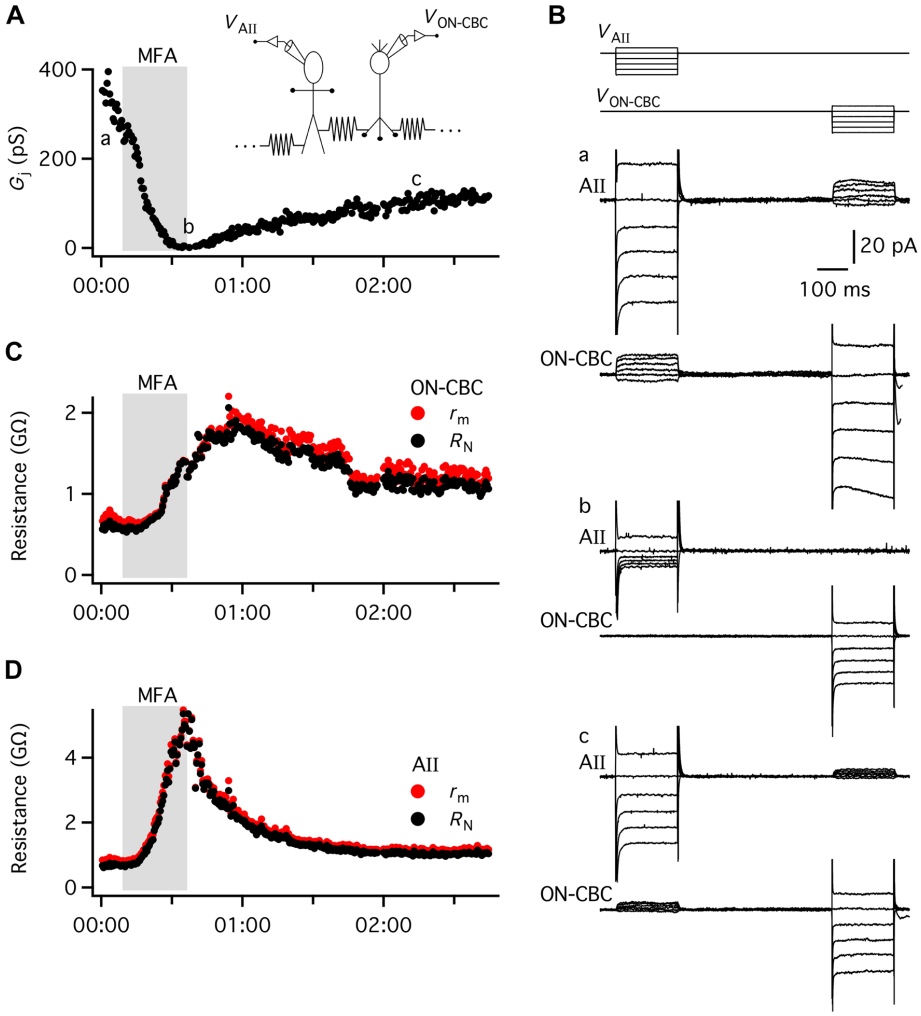

there was a gradual increase of R_N, with a maximum of ~2.0 GΩ (Fig. 3c). There was a slight reduction of R_s during the recording period, but no consistent change in I_{hold}.

Similar results were observed for a total of 19 ON-cone bipolar cells (Fig. 3d). Of these cells, nine were type 5, four were type 6, four were type 7, and two were type 8. For all but one cell (a type 6), application of MFA evoked a marked increase of R_N relative to the value obtained for the control condition (with pharmacological blockers). In control, the average value of R_N was 1.37 ± 0.68 GΩ (range 0.52–2.85 GΩ) and in MFA, the average value of R_N was 2.79 ± 0.86 GΩ (range 1.89–4.88 GΩ; $P = 3.8 \times 10^{-7}$, paired t test; $n = 19$ cells; Fig. 3d).

MFA Does Not Increase the Input Resistance of OFF-Cone Bipolar Cells

Similar to the experiments with ON-cone bipolar cells, we also recorded from single OFF-cone bipolar cells in voltage clamp ($V_{hold} = -60$ mV) and repeatedly measured R_N by applying small voltage pulses (− 5 and − 10 mV) relative to V_{hold}. For the cell illustrated in Fig. 4a–c (a type 3 cone bipolar cell), R_N in the control condition was ~2.5 GΩ. For comparison, we have also illustrated R_s and I_{hold} in the same graph (Fig. 4c). After 15 min of recording, we added MFA to the bath and continued recording for another 30 min (Fig. 4c). During this period, there was only a small, gradual reduction of R_N to ~2.2

◂**Fig. 2** Changes in apparent membrane resistance (apparent r_m) and input resistance (R_N) of ON-cone bipolar and AII amacrine cells accompany block of electrical coupling by meclofenamic acid (MFA). **a** Junctional conductance (G_j) as a function of time during paired recording of an AII amacrine cell and an ON-cone bipolar cell (type 5 or 6) electrically coupled to each other (dual whole-cell voltage-clamp recording with DSEVC amplifiers). G_j is calculated as the average of the conductance values measured for each direction of coupling (with voltage pulses applied to either ON-cone bipolar or AII amacrine). MFA was applied in the extracellular solution during the period indicated by the shaded area (duration ~ 30 min). The lowercase letters a, b, and c indicate time points during control (a), in the presence of MFA (b), and after washout of MFA (c), where current responses are displayed in (**b**). Same cell pair in (**a**–**d**). *Inset* schematic diagram of recording configuration with resistor between the two recorded cells to indicate electrical coupling and dots extending laterally from resistors attached to each cell to indicate electrical coupling to other AII amacrine and ON-cone bipolar cells. **b** Top: voltage protocol with 200-ms voltage pulses (from − 40 to + 10 mV relative to $V_{hold} = -60$ mV; increments of 10 mV) applied to the cells (V_{AII}, $V_{ON\text{-}CBC}$). Bottom a, b, and c: current responses recorded from AII amacrine cell (AII) and ON-cone bipolar cell (ON-CBC) in response to voltage pulses in the control condition before application of MFA (a), after complete block of G_j in the presence of MFA (b), and after partial recovery of electrical coupling after washout of MFA (c). Notice that the asymmetry of the voltage pulses relative to V_{hold} helps to identify the corresponding current responses in the two cells. Current traces are individual responses. Capacitative current transients have been truncated for clarity. **c**, **d** Apparent r_m and R_N for ON-cone bipolar cell (**c**) and AII amacrine cell (**d**) as a function of time in the control condition, during application of MFA, and during washout of MFA. For both cells, r_m and R_N increased during application of MFA. Throughout the recording period, ionotropic neurotransmitter receptors (non-NMDA glutamate receptors, $GABA_A$ receptors, glycine receptors), and voltage-gated Na^+ channels were blocked by drugs added to the extracellular solution (see "Materials and Methods" section for details)

GΩ by the end of the recording period (Fig. 4c). There were only minimal changes in the values for R_s and I_{hold} (Fig. 4c).

Similar results were observed for a total of eight OFF-cone bipolar cells (Fig. 4d). Of these cells, two were type 2, three were type 3, and three were type 4. In the control condition (with pharmacological blockers), the average value of R_N was 2.63 ± 0.95 GΩ (range 1.05–4.04 GΩ) and after applying MFA the average value of R_N was 2.47 ± 1.02 GΩ (range 0.99–3.97 GΩ; $P = 0.0605$, paired t test; $n = 8$ cells; Fig. 4d). It is possible that the small reduction of R_N observed in the presence of MFA for seven of the cells might be caused by an effect of MFA on ion channels other than gap junction channels. For example, MFA has been shown to inhibit hKv2.1 potassium channels (Lee and Wang 1999), open KCNQ2/Q3 potassium channels (Peretz et al. 2005) and stimulate BK channel activity (Wu et al. 2001).

MFA Does Not Increase the Input Resistance of Rod Bipolar Cells

Gap junctions between rod bipolar cells have not been reported (e.g., Strettoi et al. 1990). Consistent with this, in a previous study from our laboratory, we never observed any evidence for electrical coupling during paired recordings between neighboring rod bipolar cells (Veruki et al. 2006). To examine the effect of MFA, we recorded from single rod bipolar cells in voltage clamp ($V_{hold} = -60$ mV) and measured R_N by applying small voltage pulses (− 5 and − 10 mV) relative to V_{hold}. For the cell illustrated in Fig. 5a–c, the input resistance in the control condition was ~ 4.0 GΩ. After 15 min of recording, we added MFA to the bath and continued the recording for another ~ 33 min (Fig. 5c). During this period, R_N was relatively stable, with minor fluctuations around 4 GΩ during the period of ~ 20 min when MFA was applied (Fig. 5c). There were only moderate changes of R_s and I_{hold} during the recording period. Similar results were observed for a total of five rod bipolar cells (Fig. 5d). In control, the average value of R_N was 3.3 ± 1.1 GΩ (range 1.9–4.6 GΩ) and in MFA, the average value of R_N was 3.1 ± 0.9 GΩ (range 2.1–4.0 GΩ; $P = 0.1847$, paired t test; $n = 5$ cells; Fig. 5d).

Comparisons Within ON- and OFF-Cone Bipolar Cells Reveal No Type-Specific Effects of MFA

The results so far presented reveal that MFA evoked a marked increase of R_N for ON-cone bipolar cells, but not for OFF-cone and rod bipolar cells. When we compared the average values of R_N for the different cell types in the control condition, we observed little difference between R_N for OFF-cone and rod bipolar cells, but both values were higher than R_N for ON-cone bipolar cells (Fig. 6a). Notably, the average R_N for ON-cone bipolar cells in MFA was very similar to R_N for both OFF-cone and rod bipolar cells in control (Fig. 6a). A statistical comparison of the values of R_N for the four groups illustrated in Fig. 6a, confirmed that there was no difference between R_N for ON-cone bipolars in MFA, OFF-cone bipolars in control, and rod bipolars in control, whereas R_N for ON-cone bipolars in control was significantly smaller than R_N for the other three groups ($P \geq 0.5055$ and $P \leq 0.0044$, respectively, $F_{(3,47)} = 0.6581$; one-way ANOVA, Tukey's multiple comparison test, adjusted P values). This suggests that with respect to R_N, closing gap junction channels makes ON-cone bipolar cells electrically similar to OFF-cone and rod bipolar cells.

We next asked whether there was any evidence for type-specific effects of MFA on R_N that were potentially masked in our previous analysis where all types among ON- and OFF-cone bipolar cells were grouped together. When we compared the different types of ON- and OFF-cone bipolar cells (cells in Figs. 3d and 4d, respectively,) in the control condition, we found no statistically significant difference between the values of R_N for the different types of ON-cone bipolar cells ($F_{(3,15)} = 0.4214$, $P = 0.7403$, one-way ANOVA) or for the different types of OFF-cone bipolar cells

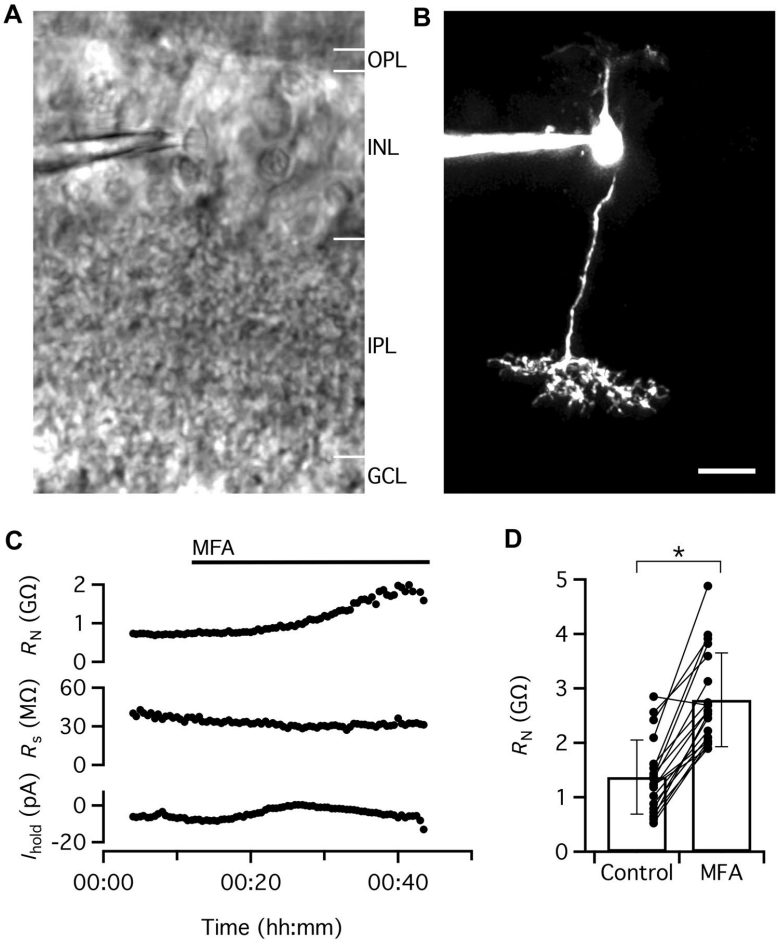

Fig. 3 MFA evokes a marked increase of R_N of ON-cone bipolar cells. **a** Infrared laser scanning gradient contrast (IR-LSGC) image shows recording pipette and retinal slice during whole-cell recording and multiphoton excitation (MPE) microscopy. **b** ON-cone bipolar cell filled with Alexa 594 via patch pipette during whole-cell recording. MIP (along *Z* axis) generated from MPE microscopy fluorescence image stack after deconvolution. Morphological characteristics and level of stratification of axon terminal in inner plexiform layer allow identification of cell as a type 6 ON-cone bipolar cell. Same cell in (**a**–**c**). **c** R_N, R_s, and voltage-clamp holding current (I_{hold}; $V_{hold} = -60$ mV) obtained in control condition and after addition of MFA (100 µM) to the extracellular solution to block electrical coupling via gap junctions (period of application indicated by the horizontal line at top). Here and in Figs. 4 and 5, the time series plots of R_N, R_s, and I_{hold} were obtained by analyzing the current responses evoked by repeated application of − 5 and − 10 mV voltage pulses (20 ms). Each data point was obtained by analysis of a current waveform obtained by averaging 100 consecutive responses (see "Materials and Methods" section for details on analysis procedures). Throughout the recording period illustrated here (and in Figs. 4 and 5), ionotropic neurotransmitter receptors (non-NMDA and NMDA glutamate receptors, $GABA_A$ and $GABA_C$ receptors, glycine receptors), voltage-gated Na^+ channels, and I_h were blocked by drugs added to the extracellular solution (see "Materials and Methods" section for details). Notice marked increase of R_N following application of MFA (with smaller changes in R_s and I_{hold}). **d** R_N in the control condition and in the presence of MFA (100 µM) for ON-cone bipolar cells ($n = 19$ cells) investigated as in (**c**). Here and later, bars represent mean ± SD, data points for the same cell are connected by lines, and the results from statistical comparisons between averages are indicated by n.s. (no significant difference; $P > 0.05$) or a single asterisk (statistically significant difference; $P \leq 0.05$). Notice that the majority of ON-cone bipolar cells display a marked increase of R_N in the presence of MFA. Scale bar: 10 µm (**a**, **b**)

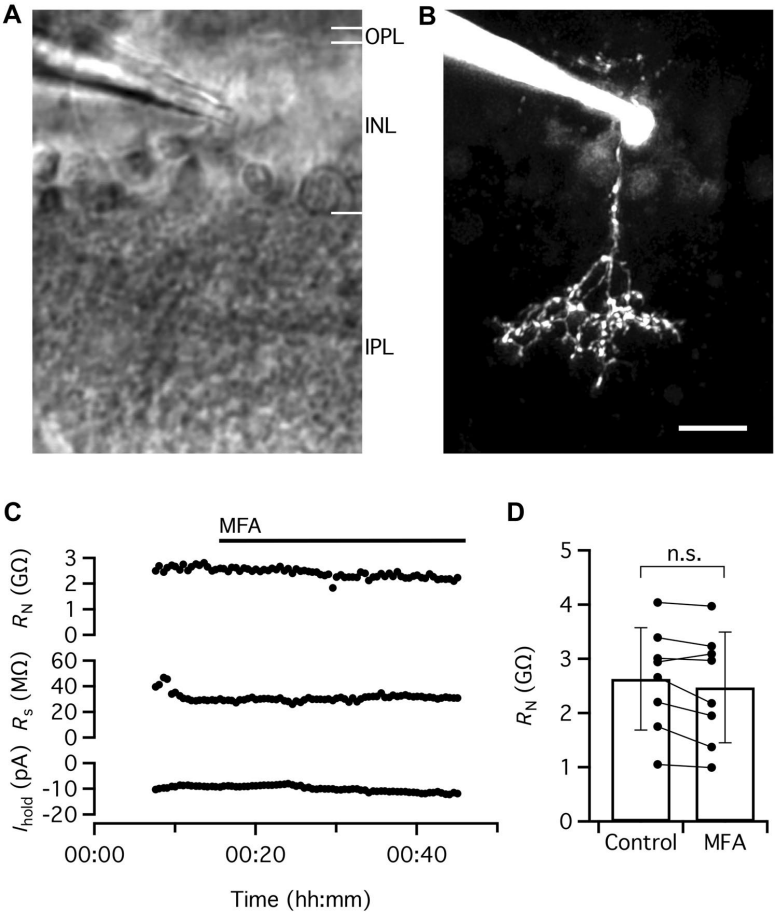

Fig. 4 MFA does not increase R_N of OFF-cone bipolar cells. **a** IR-LSGC image shows recording pipette and retinal slice during whole-cell recording and MPE microscopy. **b** OFF-cone bipolar cell filled with Alexa 594 via patch pipette during whole-cell recording. MIP (along *Z* axis) generated from MPE microscopy fluorescence image stack after deconvolution. Morphological characteristics and level of stratification of axon terminal in inner plexiform layer allow identification of cell as a type 3 OFF-cone bipolar cell. Same cell in (**a**–**c**). **c** R_N, R_s and voltage-clamp I_{hold} ($V_{hold} = -60$ mV) obtained in control condition and after addition of MFA (100 µM) to the extracellular solution (period of application indicated by the horizontal line at top). Notice small decrease of R_N following application of MFA (with little change in R_s and I_{hold}). **d** R_N in the control condition and in the presence of MFA (100 µM) for OFF-cone bipolar cells ($n = 8$ cells) investigated as in (**c**). Scale bar: 10 µm (**a**, **b**)

($F_{(2,5)} = 0.8162$, $P = 0.4935$, one-way ANOVA). Accordingly, the relatively large variability of R_N in the control condition for both OFF- and ON-cone bipolar cells (Figs. 3d and 4d) cannot be explained by systematic differences between the different types of bipolar cells within each group.

We next compared the effect of MFA on the different types of OFF- and ON-cone bipolar cells (Fig. 6b, c). Although the group sizes are small, MFA had no statistically significant effect on R_N for any of the three types of OFF-cone bipolar cells (Fig. 6b). For ON-cone bipolar cells, MFA had the same qualitative effect on all types of cells, with clear increases in R_N (Fig. 6c). Here, the increase in R_N was statistically significant for cell types 5 and 7, but not for type 8 (where we only had two cells) and type 6 (where one of the cells showed a decrease). We were unfortunately not successful in obtaining recordings for type 1 (OFF) and type 9 (ON) cone bipolar cells, both of which are relatively rare types (Euler et al. 2014). Taken together, we can summarize these results by concluding that we find no evidence for a type-specific effect of MFA within either ON- or OFF-cone bipolar cells.

Finally, we compared the relative magnitude of the gap junctional conductance and the non-gap junctional conductance for the different types of ON-cone bipolar cells (Fig. 6D). The non-gap junctional conductance was estimated as the input conductance ($1/R_N$) after blocking gap junctions in the presence of MFA. The gap junctional conductance was calculated by subtracting the non-gap junctional conductance from the total input conductance measured in the control condition. There was no statistically significant difference between either the gap junctional conductance ($F_{(3,15)} = 1.008$, $P = 0.4166$, one-way ANOVA) or the non-gap junctional conductance for the four cell types ($F_{(3,15)} = 1.911$, $P = 0.1712$,, one-way ANOVA). This

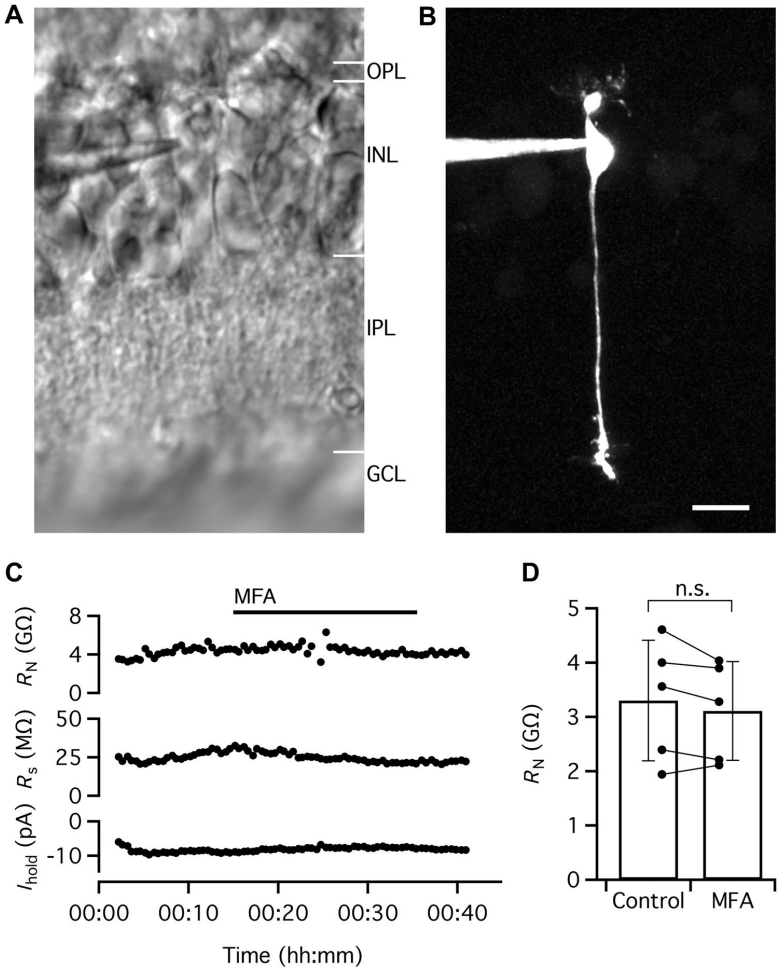

Fig. 5 MFA does not increase R_N of rod bipolar cells. **a** IR-LSGC image shows recording pipette and retinal slice during whole-cell recording and MPE microscopy. **b** Rod bipolar cell filled with Alexa 594 via patch pipette during whole-cell recording. MIP (along *Z* axis) generated from MPE microscopy fluorescence image stack after deconvolution. Morphological characteristics and level of stratification of axon terminal in inner plexiform layer allow identification of cell as a rod bipolar cell. Same cell in (**a**–**c**). **c** R_N, R_s, and voltage-clamp I_{hold} ($V_{hold} = -60$ mV) obtained in control condition and after addition of MFA (100 µM) to the extracellular solution (period of application indicated by the horizontal line at top). Notice that there is no consistent change of R_N following application of MFA (with smaller changes in R_s and I_{hold}). **d** R_N in the control condition and in the presence of MFA (100 µM) for rod bipolar cells ($n = 5$ cells) investigated as in (**c**). Scale bar: 10 µm (**a**, **b**)

suggests that for the four types of ON-cone bipolar cells recorded from here, the contributions of gap junctional and non-gap junctional conductance to the total membrane conductance are similar.

Discussion

The function of morphologically identified gap junctions between cone bipolar cells is puzzling. As a first step towards elucidating potential roles for these gap junctions, we investigated whether their presence between bipolar cells makes a measurable contribution to the total input resistance of these cells. We measured R_N of single bipolar cells in a rat retinal slice preparation under control conditions and in the presence of MFA, a well-documented pharmacological blocker of gap junctions (Pan et al. 2007; Veruki and Hartveit 2009). For ON-cone bipolar cells, we observed a marked increase of R_N in MFA. For OFF-cone bipolar cells, however, MFA did not increase R_N and these cells appeared similar to rod bipolar cells, for which there is no morphological evidence for gap junctions. If we accept the existing evidence for the presence of gap junctions between cone bipolar cells, the simplest interpretation of our results is that for OFF-cone bipolar cells, the open probability of the corresponding gap junction channels (connexons) is so low that blocking the channels has no detectable influence on the electrotonic properties of the cells. In the following, we discuss our results in the context of the evidence for gap junctions between cone bipolar cells.

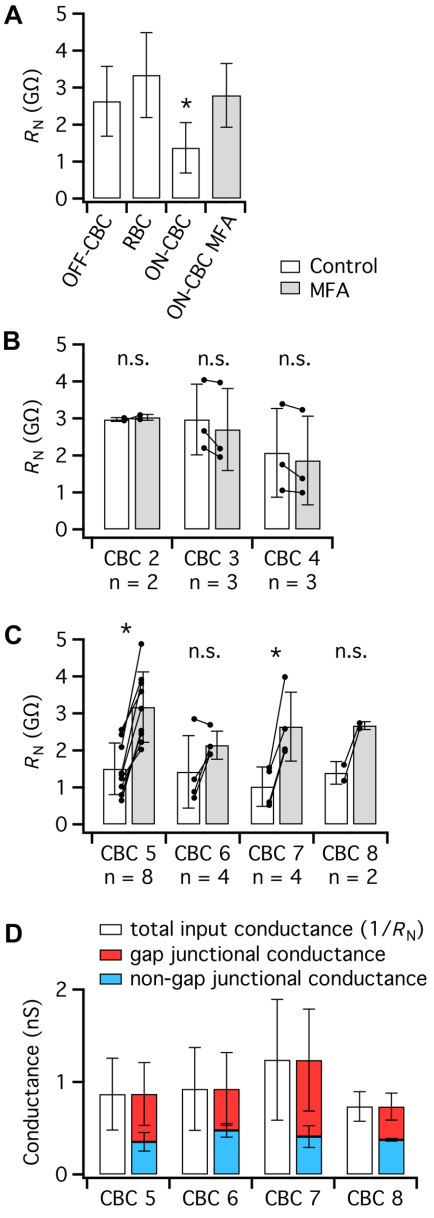

Fig. 6 Overview of R_N and non-gap junctional versus gap junctional conductance for different types of OFF- and ON-cone bipolar cells. **a** Comparison of R_N for OFF-cone, rod, and ON-cone bipolar cells in control condition and ON-cone bipolar cells in the presence of MFA (100 µM) to block gap junctions. Notice that R_N of ON-cone bipolar cells in control is significantly different from the other three groups, which are not significantly different from each other (for statistics, see "Results" section). Here and in **b** and **c**, open bars indicate control and gray bars indicate MFA. **b** R_N in control condition and in MFA for three different types of OFF-cone bipolar cells. **c** R_N in the control condition and in the presence of MFA for four different types of ON-cone bipolar cells. Notice that except for one type 6 cell, all types of ON-cone bipolar cells display a marked increase of R_N in the presence of MFA. **d** Total input conductance ($=1/R_N$) and the relation between gap junctional conductance and non-gap junctional conductance for four different types of ON-cone bipolar cells. To illustrate the variability of the total input conductance and its two components, each cell type is represented with two bars. There was no statistically significant difference between either the gap junctional conductance or the non-gap junctional conductance for the four cell types (see "Results" section)

Evidence for Gap Junctions Involving Cone Bipolar Cells

For OFF-cone bipolar cells, there are a number of studies in a variety of species that strongly suggest the presence of gap junctions, both between the dendrites (Mills 1999; Feigenspan et al. 2004; O'Brien et al. 2012; Kántor et al. 2016) and the axon terminals (Kolb 1979; Jacoby and Marshak 2000; Tsukamoto and Omi 2015, 2017; Kántor et al. 2017) of these cells. In addition, there is evidence that the gap junctions at the dendrites of OFF-cone bipolar cells contain Cx36 (Feigenspan et al. 2004; O'Brien et al. 2012; Kántor et al. 2016). Heterologous gap junctions between adjacent ON-cone bipolars have also been reported (Cohen and Sterling 1990; Tsukamoto and Omi 2017). In mouse retina, it has been reported that the gap junctions between OFF-cone bipolar cells were more frequently encountered than those between ON-cone bipolar cells (Tsukamoto and Omi 2017). The majority of gap junction connections involving ON-cone bipolar cells are with AII amacrine cells (Kolb and Famiglietti 1974; McGuire et al. 1984; Strettoi et al. 1992, 1994; Chun et al. 1993). In addition, there is direct evidence from dual recordings of pairs of ON-cone bipolar and AII amacrine cells that these gap junctions function as electrical synapses (Veruki and Hartveit 2002b, 2009). There is also morphological evidence that the axon terminals of ON-cone bipolar cells make gap junctions with the bistratified, narrow-field A8 amacrine cell (Kolb and Nelson 1996; Lee et al. 2015), but as far as we know, direct evidence for functional coupling between these cell types is lacking.

Why Does MFA Not Increase the Input Resistance of OFF-Cone Bipolar Cells?

Given the strong evidence for gap junctions located at both the dendrites and axon terminals of OFF-cone bipolar cells, it is surprising that MFA did not increase R_N of these cells.

Such an increase would be expected if MFA blocked open gap junction channels that contributed to the input conductance of the cells, similar to the results observed here for ON-cone bipolar cells and the results for AII amacrine cells, A17 amacrine cells, and Golgi cell interneurons, as discussed earlier. There are several possible explanations for the lack of effect of MFA which will be discussed below.

First, the possibility has to be considered whether MFA is unable to block the channels (connexons) of OFF-cone bipolar gap junctions. For several reasons, we consider this possibility unlikely. In rabbit retina, MFA blocks dye/tracer coupling of both A-type horizontal cells, B-type horizontal cells and AII amacrine cells (Pan et al. 2007), all of which are thought to express different connexins (Cx50, Cx57 and Cx36, respectively). In rat retina, MFA blocks electrical coupling between pairs of AII amacrine cells, pairs of ON-cone bipolar cells and AII amacrine cells, and pairs of A17 amacrine cells (Veruki and Hartveit 2009; Veruki et al. 2010; Elgueta et al. 2018; Zandt et al. 2018). There is evidence that gap junctions between ON-cone bipolar cells and AII amacrine cells are either homomeric, with both neurons expressing Cx36, or heteromeric with the AII expressing Cx36 and the bipolar cell expressing Cx45 (Maxeiner et al. 2005; Han and Massey 2005; Lin et al. 2005; Dedek et al. 2006). Taken together, these results suggest that there is little selectivity between different connexins for block by MFA. A similar lack of selectivity was also found for the potent block of Cx36 and Cx50 by mefloquine (Cruikshank et al. 2004). Although it is hard to exclude the possibility that OFF-cone bipolar cell gap junctions contain a connexin with little sensitivity to MFA, the existing evidence suggests the presence of Cx36 and/or Cx45 in bipolar cells (Feigenspan et al. 2004; Han and Massey 2005; Maxeiner et al. 2005; Lin et al. 2005) which should be blocked by MFA (Pan et al. 2007; Veruki and Hartveit 2009). In addition, the nearly identical values obtained for the R_N of ON-cone bipolar cells in MFA and OFF-cone bipolar cells in the control condition suggest that the lack of effect of MFA on OFF-cone bipolar cells is due to the absence of electrical coupling (open gap junction channels) between these cells, rather than the presence of MFA-resistant electrical coupling. This observation suggests that OFF-cone bipolar cells in the rat retina are effectively uncoupled electrically.

Second, it seems difficult to escape the conclusion that the gap junction channels between OFF-cone bipolar cells, irrespective of whether they are located at dendrites or axon terminals (or both), do not contribute a measurable conductance under our recording conditions. The total conductance contributed by gap junction channels is a function of the number of channels, the single-channel conductance, and the (average) open probability. To our knowledge, there are no estimates of the total number of connexons associated with OFF-cone bipolar cells, although there are reports that the gap junctions are relatively small (Kolb 1979). It is also possible that the open probability could be very low. Because of the electrical coupling between ON-cone bipolar cells and AII amacrine cells, the present results do not permit strong conclusions about the functional properties of the gap junctions directly between ON-cone bipolar cells. Currently, it is not possible to differentiate experimentally between the relative contribution of heterologous and (potential) homologous electrical synapses of ON-cone bipolar cells. However, it is a possibility that the gap junctions between ON-cone bipolar cells, analogous to those between OFF-cone bipolar cells, contribute little measurable conductance to these cells.

A Functional Role for Electrical Coupling Between Cone Bipolar Cells?

If we assume that at least under some conditions, the strength of gap junction coupling between OFF-cone bipolar cells and, potentially, directly between ON-cone bipolar cells is sufficiently strong to mediate measurable electrical coupling, this raises the question of a functional role. To our knowledge, the only bipolar cells for which electrical coupling has been unequivocally demonstrated are the Mb1 (ON) bipolar cells in goldfish retina (Arai et al. 2010). These cells are electrically coupled to each other at their distal dendrites. With dual recording of electrically coupled cell pairs, it was demonstrated that the electrical coupling acted as a low-pass filter that could transmit Ca^{2+} spikes, leading to a prolongation of postsynaptic currents in ganglion cells, and it was suggested that the electrical coupling might play a role in lateral interactions (Arai et al. 2010). Interestingly, it was also reported that the strength of coupling was larger under light-adapted conditions.

It has been suggested that although electrical coupling between OFF-cone bipolar cells would reduce spatial acuity, it could contribute to an improved signal-to-noise ratio (Mills 1999; Feigenspan et al. 2004). There does not seem to be experimental data to verify or refute this idea, but unless this mechanism could work at very low levels of coupling, it does not seem consistent with the results for OFF-cone bipolar cells obtained in our study.

Recently it has been shown that electrical synapses at the axons of ON-cone bipolar cells in mouse retina contribute to a lateral spread of visual signals that leads to increased sensitivity in retinal ganglion cells to spatiotemporally correlated inputs such as motion (Kuo et al. 2016). This lateral spread was postulated to be mediated via electrical synapses between AII amacrine cells and ON-cone bipolar cells, but additional contributions from direct coupling between ON-cone bipolar cells could not be ruled out (Kuo et al. 2016). A similar lateral spread could be mediated by gap junctions between OFF-cone bipolar cell axon terminals, but as discussed above, it is

unclear whether such lateral spread could be mediated by the very low levels of coupling consistent with our results.

In general, there is strong evidence that the open probability of different connexons is under modulatory control (for review, see O'Brien 2019), including connexons expressed in retinal neurons (for review, see Trenholm and Awatramani 2017; O'Brien and Bloomfield 2018). Currently, nothing is known concerning potential modulation of the strength of gap junction coupling between OFF-cone bipolar cells in the mammalian retina, but it is possible that the strength of coupling could be stronger under conditions not explored in our recordings. However, if the strength of coupling between OFF-cone bipolar cells (and, by analogy, between ON-cone bipolar cells) is permanently too weak to impart functionally relevant electrical coupling, the main purpose of the gap junction channels could be to enable chemical and/or metabolic coupling within local subcellular domains, or to play a structural role, e.g., as adhesion molecules (cf. Mills 1999; Pereda 2016).

Future Perspectives

It will be experimentally challenging to systematically investigate potential electrical coupling between cone bipolar cells by attempting to perform simultaneous dual patch-clamp recording from pairs of coupled cells. Without access to animals with fluorescently labeled cell types, the success rate of targeting two specific OFF-cone bipolar cells or two specific ON-cone bipolar cells is likely to be discouragingly low, given the number of different types of bipolar cells in mammalian retina, including rat (Euler and Wässle 1995; Hartveit 1997) and mouse (Ghosh et al. 2004; Helmstaedter et al. 2013; Euler et al. 2014) which are the experimentally most relevant species. In addition, the findings from our study suggest that the strength of coupling is likely to be very low. If the coupling strength is physiologically regulated, a favorable strategy might be to first identify the condition(s) under which the junctional conductance is upregulated.

Acknowledgements Open Access funding provided by University of Bergen. This project received funding from the European Union's Horizon 2020 research and innovation program under the Marie Skłodowska-Curie Grant Agreement No 674901. Additional financial support from The Research Council of Norway (NFR 182743, 189662, 214216 to EH; NFR 261914 to MLV) and the University of Bergen is gratefully acknowledged. We thank Áurea Castilho and Torhild Fjordheim Sunde for excellent technical assistance.

Author Contributions RF, EH and MLV performed electrophysiological recording. EH and MLV performed MPE imaging. RF, EH and MLV analyzed data. EH developed and contributed analytic tools. EH and MLV designed research, interpreted data and wrote the paper. All authors approved the final version of the paper.

Compliance with Ethical Standards

Conflict of interest The authors have nothing to disclose.

References

Alcamí P, Pereda AE (2019) Beyond plasticity: the dynamic impact of electrical synapses on neural circuits. Nat Rev Neurosci 20:253–271

Arai I, Tanaka M, Tachibana M (2010) Active roles of electrically coupled bipolar cell network in the adult retina. J Neurosci 30:9260–9270

Bloomfield SA, Dacheux RF (2001) Rod vision: pathways and processing in the mammalian retina. Prog Retin Eye Res 20:351–384

Castilho Á, Ambrósio AF, Hartveit E, Veruki ML (2015) Disruption of a neural microcircuit in the rod pathway of the mammalian retina by diabetes mellitus. J Neurosci 35:5422–5433

Chun MH, Han SH, Chung JW, Wässle H (1993) Electron microscopic analysis of the rod pathway of the rat retina. J Comp Neurol 332:421–432

Cohen E, Sterling P (1990) Demonstration of cell types among cone bipolar neurons of cat retina. Philos Trans R Soc Lond B Biol Sci 330:305–321

Cruikshank SJ, Hopperstad M, Younger M, Connors BW, Spray DC, Srinivas M (2004) Potent block of Cx36 and Cx50 gap junction channels by mefloquine. Proc Natl Acad Sci USA 101:12364–12369

Dedek K, Schultz K, Pieper M, Dirks P, Maxeiner S, Willecke K, Weiler R, Janssen-Bienhold U (2006) Localization of heterotypic gap junctions composed of connexin45 and connexin36 in the rod pathway of the mouse retina. Eur J Neurosci 24:1675–1686

DeVries SH, Qi X, Smith R, Makous W, Sterling P (2002) Electrical coupling between mammalian cones. Curr Biol 12:1900–1907

Elgueta C, Leroy F, Vielma AH, Schmachtenberg O, Palacios AG (2018) Electrical coupling between A17 cells enhances reciprocal inhibitory feedback to rod bipolar cells. Sci Rep 8:3123

Euler T, Wässle H (1995) Immunocytochemical identification of cone bipolar cells in the rat retina. J Comp Neurol 361:461–478

Euler T, Haverkamp S, Schubert T, Baden T (2014) Retinal bipolar cells: elementary building blocks of vision. Nat Rev Neurosci 8:507–519

Feigenspan A, Janssen-Bienhold U, Hormuzdi S, Monyer H, Degen J, Söhl G, Willecke K, Ammermüller J, Weiler R (2004) Expression of connexin36 in cone pedicles and OFF-cone bipolar cells of the mouse retina. J Neurosci 24:3325–3334

Ghosh K, Bujan S, Haverkamp S, Feigenspan A, Wässle H (2004) Types of bipolar cells in the mouse retina. J Comp Neurol 469:70–82

Grimes WN, Hoon M, Briggman KL, Wong RO, Rieke F (2014) Cross-synaptic synchrony and transmission of signal and noise across the mouse retina. eLife 3:e03892

Han Y, Massey SC (2005) Electrical synapses in retinal ON cone bipolar cells: subtype-specific expression of connexins. Proc Natl Acad Sci U S A 102:13313–13318

Hartveit E (1996) Membrane currents evoked by ionotropic glutamate receptor agonists in rod bipolar cells in the rat retinal slice preparation. J Neurophysiol 76:401–422

Hartveit E (1997) Functional organization of cone bipolar cells in the rat retina. J Neurophysiol 77:1716–1730

Hartveit E, Veruki ML (2010) Accurate measurement of junctional conductance between electrically coupled cells with dual whole-cell voltage-clamp under conditions of high series resistance. J Neurosci Methods 187:13–25

Helmstaedter M, Briggman KL, Turaga SC, Jain V, Seung HS, Denk W (2013) Connectomic reconstruction of the inner plexiform layer in the mouse retina. Nature 500:168–174

Hilgen G, von Maltzahn J, Willecke K, Weiler R, Dedek K (2011) Subcellular distribution of connexin45 in OFF bipolar cells of the mouse retina. J Comp Neurol 519:433–450

Jacoby RA, Marshak DW (2000) Synaptic connections of DB3 diffuse bipolar cell axons in macaque retina. J Comp Neurol 4161:9–29

Kántor O, Benkő Z, Énzsöly A, Dávid C, Naumann A, Nitschke R, Szabó A, Pálfi E, Orbán J, Nyitrai M, Németh J, Szél Á, Lukáts Á, Völgyi B (2016) Characterization of connexin36 gap junctions in the human outer retina. Brain Struct Funct 221:2963–2984

Kántor O, Varga A, Nitschke R, Naumann A, Énzsöly A, Lukáts Á, Szabó A, Németh J, Völgyi B (2017) Bipolar cell gap junctions serve major signaling pathways in the human retina. Brain Struct Funct 222:2603–2624

Kolb H (1979) The inner plexiform layer in the retina of the cat: electron microscopic observations. J Neurocytol 8:295–329

Kolb H, Famiglietti EV (1974) Rod and cone pathways in the inner plexiform layer of cat retina. Science 186:47–49

Kolb H, Nelson R (1996) Hyperpolarizing, small-field, amacrine cells in cone pathways of cat retina. J Comp Neurol 371:415–436

Kujiraoka T, Saito T (1986) Electrical coupling between bipolar cells in carp retina. Proc Natl Acad Sci USA 83:4063–4066

Kuo SP, Schwartz GW, Rieke F (2016) Nonlinear spatiotemporal integration by electrical and chemical synapses in the retina. Neuron 90:320–332

Lee YT, Wang Q (1999) Inhibition of hKv2.1, a major human neuronal voltage-gated K^+ channel, by meclofenamic acid. Eur J Pharmacol 378:349–356

Lee SC, Meyer A, Schubert T, Hüser L, Dedek K, Haverkamp S (2015) Morphology and connectivity of the small bistratified A8 amacrine cell in the mouse retina. J Comp Neurol 523:1529–1547

Li W, Zhang J, Massey SC (2002) Coupling pattern of S1 and S2 amacrine cells in the rabbit retina. Vis Neurosci 19:119–131

Li PH, Verweij J, Long JH, Schnapf JL (2012) Gap-junctional coupling of mammalian rod photoreceptors and its effect on visual detection. J Neurosci 32:3552–3562

Lin B, Jakobs TC, Masland RH (2005) Different functional types of bipolar cells use different gap-junctional proteins. J Neurosci 25:6696–6701

Manookin MB, Beaudoin DL, Ernst ZR, Flagel LJ, Demb JB (2008) Disinhibition combines with excitation to extend the operating range of the OFF visual pathway in daylight. J Neurosci 28:4136–4150

Marc RE, Liu WL, Muller JF (1988) Gap junctions in the inner plexiform layer of the goldfish retina. Vision Res 28:9–24

Massey SC, O'Brien JJ, Trexler EB, Li W, Keung JW, Mills SL, O'Brien J (2003) Multiple neuronal connexins in the mammalian retina. Cell Commun Adhes 10:425–430

Maxeiner S, Dedek K, Janssen-Bienhold U, Ammermüller J, Brune H, Kirsch T, Pieper M, Degen J, Krüger O, Willecke K, Weiler R (2005) Deletion of connexin45 in mouse retinal neurons disrupts the rod/cone signaling pathway between AII amacrine and ON cone bipolar cells and leads to impaired visual transmission. J Neurosci 25:566–576

McGuire BA, Stevens JK, Sterling P (1984) Microcircuitry of bipolar cells in cat retina. J Neurosci 4:2920–2938

Mills SL (1999) Unusual coupling patterns of a cone bipolar cell in the rabbit retina. Vis Neurosci 16:1029–1035

Münch TA, da Silveira RA, Siegert S, Viney TJ, Awatramani GB, Roska B (2009) Approach sensitivity in the retina processed by a multifunctional neural circuit. Nat Neurosci 12:1308–1316

O'Brien J (2019) Design principles of electrical synaptic plasticity. Neurosci Lett 695:4–11

O'Brien J, Bloomfield SA (2018) Plasticity of retinal gap junctions: roles in synaptic physiology and disease. Annu Rev Vis Sci 4:79–100

O'Brien JJ, Chen X, MacLeish PR, O'Brien J, Massey SC (2012) Photoreceptor coupling mediated by connexin36 in the primate retina. J Neurosci 32:4675–4687

Pan F, Mills SL, Massey SC (2007) Screening of gap junction antagonists on dye coupling in the rabbit retina. Vis Neurosci 24:609–618

Pereda AE (2016) The variable strength of electrical synapses. Neuron 90:912–914

Peretz A, Degani N, Nachman R, Uziyel Y, Gibor G, Shabat D, Attali B (2005) Meclofenamic acid and diclofenac, novel templates of KCNQ2/Q3 potassium channel openers, depress cortical neuron activity and exhibit anticonvulsant properties. Mol Pharmacol 67:1053–1066

Pologruto TA, Sabatini BL, Svoboda K (2003) ScanImage: flexible software for operating laser scanning microscopes. Biomed Eng Online 2:13

Raviola E, Gilula NB (1975) Intramembrane organization of specialized contacts in the outer plexiform layer of the retina. A freeze-fracture study in monkeys and rabbits. J Cell Biol 65:192–222

Strettoi E, Dacheux RF, Raviola E (1990) Synaptic connections of rod bipolar cells in the inner plexiform layer of the rabbit retina. J Comp Neurol 295:449–466

Strettoi E, Raviola E, Dacheux RF (1992) Synaptic connections of the narrow-field, bistratified rod amacrine cell (AII) in the rabbit retina. J Comp Neurol 325:152–168

Strettoi E, Dacheux RF, Raviola E (1994) Cone bipolar cells as interneurons in the rod pathway of the rabbit retina. J Comp Neurol 347:139–149

Szoboszlay M, Lörincz A, Lanore F, Vervaeke K, Silver RA, Nusser Z (2016) Functional properties of dendritic gap junctions in cerebellar Golgi cells. Neuron 90:1043–1056

Trenholm S, Awatramani GB (2017) Dynamic properties of electrically coupled retinal networks. In: Jing J (ed) Network functions and plasticity. Academic, New York, pp 183–208

Trexler EB, Li W, Massey SC (2005) Simultaneous contribution of two rod pathways to AII amacrine and cone bipolar cell light responses. J Neurophysiol 93:1476–1485

Tsukamoto Y, Omi N (2015) OFF bipolar cells in macaque retina: type specific connectivity in the outer and inner synaptic layers. Front Neuroanat 9:122

Tsukamoto Y, Omi N (2017) Classification of mouse retinal bipolar cells: type-specific connectivity with special reference to rod-driven AII amacrine pathways. Front Neuroanat 11:92

Umino O, Maehara M, Hidaka S, Kita S, Hashimoto Y (1994) The network properties of bipolar-bipolar cell coupling in the retina of teleost fishes. Vis Neurosci 11:533–548

Vaney DI (1991) Many diverse types of retinal neurons show tracer coupling when injected with biocytin or Neurobiotin. Neurosci Lett 125:187–190

Veruki ML, Hartveit E (2002a) AII (rod) amacrine cells form a network of electrically coupled interneurons in the mammalian retina. Neuron 33:935–946

Veruki ML, Hartveit E (2002b) Electrical synapses mediate signal transmission in the rod pathway of the mammalian retina. J Neurosci 22:10558–10566

Veruki ML, Hartveit E (2009) Meclofenamic acid blocks electrical synapses of retinal AII amacrine and ON-cone bipolar cells. J Neurophysiol 101:2339–2347

Veruki ML, Mørkve SH, Hartveit E (2006) Activation of a presynaptic glutamate transporter regulates synaptic transmission through electrical signaling. Nat Neurosci 9:1388–1396

Veruki ML, Oltedal L, Hartveit E (2010) Electrical coupling and passive membrane properties of AII amacrine cells. J Neurophysiol 103:1456–1466

Völgyi B, Kovács-Oller T, Atlasz T, Wilhelm M, Gábriel R (2013) Gap junctional coupling in the vertebrate retina: variations on one theme? Prog Retin Eye Res 34:1–18

Wu S-N, Jan C-R, Chiang H-T (2001) Fenamates stimulate BK_{Ca} channel activity in the human osteoblast-like MG-63 cells. J Investig Med 49:522–533

Yasuda R, Nimchinsky EA, Scheuss V, Pologruto TA, Oertner TG, Sabatini BL, Svoboda K (2004) Imaging calcium concentration dynamics in small neuronal compartments. Sci STKE 219:l5

Zandt B-J, Liu JH, Veruki ML, Hartveit E (2017) AII amacrine cells: quantitative reconstruction and morphometric analysis of electrophysiologically identified cells in live rat retinal slices imaged with multi-photon excitation microscopy. Brain Struct Funct 222:151–182

Zandt B-J, Veruki ML, Hartveit E (2018) Electrotonic signal processing in AII amacrine cells: compartmental models and passive membrane properties for a gap junction-coupled retinal neuron. Brain Struct Funct 223:3383–3410

Zhang A-J, Wu SM (2009) Receptive fields of retinal bipolar cells are mediated by heterogeneous synaptic circuitry. J Neurosci 29:789–797

Paper II

Digital reconstruction and quantitative morphometric analysis of bipolar cells in live rat retinal slices

Rémi Fournel, Margaret Lin Veruki and Espen Hartveit

University of Bergen, Department of Biomedicine, Bergen, Norway.

Corresponding author: Espen Hartveit, University of Bergen, Department of Biomedicine, Jonas Lies vei 91, N-5009 Bergen, Norway.

espen.hartveit@biomed.uib.no

Phone: +47-55586350

Fax: +47-55586360

Running title: Quantitative reconstruction of cone and rod bipolar cells

Number of figures: 12

Number of tables: 3

Key words: cone bipolar cells; retina; dendrites; morphology; morphometry; branching pattern

ABSTRACT

Bipolar cells convey signals from photoreceptors in the outer retina to amacrine and ganglion cells in the inner retina. In mammals, there are typically 10-15 types of cone bipolar cells and one type of rod bipolar cell. Different types of cone bipolar cells are thought to code and transmit different features of a complex visual stimulus, thereby generating parallel channels that uniquely filter and transform the photoreceptor outputs. Differential synaptic connectivity and expression of ligand- and voltage-gated ion channels are thought to be important mechanisms for processing and filtering visual signals. Whereas the biophysical basis for such mechanisms has been investigated more extensively in rat retina, there is a lack of morphological data necessary for advancing the structure-function correlation in this species, as recent connectomics investigations have focused on mouse retina. Here, we performed whole-cell recordings from cone and rod bipolar cells in rat retinal slices, filled the cells with fluorescent dyes and acquired image stacks by multi-photon excitation microscopy. Following deconvolution, we performed quantitative morphological reconstruction and morphometric analysis of 25 cone and 14 rod bipolar cells. Compared to previous descriptions, the extent and complexity of branching of the axon terminal was surprisingly high. By precisely quantifying the level of stratification of the axon terminals in the inner plexiform layer, we have generated a reference system for reliable classification of individual cells in future studies focused on correlating physiological and morphological properties. The implemented workflow can be extended to the development of morphologically realistic compartmental models for these neurons.

INTRODUCTION

A basic tenet of neurobiology is that structure is inextricably linked to function. This has inspired numerous attempts at characterization and classification of the complete morphology of neurons in different regions of the central nervous system. The ability to acquire and analyze complete neuronal morphologies has advanced with continuous technological developments since the time of Golgi (1873) and Cajal (1894), with progressive refinements and increased understanding of the anatomical details of different types of neurons.

Retinal bipolar cells are short-range projections neurons that link the outer and inner retina. Their dendrites contact and receive input from the terminals of photoreceptors and horizontal cells in the outer plexiform layer (OPL) and their axons descend through the inner nuclear and inner plexiform layers (INL, IPL), with their axon terminals stratifying at different levels of the IPL (reviewed by Euler et al. 2014). The stratification level of the axon terminals of different bipolar cells in the IPL determines their synaptic connectivity and is an important basis for the morphological classification of different types of bipolar cells (Cajal 1893, 1894). The fundamental distinction between rod and cone bipolar cells was clearly recognized by Cajal (1893, 1894), with the two types receiving input from rod and cone photoreceptors, respectively (Dowling and Boycott 1966). Whereas there is only a single type of rod bipolar cell, that transmits signals primarily to two types of amacrine cells in the IPL, there are 10 - 15 different types of cone bipolar cells that transmit signals to a large number of different types of amacrine and ganglion cells in the IPL. Different types of cone bipolar cells are thought to be responsible for generating and transmitting different visual responses, such that different cell types constitute specific and parallel channels that filter and transform the photoreceptor output in unique ways (reviewed by Euler et al. 2014).

Data for morphology and classification of bipolar cells have been obtained from several light microscopic techniques, including investigations using Golgi impregnation (Cajal 1893, 1894, 1911; Polyak 1941; Boycott and Dowling 1969;

Famiglietti 1981; Dacheux and Raviola 1986; Boycott and Wässle 1991; Linberg et al. 1996), injection of tracers like biocytin and Neurobiotin (Euler and Wässle 1995; Oltedal et al. 2009), and dye injection combined with wide-field fluorescence microscopy (Euler and Wässle 1995; Hartveit 1997; Ghosh et al. 2004; Ivanova and Müller 2006). The morphological analysis of bipolar cells injected with fluorescent dyes has been improved by the increased spatial resolution offered by confocal microscopy (Haverkamp et al. 2008; Light et al. 2012; Hellmer et al. 2016; Vielma and Schmachtenberg 2016). In parallel with light microscopic investigations, bipolar cell morphology and classification have been investigated at the ultrastructural level, using serial section reconstruction based on transmission electron microscopy (Sterling 1983; McGuire et al. 1984; Cohen and Sterlin 1990; Tsukamoto et al. 2001; Tsukamoto and Omi 2015, 2017) or, more recently, serial block face scanning electron microscopy (Helmstaedter et al. 2013; Greene et al. 2016).

The need for high spatial resolution is underscored by the recent discovery of new types of cone bipolar cells when complete reconstructions at the ultrastructural level were performed for relatively large volumes of the mouse retina (Helmstaedter et al. 2013). First, such investigations allowed a more precise determination of the level of axon terminal stratification in the IPL, suggesting that specific bipolar cell types in reality encompassed several types (Helmstaedter et al. 2013; Greene et al. 2016). Second, because such "deep connectomics" investigations are able to provide complete reconstruction of all neuronal arbors within a given volume, the classification of types can be aided by the observation of potential "tiling violations" among the axon terminals, suggesting that individual cells belong to different types that tile the retina independently of each other.

Although morphology correlates with and predicts some functional properties, it does not predict every functional property. This means that morphological characterization and classification must be combined with physiological investigations. Functional imaging studies have verified that different types of cone bipolar cells display different visual response properties (Franke et al. 2017), but the mechanisms

that are responsible for generating these differences are mostly unknown. In contrast, electrophysiological recording from single neurons is still unsurpassed with respect to resolution and specificity, but does not by itself provide the morphological information necessary to correlate structure and function. Whereas several studies have used wide-field or confocal fluorescence microscopy to characterize the morphology following whole-cell electrophysiological recording in slices, it is a challenge that the morphological classification tends to be qualitative and based on illustrations of "typical" cells (e.g. Ichinose et al. 2014). Therefore, it can often be difficult to classify any individual cell based on morphology and axon terminal stratification when it is similar to two (or more) types with overlapping levels of stratification in the IPL.

It is a disadvantage that the recent high-resolution structural maps lack information about important functional properties, e.g. passive membrane properties that determine the electrotonic characteristics of neurons. It is also difficult to see how such deep connectomics can be extended to a workflow incorporating compartmental modeling, where physiological measurements are made on the same cells used for morphological reconstruction. This raises the question whether the morphological classification can be made more precise by imaging cells with a combination of multi-photon excitation (MPE) and infrared laser scanning gradient contrast (IR-LSGC) microscopy. This provides images of both fluorescence and well-defined retinal landmarks (e.g. borders between retinal layers) and can be used for accurate, quantitative morphological reconstruction. Here, we present a characterization of the morphological properties of different types of rat retinal bipolar cells, with a focus on soma size, dendritic tree size and structure, and axon terminal branching and stratification. All imaging was performed by MPE microscopy during patch-clamp recording from visually targeted neurons in slices. The choice of rat retina was motivated by the more extensive knowledge of biophysical mechanisms and physiological properties of bipolar cells in this species compared to e.g. mouse. A major goal was to implement a workflow that can be extended to the development of morphologically realistic compartmental models for these neurons.

MATERIAL AND METHODS

Retinal slice preparation

General aspects of the methods have previously been described in detail (Zandt et al. 2017). The use of animals in this study was carried out under the approval of and in accordance with the Animal Laboratory Facility at the Faculty of Medicine at the University of Bergen (accredited by AAALAC International). Male and female albino rats (Wistar HanTac, bred in-house or purchased from Taconic Biosciences (Denmark); 4-7 weeks postnatal) had *ad libitum* access to food and water and were kept on a 12/12 light/dark cycle. Under normal room illumination, animals were deeply anaesthetized with isoflurane (IsoFlo vet 100%; Abbott Laboratories Ltd., Maidenhead, UK) in 100% O_2 and killed by cervical dislocation. After dissecting the retina, vertical retinal slices were cut by hand and visualized with MPE microscopy using a custom-modified "Movable Objective Microscope" (MOM; Sutter Instrument, Novato, CA, USA) with a ×20 water immersion objective (XLUMPLFL; NA = 0.95; Olympus) and infrared Dodt gradient contrast videomicroscopy (IR-DGC), using an IR-sensitive analog CCD camera (VX55; TILL Photonics, Gräfelfing, Germany). All recordings were carried out at room temperature (22 - 25 °C).

Solutions and drugs

The standard extracellular perfusing solution was continuously bubbled with 95% O_2 - 5% CO_2 and had the following composition (in mM): 125 NaCl, 25 $NaHCO_3$, 2.5 KCl, 2.5 $CaCl_2$, 1 $MgCl_2$, 10 glucose, pH 7.4. The recording pipettes were filled with an intracellular solution of the following composition (in mM): 125 K-gluconate, 5 KCl, 8 NaCl, 10 Hepes, 0.2 EGTA, 4 MgATP, 0.4 Na_3GTP (pH adjusted to 7.3 with KOH). The pipette solution also contained Alexa Fluor 594 hydrazide as sodium salt (40 or 60 μM; Invitrogen / Thermo Fisher Scientific; henceforth referred to as Alexa 594). For one cell, the pipette solution contained Lucifer yellow (1 mg/ml) instead of Alexa 594. The osmolality was ~290 mOsmol · kg^{-1} H_2O.

Whole-cell recording

Patch pipettes were pulled from thick-walled borosilicate glass (outer diameter, 1.5 mm; inner diameter, 0.86 mm). The open-tip resistance of the pipettes (R_{pip}) ranged from 7 to 10 MΩ when filled with intracellular solution. Whole-cell voltage-clamp recordings were performed with an EPC10-triple or an EPC10-USB-dual amplifier (Patchmaster; HEKA Elektronik, Lambrecht / Pfalz, Germany) controlled by Patchmaster software. To keep the background fluorescence in the area immediately surrounding the cell body to a minimum, only a small positive pressure (5 - 10 mbar) was applied to the pipette as it approached the cell. After making a GΩ-seal (≥ 2 GΩ), the whole-cell recording configuration was established by a combination of brief electrical pulses and negative pressure pulses.

Image acquisition for MPE microscopy and deconvolution

For MPE microscopy, fluorescence from neurons filled with Alexa 594 was imaged with the MOM equipped with a mode-locked Ti:sapphire laser (Mai Tai DeepSee; Spectra-Physics) tuned to 810 nm. For the cell filled with Lucifer yellow, the laser was tuned to 850 nm. Scanning was performed by galvanometric scanners (XY; Cambridge Technology), fluorescence was detected by multialkali photomultiplier tubes (R6357; Hamamatsu Corp.), and the analog signals were digitized by an acquisition board (PXIe-6356, National Instruments). The intensity of the laser was attenuated and controlled by an electro-optic modulator (350-80LA with BK option; ConOptics). During image acquisition, exposure to IR laser light was controlled by an electronic shutter (LS6ZM2; Vincent Associates), thereby minimizing the total exposure time. An image stack was acquired as a series of optical sections (1024 × 1024 pixels) with XY pixel size ~70 to ~80 nm (depending on the magnitude of the digital zoom factor) and collected at a focal plane interval (ΔZ) of 0.4 μm (for one cell the image stack was acquired at 512 × 512 pixels). For each image stack, we acquired two channels and at each focal plane two images were averaged on-line. The first channel sampled the

fluorescence light as described above. The second channel was used for IR-LSGC (Yasuda et al. 2004) and sampled the forward-scattered IR laser light after it passed the substage condenser and a Dodt gradient contrast tube (Luigs & Neumann, Ratingen, Germany). MPE microscopy and image acquisition were controlled by ScanImage software (versions 3.8.1 and 2018) running under Matlab (The Mathworks).

To ensure that the distal processes of bipolar cells were adequately filled with dye, acquisition of an image stack typically started 10 - 12 min after establishing the whole-cell recording configuration. The physiological condition of the cell was monitored by recording the holding current and input resistance throughout the acquisition period. A complete stack was generally acquired within 20 - 30 min. In some cases, additional stacks were sampled to take advantage of the enhanced fluorescence intensity obtained in the thin dendritic processes after a longer period of filling the cell with dye. Deconvolution of MPE image stacks for morphological reconstruction was performed with Huygens software (version 14, 64 bit; Scientific Volume Imaging), as described in Zandt et al. (2017). Following deconvolution, the image stacks were also processed with the "stabilization" tool in Huygens that corrected (aligned) any slices in the image stack to compensate for movement and drift (in the XY plane) during acquisition.

Three-dimensional (3D) digital reconstruction

Quantitative morphological reconstruction of the fluorescently labeled cells was done manually with Neurolucida 360 software (versions 2017-2020, 64 bit; MBF Bioscience, Williston, VT, USA), for a detailed description, see Zandt et al. (2017). The 3D reconstruction of the soma was based on manually tracing a single contour around the cell body, at the focal plane where it appeared the largest. As we only imaged live cells, there was no need to correct for errors related to shrinkage. Cells that displayed clear signs of mechanical injury or phototoxicity (visible as "beading" of processes) were not included in the material for reconstruction.

With an excitation wavelength of 810 nm and NA = 0.95 for the objective used,

the resolution limit becomes approximately 0.37 μm in the ideal (diffraction-limited) case. Processes that are thinner than this can be detected if the intensity is sufficiently high, but it is not possible to resolve their true diameter. Electron microscopy is currently the only reliable source of information when the diameters of the thinnest dendritic and axonal processes are below the light microscopic resolution limit. We therefore made measurements from the thinnest (yet clearly discernable) axonal and dendritic processes illustrated in the few published electron micrographs from rat retina. For dendritic processes, we found the minimum diameter to be 0.12 ± 0.02 μm (range 0.10 - 0.14, $n = 6$ processes, Koulen et al. 1997; Brandstätter et al. 2004; Cao et al. 2015). For processes in the axon terminal, we found the minimum diameter of intervaricosity segments to be 0.15 ± 0.01 μm (range 0.14 - 0.15, $n = 3$ processes, Chun et al. 1993; Sassoè-Pognetto et al. 1994; Chun et al. 1999). Accordingly, we have, when necessary, constrained the dendrites and axon terminal intervaricosity segments to a minimum diameter of 0.12 and 0.15 μm, respectively.

Even for reconstruction of the thicker axon shafts (see Results for explanations of anatomical terminology), a subjective element is involved when deciding the diameters of processes visualized by imaging cells filled with fluorescent dye (cf. Jaeger 2001). To guide our judgement, we made measurements from digital image stacks acquired with confocal microscopy of flatmount retinal tissue immunolabeled for protein kinase C (PKC) that is specific for rod bipolar cells (Greferath et al. 1990). The XY plane of the image stack corresponded to the surface of the retina such that in each slice, the axons of rod bipolar cells appeared in cross section as ring-shaped, membrane-associated fluorescent structures surrounding a non-fluorescent center. For three image stacks (acquired from separate quadrants; deconvolved with Huygens) we selected a single slice, located approximately midway between the cell bodies and the axon terminals, and measured transverse intensity profiles (Huygens) of randomly selected axons that were adequately labeled. Each intensity profile passed through the center of the profile and was oriented to follow the smallest diameter if the profile had an oval shape (corresponding to an oblique orientation of the axon relative to the plane

of the confocal slice). Each intensity profile was fitted with the sum of two Gaussian functions (MultiPeak Fit package in IGOR Pro; WaveMetrics, Lake Oswego, OR, USA) and the axon diameter was estimated as the distance between the locations of the two peaks. For a total of 90 axons (30 axons in each of three slices), the average diameter was 0.77 ± 0.11 (SD) μm (range 0.51 - 1.05 μm).

Although the measurements from the PKC-labeled retinas could be used as a guide for setting process diameters during reconstruction of rod bipolar cell axons, it cannot be assumed *a priori* that they can also be used as a guide for cone bipolar cell axons. To compare the thickness of axon shafts of rod and cone bipolar cells, we generated transverse intensity profiles along straight lines oriented perpendicularly to the local longitudinal axis of the axon (Huygens). For each axon, we generated five profiles at approximately equidistant locations between the cell body and the axon terminal, avoiding local extreme values (both maxima and minima) as well as the larger diameters of the most proximal and distal parts where the axon arises from the cell body and transitions to the axon terminal. All intensity profiles were generated from the deconvolved image stacks used for morphological reconstruction and for a given location the intensity profile was generated from the focal plane (slice) where the width was at its maximum. Each intensity profile was fit with a Gaussian function (IGOR Pro) and the width was taken as the full width at half-maximum (FWHM), calculated as $SD \times 2^{3/2} \times \sqrt{ln2}$, where SD is the standard deviation obtained from the Gaussian fit. Because the FWHM values of the axons of rod and cone bipolar cells in our material overlapped completely (Supplementary Fig. 1), we used the estimates of axon diameters obtained for immunolabeled rod bipolar cells to guide the reconstruction of both rod and cone bipolar cells.

Detection and reconstruction of axon terminal varicosities

Detection of varicosities was performed manually in Neurolucida 360. A varicosity was defined as a spatially discrete swelling where the maximum diameter increased ≥70% relative to the diameter immediately before and after the swelling, as visualized

in the XY plane. In addition, the swelling was classified as a varicosity only if the length of the swelling (as measured along the length of the process) was ≤4 times the diameter of the process before the swelling. We used the "marker" functionality of Neurolucida 360 to indicate the size and location (XYZ) of each varicosity. The size was determined as the diameter of the largest circle that would fit inside the varicosity in the XY plane. The location in Z was determined by the reconstruction point corresponding to the largest diameter of the varicosity. After detection, we used the 3D viewer of Neurolucida 360 to verify that no marker had been misplaced along the Z axis. Subsequently, all markers were "attached" to the corresponding (nearest) part of the axon terminal (using the appropriate functions in Neurolucida 360) to enable analysis in relation to the neuronal arborization.

Rotating image stacks and reconstructions in 3D

For illustration purposes, each reconstruction was rotated around the Z axis in the plane of the image slice (i.e., around the axis oriented orthogonally to the plane of the image slice) such that the axon was aligned vertically and the retinal layers above and below the reconstructed cell were aligned approximately horizontally. In this way, the X axis of the reconstruction was parallel to the retinal layers in the plane of the image slice and the Y axis of the reconstruction was perpendicular to the retinal layers in the plane of the image slice.

For analysis purposes, it was in several cases necessary to rotate the reconstruction and the associated image stack sampled in the IR-LSGC channel not only around the Z axis (as described above), but also around the X axis. When the cut surfaces of a slice are not oriented perfectly vertically through the retina, the plane of a bipolar cell axon terminal field (i.e., the plane parallel to the planes defining the retinal layers) becomes tilted relative to the XZ plane of the image stack (as defined during image acquisition). Accordingly, when the axon terminal is projected onto the XY plane, the height (along the Y axis) and area of projection (onto the XY plane) become artificially enlarged. The required correction was performed in three steps. In the first,

we determined the required rotation by reading the 3D coordinates of the reconstruction (generated in Neurolucida 360) into IGOR Pro and rotating the cell around the X and Z axes such that the plane of the axon terminal was aligned parallel to the XZ plane (as judged by eye during simultaneous projection of the reconstruction onto the XY and YZ planes). Often, but not always, this also oriented the axon vertically in both planes (XY, YZ). In the second step, the Neurolucida 360 reconstruction was rotated by the determined angles (around the X and Z axes), using a combination of Python code and functionality in Neurolucida 360. In the third step, the IR-LSGC image stack was rotated by the same angles (around the X and Z axes) using functions in Amira (version 2019, FEI SAS / Thermo Fisher Scientific) that aligned the 3D coordinates of the stack with those of the absolute reference system. This was followed by resampling of the transformed stack by interpolation (Lanczos), with preservation of the voxel size from the original stack. The rotated reconstruction and IR-LSGC image stack were then used to analyze the projection onto, and the distribution of the reconstructed processes across, the INL, the IPL, and the ganglion cell layer (GCL).

Quantitative morphological analysis

For general morphological analysis and quantification of dendritic and axonal branching metrics we used Neurolucida Explorer (versions 2017-2020, 64 bit; MBF Bioscience), L-measure (version 5.2; Scorcioni et al. 2008), and IGOR Pro. The single contour used to trace the cell body in the XY plane was used to calculate the perimeter and the Feret maximum and minimum (henceforth termed Feret max and Feret min) of the cell body. Dendritic length was calculated as the total length of all processes from the cell body that projected towards the OPL. A branch segment was defined as the part of a branch between two nodes (branch points) or between a node and a termination point (ending; Capowski 1989). Thus, the number of segments equals the sum of the number of nodes and the number of termination points. Axon shaft diameter was calculated as the average diameter of the length-weighted segments as

follows. First, diameter and length for each segment of the axon shaft were obtained from Neurolucida Explorer 360. Then, the diameter of each segment was multiplied by its associated length and the values obtained were summed for each axon shaft. The sum was divided by the total length of the axon shaft to obtain the average axon shaft diameter. The 2D convex hull (area) was measured separately for the dendritic tree in the OPL and for the axon terminal in the IPL. In both cases, the 2D convex hull was measured for the projection onto the XZ plane, i.e., the surface of the retina, after rotating the reconstruction (as described above). The rotation was identical for measuring the 2D convex hull of the axon terminal and for analyzing the stratification in the IPL. For approximately 50% of the cells, it was necessary to perform a separate rotation when calculating the 2D convex hull of the dendritic tree to ensure that distortions of the tissue did not introduce errors. For the axon terminals we also calculated the volume and surface area of the 3D convex hull (excluding the dendrites, cell body, and axon).

Sholl and branch order analysis of the axon terminal arbors

To perform Sholl analysis (Sholl 1953) of the bipolar cell arborizations, we considered that the interesting target for the analysis would be the axon terminal system, excluding the axon shaft itself. To achieve this, we positioned the center point of the Sholl spheres at the origin of the axon terminal system (i.e., the end of the axon shaft). To implement this in Neurolucida 360, we modified the digital reconstruction by detaching the axon terminal from the axon shaft, with the point of detachment set to the first branch point where the axon shaft divided into (at least) two daughter branches, if at least two of three criteria were fulfilled: 1) the daughter branches had similar diameters; 2) the daughter branches had different angles of projection than the parent axon shaft; 3) each of the daughter branches displayed at least three nodes. Finally, a small circular contour was positioned just distal to the point of detachment. This served as the center point of the Sholl spheres and ensured that the Sholl analysis was performed only for the branches of the axon terminal. The Sholl analysis was

performed in 3D by a set of nested, concentric spheres with a starting radius of 1 μm and an increment of 1 μm. For branch order analysis of cone bipolar cells, we used the "central shaft" branch ordering scheme (Neurolucida Explorer 360). The end of the central shaft corresponded to the point of detachment used for the Sholl analysis (see above).

Analysis of axon terminal stratification in the IPL

To calculate the axon terminal stratification profiles of the different types of cone bipolar cells, we applied a modified version of the procedures used by Helmstaedter et al. (2013) and Greene et al. (2016). The stratification profile was defined as the density of surface area versus depth in the IPL. The borders between the IPL and the INL, and between the IPL and the GCL, were defined as IPL relative depths 0 and 1, respectively. The IPL was divided into 100 equally sized bins, with borders parallel to the IPL - INL and IPL - GCL borders, and process surface area was assigned to each bin. To exclude the shafts (trunks) of the axonal arbors, the analysis restricted the domain of the stratification profile to the branches of the axon terminal (as defined above), with all other bin values set to zero. Each stratification profile was normalized like a probability density function, such that the profile area integrated to unity. Percentiles were defined for a stratification profile in the same way as for a probability density function such that the interval from the nth percentile depth to the 0th percentile depth contains n percent of the area of the stratification profile (cf. Greene et al. 2016). The thickness of a stratification profile was defined as the difference between the 85th and 15th percentile depths. The center location of the stratification profile was defined as the 50th percentile depth.

Statistical analysis and data presentation

Data are presented as mean ± SD (n = number of cells, processes or varicosities). Statistical analyses with comparisons between groups were performed with Prism (GraphPad software) using Student's two-tailed t test (unpaired). Differences were

considered statistically significant at the $P < 0.05$ level.

Fig. 1 near here

RESULTS

Visual targeting and identification of bipolar cells in retinal slices

In the INL, the cell bodies of bipolar cells are positioned roughly in the most distal two-thirds, with the cell bodies of amacrine cells positioned in the proximal third (Cajal 1893). Among the bipolar cells, there is a preference for the cell bodies of rod bipolar cells to be located in the most distal region and those of cone bipolar cells to be located in the midregion of the INL (Cajal 1893; Greferath et al. 1990). However, apart from using the location of a bipolar cell-like soma in the most distal part of the INL as a sufficient, but not necessary criterion for targeting rod bipolar cells, we found that soma depth (i.e., height in the INL) could not be used as a reliable criterion to target specific types of bipolar cells (cf. Cohen and Sterling 1990). After establishing the whole-cell recording configuration, and switching the optical pathway from IR-DGC videomicroscopy to MPE fluorescence microscopy, we were able to verify the morphology of the recorded cell as either a cone bipolar cell or a rod bipolar cell and to acquire a complete image stack (Fig. 1A-C; rightmost columns). The forward-scattered IR laser light enabled simultaneous acquisition of IR-LSGC images of the retinal slice (Fig. 1A-C; leftmost column). On-line overlaying of the fluorescence and IR-LSGC images (in perfect register with each other) allowed us to identify the location (width, thickness, and stratification level) of the axon terminal of the cell within the IPL (Fig. 2A). In total, 39 bipolar cells were selected for quantitative digital reconstruction and morphometric analysis.

Fig. 2 near here

Workflow for morphological reconstruction of bipolar cells

Following deconvolution and spatial alignment (to correct for drift and small movements), an accurate digital reconstruction was generated for each cell by

manually tracing the fluorescent processes through the image stack (see Materials and Methods). The workflow for such reconstruction is illustrated in Fig. 2, with maximum intensity projections of the fluorescence image stack, before (Fig. 2A) and after (Fig. 2B) deconvolution and alignment, overlaid on a single, representative slice of the IR-LSGC channel image stack. A corresponding overlay of the final digital reconstruction is illustrated in Fig. 2C. For enhanced visualization of finer details of the dendritic and axonal arbors, we used shape plots (two-dimensional (2D) projections; Fig. 2D) or 3D visualizations (Fig. 2E).

Fig. 3 near here

Qualitative morphological characteristics of bipolar cells

Despite morphological variability, bipolar cells display a set of common characteristics that together contribute to defining them as a major cell class in the retina (Fig. 3). First, bipolar cells generally have a medium size soma located in the distal two-thirds of the INL. Second, they have a dendritic tree (tuft) that arises from one or more processes at the distal pole of the soma and displays terminal branches ramifying in the OPL. Third, they have a single long axon that arises from the proximal pole of the soma and courses through the INL before it terminates at a specific level of the IPL and branches laterally into an elaborate axon terminal with beadlike swellings or varicosities (Fig. 3). The portion of the axon between the cell body and the axon terminal will be referred to as the axon shaft. The bipolar cell axon shaft is equivalent to "axis cylinder" or "vitreal fiber" and the terminal ramifications are equivalent to the "teledendrons", as defined and used by Polyak (1941). Many of the small branchlets in the axon terminal or teledendron assume a horizontal course.

The level at which the axon terminal stratification takes place in the IPL is an important defining characteristic and of fundamental importance for classifying the different types of cone bipolar cells (for rat, see Euler and Wässle 1995). Two examples of cone bipolar cells stratifying at different levels are illustrated in Fig. 3A, B. In contrast, the axon terminals of rod bipolar cells correspond to a smaller number of

considerably larger varicosities located in the proximal part of the IPL (Fig. 3C; Greferath et al. 1990; Euler and Wässle 1995).

Following Cajal (1893), the IPL of mammalian retinas is divided into five strata. In contrast to Cajal, however, who considered the strata to be of unequal thickness, it is customary to divide the IPL arbitrarily into five equally thick strata designated S1 - S5 (from the most distal to the most proximal part of the IPL; Fig. 3). Collectively, S1 and S2 are referred to as sublamina *a* and S3 - S5 are referred to as sublamina *b* (Fig. 3). Based on the morphology of their contacts with cone photoreceptors (invaginating versus flat), it was postulated that cone bipolar cells (in cat retina) with axon terminals stratifying in sublamina *a* and *b* correspond functionally to OFF- and ON-bipolar cells, respectively (Famiglietti and Kolb 1976; Kolb 1979). Several years later, it was demonstrated that rat cone bipolar cells with axon terminals ending in sublamina *a* or *b* display responses to ionotropic non-NMDA-type glutamate receptors consistent with OFF- and ON-type visual response polarities, respectively (Hartveit 1997; see also Euler et al. 1996). For the examples of cone bipolar cells illustrated in Fig. 3, one has an axon terminal that stratifies in S1 and S2, corresponding to the pattern associated with OFF-cone bipolar cells (Fig. 3A). The cell illustrated in Fig. 3B has an axon terminal that stratifies in the proximal part of S3 and the distal part of S4, corresponding to the pattern associated with ON-cone bipolar cells. For the initial classification of cone bipolar cells in our material, we used the morphological criteria based on the level of stratification first developed by Euler and Wässle (1995; see also Hartveit 1997). Based on these criteria, the cell in Fig. 3A corresponds to a cone bipolar cell type 2 and the cell in Fig. 3B corresponds to a cone bipolar cell type 6. The rod bipolar cell illustrated in Fig. 3C has a distinctive appearance compared to the cone bipolar cells, with relatively short dendritic processes, and an axon with only minor side branches (in S3 and S5) before dividing into a limited number of shorter branches that end in large, varicose terminals (in S5).

Fig. 4 near here

The shape plots (corresponding to projections in the XY plane) of all 39 bipolar

cells reconstructed in this study are displayed in Fig. 4, after appropriate rotation around the Z and X axes (see Materials and Methods). Of these cells, 25 were classified as cone bipolar cells and 14 were classified as rod bipolar cells. Of the cone bipolar cells, 10 were classified as OFF-cone bipolar cells and 15 were classified as ON-cone bipolar cells. According to the scheme proposed for cone bipolar cells in rat retina (Euler and Wässle 1995; see also Hartveit 1997), our material included type 2 (CBC2; $n = 2$), type 3 (CBC3; $n = 6$), type 4 (CBC4; $n = 2$), type 5 (CBC5; $n = 6$), type 6 (CBC6; $n = 6$), type 7 (CBC7; $n = 2$), and type 8 (CBC8; $n = 1$) cone bipolar cells. Of these, types 2, 3, and 4 are considered to be OFF-cone bipolar cells, whereas types 5, 6, 7, and 8 are considered to be ON-cone bipolar cells (Hartveit 1997; see also Ivanova and Müller 2006). Unfortunately, our material did not include cone bipolar cells corresponding to type 1 and type 9, most likely because these cells are relatively rare (Euler and Wässle 1995; Hartveit 1997; Ivanova and Müller 2006).

Figure 5 near here

Whereas the individual shape plots for the reconstructed bipolar cells (Figs. 3, 4) provide some qualitative insight into the complexity of the branching patterns of both the dendrites and the axon terminals, the high density of and considerable overlap among the processes as visualized in 2D shape plots make it difficult to appreciate the extent of branching and the number of individual processes. To more readily observe and inspect the branching patterns, especially of the axon terminals, we generated dendrograms for all the reconstructed cells. These display the relative path lengths, branch segments, and nodes in 2D, but without any overlap. As an example of the considerable complexity of branching that can be observed for these cells, we have illustrated examples of dendrograms for both an OFF-cone (Fig. 5A, B) and an ON-cone bipolar cell (Fig. 5C, D), and for comparison also for a rod bipolar cell (Fig. 5E, F). Dendrograms for all the other reconstructed cells are illustrated in Supplementary Fig. 2.

Tables 1, 2 and 3 near nere

Quantitative morphological characteristics of bipolar cells

The conventional, qualitative description of the morphological properties of bipolar cells is fully adequate to distinguish between rod and cone bipolar cells and to distinguish between types of cone bipolar cells where the axon terminals display markedly different stratification levels, e.g., at opposite ends of the IPL. However, for some types of cone bipolar cells it can be challenging to reliably assign individual cells to one or the other type with similar or overlapping axon terminal stratification. For example, it can be difficult to correctly classify a specific cell as a cone bipolar cell type 5 or 6, or as a type 3 or 4. Two developments have contributed to make this challenge even more difficult. First, physiological and immunocytochemical investigations have suggested that some morphologically defined types of cone bipolar cells in reality encompass more than one type. The redefined cell types may for example have almost identical morphological properties (i.e., level of stratification in the IPL), but may be distinguished by a difference in physiological properties, e.g. expression of specific types of ion channels (Ivanova and Müller 2006; Fyk-Kolodziej and Pourcho 2007; Cui and Pan 2008; Vielma and Schmachtenberg 2016). In some cases, the purported morphological differences are subtle and have not been subjected to a rigorous morphological analysis based on high-resolution imaging (e.g. Ivanova and Müller 2006). Second, separation of cell types based on minor differences in the level of stratification in the IPL has resulted from ultrastructural connectomics data from the mouse retina where complete reconstructions of all cells within a tissue volume enabled combined analysis of stratification and tiling properties. Specifically, observation of tiling violations enabled re-classification of cone bipolar cells as different types, despite very similar stratification (Helmstaedter et al. 2013; Greene et al. 2016). Importantly, such decisions depended on the subjective judgement of human observers.

Because of the paucity of quantitative morphological data at the light microscopic level that can potentially contribute to our ability to classify bipolar cells,

in particular for physiological investigations with intracellular recording, we used our reconstructions to obtain data for neuronal arborization, including branching pattern, process lengths and diameters, surface area, and number and distribution of axon terminal varicosities. The results of our analysis of a series of geometric and topological parameters of neuronal morphology are summarized in Tables 1, 2, and 3 for OFF-cone bipolar cells, ON-cone bipolar cells, and rod bipolar cells, respectively.

As can be seen in Tables 1-3, there was considerable overlap between the different types of OFF- and ON-cone bipolar cells for almost all morphological parameters analyzed. Despite the considerable variability both between and within specific types of cone bipolar cells, it seems that the arborizations of their axon terminals follow the same, or at least very similar, underlying geometric rules. Rod bipolar cells display qualitatively different morphology from the majority of cone bipolar cells and this is reflected in several morphological parameters. On average, they also have larger cell bodies than cone bipolar cells, but with considerable overlap.

Fig. 6 near here

Dendritic and axon terminal fields

We analyzed the dendritic and axonal fields of all the reconstructed bipolar cells after projecting the reconstruction points of the dendritic and axonal arbors onto the XZ plane (equivalent to the retinal surface) and estimated the 2D convex hulls for both fields. Prior to generating the XZ projections, each cone bipolar cell was first rotated around the X and Z axes to ensure that the plane of the axon terminal and/or the dendritic tree was oriented approximately horizontal, i.e., parallel to the XZ plane (see Materials and Methods). For rod bipolar cells, similar rotations were done, but with the goal of orienting the distal axon and the axon terminals approximately vertical in both the XY and YZ planes. After generating the 2D convex hulls for both the dendritic and the axonal arborizations, we calculated the area, perimeter, Feret max, Feret min, aspect ratio (Feret max / Feret min), and the ratio between the areas of dendritic and axonal fields (Tables 1 - 3). Projections of the reconstruction points (appearing as

reconstruction skeletons) together with the 2D convex hulls for both the dendritic and axon terminal fields are shown for all reconstructed cells in Fig. 6.

Fig. 7 near here

For most cone bipolar cells (both OFF and ON), the area of the dendritic field was consistently smaller than that of the axon terminal field (Fig. 7A). The smallest ratio between dendritic and axon terminal area was observed for CBC2 (0.15 ± 0.06, n = 2) and the largest ratio was seen for CBC7 (0.68 ± 0.45, n = 2) and CBC8 (0.98, n = 1; see Tables 1, 2 for complete data). No type of cone bipolar cell displayed a larger area for the dendritic field than for the axon terminal field (Figs. 6A-G, 7A). In contrast, for rod bipolar cells the area of the dendritic field was consistently larger than the area of the axon terminal field, with an average ratio of 3.0 ± 1.5 (range 1.4 - 7.0; Figs. 6H, 7A, B). The dendritic field area was approximately 100 - 400 μm^2 for both rod and cone bipolar cells, but the axon terminal field area was several-fold larger for cone than rod bipolar cells (Fig. 6, Fig. 7A, B).

For the cone bipolar cells, there was a weak positive correlation between the area of the dendritic field and the area of the axonal field (Fig. 7A). We also examined the scaling of the axonal and dendritic fields by plotting the axonal and dendritic process lengths versus the corresponding areas (Fig. 7C, D). For the axonal fields, there was an almost linear relationship between these two parameters (Fig. 7C), indicating that larger axon terminal field sizes are not simply generated by a different structural organization of a more or less constant total length of axonal processes. For the dendritic fields, a similar relationship was observed, but with larger scatter (Fig. 7D).

To examine whether larger axon terminal and dendritic fields of cone bipolar cells primarily correspond to a simple scaling or rather to an increase in branching density and/or complexity, we plotted the number of axon terminal (or dendritic) segments (equal to the sum of the number of nodes and the number of endings) as a function of the axon terminal (or dendritic) field area (Fig. 7E, F). For the axon terminal fields, there was an almost linear relationship, suggesting that larger field sizes correspond to an increase in the branching complexity and not a simple scaling (Fig.

7E). The relationship between the number of dendritic segments and field size was similar, but less pronounced, with considerable variability of the number of segments for a given dendritic field area (Fig. 7F).

For rod bipolar cells, both dendritic and axonal fields were considerably smaller than for cone bipolar cells (Fig. 7A), with larger dendritic than axon fields (Fig. 7B). Overall, the rod bipolar cells adhered to the same relationships as the cone bipolar cells for axon terminal fields (Fig. 7C, E). However, for the dendritic fields rod bipolar cells displayed longer process lengths and a larger number of segments for a given dendritic field size (Fig. 7D, F).

Fig. 8 near here

Axon terminal parameters as a function of branch order

From the shape plots (Fig. 4) it is readily apparent that the axon terminals of our cone bipolar cells display a much larger extent and complexity of branching compared to earlier illustrations based on Golgi impregnation or cells filled (or labeled) with fluorescent dyes (e.g. Euler and Wässle 1995; Hartveit 1997; Ghosh et al. 2004; Ivanova and Müller 2006; Keeley and Reese 2010; Hellmer et al. 2016; Vielma and Schmachtenberg 2016). We are not aware of previous studies that have attempted to quantify and compare the extent and complexity of branching, e.g. by calculating the maximum branch order and the average length of processes for each branch order. There are two generally used branch ordering schemes that can be applied to analyze axon terminal parameters as a function of branch order. In the centrifugal branch ordering scheme, each branch point leads to an increase in branch order of the daughter segments, whereas in the central shaft branch ordering scheme, the branch order of a main process (in this case, the axon shaft; Fig. 3) remains constant at 1 along its length. Any smaller segments that branch off the main process are each assigned a branch order of 2. A bipolar cell axon shaft is essentially unbranched, despite the presence in some cells of short side branches ("twigs") as the axon shaft passes between its origin at the soma and its end at the beginning of the axon terminal in the IPL (Figs.

3, 4). Accordingly, applying the central shaft branch ordering is a natural choice for the analysis of cone bipolar cell axon terminals (Fig. 8). Among these cells, the highest branch order was 21 - 23, except for CBC6 and CBC8 where it was 29 and 9, respectively (Fig. 8A). The number of segments peaked between branch order 8 and 12 (Fig. 8B). Importantly, for all types of cone bipolar cells, process length (Fig. 8C), process surface area (Fig. 8D), process volume (Fig. 8E), number of nodes (Fig. 8F), and number of endings (Fig. 8G) were moderately skewed towards lower branch orders, with few or no consistent differences between different types.

Fig. 9 near here

Distribution of axon terminals across the IPL

Because the classification of cone bipolar cells into different types relies heavily on the stratification level of their axon terminals, we performed a detailed analysis of the distribution of process length, number of varicosities, process surface area, number of endings, and number of nodes as a function of location across the height of the IPL. For each cell, the distal and proximal borders of the IPL was determined by eye on a representative slice of the IR-LSGC image stack acquired in parallel with the fluorescence image stack. If necessary, the neuronal reconstruction and the IR-LSGC stack were rotated such that the plane of the axon terminal was horizontal (and the long axis of the axon typically vertical; see Materials and Methods). For the quantitative analysis, the depth of the IPL was defined by assigning the borders to the INL and the GCL as relative depths 0 and 1, respectively (Fig. 9). The thickness of the IPL was then divided into 100 equally thick strata (corresponding to bins in a histogram) that were projected onto the digital reconstructions and used to estimate the distributions. The axon shaft itself was excluded from analysis. Whereas the average stratification properties differed markedly between the different types of cone bipolar cells, the differences seemed relatively insensitive with respect to specific morphological properties (Fig. 9A - E).

To facilitate quantitative comparisons between the different types of cone

bipolar cells, we calculated probability density functions for the distribution of surface area of the axon terminal processes, with normalization of the cumulative stratification profiles such that the profile density between 0 and 1 normalized to unity (Helmstaedter et al. 2013; Greene et al. 2016). We then calculated specific percentiles for the stratification profiles (see Materials and Methods) and defined the vertical thickness of each stratification profile as the difference between the 85th and 15th percentile depths. The probability density functions for process surface area of the different types of cone bipolar cells are displayed in Fig. 9F and the values for thickness (relative to the depth of the IPL) are displayed in Fig. 9G. The probability density functions in Fig. 9F clearly demonstrate the difference between and variability within the different types of cone bipolar cells, both with respect to location across the depth of the IPL and with respect to the thickness of the distribution. From Fig. 9F, it can be seen for CBC5 that three cells display a tendency towards a bi-stratified distribution, apparent as a segment with reduced slope between 0.6 and 0.8 relative density (located at 50 - 60% relative IPL depth). If this reflects the potential division of cells classified as CBC5 into two (or more) different types, it may be of importance that these three cells stratify deeper into the IPL than the other three CBC5 cells in our material. The thickness profiles (85th - 15th percentiles) illustrated in Fig. 9G strongly suggest that despite overlap between the different types, quantitative morphological reconstruction based on MPE microscopy can provide adequate data for robust classification of individual cells.

Fig. 10 near here

Quantitative analysis of axon terminal varicosities

Varicosities appear as discrete swellings along the axon terminal branches and are a characteristic feature of all cone bipolar cells. They are thought to represent the major location of synaptic inputs and outputs, with inputs from amacrine cells and outputs to amacrine cells and ganglion cells, respectively (Boycott and Dowling 1969; Kolb 1979; McGuire et al. 1984; Cohen and Sterling 1990; Strettoi et al. 1994). From the

stratification analysis in Fig. 9B, it can be seen that the distribution profiles of the average density of axon terminal varicosities for the different types of cone bipolar cells are fairly similar to the other branching properties analyzed. This suggests that, to the extent that varicosities are indeed the predominant sites of synaptic inputs and outputs, the distribution of both branch length and surface area closely reflect the region over which a bipolar cell can interact directly with its pre- and postsynaptic partners.

In addition to the distribution across the IPL, we also analyzed the size of the axon terminal varicosities, measured as the diameter of the largest sphere that could be fitted within the largest projection of a given varicosity onto the XY plane. Figure 10 illustrates the distribution of varicosity diameters as a function of IPL depth for the different types of cone bipolar cells. The large majority of varicosities had a diameter between ~0.25 and ~1.25 μm, with essentially no difference between different cells within a given type (Fig. 10A - G) or between different cone bipolar cell types (Fig. 10H). Following from these observations, there was also no marked difference between varicosities located at different IPL depths (Fig. 10A - H).

Fig. 11 near here

Sholl analysis of the axon terminal

In addition to examining the morphological properties of bipolar cell axon terminals as a function of the stratification level in the IPL, we also analyzed a number of morphological properties as a function of local eccentricity, i.e., relative to the center of the axon terminal. For this we used Sholl analysis, with the concentric Sholl spheres centered at the transition point between the end of axon shaft and the start of the axon terminal (Fig. 11A; see Materials and Methods). This differs from conventional Sholl analysis where the spheres are centered at the cell body.

For the total population of reconstructed cone bipolar cells, the average radius of the outermost sphere was 26.4 $\pm$ 6.3 μm (range 17 - 41 μm), with no difference between ON- and OFF-cone bipolar cells (ON: 24.9 $\pm$ 6.4 μm, range 17 - 41 μm, n = 15;

OFF: 28.7 ± 5.9 μm, range 21 - 41 μm; n = 10; P = 0.1475, unpaired t test). For rod bipolar cells, the average radius of the outermost sphere was lower: 16.5 ± 3.4 μm (range 12 - 25 μm, n = 14). For cone bipolar cells, the relative occurrence of Sholl sphere intersections (crossings) dropped below 1 in the range between 20 and 30 μm (Fig. 11B). The number of intersections peaked at a Sholl radius of 10 - 20 μm, with only minor differenes between the different types of cone bipolar cells (Fig. 11C). When process length, surface area, volume, number of nodes, and number of endings were analyzed in the same way, there was considerable overlap between the different types of cells (Fig. 11D - H). For CBC2 - CBC7, the average process diameter as a function of Sholl radius appeared essentially indistinguishable, with a tendency towards a gradual reduction with increasing Sholl radius (Fig. 11I). For CBC8, we observed a different profile with overall larger average diameters, but we only had data for one cell (Fig. 11I). The distribution of the number of varicosities as a function of Sholl radius also appeared very similar between the different types of cone bipolars, with a maximum between 10 and 20 μm (Fig. 11J).

Fig. 12 near here

Relationship between arbor volume and branch density

In a study that investigated multiple types of neurons, Teeter and Stevens (2011) reported a general structural design (scaling) principle of neural arbors. They observed that an increase in territory size was accompanied by a systematic decrease in arbor density. To analyze this for dendrites and axon terminals of bipolar cells, we calculated the average branch density as the total branch length divided by the territory volume, with the latter defined by the volume of the corresponding 3D convex hull (calculated separately for the dendrites and axon terminal of each cell). For both the dendrites (Fig. 12A) and the axon terminals (Fig. 12B), there was an inverse relationship between the convex hull volume and the branch density. When we analyzed the relationship in logarithmic space and fitted the relationship with a straight line, the slope was -0.44 for the dendritic branches (Fig. 12A) and -0.33 for the axon terminal branches (Fig. 12B). In

both cases, this corresponds to an exponent in linear space (cf. Teeter and Stevens 2011). These results suggest that bipolar cells adhere to the general design principle where branching density decreases as arbor territory increases. Compared to the relationship reported by Teeter and Stevens (2011), however, the bipolar cells consistently displayed a higher branch density for a given convex hull volume (Fig. 12). This was observed for both dendritic and axon terminal arbors.

Comparing morphology of rod bipolar cells visualized by MPE fluorescence microscopy or biocytin histology

Instead of obtaining the cellular morphology by MPE microscopy after filling cells with fluorescent dyes during whole-cell recording, cells can be filled with tracers like biocytin and Neurobiotin. After the recording, the tissue must be processed to visualize the tracer by fluorescence or development of an insoluble reaction product. In an earlier study from our laboratory, we filled rod bipolar cells (n = 10) in rat retinal slices with biocytin and reconstructed the morphology after histochemical detection (Oltedal et al. 2009). In the following, we will present a comparison of morphological properties analyzed for the two populations of cells in Oltedal et al. (2009; "earlier cells") and the current study.

The total surface area was very similar for the two populations (525 ± 61 μm^2 for the earlier cells vs. 601 ± 120 μm^2 for the current cells. For the earlier cells, however, the average surface area of the cell bodies was larger and the average surface area of the dendritic processes was smaller than for the current cells. We think there are two reasons for these differences. First, in the Oltedal et al. (2009) study, cells in the outermost part of the INL were specifically targeted to maximize the likelihood of obtaining rod bipolar cells. In the current study, we typically targeted cells in the middle of the INL, with the intention of obtaining different types of cone bipolar cells. In addition to cone bipolar cells, however, we also obtained a number of rod bipolar cells with cell bodies located more proximally (vitread) in the INL. Several of these cells have a dendritic expansion closer to the OPL, almost appearing as a "satellite"

soma-like structure from which the final dendritic tree sprouts (Fig. 4C). For the morphometric analysis, these structures were included as part of the dendritic tree. The selection bias introduced by targeting cells in the middle of the INL increased the proportion of such rod bipolar cells compared to Oltedal et al. (2009), resulting in a larger average dendritic surface area for the rod bipolar cells.

Second, in the current study the reconstructions of rod bipolar cells contain a larger number of dendritic endings and larger total dendritic length than in the earlier study. For comparison, Oltedal et al. (2009) reported 9.6 ± 3.7 dendritic endings and a total dendritic length of 46 ± 18 μm, whereas in the current study we found 39 ± 12 endings and a total dendritic length of 175 ± 59 μm. When we compared the axon terminal processes, we found a smaller number of endings in the earlier (2.4 ± 0.8) than in the current (9.1 ± 3.5) reconstructions. Taken together, this is similar to a previous comparison between reconstructions performed in our laboratory using MPE microscopy or tracer histochemistry for AII amacrine cells (Zandt et al. 2017). In both cases, it seems that the processing involved in biocytin histology increases the risk of missing a number of thin processes during the subsequent reconstruction.

DISCUSSION

In this study, we have used MPE microscopy to acquire image stacks of bipolar cells after filling them with fluorescent dye during whole-cell recording of visually targeted cells in rat retinal slices. After image deconvolution, we digitally and quantitatively reconstructed complete morphologies of the bipolar cells and performed detailed morphometric analysis to investigate which morphological properties can best be used for characterization and classification in experiments with combined structural and functional analysis. In the following, we will discuss the most important results and how they can be useful for future investigations of the relation between structure and function of retinal bipolar cells, including the development of compartmental models to study the functional importance of passive and active membrane properties of these cells for the signal processing that takes place during vision.

Quantitative morphological analysis of bipolar cells

Although the morphology of bipolar cells has been studied extensively in a number of different mammalian retinas, there has been a surprising lack of quantitative information about morphological parameters, including the pattern and extent of branching of the axon terminals in the IPL. The "classical" studies were based on Golgi impregnation (Cajal 1893, 1894, 1911; Polyak 1941; Boycott and Dowling 1969; Famiglietti 1981; Boycott and Wässle 1991; Linberg et al. 1996; MacNeil et al. 2004) in a number of species (cat, dog, rabbit, ox, ground squirrel, primate, and human). However, more recent studies have investigated rodent retinas (rat and mouse) because of the ease with which morphological characterization can be combined with physiological recording and because the mouse has become the source of a rich variety of genetically manipulated lines.

Compared to illustrations of bipolar cells based on Golgi impregnation and wide-field fluorescence microscopy, the axon terminal branching observed for our reconstructed cells seems considerably more extensive. Older studies have often used simple hand drawings where the main focus most likely was to capture essential aspects of the morphology, without representing all details in a faithful manner. To our knowledge, no studies have performed quantitative morphological reconstructions of dye-filled bipolar cells after imaging with confocal microscopy. Whereas older studies with morphological reconstructions based on ultrastructural imaging with transmission electron microscopy probably suffered from a fair number of lost sections (e.g. McGuire et al. 1984; Cohen and Sterling 1990), newer studies with deep connectomics, in particular the near-complete representations based on the serial block face scanning EM (SBFSEM) technique applied to mouse bipolar cells (Helmstaedter et al. 2013; Behrens et al. 2016; Greene et al. 2016), seem to have generated axon terminal morphologies very similar to those obtained in our study. For extensive and detailed comparisons, it is a challenge that although the SBFSEM reconstructions are complete for the imaged volume of retinal tissue, most cells have been reconstructed only by

their (center line) skeletons (Helmstaedter et al. 2013) as opposed to complete volumetric segmentation. Volumetric segmentation and reconstruction of EM material is also very important to constrain the diameters of the thinnest processes when they are below the limit of resolution of light microscopy, as is the case for many retinal neurons. In the current study, we used such data to guide the reconstruction of thin dendritic branches and the intervaricosity segments of axon terminal branches.

Our morphological reconstructions of several cone bipolar cells allowed comparison of the size of the dendritic field in the OPL and the axon terminal field in the IPL. From a detailed study of the tiling of the retinal surface by different types of cone bipolar cells in mouse retina, Wässle et al. (2009) concluded that the coverage factors for the axonal and dendritic fields for cell types considered to be homogeneous were close to 1, i.e., with little overlap and no "missed" regions between cells. In a recent study of mouse bipolar cells, Behrens et al. (2016) reported that for most cone bipolar types the coverage factors for dendritic and axonal fields were moderately larger than 1, and generally larger for the axonal than for the dendritic fields. Unfortunately, however, the authors did not provide information about the areas of the dendritic and axon terminal fields for individual bipolar cells. In our study, we typically found that the area of the axon terminal fields (measured as the area of the 2D convex hull in the plane of the retina) was consistently larger than the area of the dendritic field. For most cells, the difference was moderate and we suspect that for the small number of cells where the dendritic field was much smaller than the axonal field, the dendrites may have been damaged during slice preparation. To understand the extent of this variability, it is necessary to obtain data for a larger number of cells in multiple regions across the intact retina.

Classification of bipolar cells

Whereas the distinction between rod and cone bipolar cells, as well as the existence of different types of cone bipolar cells, were clearly recognized by Cajal (1893, 1894, 1911), it was Polyak (1941) who initiated a systematic classification of the different types of

cone bipolar cells, as studied in the primate retina. For rat retina, the initial characterization and classification of different types of cone bipolar cells (CBC1 - CBC9) was based on wide-field fluorescence microscopy of cells in retinal slices injected with fluorescent dyes using sharp microelectrodes (Euler and Wässle 1995). Subsequent investigations both confirmed (Hartveit 1997) and extended the classification by proposing the existence of additional cell types (Ivanova and Müller 2006; Cui and Pan 2008). Ivanova and Müller (2006) suggested that type CBC6 should be split into two different types (CBC6a and CBC6b) with different morphological (CBC6a with narrowly stratifying and CBC6b with broadly stratifying axon terminals, respectively) and physiological properties (differential expression of HCN channels). Subsequent investigations of rat retina have suggested potential re-definitions of several types of cone bipolar cells. First, that CBC5 should be split into two different types (CBC5a and CBC5b), based on differences in expression of HCN channels and voltage-gated Na^{+} and Ca^{2+} channels (Fyk-Kolodziej and Pourcho 2007; Cui and Pan 2008). More recently, Vielma and Schmachtenberg (2016) suggested that CBC3 should be split into two types (CBC3a and CBC3b) and that, potentially, the same should be done for CBC2 (CBC2 and CBC2'). For both CBC3 and CBC2, the re-classification was primarily based on differences in physiological response properties. Despite the strong evidence provided by these studies for variability in expression patterns (studied by immunolabeling) and physiological response properties (studied by whole-cell recording), it is less clear that the observed differences correspond to clear morphological differences and that they constitute a strong basis on which to propose the existence of different cell types that independently tile the retina. We did not record relevant physiological responses or immunolabel for relevant ion channel proteins. Thus, our study cannot contribute to clarifying the relation between morphology and expression of specific types of ion channels.

The suggestions for redefining the classification of cone bipolar cells in rat retina have been paralleled by corresponding investigations in mouse retina, but with an overall stronger justification. First, in their initial classification study, Ghosh et al.

(2004) noted considerable variability in the axonal ramification pattern of CBC5. In a subsequent study from the same laboratory, Wässle et al. (2009) proposed a split of CBC5 into two separate types. In their ultrastructural connectomics study, Helmstaedter et al. (2013) split CBC3 into two separate types (termed CBC3a and CBC3b) and split CBC5 into two (potentially three) different types. In addition, they described a new type whch they termed "XBC" or CBC-X. Shortly after, Greene et al. (2016) distinguished between CBC5i, CBC5o and CBC5t, with subtle differences in the stratification pattern of the axon terminals in the IPL. These types were verified and recognized by Tsukamoto and Omi (2017) who proposed an alternative nomenclature (CBC5i = CBC5a, CBC5o = CBC5b, CBC5t = CBC5c) and renamed CBC-X to CBC5d. The classification of a population of cells within a retinal tissue volume was strongly improved by the complete reconstructions which permit tiling violations to be observed, thereby guiding the classification of cells with subtle differences in the stratification patterns. Although the powerful ultrastructural connectomics remains unsurpassed with respect to complete classification of cells within a given tissue volume, progress has been slow regarding the parallel investigation of physiological response properties, in particular the characterization of physiological response properties that can provide mechanistic insight into the basis for differences in visual response properties. Unfortunately, the technical difficulty of the required investigations is compounded by the fact that although mouse and rat cone bipolar cells follow the same overall naming conventions (CBC1 - CBC9), the different types in one species may not have consistent corresponding partners in the other species. Even for types with morphological similarity between species, it cannot be taken for granted that their physiological properties and expression patterns of relevant ion channels are identical.

In our study, we searched extensively for morphological characteristics and parameters that could serve as "markers", with quantitative differences between types sufficient to contribute to classification of individual cells in future investigations. Perhaps unsurprisingly, the only consistent and (relatively) robust morphological

difference is the level and thickness of the stratification of the axon terminals in the IPL. We believe, however, that the increased resolution offered by MPE microscopy of cells filled with fluorescent dye, combined with quantitative morphological reconstruction and correlated MPE microscopy and IR-LSGC imaging, will facilitate future experimental investigations that combine electrophysiological recording and imaging.

In mouse retina, the strongest basis for increasing the number of bipolar cell types (including splitting pre-existing types) has come from methodological advances exemplified by high-resolution ultrastructural imaging (SBFSEM; Helmstaedter et al. 2013; Greene et al. 2016) and from large-scale genetic profiling (Shekhar et al. 2016), with good internal consistency between the different studies. Shekhar et al. (2016) identified a number of genes that differed in their expression between the different types of bipolar cells, but the potential relation and contribution to differences in physiological properties is still not resolved. However, to understand how the different visual response properties of bipolar cells are generated, we will need more detailed correlative studies that examine passive and active membrane properties of specific cell types.

Correlating structure and function of bipolar cells

Although connectivity is fundamental, it is not everything (cf. Seung and Sümbül, 2014) and in addition to the structural information, we need information about passive and active membrane properties, including the identity, localization and functional properties of ion channels and synaptic receptors. It is a considerable challenge, however, to correlate the structure and function of cone bipolar cells. First, even with the advent of a variety of distinct mouse lines with genetically labeled cell types, it is currently not possible to perform physiological experiments based on visual targeting of all the different types of cone bipolar cells with distinct fluorescent labels. If experiments are performed on wild-type mice without genetically labeled cell types, it is currently unknown if all the different types of cone bipolar cells suggested to be

present in mouse retina can be identified based on morphological properties, e.g. stratification in the IPL. Importantly, it is not a prerequisite that a cell's identity must be determined during the experiment itself. It is sufficient if the morphological data can be acquired during the experiment, potentially in parallel with physiological measurements, but the imaging technique must be compatible with the procedures for physiological recording. It will be interesting to see if complete ultrastructural reconstruction can be applied routinely in combination with whole-cell recording in physiological experiments. Currently, it seems unlikely that deep connectomics can replace light microscopic imaging anytime soon.

The rat retina as an experimental system for investigating bipolar cells

As discussed above, the potential availability of mouse lines with genetically labeled cell types makes this species a very useful model system for studies of the mammalian retina. Nevertheless, this needs to be weighted against other potential advantages or disadvantages of alternative model systems. At this time, the rat retina has some advantages as a model system for investigating cone bipolar cells. First, compared to mouse, voltage-gated ion channels have been more extensively characterized in rat cone bipolar cells, e.g., I_{Na} (Ivanova and Müller 2006; Cui and Pan 2008), I_K (Ma et al. 2003, 2005), I_{Ca} (Pan 2000; Hu et al. 2009), and I_h (Ivanova and Müller 2006; Cui and Pan 2008; Vielma and Schmachtenberg 2016).

Morphological reconstruction for compartmental modeling

It was an explicit goal of the present study to establish a workflow for MPE microscopy of bipolar cells filled with fluorescent dye during whole-cell recording that can be extended to encompass compartmental modeling. For high-quality models, it is imperative that the morphological reconstructions are generated from the same neurons from which electrophysiological data are obtained (Major 2001; Holmes 2010; Carnevale and Hines 2006). The published reconstructions generated from deep connectomics data (Helmstaedter et al. 2013; Greene et al. 2016) do not have

accompanying physiological data and should not be used for high-quality compartmental modeling.

Our laboratory has previously used MPE microscopy of cells filled with fluorescent dye during whole-cell recording to study the morphology of AII amacrine cells (Zandt et al. 2017, 2018). For typical microscope hardware, confocal microscopy can provide higher spatial resolution than MPE microscopy, but involves high phototoxicity and is better suited for imaging of fixed tissue slices after the physiological recording. This additional step adds the risk of losing or destroying valuable material, however, and it is often difficult to maintain an optimal orientation of the retinal slice for imaging. A well-established advantage of performing MPE imaging during the physiological experiment, compared to filling cells with tracer and processing slices after fixation (either by coupling the tracer with fluorescent dyes or by developing a visible reaction product), is that it completely avoids the shrinkage accompanying tissue fixation. To varying extents, such shrinkage always occurs during fixation and histological processing and can compromise the accuracy of cell reconstructions (Jaeger 2001; Groh and Krieger 2011). For small neurons like retinal bipolar cells it is straightforward to acquire the complete morphology at sufficiently high resolution for Nyquist sampling in a single image stack.

REFERENCES

Behrens C, Schubert T, Haverkamp S, Euler T, Berens P (2016). Connectivity map of bipolar cells and photoreceptors in the mouse retina. *Elife* 5. pii: e20041.

Boycott BB, Dowling JE (1969). Organization of the primate retina: light microscopy. *Philos Trans R Soc Lond B Biol Sci* 255, 109-194.

Boycott BB, Wässle H (1991) Morphological classification of bipolar cells of the primate retina. *Eur J Neurosci* 3, 1069-1088.

Brandstätter JH, Dick O, Boeckers TM (2004). The postsynaptic scaffold proteins ProSAP1/Shank2 and Homer1 are associated with glutamate receptor complexes at rat retinal synapses. *J Comp Neurol* 475, 551–563.

Cajal SRy (1893). La rétine des vertébrés. *La Cellule* 9, 119-257. English translation in *The Structure of the Retina* (1972), compiled and translated by SA Thorpe and M Glickstein. Charles C Thomas, Springfield, IL, USA.

Cajal SRy (1894). *Les Nouvelles Idées sur la Structure du Système Nerveux chez l'Homme et chez les Vertébrés*. Reinwald & C^{ie}, Paris, France.

Cajal SRy (1911). *Histologie du Système Nerveux de l'Homme et des Vertébrés*, Vol. II. Maloine, Paris, France. English translation in *Histology of the Nervous System of Man and Vertebrates,* Vol. II (1995), translated by N Swanson and LW Swanson. Oxford University Press, New York, NY, USA.

Camerino MJ, Engerbretson IJ, Fife PA, Reynolds NB, Berria MH, Doyle JR, Clemons MR, Gencarella MD, Borghuis BG, Fuerst PG (2021). OFF bipolar cell density varies by subtype, eccentricity, and along the dorsal ventral axis in the mouse retina. *J Comp Neurol* 529, 1911-1925.

Cao Y, Sarria I, Fehlhaber KE, Kamasawa N, Orlandi C, James KN, Hazen JL, Gardner MR, Farzan M, Lee A, Baker S, Baldwin K, Sampath AP, Martemyanov KA (2015). Mechanism for selective synaptic wiring of rod photoreceptors into the retinal circuitry and its role in vision. *Neuron* 87, 1248–1260.

Capowski JJ (1989). *Computer Techniques in Neuroanatomy*. New York and London: Plenum Press.

Carnevale NT, Hines ML (2006). *The NEURON Book*. Cambridge University Press, Cambridge.

Chun M-H, Han S-H, Chung J-W, Wässle H (1993). Electron microscopic analysis of the rod pathway of the rat retina. *J Comp Neurol* 332, 421-432.

Chun M-H, Oh S-J, Kim I-B, Kim K-Y (1999). Light and electron microscopical analysis of nitric oxide synthase-like immunoreactive neurons in the rat retina. *Vis Neurosci* 16, 379–389.

Cohen E, Sterling P (1990). Demonstration of cell types among cone bipolar neurons of cat retina. *Philos Trans R Soc Lond B Biol Sci* 330, 305-321.

Cui J, Pan Z-H (2008). Two types of cone bipolar cells express voltage-gated Na^+ channels in the rat retina. *Visual Neurosci* 25, 635-645.

Dacheux RF, Raviola E (1986). The rod pathway in the rabit retina: a depolarizing bipolar and amacrine cell. *J Neurosci* 6, 331-345.

Dowling JE, Boycott BB (1966). Organization of the primate retina: electron microscopy. *Proc R Soc Lond B Biol Sci* 166, 80-111.

Euler T, Wässle H (1995). Immunocytochemical identification of cone bipolar cells in the rat retina. *J Comp Neurol* 361, 461-478.

Euler T, Schneider H, Wässle H (1996). Glutamate responses of bipolar cells in a slice preparation of the rat retina. *J Neurosci* 16, 2934-2944.

Euler T, Haverkamp S, Schubert T, Baden T (2014). Retinal bipolar cells: elementary building blocks of vision. *Nat Neurosci Rev* 15, 507-519.

Famiglietti EV (1981). Functional architecture of cone bipolar cells in mammalian retina. *Vision Res* 21, 1559-1563.

Famiglietti EV, Kolb H (1976). Structural basis for ON-and OFF-center responses in retinal ganglion cells. *Science* 194, 193-195.

Franke K, Berens P, Schubert T, Bethge M, Euler T, Baden T (2017). Inhibition decorrelates visual feature representations in the inner retina. *Nature* 542, 439-444.

Fyk-Kolodziej B, Pourcho RG (2007). Differential distribution of hyperpolarization-activated and cyclic nucleotide-gated channels in cone bipolar cells of the rat retina. *J*

Comp Neurol 501, 891-903.

Ghosh K, Bujan S, Haverkamp S, Feigenspan A, Wässle H (2004). Types of bipolar cells in the mouse retina. *J Comp Neurol* 469, 70-82.

Golgi C (1873). Sulla struttura della sostanza grigia del cervello (Communicazione preventiva). Gazzetta Medica Italiana 33:244-246. Reprinted as: Sulla sostanza grigia del cervello, Opera Omnia, 1903, Vol. 1, Istologia Normale, pp. 91-98. Ulrico Hoepli, Milan.

Greene MJ, Kim JS, Seung HS, EyeWirers (2016). Analogous convergence of sustained and transient inputs in parallel on and off pathways for retinal motion computation. *Cell Rep* 14, 1892-1900.

Greferath U, Grünert U, Wässle H (1990). Rod bipolar cells in the mammalian retina show protein kinase C-like immunoreactivity. *J Comp Neurol* 301, 433-442.

Groh A, Krieger P (2011). Structure-function analysis of genetically defined neuronal populations. In: Helmchen F, Konnerth A. Series ed. Yuste R. *Imaging in Neuroscience*. Cold Spring Harbor: Cold Spring Harbor Laboratory Press. p 377-386.

Hartveit E (1997). Functional organization of cone bipolar cells in the rat retina. *J Neurophysiol* 77, 1716-1730.

Haverkamp S, Specht D, Majumdar S, Zaidi NF, Brandstätter JH, Wasco W, Wässle H, Tom Dieck S (2008). Type 4 OFF cone bipolar cells of the mouse retina express calsenilin and contact cones as well as rods. *J Comp Neurol* 507, 1087–1101.

Hellmer CB, Zhou Y, Fyk-Kolodziej B, Hu Z, Ichinose T (2016). Morphological and physiological analysis of type-5 and other bipolar cells in the mouse retina. *Neuroscience* 315, 246–258.

Helmstaedter M, Briggman KL, Turaga SC, Jain V, Seung HS, Denk W (2013). Connectomic reconstruction of the inner plexiform layer in the mouse retina. *Nature* 500, 168-174.

Holmes WR (2010). Passive cable modeling. In: De Schutter E (ed) *Computational Modeling Methods for Neuroscientists*. MIT Press, Cambridge, MA, pp 233–258.

Hu C, Bi A, Pan Z-H (2009). Differential expression of three T-type calcium channels in

retinal bipolar cells in rats. *Vis Neurosci* 26, 177-187.

Ichinose T, Fyk-Kolodziej B, Cohn J (2014). Roles of ON cone bipolar cell subtypes in temporal coding in the mouse retina. *J Neurosci* 34, 8761-8771.

Ivanova E, Müller F (2006). Retinal bipolar cell types differ in their inventory of ion channels. *Vis Neurosci* 23, 143-154.

Jaeger, D (2001). Accurate reconstruction of neuronal morphology. In: De Schutter E, editor. *Computational Neuroscience. Realistic Modeling for Experimentalists*. Boca Raton: CRC Press. pp 159-178.

Keeley PW, Reese BE (2010). Role of afferents in the differentiation of bipolar cells in the mouse retina. *J Neurosci* 30, 1677-1685.

Kolb H (1979). The inner plexiform layer in the retina of the cat: electron microscopic observations. *J Neurocytol* 8, 295-329.

Koulen P, Kuhn R, Wässle H, Brandstätter JH (1997). Group I metabotropic glutamate receptors mGluR1alpha and mGluR5a: localization in both synaptic layers of the rat retina. *J Neurosci* 17, 2200–2211.

Light AC, Zhu Y, Shi J, Saszik S, Lindstrom S, Davidson L, Li X, Chiodo VA, Hauswirth WW, Li W, DeVries SH (2012). Organizational motifs for ground squirrel cone bipolar cells. *J Comp Neurol* 520, 2864-2887.

Linberg KA, Suemune S, Fisher SK (1996). Retinal neurons of the California ground squirrel, *Spermopilus beecheyi*: A Golgi study. *J Comp Neurol* 365, 173—216.

Ma Y-P, Cui J, Hu H-J, Pan Z-H (2003). Mammalian retinal bipolar cells express inwardly rectifying K^+ currents (I_{Kir}) with a different distribution than that of I_h. *J Neurophysiol* 90, 3479-3489.

Ma Y-P, Cui J, Pan Z-H (2005). Heterogeneous expression of voltage-dependent Na^+ and K^+ channels in mammalian retinal bipolar cells. *Vis Neurosci* 22, 119-133.

MacNeil MA, Heussy JK, Dacheux RF, Raviola E, Masland RH (2004). The population of bipolar cells in the rabbit retina. *J Comp Neurol* 472, 73–86.

Major G (2001). Passive cable modeling - a practical introduction. In *Computational Neuroscience. Realistic Modeling for Experimentalists*, ed. De Schutter E, pp. 209-232. CRC

Press, Boca Raton.

McGuire BA, Stevens JK and Sterling P (1984). Microcircuitry of bipolar cells in cat retina. *J Neurosci* 4, 2920-2938.

Oltedal L, Veruki ML, Hartveit E (2009). Passive membrane properties and electrotonic signal processing in retinal rod bipolar cells. *J Physiol* 587, 829-849.

Pan Z-H (2000). Differential expression of high- and two types of low-voltage-activated calcium currents in rod and cone bipolar cells of the rat retina. *J Neurophysiol* 83, 513-527.

Polyak SL (1941). *The Retina*. Chicago: Chicago University Press

Sassoè-Pognetto M, Wässle H, Grunert U (1994). Glycinergic synapses in the rod pathway of the rat retina: cone bipolar cells express the alpha 1 subunit of the glycine receptor, *J Neurosci* 14, 5131–5146.

Scorcioni R, Polavaram S, Ascoli GA (2008). L-measure: a web-accessible tool for the analysis, comparison and search of digital reconstructions of neuronal morphologies. *Nat Prot* 3, 866-876.

Seung HS, Sümbül U (2014). Neuronal cell types and connectivity: lessons from the retina. *Neuron* 83, 1262-1272.

Shekhar K, Lapan SW, Whitney IE, Tran NM, Macosko EZ, Kowalczyk M, Adiconis X, Levin JZ, Nemesh J, Goldman M, McCarroll SA, Cepko CL, Regev A, Sanes JR (2016). Comprehensive classification of retinal bipolar neurons by single-cell transcriptomics. *Cell* 166, 1308-1323.

Sholl DA (1953). Dendritic organization in the neurons of the visual and motor cortices of the cat. *J Anat* 87, 387-406.

Sterling P (1983). Microcircuitry of the cat retina. *Annu Rev Neurosci* 6, 149-185.

Strettoi E, Dacheux RF, Raviola E (1994). Cone bipolar cells as interneurons in the rod pathway of the rabbit retina. *J Comp Neurol* 347, 139-149.

Teeter CM, Stevens CF (2011). A general principle of neural arbor branch density. *Curr Biol* 21, 2105-2108.

Tsukamoto Y, Morigiwa K, Ueda M, Sterling P (2001). Microcircuits for night vision in

mouse retina. *J Neurosci* 21, 8616-8623.

Tsukamoto Y, Omi N (2015). OFF bipolar cells in macaque retina: type specific connectivity in the outer and inner synaptic layers. *Front Neuroanat* 9, 122.

Tsukamoto Y, Omi N (2017). Classification of mouse retinal bipolar cells: type-specific connectivity with special reference to rod-driven AII amacrine pathways. *Front Neuroanat* 11, 92.

Vielma AH, Schmachtenberg O (2016). Electrophysiological fingerprints of OFF bipolar cells in rat retina. *Sci Rep* 6, 30259, doi: 10.1038/srep30259.

Wässle H, Puller C, Müller F, Haverkamp S (2009). Cone contacts, mosaics, and territories of bipolar cells in the mouse retina. *J Neurosci* 29, 106-117.

Yasuda R, Nimchinsky EA, Scheuss V, Pologruto TA, Oertner TG, Sabatini BL, Svoboda K (2004). Imaging calcium concentration dynamics in small neuronal compartments. *Sci STKE* pl5.

Young HM, Vaney DI (1991). Rod-signal interneurons in the rabbit retina: 1. Rod bipolar cells. *J Comp Neurol* 310, 139-153.

Yu WQ, El-Danaf RN, Okawa H, Pacholec JM, Matti U, Schwarz K, Odermatt B, Dunn FA, Lagnado L, Schmitz F, Huberman AD, Wong ROL (2018). Synaptic convergence patterns onto retinal ganglion cells are preserved despite topographic variation in pre- and postsynaptic territories. *Cell Rep* 25, 2017-2026.

Zandt B-J, Liu JH, Veruki ML, Hartveit E (2017). AII amacrine cells: quantitative reconstruction and morphometric analysis of electrophysiologically identified cells in live rat retinal slices imaged with multi-photon excitation microscopy. *Brain Struct Funct* 222, 151-182.

Zandt B-J, Veruki ML, Hartveit E (2018). Electrotonic signal processing in AII amacrine cells: compartmental models and passive membrane properties for a gap junction-coupled retinal neuron. *Brain Struct Funct* 223, 3383-3410.

AUTHOR CONTRIBUTIONS

RF performed morphological reconstruction and morphometric analysis. RF and EH developed software for morphological analysis. MLV and EH performed electrophysiological recording and multiphoton excitation microscopy. MLV and EH conceived and designed experiments, supervised the project and interpreted data. MLV and EH wrote the manuscript. RF and MLV made the figures. All authors commented on and approved the final version of the manuscript.

ACKNOWLEDGMENTS

This work was supported by funding from the European Union's Horizon 2020 research and innovation program under the Marie Skłodowska-Curie grant agreement No 674901 (*switchBoard*). Additional financial support from The Research Council of Norway (NFR 182743, 189662, 214216 to E.H.; NFR 26194 to MLV) is gratefully acknowledged. We thank Torhild Fjordheim Sunde and Áurea Castilho for excellent technical assistance.

FIGURE LEGENDS

Figure 1. Visual targeting and multi-photon excitation (MPE) microscopy with live imaging of dye-filled bipolar cells in retinal slices. *A*, Left panel: Image of retinal slice acquired with infrared (IR) laser scanning gradient contrast (IR-LSGC) microscopy. The tip of the recording pipette is located at cell body of an OFF-cone bipolar cell. Here, and in *B* and *C*, the retinal layers are indicated by abbreviations (OPL, outer plexiform layer; INL, inner nuclear layer; IPL, inner plexiform layer; GCL, ganglion cell layer). Two middle panels: Individual image slices acquired with MPE microscopy after filling the OFF-cone bipolar cell with the fluorescent dye Alexa Fluor 594. Here and in *B* and *C*, each image slice is the average of two individual frames. Here and later, the brightly fluorescent recording pipette can be seen on the left side of the cell body. Right panel: Maximum intensity projection (MIP) of complete image stack of the OFF-cone bipolar cell (155 image slices, separated by 0.4 μm). Scale bar, 10 μm. *B*, Left panel: IR-LSGC image of retinal slice with pipette tip at cell body of an ON-cone bipolar cell. Two middle panels: Individual MPE microscopy slices after filling ON-cone bipolar cell with Alexa Fluor 594. Right panel: MIP of complete image stack of ON-cone bipolar cell (162 image slices, separated by 0.4 μm). Scale bar, 10 μm. *C*, Left panel: Left panel: IR-LSGC image of retinal slice with pipette tip at cell body of an rod bipolar cell. Two middle panels: Individual MPE microscopy slices after filling rod bipolar cell with Alexa Fluor 594. Right panel: MIP of complete image stack of rod bipolar cell (72 image slices, separated by 0.4 μm). Scale bar, 10 μm.

Figure 2. Workflow for MPE microscopic imaging and quantitative morphological reconstruction of bipolar cells. *A*, MIP of raw image stack of an ON-cone bipolar cell filled with Alexa Fluor 594 during whole-cell recording (dye-filled pipette attached to the cell body) overlaid on image of retinal slice acquired with IR-LSGC microscopy. Scale bar, 10 μm (*A* - *C*). *B*, Same as in *A*, but after deconvolution. *C*, Shape plot generated by digital morphological reconstruction of cell in *A* and *B*. Brightness and contrast of background image of retina had to be re-adjusted for composite images in *A*

- *C*. *D*, Shape plot of reconstructed cell showing details of dendritic and axonal arborizations. Scale bar, 10 μm. *E*, Three-dimensional (3D) view of morphological reconstruction.

Figure 3. Shape plots of morphologically reconstructed cone and rod bipolar cells and nomenclature used to describe dendritic and axonal branching and branch ordering. *A*, Type 2 OFF-cone bipolar cell (CBC2). Cellular morphology with shape of and relationships between cell body, dendrites, axon shaft and axon terminal. "Branch segment" illustrates definition of segment between two points of arborization. Axon shaft refers to length of axon from origin at the cell body to the beginning of the axon terminal. Notice varicosities in the axon terminal. The borders between retinal layers and strata are indicated at right. The retinal layers are indicated by abbreviations (OPL, outer plexiform layer; INL, inner nuclear layer; IPL, inner plexiform layer; GCL, ganglion cell layer) and the IPL has been divided into five equally thick strata (stratum 1 (S1) - S5), with S1 - S2 corresponding to sublamina *a* and S3 - S5 corresponding to sublamina *b*. Scale bar, 10 μm (*A* - *C*). *B*, Type 6 ON-cone bipolar cell (CBC6), details as in *A*. *C*, Rod bipolar cell (RBC), details as in *A*.

Figure 4. Shape plots of all morphologically reconstructed cone and rod bipolar cells (n = 39). Cells were filled with Alexa Fluor 594 by whole-cell recording in retinal slices, imaged with MPE microscopy and morphologically reconstructed. Notice common morphological properties as well as considerable heterogeneity between cell types, *A*, OFF-cone bipolar cells (CBC2 - CBC4). *B*, ON-cone bipolar cells (CBC5 - CBC8). *C*, Rod bipolar cells (RBC). Some cells have been rotated in the XY plane to orient the long axis vertically. Scale bars, 10 μm.

Figure 5. Correlated shape plots (*A, C, E*) and dendrograms (*B, D, F*) for morphologically reconstructed cone and rod bipolar cells. *A, B,* Type 3 OFF-cone bipolar cell (CBC3). Here and in *D, F*, dendrograms are illustrated independently for

the dendritic (d) and axonal (a) trees emanating from the cell body. The length of each horizontal line in the dendrograms corresponds to the path length of the corresponding branch segment. *C*, *D*, Type 5 ON-cone bipolar cell (CBC5). *E*, *F*, Rod bipolar cell (RBC). Scale bar, 10 μm (*A* - *F*).

Figure 6. Dendritic and axon terminal fields of all morphologically reconstructed cone and rod bipolar cells. *A* - *C*, OFF-cone bipolar cells (CBC2 - CBC4). *D* - *G*, ON-cone bipolar cells (CBC5 - CBC8). *H*, Rod bipolar cells (RBC). For each field (dendritic, axon terminal), each dot corresponds to a reconstruction point and all reconstruction points were projected onto the XZ plane. When required, a reconstruction was first rotated around the X and Z axes such that the plane of the dendritic tree and/or axon terminal was aligned parallel to the XZ plane (the plane of the retinal surface), maximizing the area of projection in this plane and minimizing the thickness when projected onto the XY and YZ planes. The two-dimensional (2D) convex hull for each dendritic and axon terminal field is indicated by the broken and continuous lines, respectively. Scale bars, 20 μm (*A* - *C*); 20 μm (*D* - *G*); 10 μm (H).

Figure 7. Morphological properties of cone and rod bipolar cells as a function of dendritic and axon terminal field areas (measured from the 2D convex hull). *A*, Dendritic field area versus axon terminal field area. Here and in *B* - *F*, each data point corresponds to an individual cell (color-coded as indicated in inset above panels). The dashed line corresponds to the identity line, i.e., identical area of dendritic field and axon terminal field. *B*, As in *A*, but with expanded range of axes to only include data points for rod bipolar cells. Notice that for all rod bipolar cells, the axon terminal field area is smaller than the dendritic field area. *C*, Length of the axon terminal processes versus axon terminal field area. *D*, Length of the dendritic processes versus dendritic field area. *E*, Number of branch segments in the axon terminal versus axon terminal field area. *F*, Number of branch segments in the dendritic tree versus dendritic field area.

Figure 8. Axon parameters as a function of segment branch order for the central shaft branch ordering scheme for cone bipolar cells. *A*, Relative occurrence of axon terminal segments of a given branch order for the different types of cone bipolar cells (CBC2 - CBC8). Here and in *B* - *G*, the color code is indicated in the inset below panels. All cone bipolar cells contained segments with branch order up to and including 9 and the highest branch order observed for any cell was 29. *B* - *G*, Different axon parameters versus branch order for the same cone bipolar cells as in *A*. Data are plotted as lines between data points, with each data point corresponding to the average value for each cell type.

Figure 9. Axon terminal parameters as a function of location in the inner plexiform layer (IPL) for the different types of cone bipolar cells (CBC2 - CBC8; color code in inset below panels). Here and later, location is indicated as relative depth, with the IPL divided into 100 equally sized bins, with 0% corresponding to the border between the IPL and the inner nuclear layer (INL) and 100% corresponding to the border between the IPL and the ganglion cell layer (GCL). For each cell, only the processes defined as belonging to the axon terminal were included in the analysis. *A*, Length of processes as a function of relative depth. Here and in *B* - *E*, data are plotted as mean (continuous line in saturated color) ± SD (shaded region in desatured color). *B*, Number of varicosities (relative). *C*, Surface area of processes (relative). *D*, Number of ending points (relative). *E*, Number of nodes (relative). Any contribution of processes located in either the INL or GCL was ignored. *F*, Distribution of surface area of axon terminal processes in the IPL, represented as the cumulative probability density distribution versus relative depth of the IPL. Each continuous line corresponds to an individual cone bipolar cell. To exclude the shafts of the axonal arbors, the analysis restricted the domain of the stratification profile to the branches defined as belonging to the axon terminal, with all other bin values set to zero. Each stratification profile was normalized like a probability density function, such that the profile area integrated to

unity. *G*, Thickness of axon terminal stratification profiles (in the XY plane) for the different types of cone bipolar cells. Thickness was defined as the difference between the 85th and 15th percentile depths, with percentiles defined for a given stratification profile (probability density function as in *F*) such that the interval from the *n*th percentile depth to the 0th percentile depth contains *n* percent of the area of the stratification profile. For each cell type, the upper and lower margins of the colored box represent the average 15th and 85th percentile depths, respectively, with the black vertical lines representing the SD value. The black square inside each box represents the average of the center location of the stratification profile, corresponding to the 50th percentile depth.

Figure 10. Size and distribution of axon terminal varicosities in the inner plexiform layer for the different types of cone bipolar cells. *A* - *G*, Location in the inner plexiform layer (expressed as relative depth) versus varicosity size for all varicosities for all cells of a given type of cone bipolar cell (*n* = number of cells): CBC2 (*n* = 2), CBC3 (*n* = 6), CBC4 (*n* = 2), CBC5 (*n* = 6), CBC6 (*n* = 6), CBC7 (*n* = 2), CBC8 (*n* = 1). The size of a varicosity was determined as the diameter of the largest circle that would fit inside the varicosity in the XY plane (see Materials and Methods). Each data point corresponds to an individual varicosity and the data points for a given cell are identical with respect to shape and color saturation. *H*, Overlay of data points for all varicosities of all cone bipolar cells (as in *A* - *G*). The data points for a given cell type are identical (color code indicated in inset).

Figure 11. Sholl analysis of axon terminals of cone and rod bipolar cells. *A*, Left: Shape plot of cone bipolar cell illustrates how the axon is composed of an axon shaft (black) and an axon terminal (green). Right (top and bottom): For the Sholl analysis, a set of nested concentric spheres (1 μm separation) were centered at the start of the axon terminal, i.e., the point of transition between axon shaft and axon terminal (marked by red dot; see Materials and Methods). For clarity, 2D projections of axon terminal

(green) are displayed in two different planes (XY, XZ), overlaid with cross sections of Sholl spheres (red lines). *B*, Relative occurrence of Sholl spheres crossed by processes at a given distance from the start of the axon terminal for the different types of bipolar cells. *C - J*, Different morphological parameters, counted either as a crossing with a specific sphere or contained in the shell between two neighboring spheres, as a function of Sholl sphere radius. Data are plotted as mean values for each cell type.

Figure 12. The relationship between arbor volume and branch density for dendritic trees and axon terminals of cone and rod bipolar cells (color code in inset between panels). *A*, Dendritic branch density (defined as total dendritic branch length divided by the convex hull volume of the dendritic tree(s); in μm^{-2}) versus convex hull volume (in μm^3) of the dendritic tree(s). Here and in *B*, each data point corresponds to an individual cell. A straight line (continuous) has been fitted to the data points and has a slope of -0.44 and an intercept of 0.50. Here and in *B*, the dashed line corresponds to the line fitted to the data points of Teeter and Stevens (2011), corresponding to pyramidal neurons and interneurons from a variety of species, with a slope of -0.55 and an intercept of 0.45. *B*, Axon terminal branch density (defined as total axon terminal branch length divided by the convex hull volume of the axon terminal; in μm^{-2}) versus convex hull volume (in μm^3) of the axon terminal. A straight line (continuous) has been fitted to the data points and has a slope of -0.33 and an intercept of 0.21.

SUPPLEMENTARY FIGURE LEGENDS

Supplementary Figure 1. Thickness of the axon shafts of cone (CBC2 - CBC8) and rod (RBC) bipolar cells at five different positions (with approximately equidistant spacing) from the cell body to the axon terminal (position 1 closest to the cell body, position 5 closest to the axon terminal). For each position, we generated a transverse intensity profile along a straight line (oriented perpendicularly to the local longitudinal axis of the axon) from the deconvolved image stack used for morphological reconstruction. For a given location the intensity profile was generated from the focal plane (slice) where the width was at its maximum. For each intensity profile, the width was taken as the full width at half-maximum (FWHM), estimated from a Gaussian fit. Notice that the FWHM values for rod and cone bipolar cells completely overlap.

Supplementary Figure 2. Dendrograms for morphologically reconstructed bipolar cells. *A*, Dendrograms for CBC2. Here and in *B* - *L*, dendrograms are illustrated independently for the dendritic (d) and axonal (a) trees emanating from the cell body. The length of each vertical line in the dendrograms corresponds to the path length of the corresponding branch segment. *B*, *C*, Dendrograms for CBC3. *D*, Dendrograms for CBC4. *E*, *F*, Dendrograms for CBC5. *G*, *H*, Dendrograms for CBC6. *I*, Dendrograms for CBC7 and CBC8. *J* - *L*, Dendrograms for RBC. Scale bars as indicated in the panels.

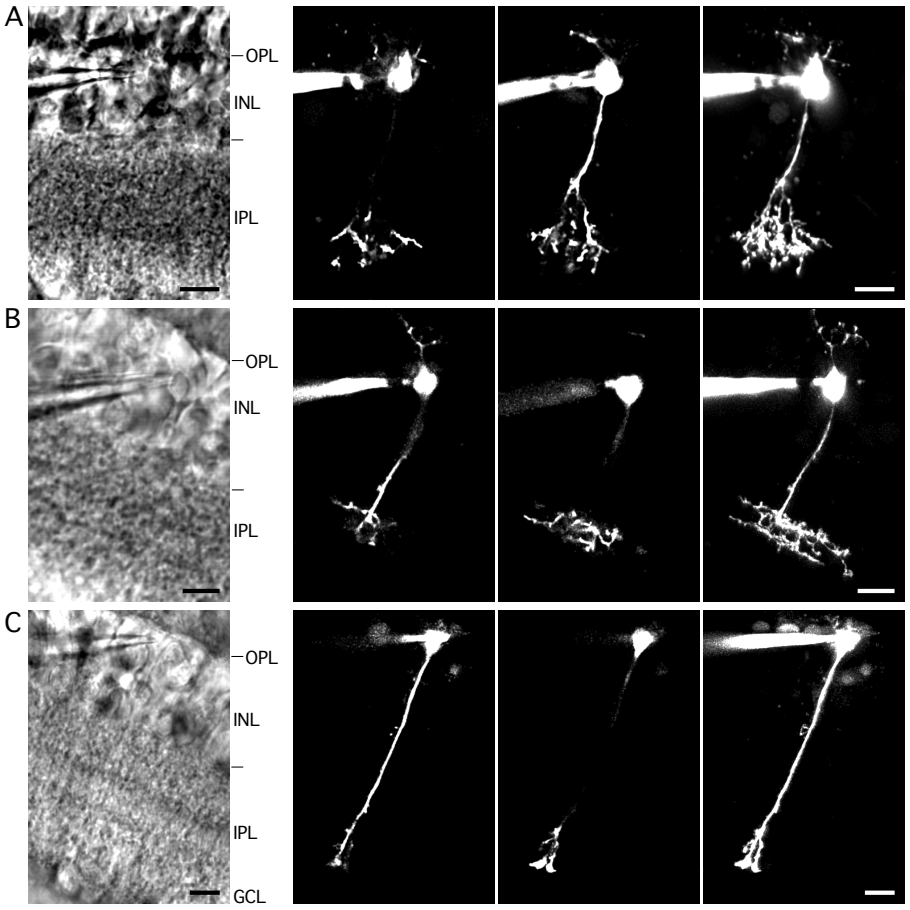

Figure 1 (Fournel et al. 2021)

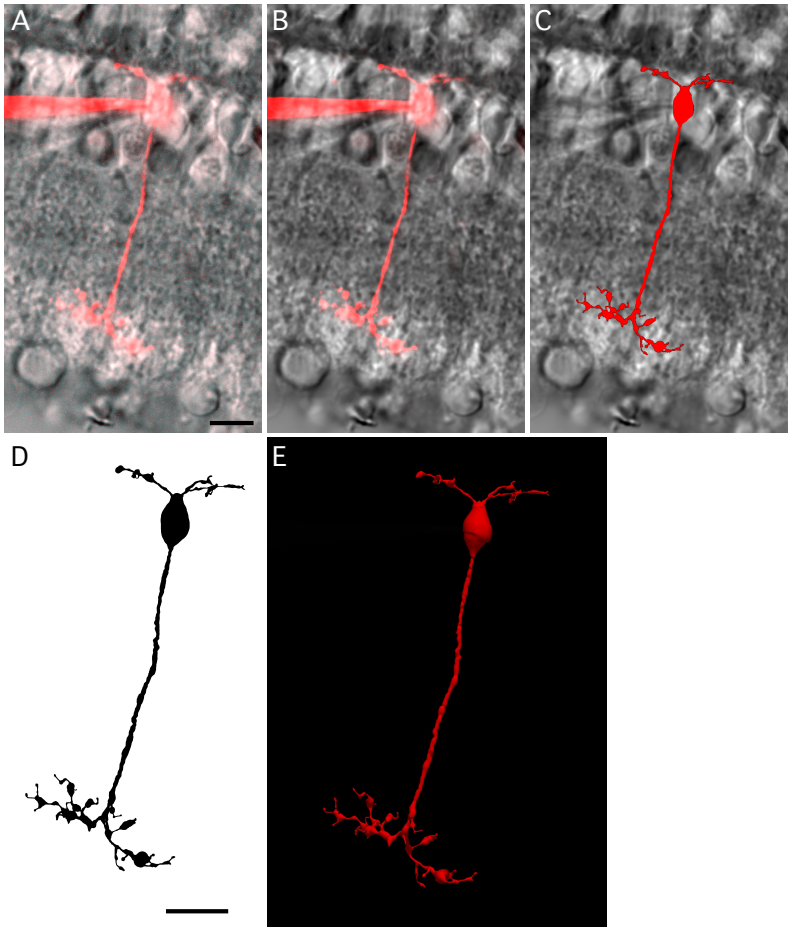

Figure 2 (Fournel et al. 2021)

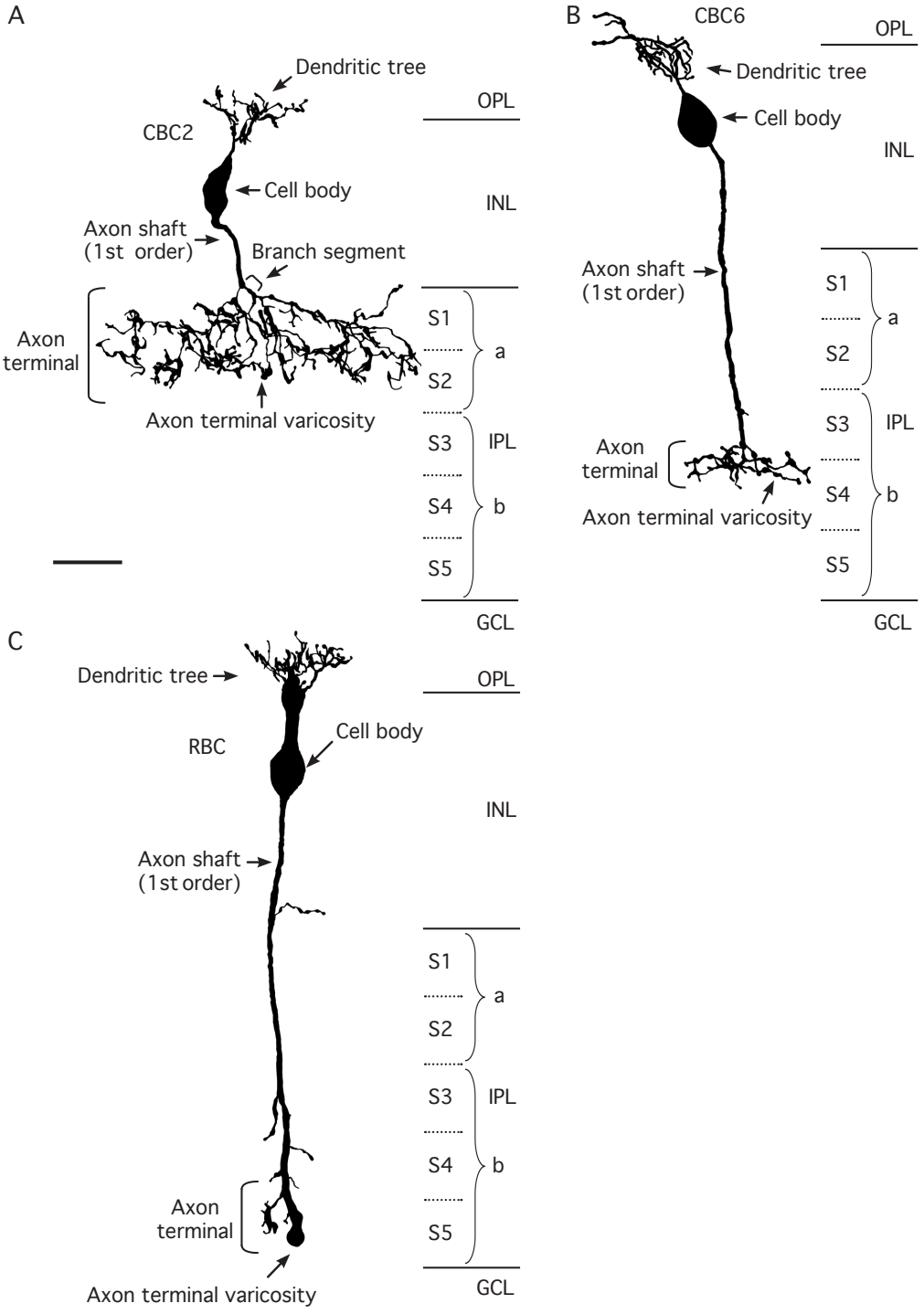

Figure 3 (Fournel et al. 2021)

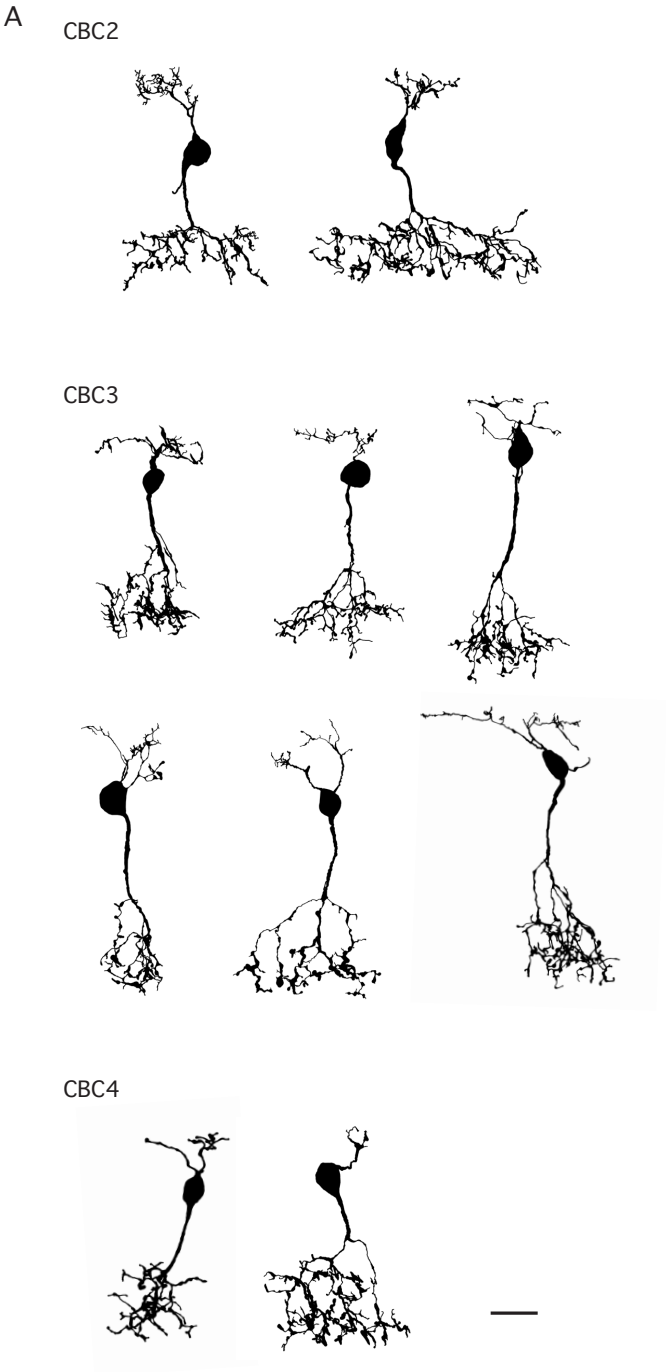

Figure 4A (Fournel et al. 2021)

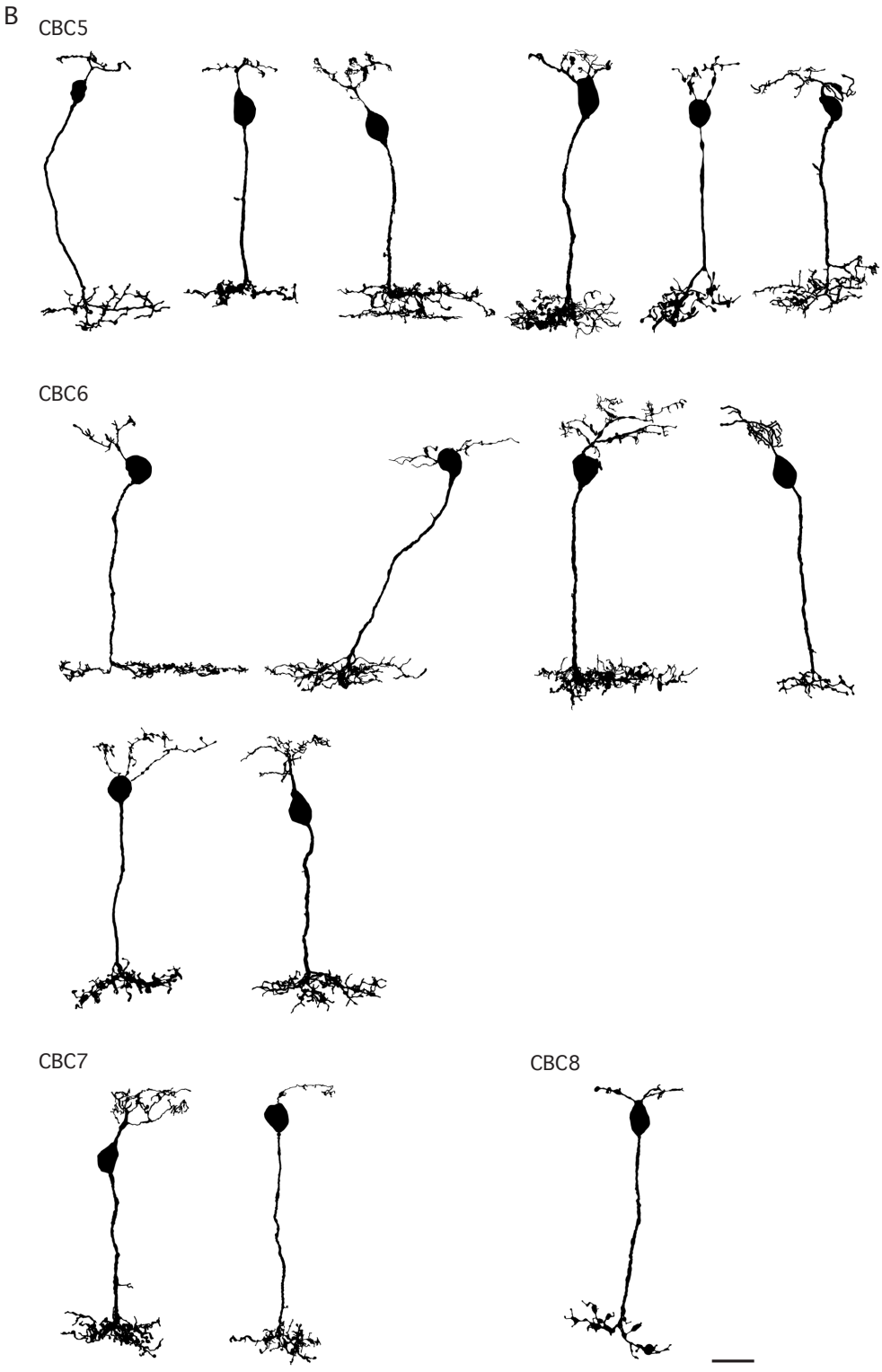

Figure 4B (Fournel et al. 2021)

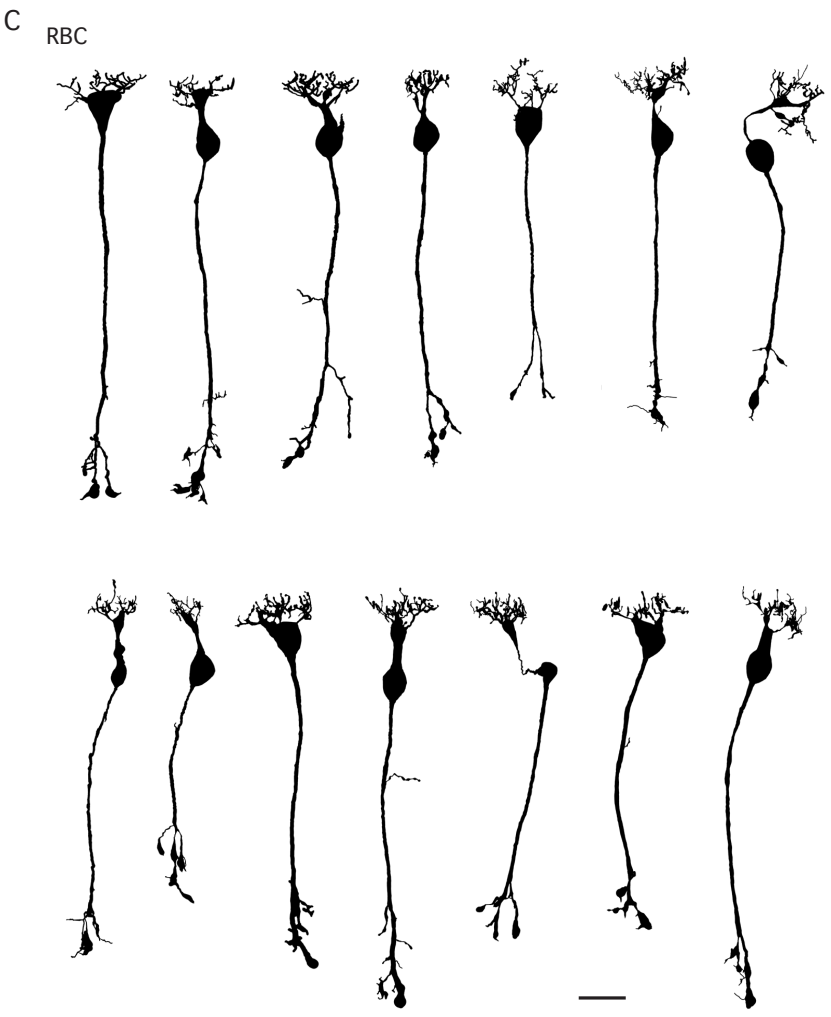

Figure 4C (Fournel et al. 2021)

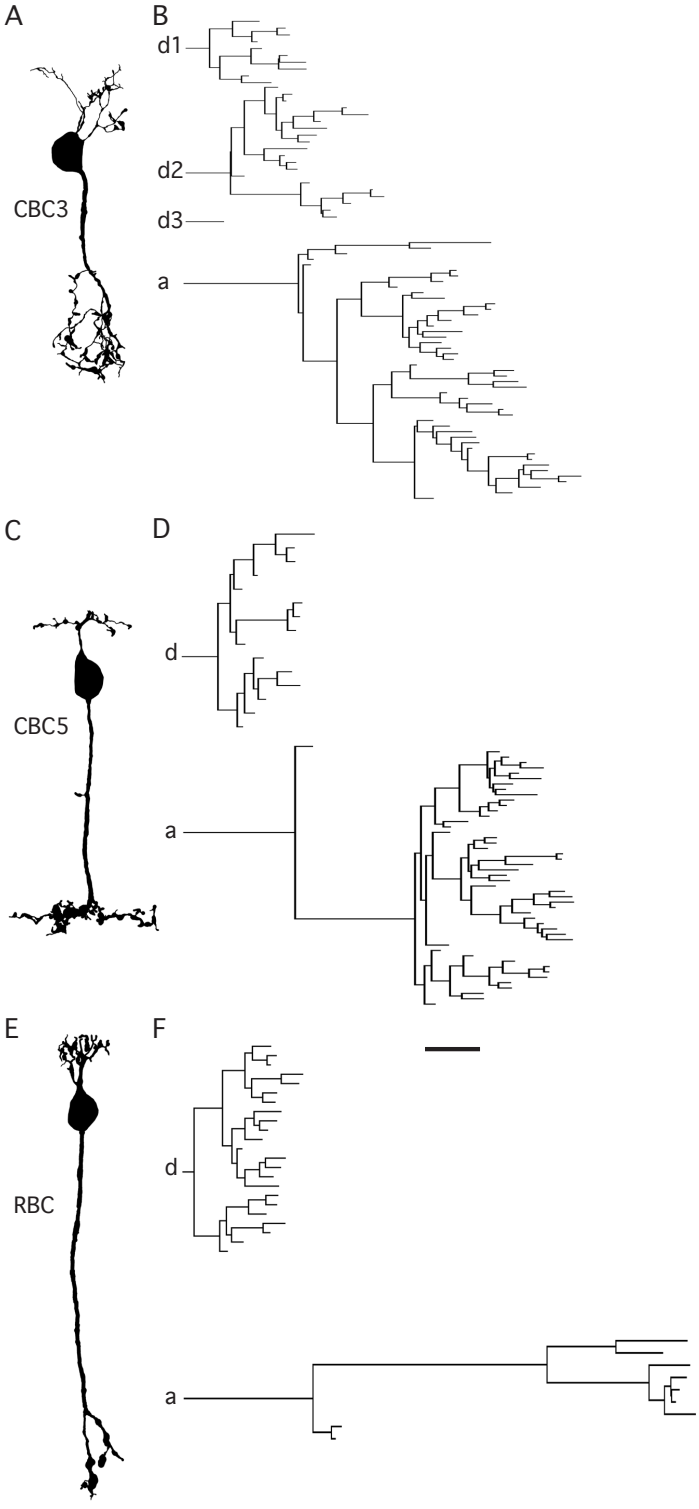

Figure 5 (Fournel et al. 2021)

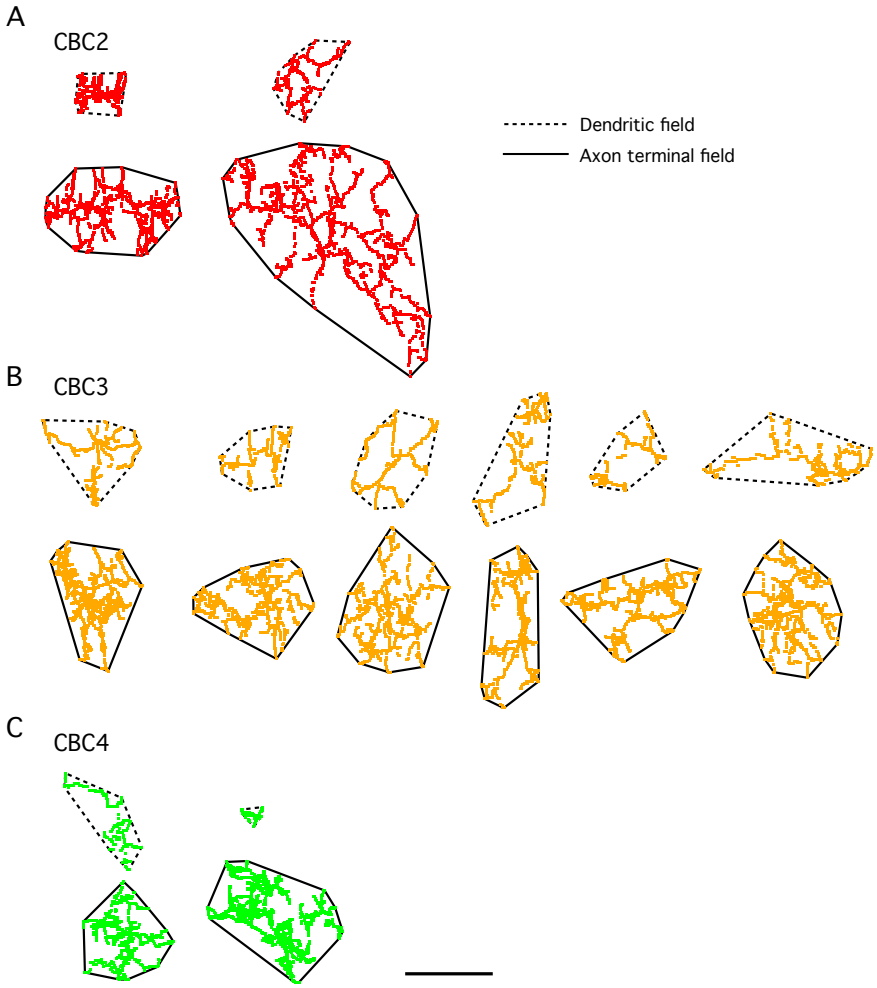

Figure 6A-C (Fournel et al. 2021)

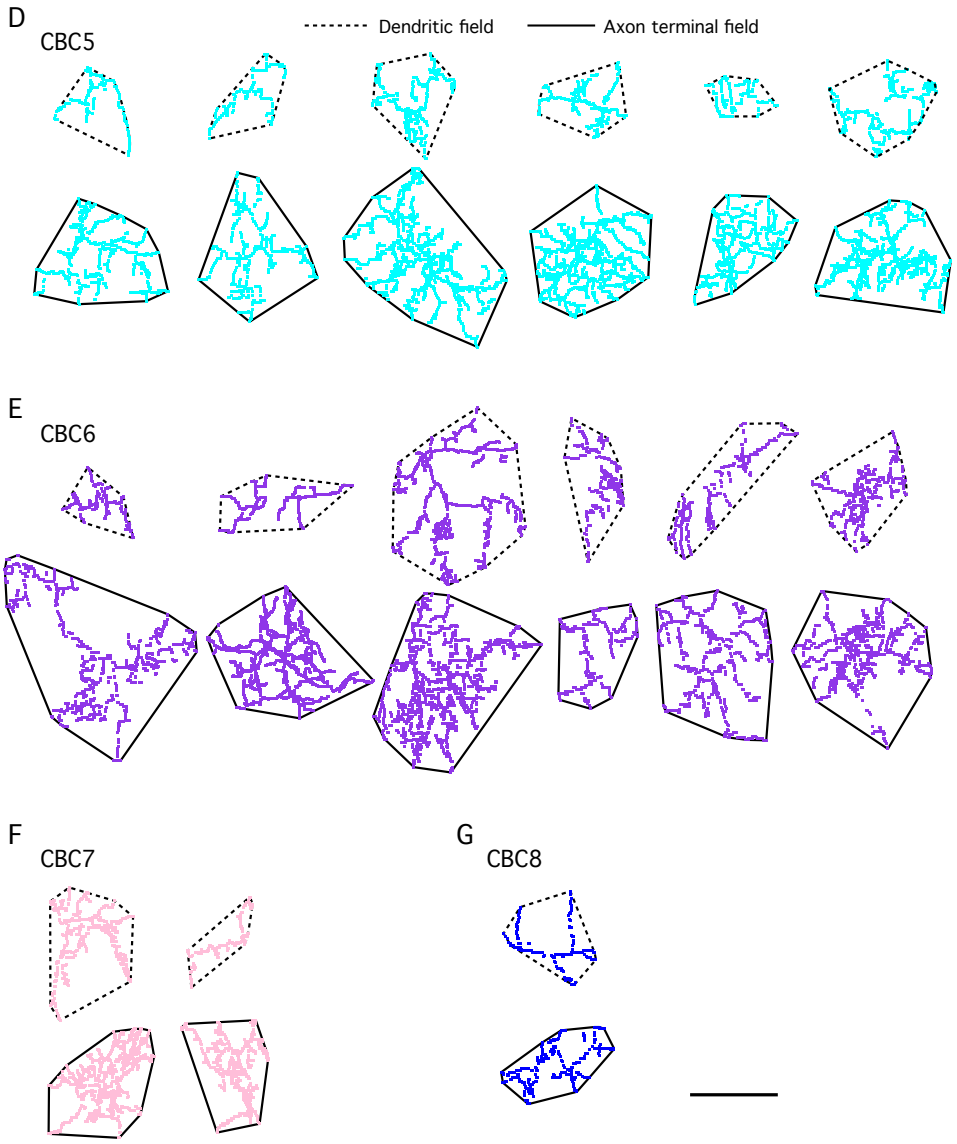

Figure 6D-G (Fournel et al. 2021)

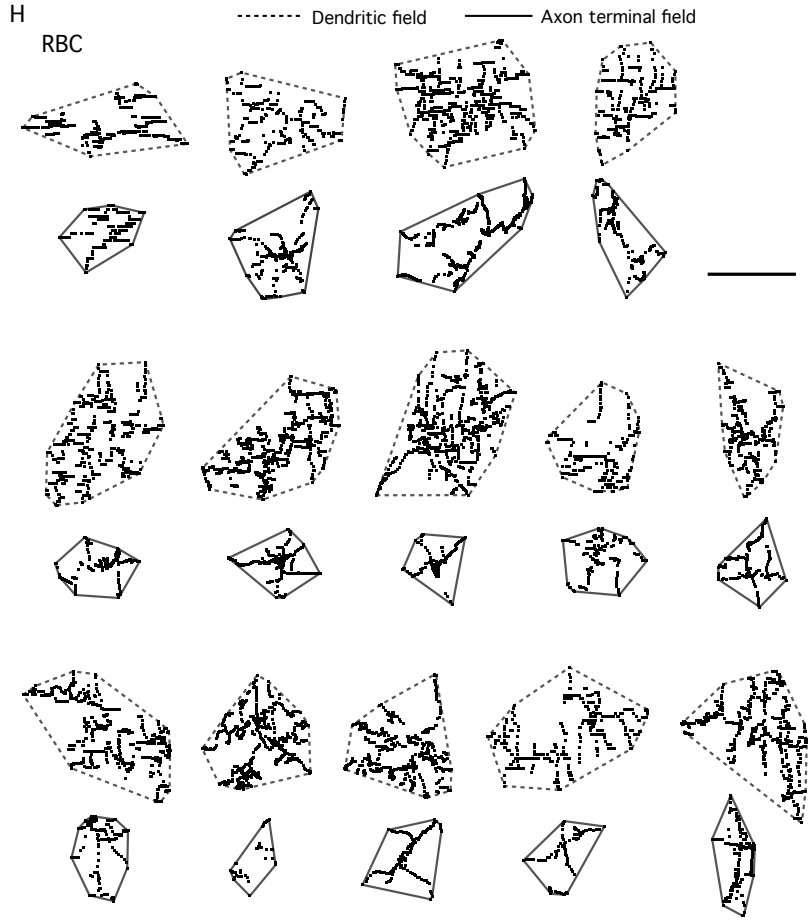

Figure 6H (Fournel et al. 2021)

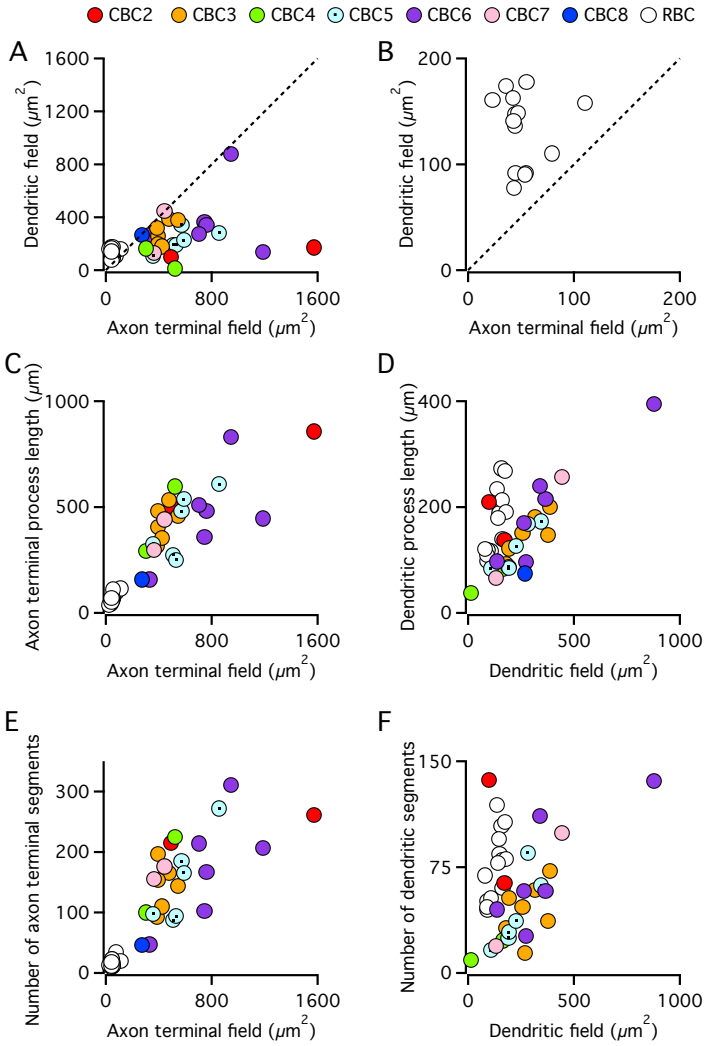

Figure 7 (Fournel et al. 2021)

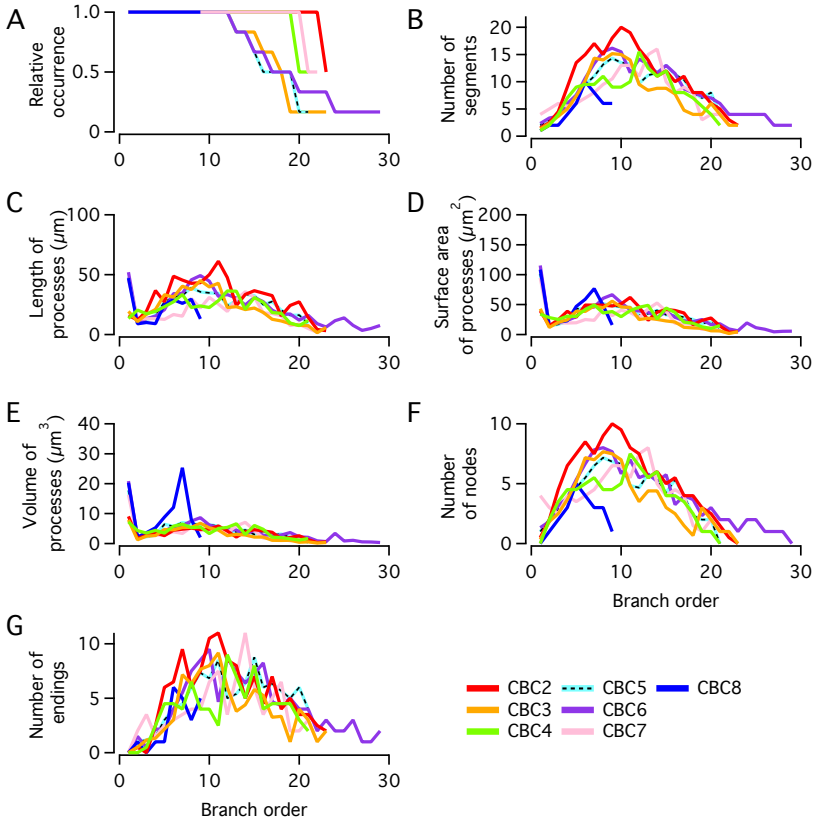

Figure 8 (Fournel et al. 2021)

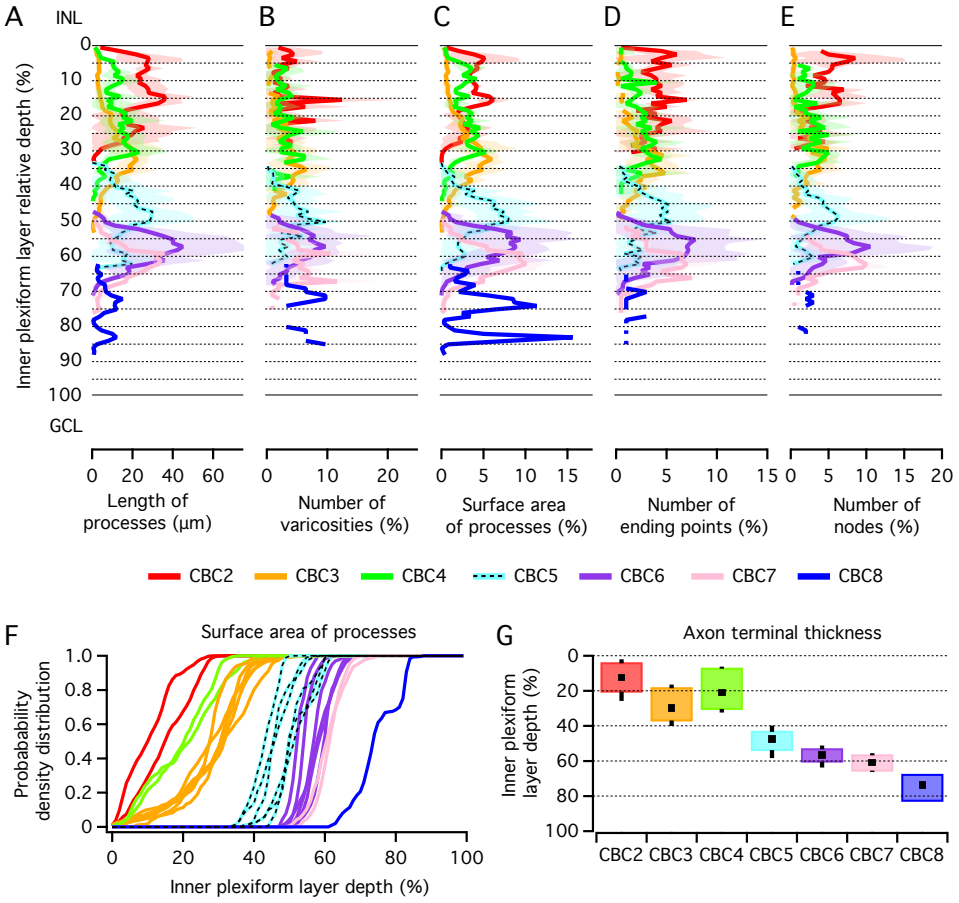

Fig. 9 (Fournel et al. 2021)

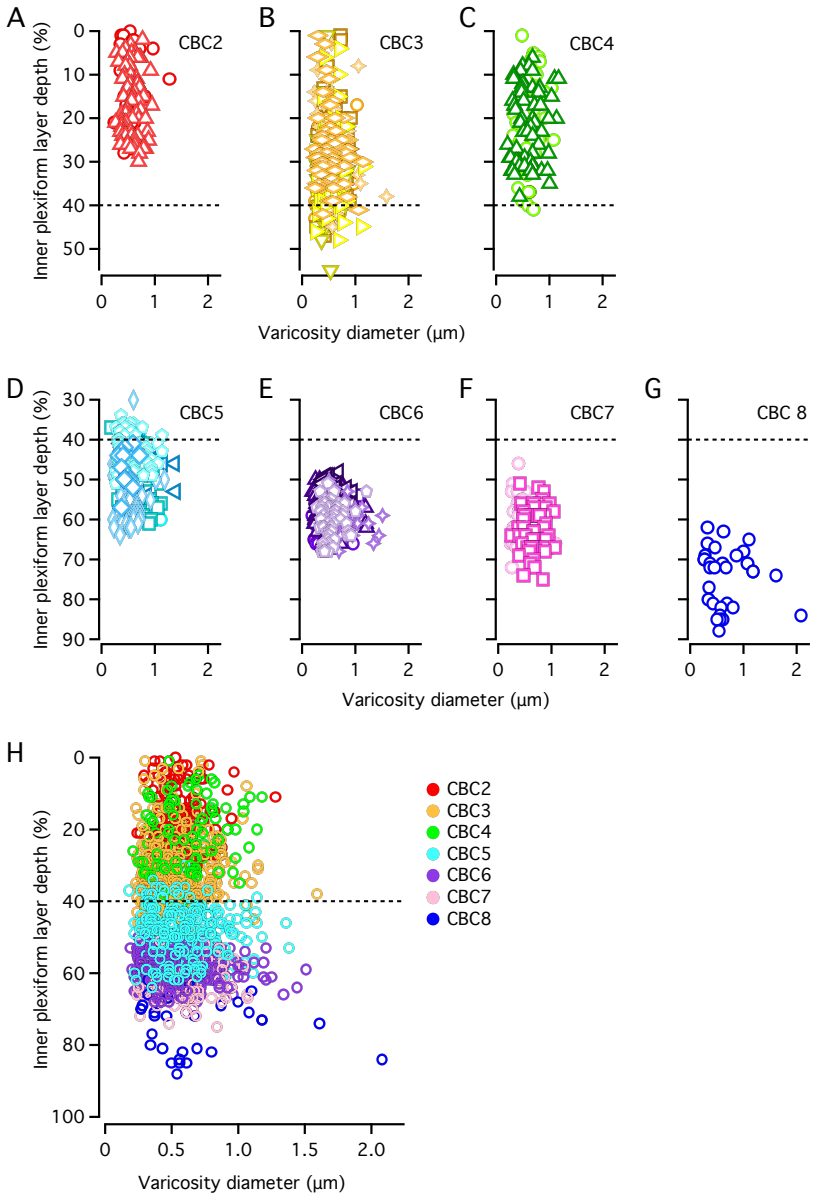

Figure 10 (Fournel et al. 2021)

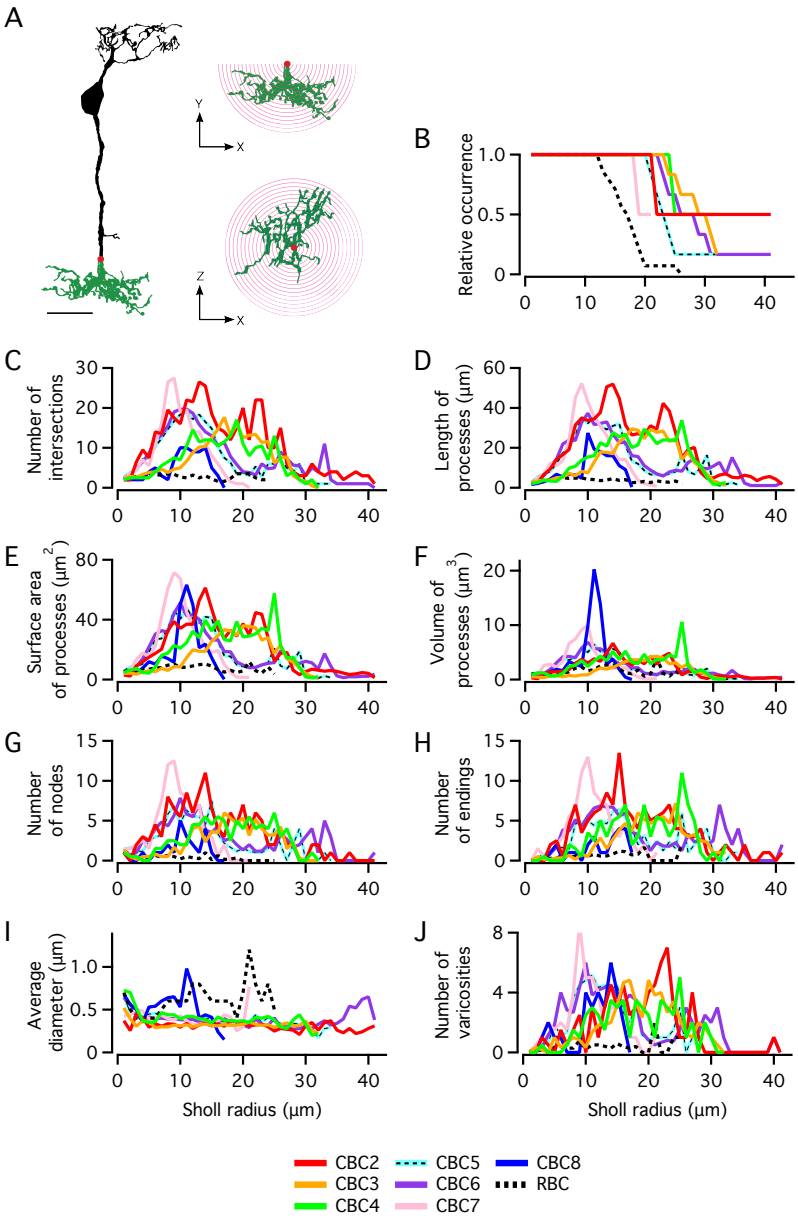

Figure 11 (Fournel et al. 2021)

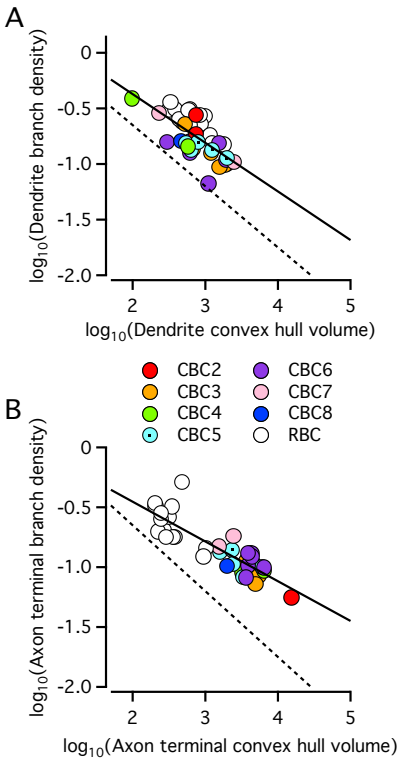

Figure 12 (Fournel et al. 2021)

TABLE 1 OFF CBCs

Morphological properties of reconstructed OFF-cone bipolar cells

	CBC2 (n = 2)	CBC3 (n = 6)	CBC4 (n = 2)
Parameter	Mean ± SD (range)	Mean ± SD (range)	Mean ± SD (range)
Total cell surface area (μm^2)	998 ± 222 (841 – 1155)	754 ± 111 (645 – 917)	836 ± 166 (718 – 953)
Total cell volume (μm^3)	153 ± 4 (150 – 156)	156 ± 18 (140 – 182)	178 ± 40 (150 – 207)
Soma surface area (μm^2)	76 ± 17 (64 – 88)	92 ± 19 (72 – 120)	91 ± 26 (72 – 109)
Soma volume (μm^3)	59 ± 27 (40 – 79)	82 ± 28 (52 – 124)	77 ± 31 (56 – 99)
Soma projection (XY) area (μm^2)	21.2 ± 2.7 (19.2 – 23.1)	25.5 ± 4.7 (21.0 – 32.7)	25.7 ± 7.4 (20.5 – 31.0)
Soma projection (XY) perimeter (μm)	18.5 ± 1.2 (17.7 – 19.3)	19.3 ± 1.9 (17.9 – 22.3)	19.8 ± 3.6 (17.3 – 22.3)
Soma projection (XY) Feret max (μm)	7.0 ± 1.4 (6.0 – 8.0)	7.1 ± 0.5 (6.5 – 8.0)	7.8 ± 1.6 (6.7 – 9.0)
Soma projection (XY) Feret min (μm)	4.3 ± 1.1 (3.5 – 5.0)	4.9 ± 0.8 (3.8 – 5.7)	4.7 ± 0.7 (4.2 – 5.1)
Number of primary dendrites	1.50 ± 0.71 (1 – 2)	1.67 ± 0.82 (1 – 3)	1.00 ± 0.00 (1 – 1)
Number of endings (dendrites)	51 ± 27 (32 – 70)	26 ± 7 (17 – 37)	9 ± 5 (5 – 24)
Number of nodes (dendrites)	50 ± 25 (32 – 67)	24 ± 7 (15 – 35)	8 ± 5 (4 – 11)
Dendritic length (μm)	174 ± 50 (138 – 209)	149 ± 39 (92 – 200)	61 ± 32 (38 – 84)
Axon shaft diameter** (μm)	0.78 ± 0.11 (0.70 – 0.86)	0.72 ± 0.07 (0.62 – 0.83)	0.82 ± 0.03 (0.80 – 0.84)
Axon shaft length (μm)	16.0 ± 3.4 (13.6 – 18.4)	19.4 ± 6.7 (6.9 – 25.1)	13.4 ± 5.8 (9.3 – 17.5)
Axon terminal surface area (μm^2)	726 ± 274 (532 – 920)	491 ± 107 (339 – 642)	617 ± 216 (464 – 770)
Axon terminal volume (μm^3)	71 ± 29 (51 – 92)	55 ± 14 (38 – 71)	80 ± 22 (65 – 96)
Axon terminal total length (μm)	680 ± 250 (503 – 856)	424 ± 82 (315 – 533)	445 ± 215 (293 – 598)
Axon terminal average branch	2.82 ± 0.65	3.03 ± 0.35	2.78 ± 0.21

segment path length (μm)*	(2.40 – 3.28)	(2.50 – 3.41)	(2.63 – 2.93)
Maximum branch order (central shaft ordering)	22.5 ± 0.7 (22 – 23)	17.2 ± 3.7 (12 – 23)	20.0 ± 1.4 (19 – 21)
Number of nodes (Axon shaft)	1.5 ± 0.7 (1 – 2)	1.2 ± 1.1 (0 – 3)	1.0 ± 0.0 (1 – 1)
Number of endings (Axon shaft)	0.50 ± 0.71 (0 – 1)	0.33 ± 0.89 (0 – 2)	0.00 ± 0.00 (0 – 0)
Number of nodes (axon terminal)	118 ± 17 (106 – 130)	71 ± 19 (46 – 97)	80 ± 43 (49 – 111)
Number of endings (axon terminal)	119 ± 14 (109 – 129)	73 ± 19 (47 – 99)	82 ± 45 (50 – 114)
Average partition asymmetry (axon terminal)*	0.644 ± 0.014 (0.634 – 0.654)	0.600 ± 0.044 (0.551 – 0.668)	0.645 ± 0.031 (0.624 – 0.667)
Number of varicosities	55 ± 41 (26 – 84)	55 ± 11 (46 – 74)	49 ± 15 (38 – 59)
Average diameter of varicosities (μm)	0.570 ± 0.014 (0.56 – 0.58)	0.538 ± 0.032 (0.49 – 0.58)	0.630 ± 0.028 (0.61 – 0.65)
2D convex hull area (XZ), dendrites (μm^2)†	135 ± 53 (97 – 172)	286 ± 90 (179 – 389)	88 ± 107 (12 – 164)
2D convex hull perimeter (XZ), dendrites (μm)†	46 ± 12 (38 – 55)	64 ± 17 (46 – 88)	37 ± 32 (15 – 59)
2D convex hull Feret max (XZ), dendrites (μm)†	18 ± 6 (14 – 22)	28 ± 8 (20 – 39)	16 ± 15 (5 – 26)
2D convex hull Feret min (XZ), dendrites (μm)†	10.3 ± 0.8 (9.7 – 10.8)	14.9 ± 1.7 (12.0 – 17.3)	6.7 ± 3.5 (4.2 – 9.2)
Aspect ratios (Feret max / Feret min), dendrites†	1.65 ± 0.14 (1.55 – 1.74)	1.77 ± 0.55 (1.34 – 2.49)	1.35 ± 0.26 (1.17 – 1.53)
2D convex hull area (XZ), axon terminal (μm^2)†	1031 ± 764 (491 – 1572)	436 ± 62 (388 – 543)	414 ± 154 (332 – 523)
2D convex hull perimeter (XZ), axon terminal (μm)†	121 ± 53 (83 – 158)	83 ± 5 (77 – 89)	77 ± 16 (67 – 88)
2D convex hull Feret max (XZ), axon terminal (μm)†	47 ± 23 (31 – 63)	32 ± 3 (28 – 37)	27 ± 7 (23 – 32)
2D convex hull Feret min (XZ), axon terminal (μm)†	28 ± 12 (20 – 36)	19 ± 3 (13 – 22)	20 ± 1 (19 – 21)
Aspect ratios (Feret max / Feret min), axon terminal†	1.7 ± 0.4 (1.4 – 2.0)	1.9 ± 0.5 (1.3 – 2.5)	2.0 ± 1.2 (1.2 – 2.9)
3D convex hull surface area axon terminal (μm^2)	2807 ± 1729 (1584 – 4030)	1561 ± 199 (1279 – 1790)	1549 ± 533 (1172 – 1926)
3D convex hull volume axon	10024 ± 7523	4561 ± 976	4814 ± 2209

terminal (μm^3)	(4705 – 15344)	(3612 – 5872)	(3253 – 6376)
Ratios of the area between the dendritic tree and axon terminal 2D convex hulls†	0.15 ± 0.06 (0.11 – 0.20)	0.65 ± 0.16 (0.42 – 0.82)	0.28 ± 0.36 (0.02 – 0.54)
Bifurcation angle (mean; axon terminal)	91.3 ± 1.7 (90.1 – 92.5)	91.7 ± 5.4 (84.8 – 98.5)	95.8 ± 2.6 (94.0 – 97.7)
Bifurcation angle (standard deviation*; axon terminal)	34.5 ± 0.2 (34.4 – 34.6)	32.7 ± 2.5 (29.7 – 36.2)	27.9 ± 1.6 (26.7 – 29.1)

Metrics were obtained from Neurolucida Explorer, except those marked with * (from L-measure) and † (from IGOR Pro). For some metrics where it would otherwise not be obvious, the L-measure function names are stated in parenthesis. For all metrics except bifurcation angle, each cell contributed one data point and the averages and SDs were calculated for the 10 data points (OFF-cone bipolar cells).

Average partition asymmetry: a measure for how much a neuronal tree deviates from a symmetrically partitioned tree where each node gives rise to two subtrees that contain an equal number of nodes, with 0 corresponding to a perfectly symmetric tree and 1 corresponding to a maximally uneven distribution of nodes, i.e. a tree containing a single long process with only single branches sprouting off.

Bifurcation angle: measures the angle between the two daughter branch segments of a bifurcation (angle measured between lines connecting the start and end points of the daughter segments).

** See description of calculation of axon diameter in Materials and Methods.

TABLE 2. ON-cone bipolar cells

Morphological properties of reconstructed ON-cone bipolar cells

	CBC 5 ($n = 6$)	CBC 6 ($n = 6$)	CBC 7 ($n = 2$)	CBC 8 ($n = 1$)
Parameter	Mean ± SD (range)	Mean ± SD (range)	Mean ± SD (range)	Mean
Total cell surface area (μm^2)	881 ± 194 (642 - 1128)	1017 ± 359 (637 - 1670)	845 ± 351 (597 - 1094)	598
Total cell volume (μm^3)	184 ± 56 (102 - 257)	212 ± 54 (165 - 315)	183 ± 36 (158 - 209)	171
Soma surface area (μm^2)	91 ± 28 (51 - 130)	104 ± 11 (90 - 121)	96 ± 10 (89 - 103)	89
Soma volume (μm^3)	79 ± 33 (32 - 122)	97 ± 14 (81 - 119)	87 ± 18.3 (74 - 100)	72
Soma projection (XY) area (μm^2)	25.8 ± 8.1 (14.4 – 37.6)	28.6 ± 2.7 (24.21 – 31.5)	27.1 ± 2.0 (25.7 – 28.5)	26.0
Soma projection (XY) perimeter (μm)	19.6 ± 3.4 (15.0 – 25.3)	20.7 ± 1.6 (18.3 – 22.7)	20.4 ± 0.7 (19.9 – 20.9)	20.8
Soma projection (XY) Feret max (μm)	7.4 ± 1.5 (5.7 – 10.0)	7.5 ± 0.9 (6.4 – 8.6)	7.6 ± 0.5 (7.2 – 8.0)	8.5
Soma projection (XY) Feret min (μm)	4.51 ± 0.77 (3.34 – 5.25)	5.32 ± 0.36 (4.93 – 5.96)	4.89 ± 0.45 (4.57 – 5.20)	4.36
Number of primary dendrites	1.5 ± 0.8 (1 - 3)	2.0 ± 1.3 (1 - 4)	1.5 ± 0.7 (1 - 2)	2.0
Number of endings (dendrites)	22 ± 13 (9 - 43)	37 ± 21 (14 - 69)	30 ± 28 (10 - 50)	8
Number of nodes (dendrites)	20 ± 13 (7 - 42)	35 ± 21 (12 - 67)	29 ± 28 (9 - 49)	6
Dendritic length (μm)	120 ± 41 (84 - 172)	202 ± 111 (97 - 395)	161 ± 136 (66 - 257)	75
Axon shaft diameter** (μm)	0.68 ± 0.06 (0.60 – 0.75)	0.70 ± 0.08 (0.61 – 0.81)	0.67 ± 0.17 (0.55 – 0.79)	0.72
Axon shaft length (μm)	48 ± 12 (39 - 70)	53 ± 5 (44 – 56)	46 ± 9 (39 – 53)	47
Axon terminal surface area (μm^2)	545 ± 150 (355 - 748)	596 ± 272 (208 - 1051)	505 ± 211 (356 - 655)	311
Axon terminal volume (μm^3)	70 ± 21 (40 - 94)	75 ± 37 (25 - 132)	66 ± 34 (42 - 90)	68
Axon terminal total length (μm)	413 ± 149 (251 - 607)	464 ± 221 (158 - 833)	370 ± 102 (297 - 442)	158

Axon terminal average branch segment path length (μm)*	2.89 ± 0.41 (2.22 – 3.32)	2.99 ± 0.74 (2.16 – 3.92)	2.23 ± 0.42 (1.93 – 2.53)	3.43
Maximum branch order (central shaft ordering)	16.5 ± 3.4 (12 - 21)	18.8 ± 5.8 (13 - 28)	21.0 ± 2.8 (19 - 23)	9
Number of nodes (axon shaft)	2.00 ± 0.89 (1 - 3)	2.33 ± 0.82 (1 - 3)	5.00 ± 0.00 (5 - 5)	1
Number of endings (axon shaft)	1.00 ± 0.89 (0 - 2)	1.33 ± 0.82 (0 - 2)	4.00 ± 0.00 (4 - 4)	0
Number of nodes (axon terminal)	74 ± 36 (42 - 135)	87 ± 47 (22 - 155)	83 ± 8 (77 - 88)	22
Number of endings (axon terminal)	76 ± 36 (45 - 137)	88 ± 46 (25 - 156)	83 ± 7 (78 - 88)	24
Average partition asymmetry (axon terminal)*	0.567 ± 0.051 (0.528 – 0.658)	0.620 ± 0.057 (0.566 – 0.725)	0.605 ± 0.078 (0.550 – 0.660)	0.511
Number of varicosities	55 ± 23 (29 - 88)	66 ± 38 (25 - 130)	50 ± 8 (44 - 55)	31
Average diameter of varicosities (μm)	0.59 ± 0.07 (0.51 – 0.70)	0.56 ± 0.09 (0.45 – 0.71)	0.57 ± 0.15 (0.46 – 0.67)	0.68
2D convex hull area (XZ), dendrites (μm^2)†	224 ± 82 (107 - 344)	376 ± 259 (136 - 880)	288 ± 222 (131 - 445)	267
2D convex hull perimeter (XZ), dendrites (μm)†	59 ± 10 (41 – 70)	78 ± 20 (49 - 111)	68 ± 20 (54 – 82)	63.5
2D convex hull Feret max (XZ), dendrites (μm)†	22.2 ± 2.8 (17.0 – 24.5)	32.0 ± 7.7 (19.2 – 40.9)	23.6 ± 6.2 (16.9 – 29.2)	21.9
2D convex hull Feret min (XZ), dendrites (μm)†	14.4 ± 3.5 (9.2 – 18.6)	15.9 ± 7.6 (11.0 – 30.2)	12.3 ± 5.0 (8.9 – 18.0)	17.7
Aspect ratios (Feret max / Feret min), dendrites†	1.44 ± 0.17 (1.30 – 1.66)	1.48 ± 0.07 (1.38 – 1.55)	1.68 ± 0.04 (1.65 – 1.71)	1.9
2D convex hull area (XZ), axon terminal (μm^2)†	570 ± 163 (358 - 856)	778 ± 283 (329 - 1184)	403 ± 57 (363 - 444)	273
2D convex hull perimeter (XZ), axon terminal (μm)†	92 ± 12 (76 - 114)	107 ± 23 (70 - 139)	79 ± 4 (77 - 82)	66
2D convex hull Feret max (XZ), axon terminal (μm)†	33.6 ± 4.9 (30.2 – 43.3)	39.9 ± 8.2 (27.0 – 52.8)	30.7 ± 3.2 (28.4 – 32.8)	26.5
2D convex hull Feret min (XZ), axon terminal (μm)†	23.4 ± 2.7 (18.2 – 26.1)	27.0 ± 5.5 (17.8 – 34.6)	18.3 ± 2.4 (16.7 – 20.0)	14.8
Aspect ratios (Feret max / Feret min), axon terminal†	1.6 ± 0.3 (1.3 – 2.0)	2.2 ± 0.8 (1.4 – 3.5)	2.5 ± 1.2 (1.6 – 3.3)	1.2

3D convex hull surface area axon terminal (μm^2)	1482 ± 402 (1047 - 2229)	1841 ± 591 (881 - 2589)	1077 ± 109 (1000 - 1154)	1000
3D convex hull volume axon terminal (μm^3)	3632 ± 1383 (2335 - 6083)	4073 ± 1534 (1594 - 6397)	2218 ± 311 (1998 - 2438)	1998
Ratios of the area between the dendritic tree and axon terminal 2D convex hulls†	0.39 ± 0.11 (0.30 – 0.60)	0.53 ± 0.30 (0.11 – 0.93)	0.68 ± 0.45 (0.36 – 1.00)	0.98
Bifurcation angle (mean; axon terminal)	93.1 ± 4.1 (86.9 – 98.9)	93.0 ± 4.9 (87.6 – 100.7)	96.5 ± 4.2 (93.5 – 99.4)	85.8
Bifurcation angle (standard deviation*; axon terminal)	29.7 ± 2.9 (25.7 – 33.1)	33.2 ± 3.5 (28.3 – 38.5)	30.61 ± 2.7 (28.7 – 32.5)	27.7

Metrics were obtained from Neurolucida Explorer, except those marked with * (from L-measure) and † (from IGOR Pro). For some metrics where it would otherwise not be obvious, the L-measure function names are stated in parenthesis. For all metrics except bifurcation angle, each cell contributed one data point and the averages and SDs were calculated for the 15 data points (ON-cone bipolar cells).

Average partition asymmetry: see Table 1.

Bifurcation angle: see Table 1.

** See description of calculation of axon diameter in Materials and Methods.

TABLE 3. Rod bipolar cells

Morphological properties of reconstructed rod bipolar cells

	RBC (n = 14)
Parameter	Mean ± SD (range)
Total cell surface area (μm^2)	601 ± 120 (428 - 854)
Total cell volume (μm^3)	185 ± 44 (98 - 250)
Soma surface area (μm^2)	104 ± 25 (40 - 137)
Soma volume (μm^3)	95 ± 32 (23 - 132)
Soma projection (XY) area (μm^2)	29.7 ± 7.1 (11.3 – 40.6)
Soma projection (XY) perimeter (μm)	22.4 ± 4.0 (13.3 – 30.4)
Soma projection (XY) Feret max (μm)	8.6 ± 2.0 (4.9 – 13.1)
Soma projection (XY) Feret min (μm)	4.94 ± 0.90 (2.96 – 6.13)
Number of primary dendrites	2.1 ± 1.4 (1 - 5)
Number of endings (dendrites)	39 ± 12 (23 - 60)
Number of nodes (dendrites)	37 ± 12 (22 - 59)
Dendritic length (μm)	175 ± 59 (97 - 273)
Axon shaft diameter** (μm)	0.76 ± 0.10 (0.59 – 0.90)
Axon shaft length (μm)	56 ± 10 (36 – 75)
Axon terminal surface area (μm^2)	131 ± 42 (72 - 209)
Axon terminal volume (μm^3)	26.7 ± 9.7 (8.2- 46.7)
Axon terminal length (μm)	69 ± 23 (37 - 116)
Axon terminal average branch segment path	5.0 ± 2.7

length (μm)*	(2.3 – 12.3)
Maximum branch order (central shaft ordering)	3.7 ± 1.1 (2 - 6)
Number of nodes (axon shaft)	2.3 ± 1.4 (1 - 6)
Number of endings (axon shaft)	1.3 ± 1.6 (0 - 6)
Number of nodes (axon terminal)	7.4 ± 3.6 (4 - 17)
Number of endings (axon terminal)	9.1 ± 3.5 (6 - 18)
Average partition asymmetry (axon terminal)*	0.55 ± 0.18 (0.80 – 0.10)
Number of varicosities	6.1 ± 2.5 (2 - 11)
Average diameter of varicosities (μm)	1.07 ± 0.20 (0.85 – 1.52)
2D convex hull area (XZ), dendrites (μm^2)†	133 ± 34 (78 - 178)
2D convex hull perimeter (XZ), dendrites (μm)†	46.0 ± 6.6 (35.8 – 60.7)
2D convex hull Feret max (XZ), dendrites (μm)†	17.2 ± 3.5 (10.4 – 24.8)
2D convex hull Feret min (XZ), dendrites (μm)†	11.0 ± 2.2 (7.1 – 15.0)
Aspect ratios (Feret min / Feret max), dendrites†	1.75 ± 0.47 (1.33 – 2.98)
2D convex hull area (XZ), axon terminal (μm^2)†	52 ± 21 (23 - 111)
2D convex hull perimeter (XZ), axon terminal (μm)†	28.8 ± 5.6 (20.9 – 43.8)
2D convex hull Feret max (XZ), axon terminal (μm)†	11.3 ± 2.6 (8.7 – 18.3)
2D convex hull Feret min (XZ), axon terminal (μm)†	6.7 ± 1.4 (3.8 – 9.4)
Aspect ratios (Feret min / Feret max), axon terminal†	1.63 ± 0.46 (0.69 – 2.49)
3D convex hull surface area AxT (μm^2)	300 ± 123 (117 - 664)
3D convex hull volume AxT (μm^3)	333 ± 220 (73 - 943)

Ratios of the area between the dendritic tree and axon terminal 2D convex hulls†	3.0 ± 1.5 (1.4 – 7.0)
Bifurcation angle (mean; axon terminal)	74 ± 11 (61 – 93)
Bifurcation angle (standard deviation*; axon terminal)	24.4 ± 9.8 (4.3 – 35.8)

Metrics were obtained from Neurolucida Explorer, except those marked with * (from L-measure) and † (from IGOR Pro). For some metrics where it would otherwise not be obvious, the L-measure function names are stated in parenthesis. For all metrics except bifurcation angle, each cell contributed one data point and the averages and SDs were calculated for the 14 data points (rod bipolar cells).

Average partition asymmetry: see Table 1.

Bifurcation angle: see Table 1.

** See description of calculation of axon diameter in Materials and Methods.

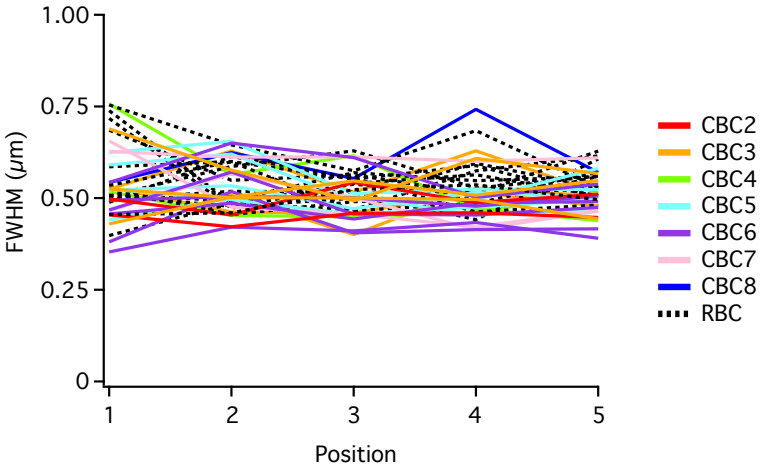

Supplementary Figure 1 (Fournel et al. 2021)

A

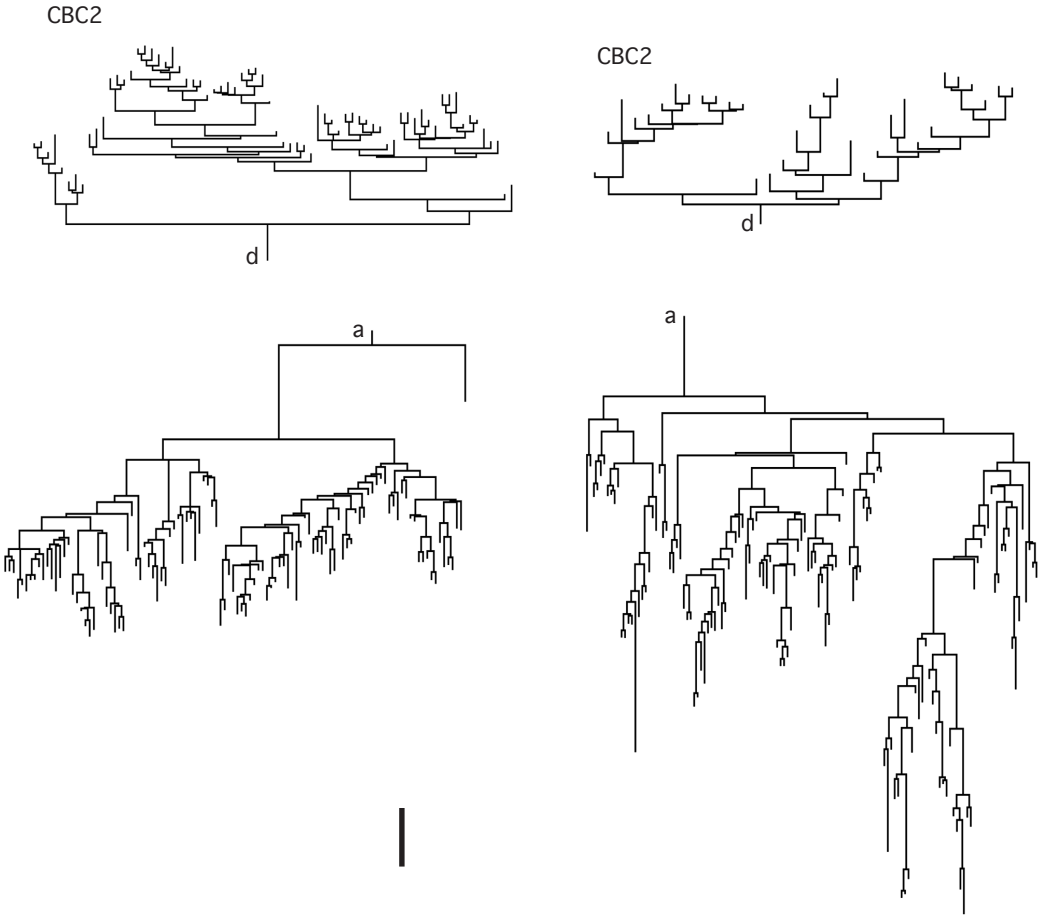

Supplementary Figure 2A (Fournel et al. 2021)

B

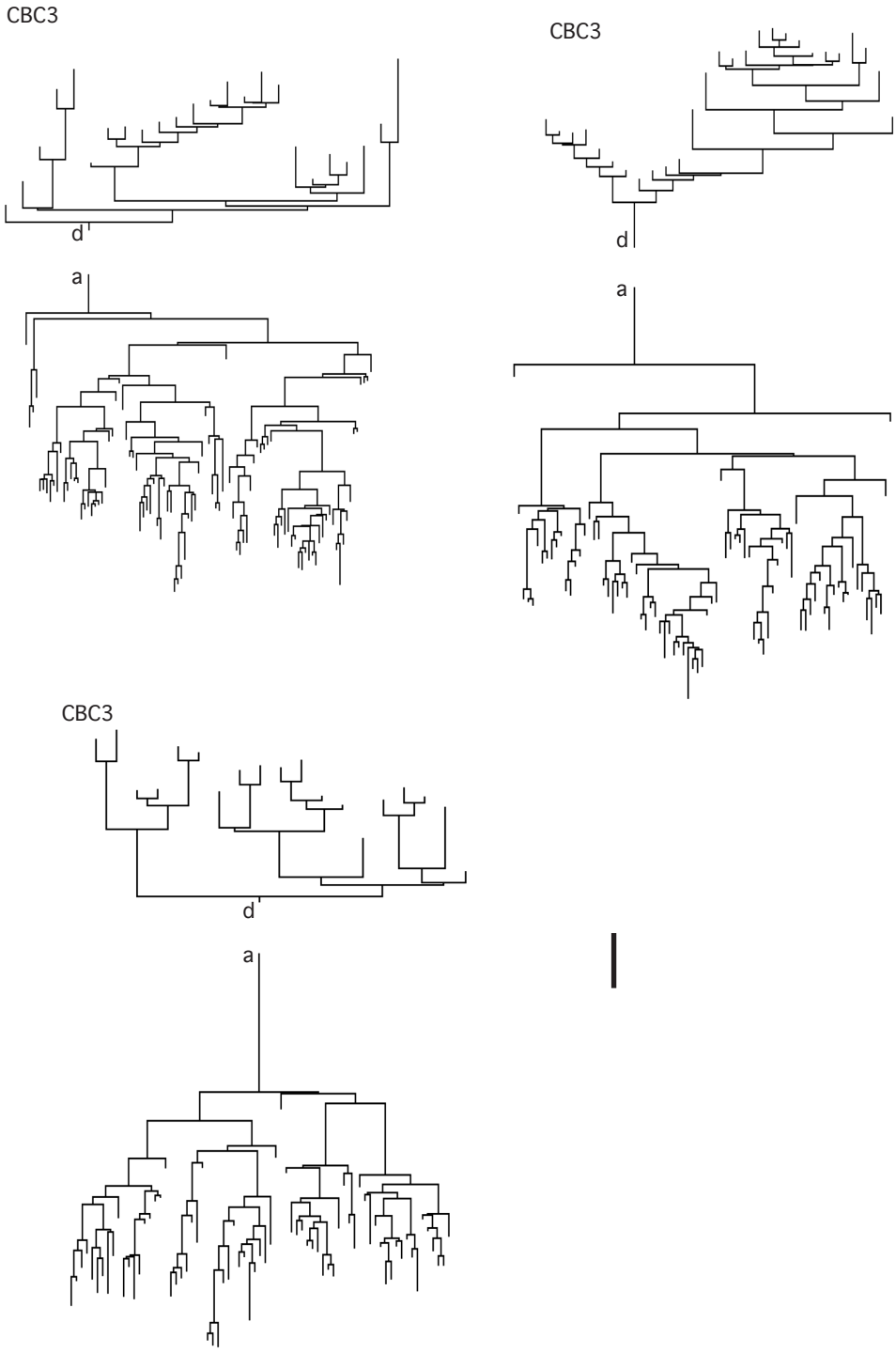

Supplementary Figure 2B (Fournel et al. 2021)

C

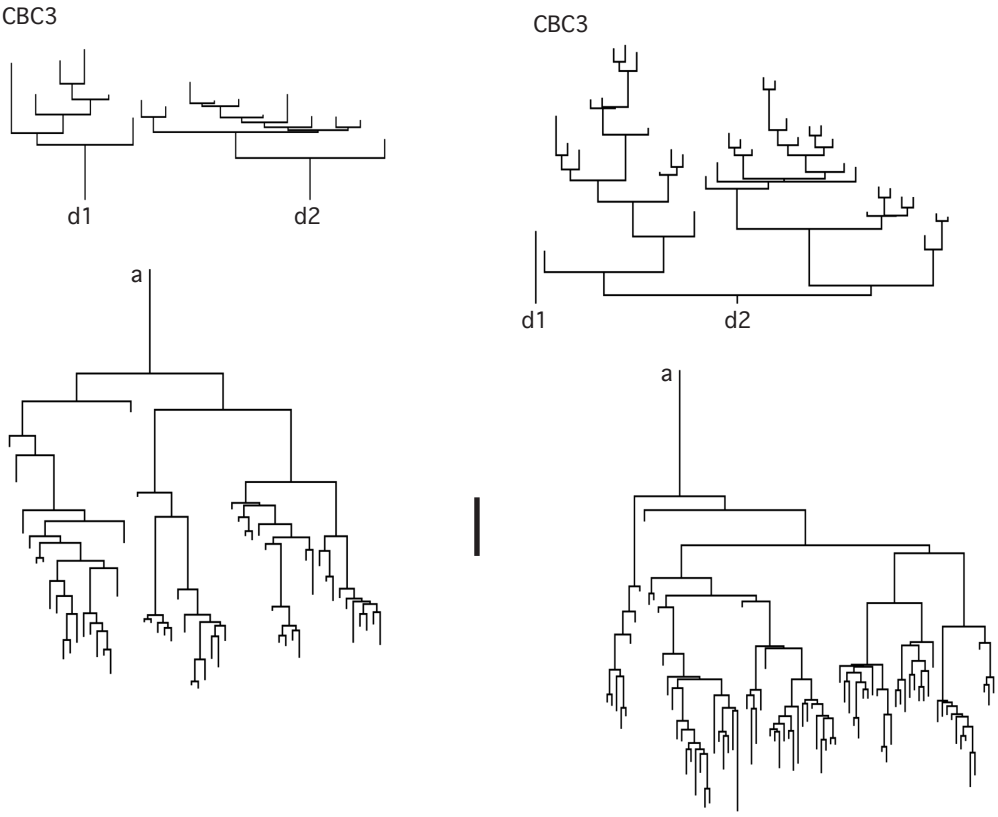

Supplementary Figure 2C (Fournel et al. 2021)

D

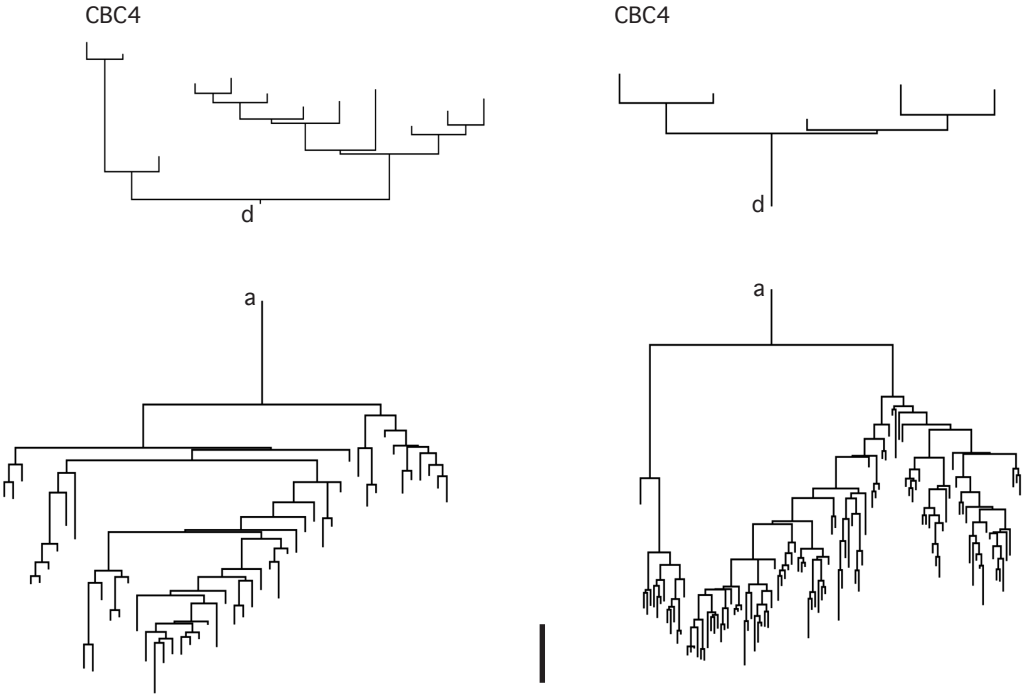

Supplementary Figure 2D (Fournel et al. 2021)

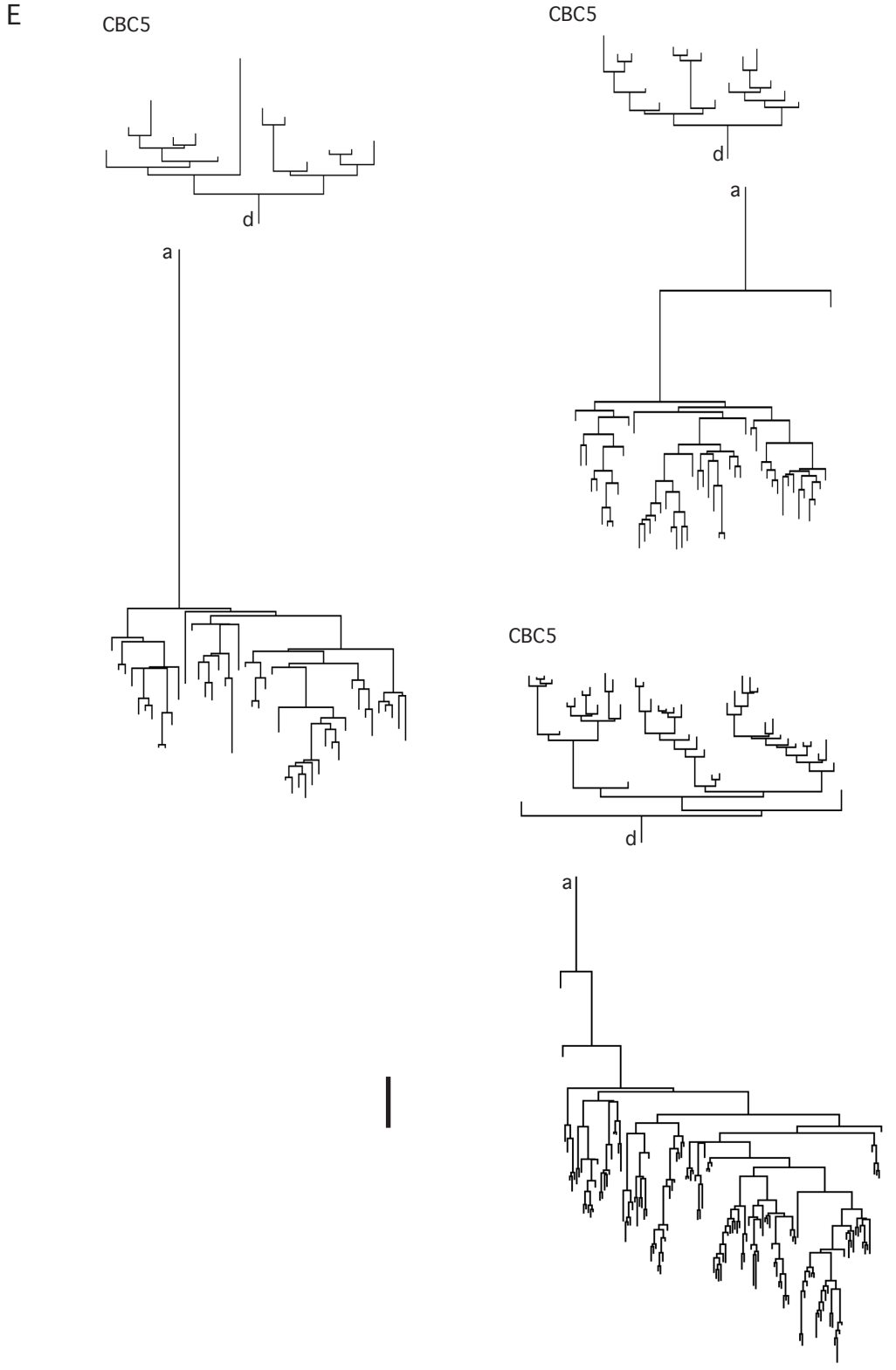

Supplementary Figure 2E (Fournel et al. 2021)

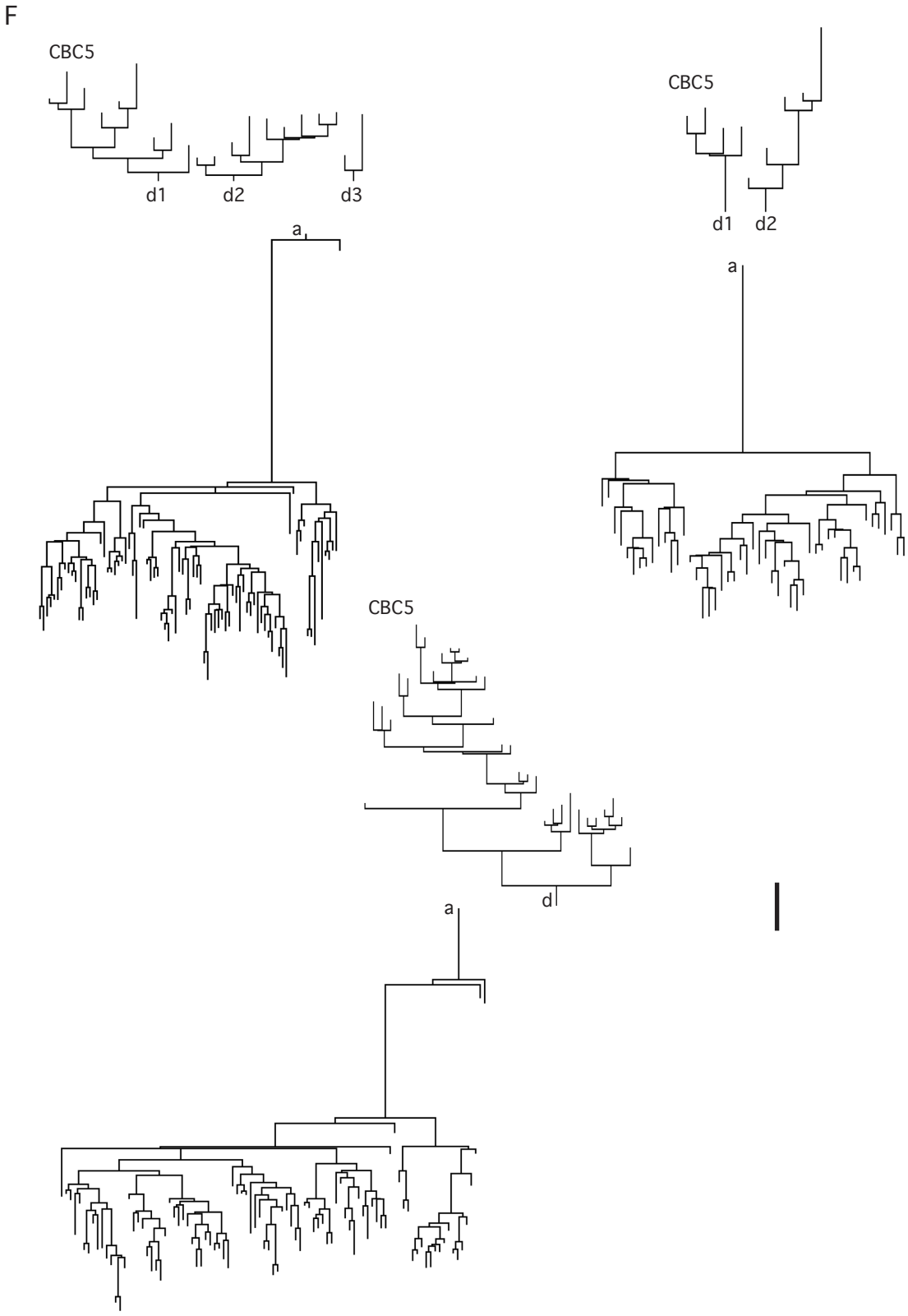

Supplementary Figure 2F (Fournel et al. 2021)

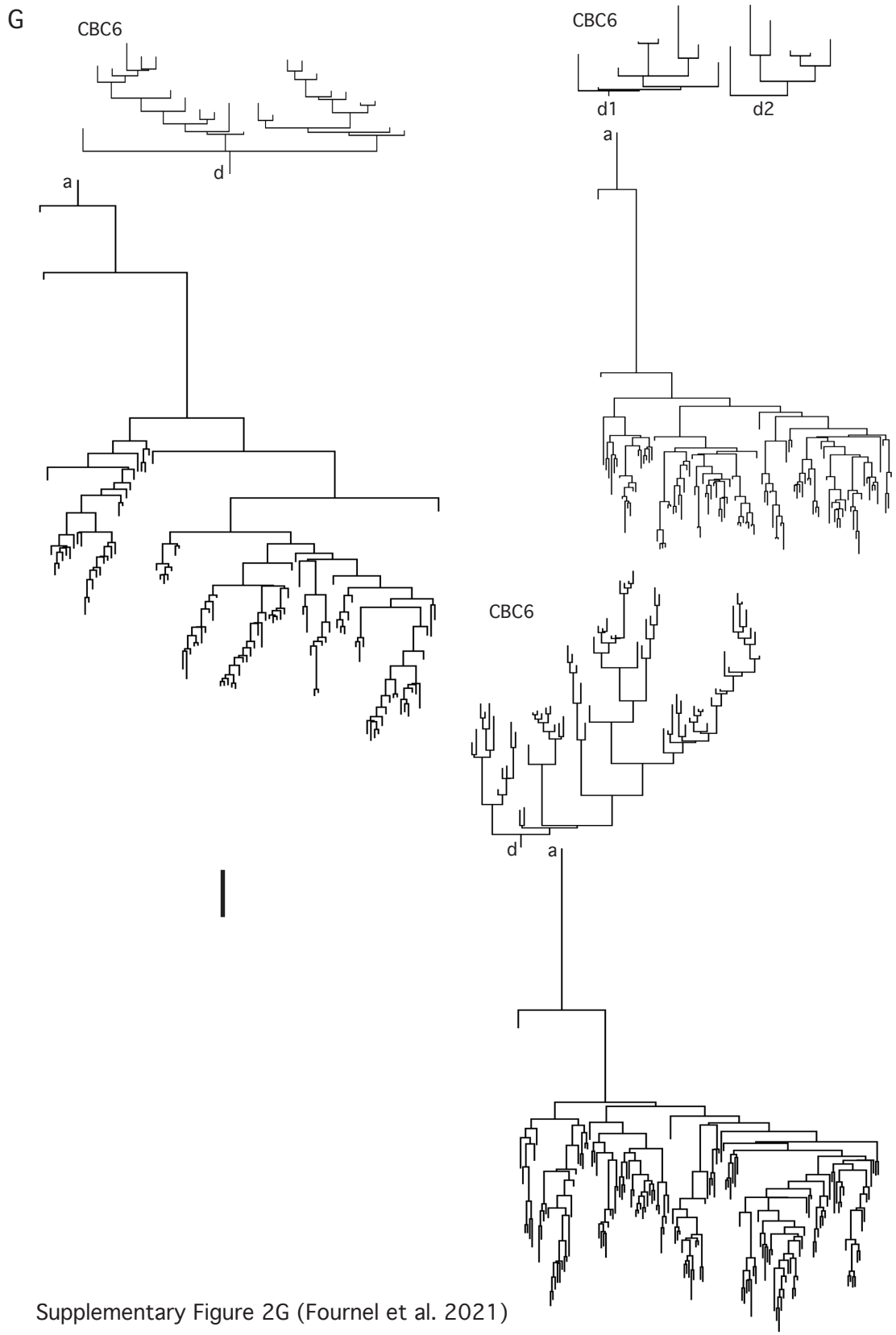

Supplementary Figure 2G (Fournel et al. 2021)

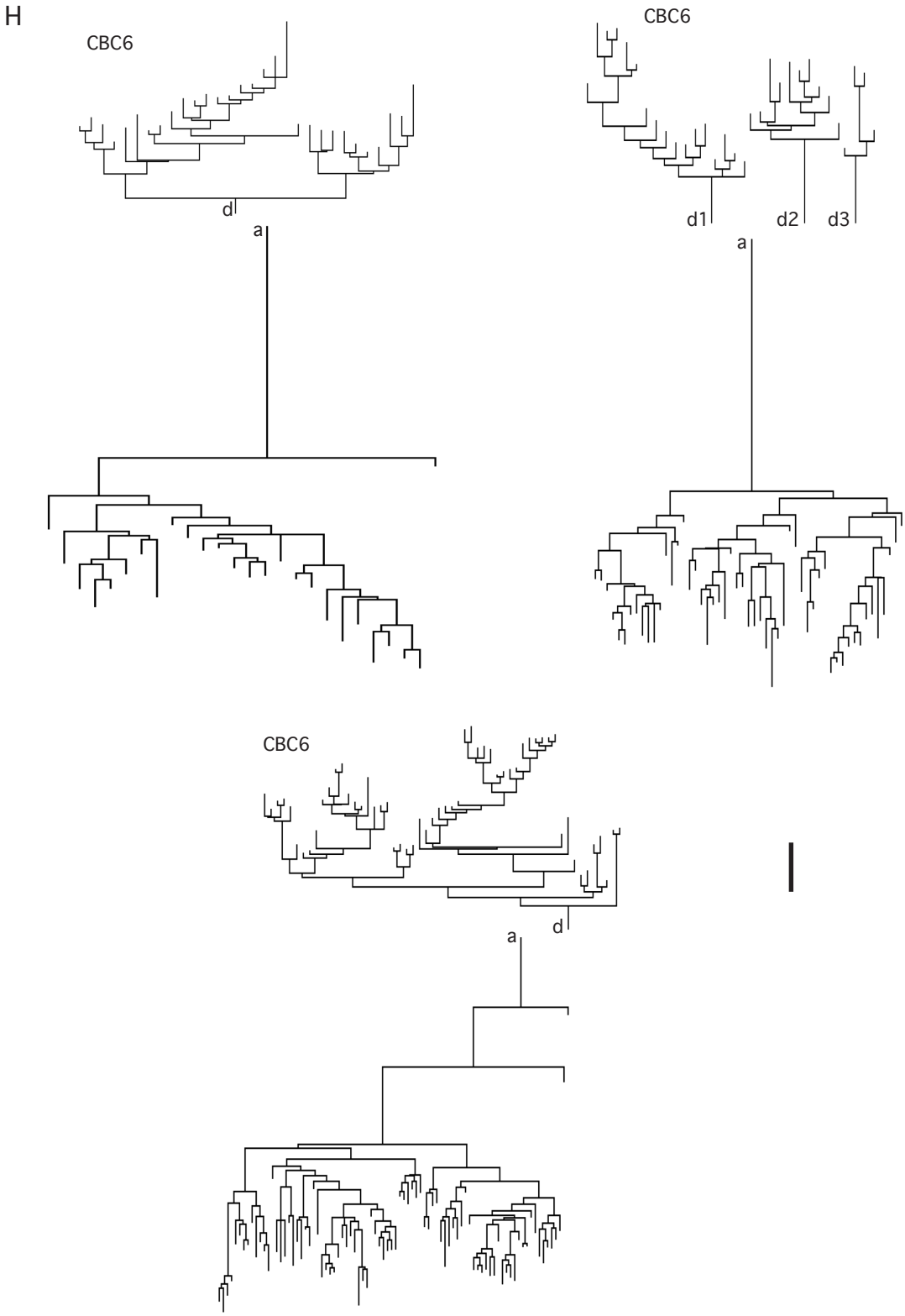

Supplementary Figure 2H (Fournel et al. 2021)

I

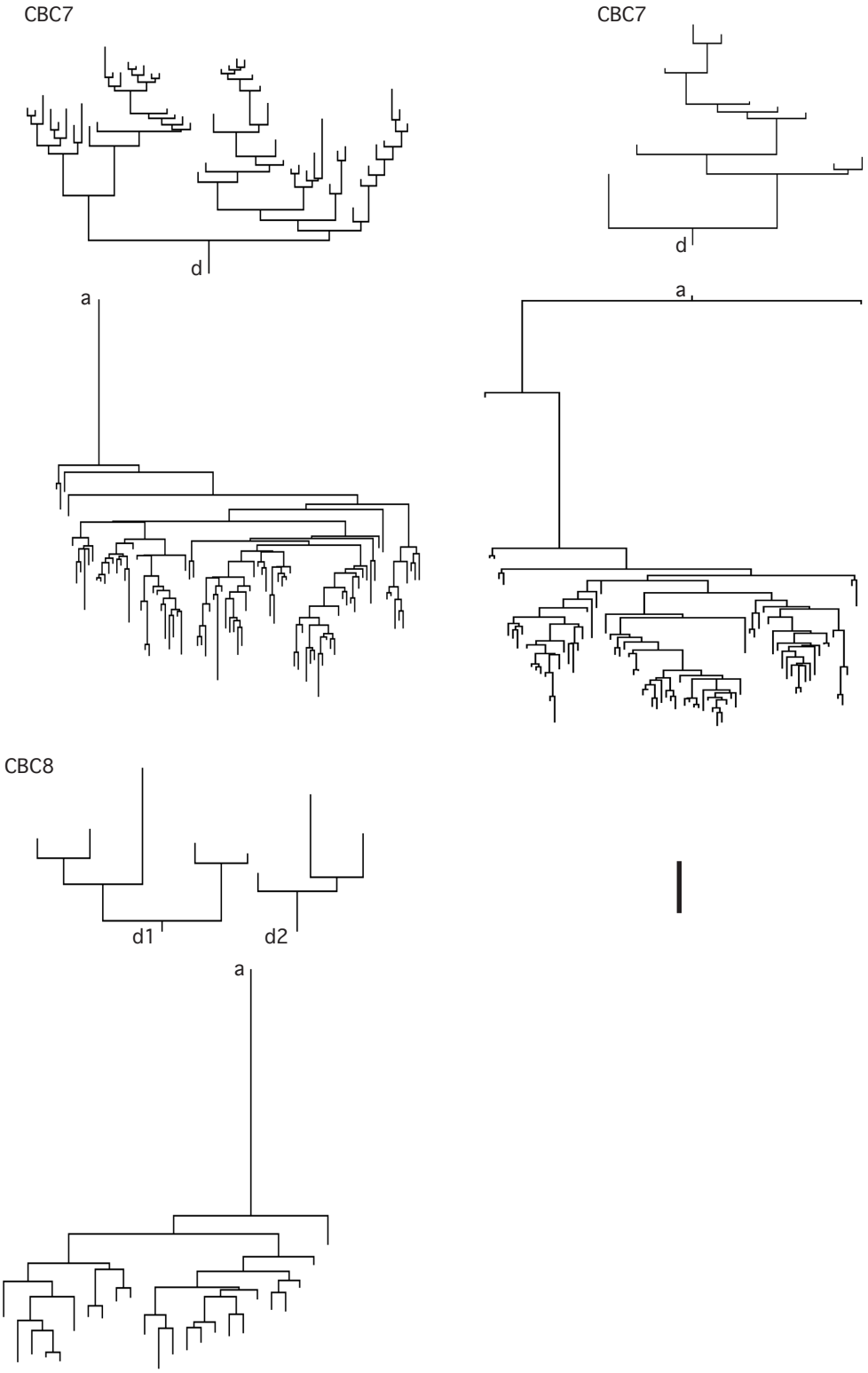

Supplementary Figure 2I (Fournel et al. 2021)

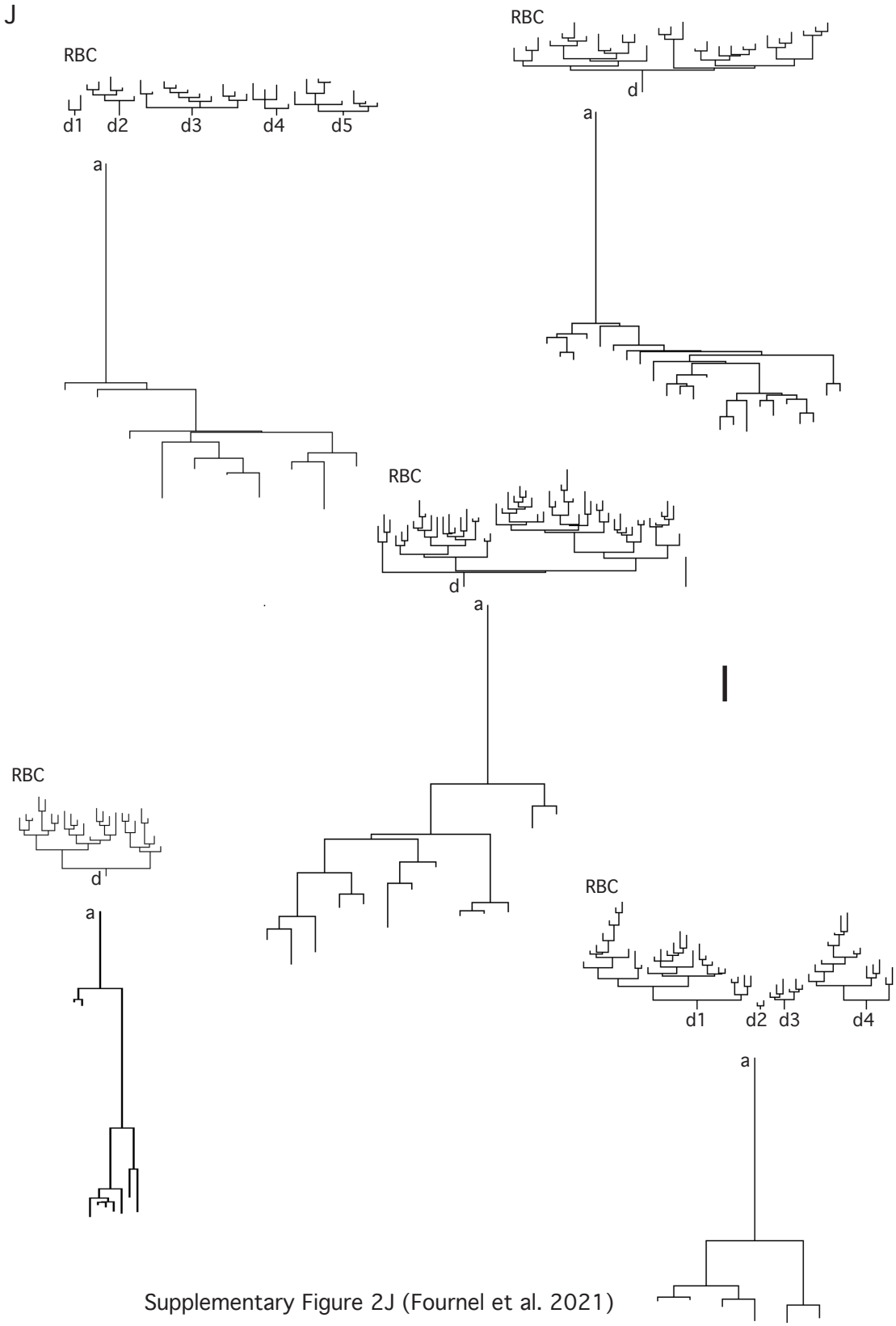

Supplementary Figure 2J (Fournel et al. 2021)

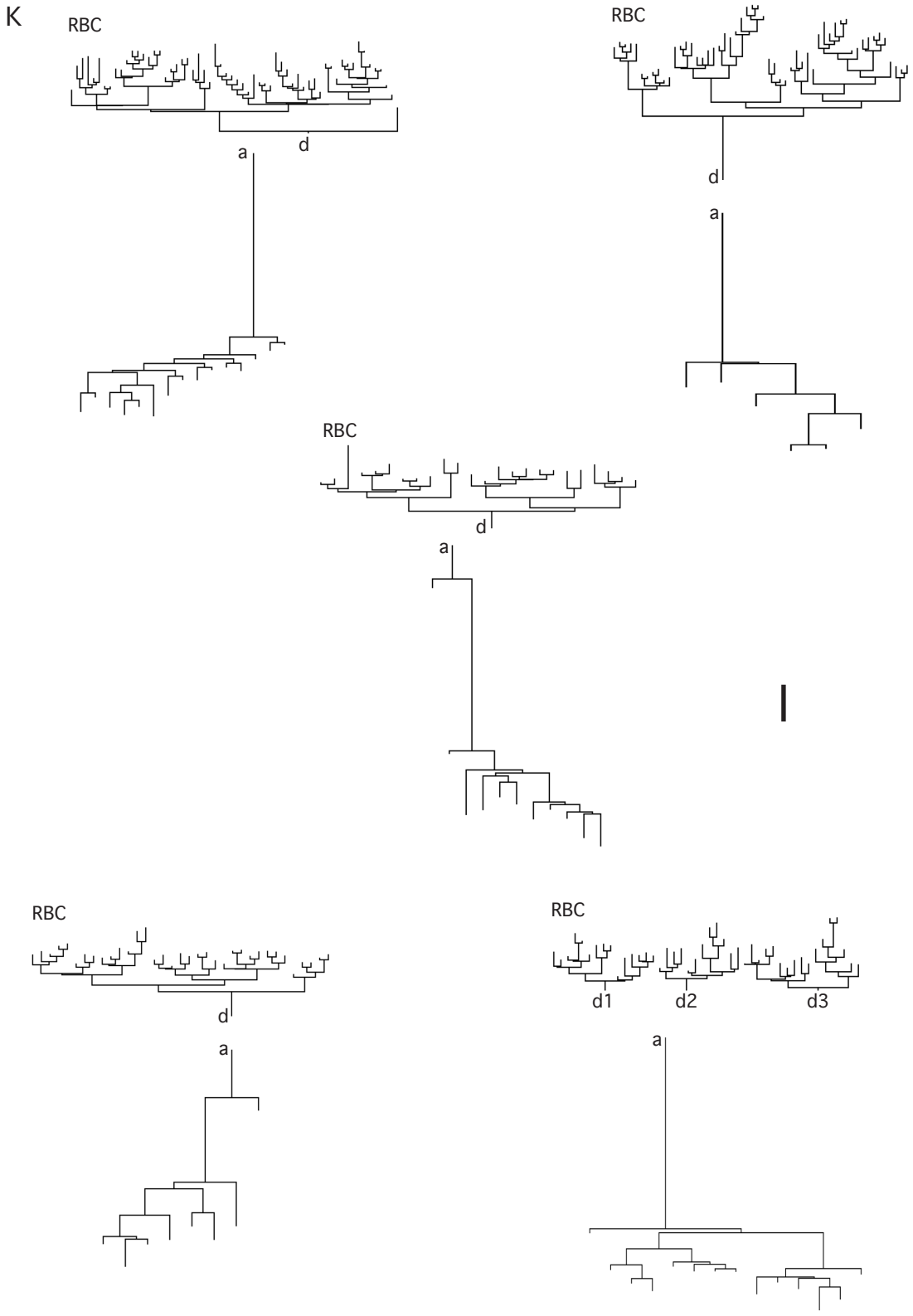

Supplementary Figure 2K (Fournel et al. 2021)

L

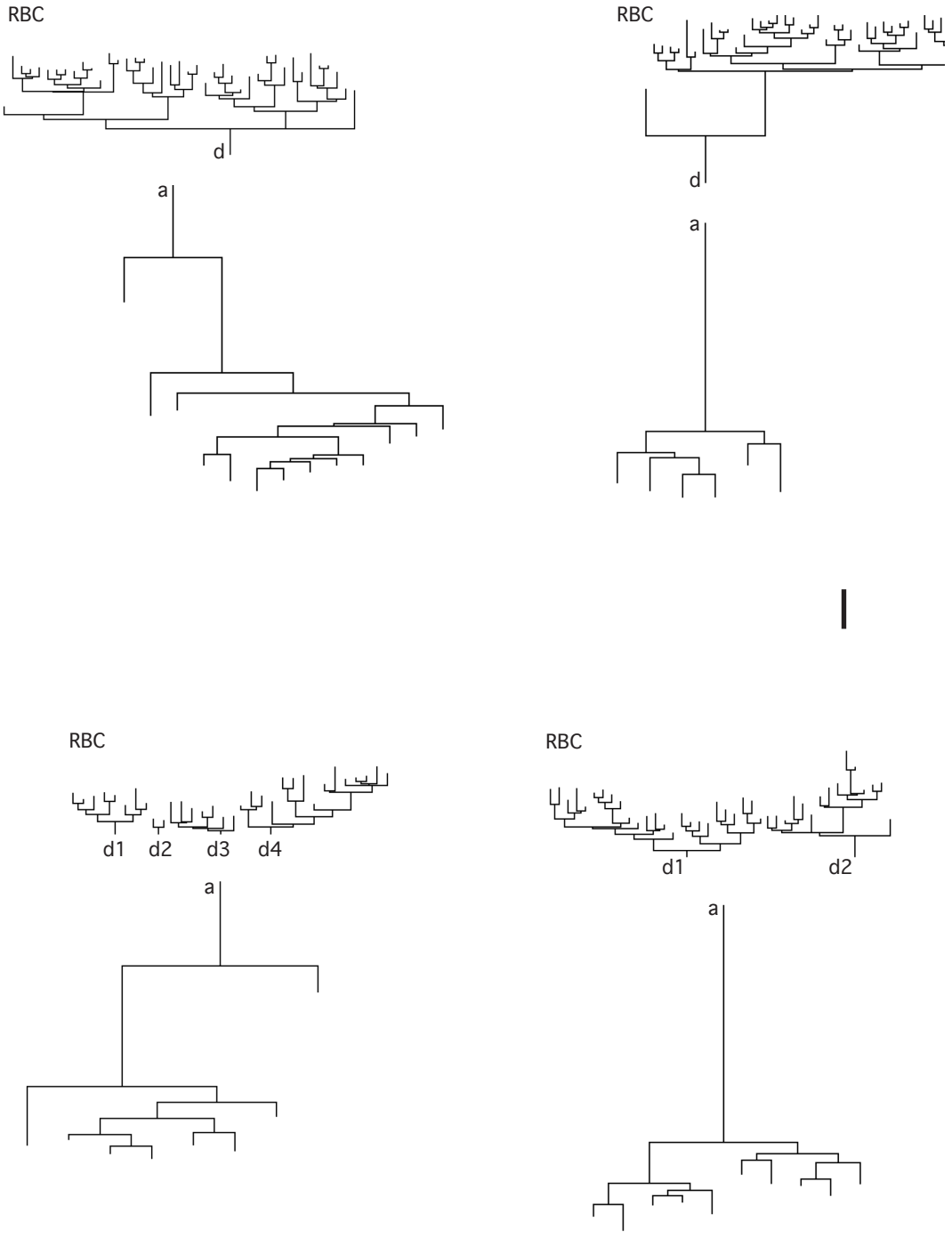

Supplementary Figure 2L (Fournel et al. 2021)

Errata

Page 10: Misused word: “scotopic” in the sentence: “Rod photoreceptors can be active at daylight (Altimus et al., 2010; Naarendorp et al., 2010; Pasquale et al., 2020; Tikidji-Hamburyan et al., 2017), and AII amacrine cells, the critical component of the rod bipolar cell pathway, are known to play a different role at scotopic luminosity (Münch et al., 2009; Oesch and Diamond, 2009).” – corrected to “photopic” giving the following sentence: “Rod photoreceptors can be active at daylight (Altimus et al., 2010; Naarendorp et al., 2010; Pasquale et al., 2020; Tikidji-Hamburyan et al., 2017), and AII amacrine cells, the critical component of the rod bipolar cell pathway, are known to play a different role at photopic luminosity (Münch et al., 2009; Oesch and Diamond, 2009).”

Graphic design: Communication Division, UiB / Print: Skipnes Kommunikasjon AS

uib.no

ISBN: 9788230859001 (print)
9788230869277 (PDF)